MANCHESTER 1824

The University of Manchester

Residual Stress and Fracture in High Temperature Ceramics

A thesis submitted to The University of Manchester for the degree of Doctor of Philosophy

in the Faculty of Engineering and Physical Sciences

2012

Mohsin Abbas Aswad

School of Materials

Table of Contents

Title....1
Table of Contents....2
List of Figures....8
List of Tables....28
Abstract....31
Declaration....32
Copyright....33
Dedication....34
Acknowledgment....35
List of Abbreviation....36
1 Introduction 37
2 Literature Review 40
2.1 Crystal Structure of Alumina 40
2.1.1 Crystalline Phase of θ–Alumina 41
2.1.2 Crystalline Phase of γ-Alumina 42
2.1.3 Crystal Structure of α–Alumina 43
2.1.3.1 Applications of α–Alumina 45
2.1.3.2 Physical properties of α–Alumina 47
2.1.3.3 Mechanical properties of α–Alumina 52
2.1.3.4 Structure of Grain Boundaries in α-Alumina 60
2.2 Diffraction Contrast Tomography of Polycrystalline Alumina 61
Summary 64
2.3 Digital Image Correlation, DIC 65
2.3.1 Principle of Digital Image Correlation 65
2.3.2 Digital Image Correlation Requirement 70
2.3.3 Application of Digital Image Correlation 71
Summary 77
2.4 Hertzian Indentation 78
2.4.1 Contact stress field 78

2.4.2 Evaluation of Hertzian Cone Crack 79
2.4.3 Hertzian Cone Crack Mechanics 81
Summary 82
3 Experimental Methods 83
3.1 Introduction 83
3.2 Microstructural Analysis 85
3.2.1 Materials and Specimen Preparation 85
3.2.1.1 Grinding and polishing 85
3.2.1.2 Thermal Etching 86
3.2.1.3 Gold and Carbon Coating 87
3.2.2 Instruments 87
3.2.2.1 Optical Microscope (OM) 87
3.2.2.2 Scanning Electron Microscope (SEM) 87
3.2.2.3 Determining Average grain Size using Lineal Intercept Procedure 89
3.3 Digital Image Correlation Analysis 91
3.3.1 Preliminary Calibrations 91
3.3.2 Digital Image Correlation for calibration specimen (glass specimen) 92
3.3.2.1 Preparation of the Glass Surface for DIC 92
3.3.2.2 Focused Ion Beam for producing notches on the glass specimen 94
3.3.2.3 Strain Measurements 95
3.3.2.4 Four Point Bending Test 96
3.3.2.5 Finite Element Model Description for Glass Specimen 98
3.3.3 Image Correlation to study of the crack nuclei in alumina 99
3.3.3.1 Surface Preparation and Fracture test for DIC 99
3.3.3.2 Digital Image Correlation (DIC) Procedure 102
3.4 Grain Boundary Plane Analysis 102
3.4.1 Preparing the Surface 102
3.4.2 Electron Backscatter Diffraction of selected regions 103
3.4.3 Focussed Ion Beam, FIB Milling 103
3.5 Hertzian Indentation 105
3.5.1 Surface Preparation for Hertzian test 105

3.5.2 Hertzian Indentation test 106
3.5.3 Surface Preparation for Microstructural Examination 107
3.5.4 Stress Intensity Factor calculations 108
3.5.5 Statistical Analyses 109
3.5.6 Determination of surface crack densities 110
4 Results I 111
4.1 Microstructural Analysis 111
4.1.1 Grain Size 111
4.1.2 Optical Microscopy 112
4.1.3 Scanning Electron Microscopy 113
4.1.4 Electron Backscatter Diffraction, EBSD 113
4.2 Digital Image Correlation Analysis 115
4.2.1 Influence of the window size and surface finish on DIC noise on the Glass specimen 115
4.2.2 Influence of the window size and surface finish on DIC noise on the P-II and Cr-II specimens 117
4.2.2.1 Surface Finish 117
4.2.2.2 Window Size and Overlap 121
4.2.3 Comparison DIC data between Glass and P-II and Cr-II Specimens 125
4.2.3.1 Interrogation Window Size 125
4.2.3.2 Shift Correction 127
4.2.3.3 Peak Locking 129
4.2.3.4 Intensity Distributions of P-II, Cr-II, and Glass specimens 133
4.2.4 The accuracy of DIC to measure bulk strain on the calibration specimen (glass specimen) 135
4.2.4.1 Curvature Calibration Test 135
4.2.4.2 Comparing between the strain gauge outputs and measured strain (DIC strain) 136
4.2.4.3 Variation of Displacement across the image 138
4.2.4.4 Variation of Strain across the Image 142
4.2.4.5 Comparing the applied strain using FEM and strain gauge outputs 145

4.2.5 The accuracy of DIC to measure bulk strain on the P-II specimen 145
4.2.5.1 Variation of Displacement across the image 147
4.2.5.2 Variation of Strain across the Image..... 150
4.2.6 The accuracy of DIC to measure bulk strain on the Cr-II specimen..... 152
4.2.6.1 Variation of Displacement across the image 154
4.2.6.2 Variation of Strain across the Image..... 157
4.2.7 Using the Finite Element Model to assess the effects of DIC parameters on the measured surface crack opening displacement (SCOD) (glass specimen) 159
4.2.7.1 Predicting SCOD using the FEM..... 159
4.2.7.2 The effect of the Window Size on the measurement of Displacement Difference using FEM data 161
4.2.8 Digital Image Correlation (DIC) for measuring surface crack opening displacement (SCOD) for the glass specimen..... 164
4.2.8.1 Strain Map for observation the strain features for the glass specimen . 164
4.2.8.2 Measuring Displacement Difference using DIC..... 165
4.2.9 Comparing the FEM and DIC data 168
4.3 Summary 172
4.3.1 Strain Measurement 172
4.3.2 Opening Displacement Measurement 175
5 Discussion I..... 176
5.1 Quantitative measurement of strains for Glass Specimen using DIC 176
5.2 Quantitative Measurement of strains for polycrystalline alumina specimen (P-II and Cr-II) using DIC 180
5.3 The Surface Crack Opening Displacement for Glass Specimen 182
Summary 185
6 Results II 186
6.1 Image correlation to study crack nuclei in polycrystalline alumina..... 186
6.1.1 Observation of Strain features for P-II Specimen 186
6.1.2 Effect of Applied Strain on the Strain Feature for P-II Specimen 188
6.1.3 Observation of strain features for Cr-II Specimen..... 192

6.1.4 Effect of Applied Strain on the Strain Feature for Cr-II Specimen 193
6.1.5 Comparing the Peak strain with Background Strain 196
6.1.6 Effect of Threshold on Feature Detection 198
6.1.7 The strain feature locations for P-II Specimen 201
6.1.8 The strain feature locations for Cr-II specimen 207
6.1.9 Behaviour of the Strain Features using Line Profile for P-II specimen 209
6.1.10 Behaviour of the Strain Feature using Line Profile for Cr-II specimen 215
6.2 Grain Boundary Plane Analysis 218
6.2.1 Preparation of the surface for electron backscatter diffraction, EBSD 218
6.2.2 Grain Boundary Plane Procedure 219
6.2.2.1 Focused Ion Beam for P-II and Cr-II Samples 220
6.2.2.2 Grain boundary plane Pole for P-II and Cr-II Specimens 235
Summary 238
6.3 Hertzian Indentation Analysis 239
6.3.1 Hertzian Ring cracks 239
6.3.2 The cumulative probability of fracture 240
6.3.3 Fracture Toughness calculation 241
6.3.4 Defect Size Population 242
6.3.5 Gumbel distribution for Defect Size 243
6.3.6 Determination of surface crack densities 245
Summary 250
7 Discussion II 251
7.1 Microstructural Analysis 251
7.2 2D Observation of Intergranular Cracking 251
7.2.1 Digital Image Correlation 251
7.2.2 Detection of Intergranular Cracks by Digital Image Correlation 252
7.2.2.1 The characteristics of Strain features 252
7.2.2.2 Measured Displacement Difference 253
7.2.3 Destructive analysis of Grain Boundary Planes 254
7.3 Modelling of Intergranular Strains 258
7.3.1 A simple model for intergranular strains 258

7.3.2 Image-based Finite Element Modelling 268
Summary 270
7.4 Indirect Observation of Defect Density and Size 271
Summary 275
8 Conclusions and Future Work 276
8.1 Conclusions 276
8.1.1 Microstructure 276
8.1.2 Digital Image Correlation 276
8.1.3 Grain Boundary Plane 277
8.1.4 Hertzian Indentation 277
8.2 Future Work 278
8.2.1 Modification to Microstructure 278
8.2.2 Surface Preparation and Measuring the Residual Stress Using FIB and DIC 278
8.2.3 DIC to Study the Crack Nuclei at the Edge in Finer Grained Alumina 279
8.2.4 DIC to Study of the Crack Nuclei in Coarser Grained Alumina 280
References 282
Appendix A: Microstructure Analysis 293
Appendix B: Grain Boundary Plane Analysis 296
Appendix C: Hertzian Indentation Analysis 305
Appendix D: Atomic Force Microscope 309
Appendix E: List of Publications 311

Number of Words: 62,209

List of Figures

Figure 1-1: The flowchart of the main aims for this thesis. 39

Figure 2-1: The alumina phases (i.e. α, γ, and θ phases) and the transition stages at different temperatures [9]. 41

Figure 2-2: Shows a unit cell for the θ–alumina phase. The oxygen atoms are shows with large blue circles and aluminium atoms with the small green circles. 42

Figure 2-3: The face centre cubic structure for the oxygen lattice and the octahedral and tetrahedral structure for the aluminium lattice. The whole structure forms the γ–alumina phase structure [17]. 43

Figure 2-4: Shows the cation and anion arrangement for the basal plane in the α-alumina phase. The large open spheres represents the anion layer and the small filled and open spheres represent the aluminium and vacant octahedral interstices respectively [18]. 44

Figure 2-5: The basal plane in the hexagonal structure and the global Cartesian and crystal coordinate system for this structure [19]. 45

Figure 2-6: Shows the crucibles which were made from the high purity re-crystallised alumina of about 99% alumina [22]. 47

Figure 2-7: a) Shows the (α) for the polycrystalline alumina and individual grain increase with increasing the temperature from various studies [10], whereas b) Shows the values (α) for the individual gains in the α-alumina [26]. 50

Figure 2-8: The firing mechanism with the six paths to describe the material transfer to the sink [10]. 51

Figure 2-9: Describes the elastic properties (E, G, and ν) against the temperature for the α-Al_2O_3 for the group a) high-purity alumina for grade A4 and this alumina has porosity with range 3% to 10% b) low-purity alumina for grade A7 in the polycrystalline alumina [21]. 53

Figure 2-10: Images showing a) the scanning electron microscopy for the Al_2O_3 with crack which was produced by indentation b) the grain orientation map for the polycrystalline alumina using (OIM) [32]. 55

Figure 2-11: a) Shows the grains orientation using EBSD for the alumina has average grain size 104 μm and b) Shows the FEM to study the microcracking distribution in the EBSD map [33]. 56

Figure 2-12: A coarse ceramic with average grain size 104 μm with the microcracks as marker with red circles and the distribution residual stress in x- and y-direction ($\sigma_{xx}+\sigma_{yy}$) map to show the high residual stress at the same location for these microcracks at different temperatures changes , a) ΔT=–450 °C, b) ΔT=–950 °C, c) ΔT=–1150 °C and d) ΔT=–1550 °C [33]. 58

Figure 2-13: Shows the tension and compression residual stresses along the facet length for the grains [47]. 59

Figure 2-14: Shows microcracks opening at the tension residual stress and these microcracks are closed at the compression residual stresses [49]. 60

Figure 2-15: a) Shows the microstructure for the coarse alumina with average grain size of 100 μm [33], b) Shows the three dimensional structural for the alumina with a volume of about 1 mm diameter and 0.5 mm high [54], c) Shows the intergranular porosity in the coarse alumina [54] d) Shows the intergranular microcracks which are observed under the compressive stresses [54]. 62

Figure 2-16: Shows the facets planes poles distribution using the stereographic projection for the (α-Al_2O_3) [51]. 63

Figure 2-17: The results from FEM, a) The three dimensional for the coarse alumina microstructure using DCT, b) The thermal stresses orthogonal to grain boundaries, c) Shows one grain boundary and the stress variation across the grain and grain boundary, d) The relationship between the intergranular stress as a function of the distance to boundary along the line AB and also the interface averaged stress at the grain interface (at the point M). (1 pixel is 1.8 μm) [55]. 64

Figure 2-18: The digital image correlation procedure for the undeformed subimage (S) and the deformed subimage (S1) [56]. 67

Figure 2-19: a) Shows two images (i.e. before and after the deformation); each one divided into many subimages and each subimage has enough features and the same distribution of features and b) Shows the matching between the deformed and underformed subimages to obtain the displacements in x- and y- direction (i.e. dx and dy) [59]. 68

Figure 2-20: The deformation of the interrogation window size after the applied load and that caused the translation and rotation of this window after the deformation [59]. 68

Figure 2-21: a) Shows the viewed area with many features on its surface. One array of pixels has two features; one of them moved one integer pixel but the another feature moved half pixel. The first feature is strong for determining the displacement but the second feature is not very clear on the charge coupled device; b) Shows the peak locking behaviour from the probability density plot [59]. 70

Figure 2-22: Shows the white and black spray paint for the large deformation; large viewed area and the feature sizes are measured [67]..... 71

Figure 2-23: Shows the strain map which is used to observe the microcracks on the nuclear graphite surface and the white line describes the failure path [68]..... 72

Figure 2-24: Shows a defect growing in the graphite sample when the sample is subjected to the flexural stress. The strain is analysed using DIC; the maximum normal strain for the area of interest a) σ_b=11.60 MPa, 2c= 1.5 mm, b) σ_b =22.80 MPa, 2c= 3.5 mm, c) σ_b = 22.90 MPa, 2c= 10.0 mm, d) σ_b = 23.00 MPa, 2c= 13.7 mm, e) σ_b = 23.05 MPa, 2c= 16.3 mm, f) σ_b = 23.10 MPa, 2c= 16.9 mm [69]..... 73

Figure 2-25: Shows the intergranular stress corrosion cracks with overlaying a stain map on the optical image after 48 hours and the red strain features show the cracks at the grain boundary [70]. 74

Figure 2-26: Shows the overlaid stain map with cracks at 24 hrs on the stainless steel microstructure at the same time [71]..... 75

Figure 2-27: a) The initial image for the microstructure of the magnesium allay, b) The microstructure after fatigue test at 1510 cycles, c) The failure path in microstructure of the magnesium allay at 1513 cycles, d) The EBSD map for the sample before fatigue test. e, and f) The map of the displacement and the strain respectively from DIC after fatigue test at 1510 cycles [72]. 76

Figure 2-28: Shows the contact between the level ceramic surface and the indenter at the applied load (P) and the produced defect size (c) using Hertzian test. Also, the stresses field around the contact region is shown [85]. 79

Figure 2-29: The cone crack development after the applied load (P) and the radial surface stress around the contact region [86]. 80

Figure 2-30: The development of the cone crack under applied load and these cracks closing after removing the load from the sample surface. This test is done using Hertzian indentation test [75]..... 80
Figure 2-31: Shows (K_I) increases with increasing the defect length at different ring defect radius. (K_I) and defect size are normalised by the contact region radius [80]. 81
Figure 3-1: Flowchart illustrating the overall sequence of the experimental work carried out in this thesis..... 84
Figure 3-2: Shows the thermal etching procedure. 86
Figure 3-3: Shows the details of the SEM to provide the beam of electron which was used to observe the detail of the microstructure [90]. 88
Figure 3-4: Shows the stages for the electron backscatter diffraction system [91]. 89
Figure 3-5: Shows the lineal intercept method to determine the average grain size for the pure alumina specimen..... 90
Figure 3-6: Four point bending sample and the sample's dimensions..... 92
Figure 3-7: Shows the steps for the surface preparation of the glass specimens for DIC. . 93
Figure 3-8: Shows FIB–SEM equipment and the interaction the ion beam with the sample surface as shown in the magnified view [97]..... 94
Figure 3-9: Schematic for the slots location (slot A and B) on the glass slide. 95
Figure 3-10: Sketch of the glass specimen and shows the strain gauge location on the upper surface of the specimen..... 96
Figure 3-11: a) Shows digital image correlation set up, b) Schematic image for DIC set up. 97
Figure 3-12: Shows the slot position and the loading direction..... 98
Figure 3-13: Shows the mesh used close of the FIB slot (nominal size 0.001mm) and large elements (nominal size 2mm) far from the FIB slot. 99
Figure 3-14: a) Rig for in–situ optical observation of the tensile surface during four point bend loading, b) Schematic illustration of experimental setup, c) Specimen under the lens (X100), and d) Sample for digital image correlation. 101
Figure 3-15: Shows the traces of a grain boundary on two adjacent specimen surfaces (Upper Surface, Lower Surface) and these surfaces are orthogonal in the alumina sample. The specimen axes are XYZ and the tilting is about 52° for the alumina surface..... 104

Figure 3-16: Shows the grain boundary plane in the 3-D for the polycrystalline alumina sample, a) Shows the schematic for the upper surface which is used to determined the projected alpha angle in the xy-plane, b) Shows the upper and lower surface and the lower surface is used to measure the projected beta angle in the xz-plane. 105
Figure 3-17: Sketch of a Hertzian test specimen 106
Figure 3-18: Shows the Hertzian indentation equipment, CK10 and also shows the acoustic sensor, indentation shift and alumina indenter. 106
Figure 3-19: Shows the Hertzian indentation diagram to observe the crack size, contact region, and radial tensile stress [102]. 107
Figure 3-20: Schematic image of the chemical etching in potassium hydroxide (50% KOH) at different temperatures and exposure timed for this solution. 107
Figure 4-1: Optical images for the specimens a) P-II specimen, and b) Cr-II specimen after thermal etching. 112
Figure 4-2: Scanning electron microscope images for the samples a) P-II specimen, and b) Cr-II specimen. 113
Figure 4-3: Electron Back Scattered Diffraction (EBSD) maps for the samples a) P-II Specimen, and d) Cr-II Specimen. EBSD for both samples have been done at step size (0.2µm) and the level of indexing achieved was about (60% to 70%). 114
Figure 4-4: Shows the pole figures for the a) P-II sample and b) Cr-II sample..... 114
Figure 4-5: Shows the microstructure for the features distribution on the glass surface using chemical etching at concentration (50% HF) for (3 min.) and gold coating for (4 min) at different magnifications a) X10 and b) X20. 115
Figure 4-6: Shows the microstructure for the features distribution on the glass surface using chemical etching at concentration (95% HF) for (3 min.) and gold coating for (4 min) at different magnification a) X10 and b) X20. 116
Figure 4-7: The relationship between the noise level (RMS) as a function of the window size for the glass specimen a) magnification X20 and b) magnification X10. Legend shows different concentrations (50%HF and 95%HF) and different overlaps (50% and 75%) and theoretical RMS. 117
Figure 4-8: Shows the surface of alumina samples, prepared for digital image correlation at different surface finish techniques a) Grinding and polishing of the sample surface b)

Grinding, polished, thermal etching and carbon coating of the sample surface c) Grinding, and polished, thermal etching and gold coating of the P-II sample surface d) Grinding, and polished, thermal etching and gold coating of the Cr-II sample surface. 119

Figure 4-9: The relationship between the noise level (RMS) as a function of the window size at magnification (X100) and overlap (50%) for a) P-II sample and b) Cr-II sample. 120

Figure 4-10: The noise level (RMS) against the window size and also, at different overlaps for the P-II sample a) at magnification X100 and b) at magnification X50. First method was used. 122

Figure 4-11: The noise level at magnification X100 against the window size and at different overlaps for the Cr-II sample. First method was used..... 123

Figure 4-12: Line profiles of displacement in the x-direction along a line across the image (viewed area) at magnification X100. The subset of 128×128 pixels and 64×64 pixels are compared and also different overlaps of 50% and 75% for a) P-II specimen and b) Cr-II specimen. Line profile of displacement was in the region outside the cracked region. Second method was used. 124

Figure 4-13: The window size for the specimens a) P-II specimen, the window size used was (64×64) pixels on the viewed area b) Cr-II specimen, the window size used was (128×128) pixels on the viewed area and c) Glass specimen, the window size used was (128×128) pixels on the viewed area. 127

Figure 4-14: Shows the shift correction and rotation correction procedure using window size (512×512 pixels) for shift correction and using several windows size (128×128 pixels) for rotation correction for Cr-II specimen..... 128

Figure 4-15: The relationship between the result of the movement (shifting) of the features during increasing the applied strain at different micrometer displacements for P-II, Cr-II, and Glass specimen. Interrogation window size of 512×512 pixels for shift correction and using several windows size 128×128 pixels for rotation correction was used for this case. 129

Figure 4-16: Shows the images with different features have different displacement using interrogation window size 64×64 pixels and overlap 50% for P-II, 128×128 pixels and overlap 50% for Cr-II, and Glass specimen; this is shown by the probability density plot of the displacement vector..... 132

Figure 4-17: Shows the microstructure data for the raw reference images which are used to observe the intensity distribution using Image-J software for a) P-II specimen b) Cr-II specimen c) Glass specimen. Figure represents for P-II and Cr-II specimens at magnification X100 and glass specimen at magnification X20. 134
Figure 4-18: Typical intensity distribution plot for P-II and Cr-II specimen at magnification X100 and Glass specimens at magnification X20. 134
Figure 4-19: Evolution of average strain (apparent strain) along the X - axis with the distance moved toward the camera in the positive and negative direction. Interrogation window size was 128×128pixels and overlap 50%. 135
Figure 4-20: Optical image showing the distance between the viewed area (FIB-milled slot A and slot B are marked) and the strain gauge position for the glass specimen is shown. 136
Figure 4-21: Shows the analysed or viewed area which used for digital image correlation and also, the arrows show the loading direction in X-direction. 137
Figure 4-22: Shows the digital image correlation mean strain at the centre of the image (viewed area) at interrogation window size of 128×128 pixels and overlap 50% against the strain gauge output for the glass specimen. DIC mean strain is measured at the centre of the viewed area with no slots. 138
Figure 4-23: Shows the displacement map at interrogation window size 128×128 pixels and overlap was 50% and also shows the line profile across the viewed area at different positions and at applied strain 0.00059 for the glass specimen at a) X-displacement, and b) Y-displacement. The white lines describe the line profile using DIC (i.e. the location for measuring the displacement). 140
Figure 4-24: The relationship between the digital image correlation strain (i.e. the strain was measured from the relative displacement) as a function of the distance at different line position across the image and also, at different applied strains a) ε_{xx} and b) ε_{yy}. Interrogation window size was 128×128 pixels and overlap was 50%. 141
Figure 4-25: Shows the mean measured strain (Mean DIC strain) and DIC strain gradient at different positions as a function of the applied strain in the X and Y-directions. Interrogation window size was 128×128 pixels and overlap 50%. Mean DIC strain and slope show the strain which was measured from the relative displacement for whole viewed area at different line profile positions. 142

Figure 4-26: Shows the strain map and also, the line profile across the viewed area at different positions at applied strain 0.00145 for the glass specimen at a) ε_{xx}, and b) ε_{yy}. Interrogation window size used was 128×128 pixels and overlap 50%. The white lines describe the line profile using DIC (i.e. the location for measuring the strain). 143
Figure 4-27: Shows the digital image correlation strain at different line positions across the analysed area as a function of the distance from the left of the viewed area for a) ε_{xx} (strain at X-direction), and b) ε_{yy} (strain at Y-direction). Interrogation window size was 128×128 pixels and overlap 50% at an applied strain of 0.00145. 144
Figure 4-28: The relationship between the strain gauge outputs and the predicted strain (FEM strain) as a function of the micrometer displacement for the glass specimen. 145
Figure 4-29: Shows the analysed area using digital image correlation and also, showing the loading direction in the X-direction for the P-II specimen. 146
Figure 4-30: Shows the digital image correlation mean strain at the centre of the image (viewed area) at interrogation window size 64×64 pixels and overlap 50% against the applied strain for the P-II specimen. DIC mean strain is measured at the centre of the viewed area with no cracks. 146
Figure 4-31: Shows the displacement map at interrogation window size 64×64 pixels and overlap 50%. It also shows the line profile across the viewed area at different positions and at applied strain of 0.00027 for the P-II specimen at a) X-displacement, and b) Y-displacement. The white lines describe the line profile using DIC (i.e. the location for measuring the displacement). 148
Figure 4-32: The relationship between the digital image correlation strain (i.e. the strain was measured from the relative displacement) as a function of the position at different line positions across the image and at different applied strains a) ε_{xx} and b) ε_{yy}. Interrogation window size was 64×64 pixels and overlap 50%. 149
Figure 4-33: Shows the mean measured strain (Mean DIC strain) and DIC strain gradient at different positions as a function of the applied strain in the X and Y-directions. Interrogation window size was 64×64 pixel and overlap 50%. Mean DIC strain and slope show the strain which was measured from the relative displacement for whole viewed area at different line profile positions. 149

Figure 4-34: Shows the strain map and the line profile across the viewed area at different positions at an applied strain of (0.00027) for the P-II specimen at a) ε_{xx}, and b) ε_{yy}. Interrogation window size was 64×64 pixels and overlap was 50%. The white lines describe the line profile using DIC (i.e. the location for measuring the displacement)..... 151

Figure 4-35: Shows the digital image correlation strain at different line positions across the analysed region against the distance from the left of the viewed area for a) ε_{xx} (strain in the X-direction), and b) ε_{yy} (strain in the Y-direction). Interrogation window size was 64×64 pixels and overlap 50% at applied strain (0.00027)..... 152

Figure 4-36: Shows the analysed area using digital image correlation and also, showing the loading direction in the X-direction for the Cr-II specimen. 153

Figure 4-37: Shows the mean strain at the centre of the image (viewed area) at interrogation window size 128×128 pixels and overlap 50% as a function of the applied strain for the Cr-II specimen. DIC mean strain is measured at the centre of the viewed area with no cracks. 153

Figure 4-38: Shows the displacement map at interrogation window size 128×128 pixels and overlap 50%; the line profiles are also shown across the viewed area at different positions and at applied strain (0.00018) for the Cr-II specimen at a) X-displacement, and b) Y-displacement. The white lines describe the line profile using DIC (i.e. the location for measuring the displacement)..... 155

Figure 4-39: The relationship between the digital image correlation strain (i.e. the strain was measured from the relative displacement) as a function of the position at different line positions across the image and also, at different applied strains a) ε_{xx} and b) ε_{yy}. Interrogation window size was 128×128 pixels and overlap 50%..... 156

Figure 4-40: Shows the mean measured strain (Mean DIC strain) and DIC strain gradient at different positions as a function of the applied strain in the X and Y-direction. Interrogation window size was 128×128 pixels and overlap 50%. Mean DIC strain and slope show the strain which was measured from the relative displacement for whole viewed area at different line profile positions. 156

Figure 4-41: Shows the strain map and also, the line profile across the viewed area at different position at 0.00018 applied strain for the Cr-II specimen at a) ε_{xx}, and b) ε_{yy}.

Interrogation window size was 128×128 pixels and overlap 50%. The white lines describe the line profile using DIC (i.e. the location for measuring the strain). 158

Figure 4-42: Shows the digital image correlation strain at different line positions across the analysed area against the distance from the left of the viewed area for a) ε_{xx} (strain in the X-direction), and b) ε_{yy} (strain in the Y-direction). Interrogation window size was 128×128 pixels and overlap 50% at an applied strain of 0.00018. 159

Figure 4-43: Shows the slot A location on the glass slide sample and the line profile for measuring the displacement across the slot A (i.e. P1) and the displacement away from slot A (i.e. P13). The loading direction shows by arrows..... 160

Figure 4-44: Shows the displacement through the slot A,P1 and also, the displacement remote of the slot A (outside the slot A, P13) as a function of the distance in X-axis as shown in Figure 4-43 at an applied strain of 0.00185..... 161

Figure 4-45: The maximum surface crack length (true surface crack opening displacement, SCOD) at the centre of a 11.64 μm deep slot as a function of the slot length at an applied strain of 0.00185, predicted using the FE model. 160

Figure 4-46: The relationship between the predicted displacement from FEM (i.e. true displacement) and measured displacements at different window sizes (i.e. measured displacement was determined using polynomial function) as a function of the distance on each side of the slot A at applied strain of 0.00185..... 162

Figure 4-47: The difference between the displacement through (across) the slot A and the displacement remote to (outside) the slot A for the predicted displacement and measured displacement against the distance on each side of the slot A. Applied strain is (0.00185).163

Figure 4-48: The relationship between the normalised surface crack opening displacement (measured SCOD / true SCOD) at the origin location of slot A and normalised SCOD after offset the slot A (16 pixels) against the window size. Applied strain is (0.00185). 163

Figure 4-49: The strain features observed from the strain map using DIC overlay on the microstructure image for the glass sample using an interrogation window size 128×128 pixels and overlap 50%. Applied strain is (0.00185) and the threshold strain is 0.08%.... 164

Figure 4-50: The displacement map from DIC overlaid on the optical image for the glass sample using a window size 128×128 pixels and overlap 50%. The applied strain is

0.00185. The slot's location was positioned on the same Figure using a white ellipse marker. The white lines show the line profile through slot A and slot B. 165
Figure 4-51: Shows the vector displacement against the distance from the left of the viewed area in the X-axis through the slot A (P1) and the fitted displacement through slot A (P13). Interrogation window size used was 128×128 pixels and overlap 50% for slot A. 166
Figure 4-52: Shows the vector displacement against the distance from the left of the viewed area in X-axis through the slot B (P1) and the fitted displacement through slot B (P13). Interrogation window size used was 128×128 pixels and overlap 50% for slot B. 166
Figure 4-53: The displacement difference between the displacement through (across) the slot and the fitted displacement through the slot as a function of the distance on each side of the slot. Window size was 128×128 pixels and overlaps 50%. Data for different applied strains are shown for a) Slot A and b) Slot B..... 168
Figure 4-54: The displacement plot for the finite element model data at applied strain (0.00185) and the digital image correlation data. Interrogation window size was 128×128 pixels and overlap 50% at applied strain (0.00185) for DIC. Also showing the measured displacement using FEM prediction data at window size is (128×128) and overlap (0%), as a function of the distance from slot A..... 169
Figure 4-55: The difference between the displacement at the region across the slot A and the fit displacement at the region through the slot A for the finite element model data and for the digital image correlation data. DIC taken with window size 128×128 pixels and overlap 50%. Also the FEM prediction data at window size 128×128 pixels and overlap 0%. The displacement difference was measured at different applied strains a) applied strain was (0.001854) for FEM and predicted data and (0.001849) for DIC data, b) applied strain was (0.00135) for FEM and predicted data and (0.00134) for DIC data, and c) applied strain was (0.000554) for FEM and predicted data and (0.000586) for DIC data. 171
Figure 4-56: Shows the strain from experimental DIC data and the strain from DIC simulation of finite element model data (predicted data) against the applied strain. The experimental data show smaller strains than expected, but the strains increase with applied strain. The finite element model has the same notch depth and length as the experiment. 172

Figure 4-57: a) Comparison digital image correlation mean strain for the P-II, Cr-II, and glass specimens as a function of the applied strain b) Extend the DIC mean strain for P-II and Cr-II samples. 174
Figure 5-1: Shows the radius of curvature (R) and the vertical displacement (V_d) and the tilt angle (θ). 177
Figure 5-2: Shows the measured vertical displacement in X-direction at different line position within the viewed area. Also shown is the predicted vertical displacement. Both vertical displacements were measured at surface strain (0.000586) for the glass specimen. 179
Figure 5-3: Shows the relationship between the tilt angle as a function of the applied strain for the glass specimen. 179
Figure 5-4: Shows the measured vertical displacement in X-direction at different line position within the viewed area and also shows the predicted vertical displacement for a) P-II specimen (surface strain for both displacement is 0.00027) and b) Cr-II specimen (surface strain for both displacement is 0.00018). 181
Figure 5-5: Shows the relationship between the tilt angle as a function of the applied strain for the P-II and Cr-II specimens 181
Figure 5-6: Shows the slots depth using focused ion beam, FIB at tilt angle 52° and voltage 30 kV and a current of 280 nA for a) Slot A and b) Slot B. 183
Figure 5-7: Comparison between the experimental data, FEM data, predicted data, and analytical model data for SCOD against the applied strain for the glass slide (slot A). 184
Figure 6-1: Identification of strain features (strain feature A, strain feature B, and strain feature C) by in-situ observation for P-II specimen, a) Low threshold (0.2%), b) High threshold (1%). Both thresholds are at an applied strain 0.00027. 188
Figure 6-2: Illustration of the nominal strain at different applied strain and strain distribution observed by digital image correlation under increasing load in the X-direction for strain feature A in P-II specimen. 191
Figure 6-3: Illustration of the nominal strain for the region around strain feature A at different applied strains and strain distributions observed by digital image correlation under increasing load in the Y-direction for P-II specimen. 192

Figure 6-4: Identification of strain feature by in- situ observation for Cr-II specimen at applied strain 0.00046. 193
Figure 6-5: Illustration of the nominal strain at different applied strain and strain distribution observed by digital image correlation under increasing applied load in the X-direction for Cr-II specimen. 195
Figure 6-6: Illustration of the region around strain feature at applied strain 0.00046 and strain distribution observed by digital image correlation under increasing applied load in the Y-direction for Cr-II specimen..... 196
Figure 6-7: Development of the peak feature strain for all the significant strain features which they observed using digital image correlation and background strain versus applied strain for the a) P-II specimen and b) Cr-II specimen. Background strain in X-direction is parallel to the applied bending stress; background strain in Y-direction is perpendicular to the applied bending stress. The background strain is measured in areas with no applied localised strains. 198
Figure 6-8: Shows the relationship between the strain features size against cumulative probability of the observation of the particular feature size in the dataset at threshold (0.002) and threshold (0.005) at different applied strain for a) P-II specimen and b) Cr-II specimen. (i.e. feature size represents surface strains feature length). Legend describes the applied strain at which the features were measured..... 200
Figure 6-9: Effect of segmentation threshold at different values (0.2% and 0.5%) on the maximum strain feature size using Matlab routine (i.e. crack track) against of the applied strain for the a) P-II Specimen b) Cr-II Specimen. 201
Figure 6-10: Shows the strain features location that observed using digital image correlation at different location and these microcracks non-visible on the raw images a) The data analysed at 25 different locations were stitched together for studying a larger area of approximately (500×500 μm), b) Magnification the location for feature B as shown in Figure 6-10a c) Magnification the location for feature A as shown in Figure 6-10a, and d) Magnification the location for feature C as shown in Figure 6-10a. 202
Figure 6-11: Overlaid the strain features from strain map using digital image correlation on the optical images and scanning electron microscope images at applied strain 0.00027 for P-II specimen for different strain features a) Strain feature A, b) Strain feature B, and c)

Strain feature C. The numbers on the SEM images show the closest grains from these strain features. 207

Figure 6-12: Shows the strain feature location that observed using digital image correlation at a certain location and these microcracks are invisible on the raw images a) Magnified the red square (see Figure 6-12b) which was represented the strain feature location as marker by the yellow arrow, b) The analyses area from 25 different locations were stitched together to study larger area of approximately (500×500μm). 208

Figure 6-13: Overlaid the strain feature on the strain map using DIC on the a) Optical image and b) Scanning electron microscope image for the Cr-II sample at applied strain (0.00046). The dotted red square shows the area of interest for these strain features. 209

Figure 6-14: The displacement map in x-direction using DIC overlaid on the optical image using window size 64×64 pixels and overlap 50%, applied strain is (0.00055). The strain feature location was positioned using black ellipse marker. The black line shows the line profile through the strain feature in P-II specimen using DIC for a) Strain feature A, b) Strain feature B, and c) Strain feature C. 211

Figure 6-15: Shows the vector displacement against the distance from the left of the viewed area in X-axis for different strain features and also, showing the best fit for the displacement through the strain features for a) Strain feature A, b) Strain feature B and c) Strain feature C. Interrogation window size and overlap as mentioned before in the Section (3.3.4.1) at different applied strains. 213

Figure 6-16: The difference between the displacement through (across) the strain feature and the best fit for the displacement through the strain feature as a function of the distance on each side of the strain feature at window size and overlaps as mention before in section (3.3.4.1) and also, at different applied strain for a) Strain feature A, b) Strain feature B, and c) Strain feature C. 215

Figure 6-17: The displacement map overlaid on the optical image using window size and overlap as mentioned in section (3.3.4.1) at applied strain of (0.00046). The strain feature location was positioned using a black ellipse marker and also, the black line shows the line profile using DIC through the strain feature for Cr-II specimen. 216

Figure 6-18: Shows the vector displacement against the distance from the left of the viewed area in x-direction for the displacement through the strain feature. Also shown is

the best fit for the displacement through the strain feature at different applied strains. Interrogation window size and overlap as mentioned previously in section (3.3.4.1)..... 217
Figure 6-19: The displacement difference between the displacement through (across) the strain feature and the best fit line for the displacement through the strain feature as a function of the distance on each side of the strain feature at window size and overlaps as mention early in section (3.3.4.1) at different applied strains for the Cr-II sample..... 217
Figure 6-20: Shows the surface preparation for electron backscatter diffraction using different techniques for P-II specimen a) Using FIB to remove gold coating, b) Using FIB to remove gold coating and thin layer of the etched layer, c) Using Gatan machine to remove gold coating and thin layer of the etched layer, and d) Using mechanical polishing to prepare the surface for EBSD. These techniques are described in detail in chapter in Section (3.4). 218
Figure 6-21: The regions of interesting for the a) strain feature A in P-II specimen and b) strain feature in Cr-II specimens. The cracks observed on these regions using digital image correlation..... 219
Figure 6-22: a) Shows the SEM image for the grain boundary of interest and b) Shows the electron backscatter diffraction for the orientation of the grain boundary of interest. Both images for strain feature A in P-II specimen and yellow arrows show the grain boundary of interest on the SEM image and EBSD map. 220
Figure 6-23: The focused ion beam region marked by the yellow rectangle across the cracked boundary observed by digital image correlation for strain feature A in P-II sample. 221
Figure 6-24: Traces of grain boundaries on the P-II specimen surfaces tilted through (52°) using a scanning electron microscope (SEM). 221
Figure 6-25: Crystal orientation for the grains of interest using channel 5 (Tango software) for the grains on the RHS and LHS of the cracked boundaries. 222
Figure 6-26: Schematic diagram showing the traces of a grain boundary on two adjoining specimen surfaces, orthogonal surfaces (upper and lower face) after FIB trench cutting. 222
Figure 6-27: Shows the EBSD map overlaid on the SEM image. The EBSD map is rotated by about (6^{o}) to match the SEM image to get true angle (α) on the upper face for the strain feature A in P-II sample to show the selected boundary and trench location. 223

Figure 6-28: a) Shows the SEM image for the grain boundary of interest as labelled by black square and b) Shows the EBSD for the orientation of the grain boundary of interest for strain feature B in P-II specimen and the grain boundary of interest as labelled by arrows on the SEM image and EBSD map. 224
Figure 6-29: focused ion beam region marked with a yellow rectangle across the cracked boundary which was observed using digital image correlation. 225
Figure 6-30: Traces of grain boundaries on the P-II specimen surfaces tilted through (52°) for strain feature B. 225
Figure 6-31: The crystal orientation using channel 5 for the grains on the either side of the cracked boundaries of feature B in sample P-II. 226
Figure 6-32: Schematic diagram showing the traces of a grain boundary on two adjoining specimen surfaces, orthogonal surfaces (upper and lower face) after FIB trench cutting. 226
Figure 6-33: Shows the EBSD map overlaid on the SEM image after rotation EBSD map is about (6^{o}) to properly match with the SEM image to get true angle (α) on the upper face for the strain feature B in P-II sample. Also shown is the selected boundary and trench location. 227
Figure 6-34: a) Shows the SEM image for the grain boundary of interest and b) Shows the EBSD (i.e. the green regions on the EBSD map shows the non-indexed regions) for the orientation of the grain boundary of interest as labelled by red arrow for the boundaries of interest for strain feature in Cr-II specimen. 228
Figure 6-35: Shows the focused ion beam region labelled by a yellow rectangle across the cracked boundary which was observed by digital image correlation for the strain feature in Cr-II sample. 228
Figure 6-36: Traces of grain boundaries on the Cr-II specimen surfaces tilted through (52°) using SEM. 229
Figure 6-37: Shows the crystal orientation using channel 5 (Tango Software) for the grains on the RHS and LHS of the cracked boundaries in Cr-II specimen. 229
Figure 6-38: Schematic diagram showing the traces of a grain boundary on two adjoining specimen surfaces, orthogonal surfaces (upper and lower face) after FIB trench cutting. Also shown is the projected beta angle. 230

Figure 6-39: Shows the EBSD map overlaid on the SEM image. The EBSD map is rotated by (10^o) to the SEM image to get the true angle (α) for the upper face for the strain feature in Cr-II sample to show the selected boundary and trench location. 231
Figure 6-40: Traces of grain boundary on two surfaces (upper and lower surfaces) for i) Strain Feature A in P-II Specimen, ii) Strain Feature B in P-II Sspecimen, and iii) Strain Feature in Cr-II Specimen at different tilt angles a) 40^o,b) 52^o, and c) 60^o. These tilt angles have been done using the scanning electron microscope. 232
Figure 6-41: The relationship between the true and projected angles as a function of the tilting angles for a) Alpha angle (α) b) Beta angle (β) in P-II specimen..... 233
Figure 6-42: The relationship between the true and projected angles as a function of the tilting angles for a) True alpha angle was measured from Figure 6-39 (α) from overlaid EBSD map on the SEM image and b) Beta angle (β) for Cr-II samples. 234
Figure 6-43: Pole figures for the grain boundary plane G12, of the basal facet plane (0001) in alumina in grains G1 (dark) and G2 (light). The boundary plane is close to the (0001) facet plane in a) G1 for strain feature A in P-II specimen, b) G2 for strain feature B in P-II specimen and c) G2 for strain feature in Cr-II specimen. 237
Figure 6-44: Shows ring cracks produced on the P-II and Cr-II specimens. The sphere indenter radius was R=2.5 μm. The ring cracks are visible after the sample was etched using KOH a, c) Smooth polished for the P-II and Cr-II specimens and b, d) Coarse polished for P-II and Cr-II specimens respectively..... 239
Figure 6-45: Cumulative probability of failure against the failure load in the P-II specimen and Cr-II specimen for the coarse and smooth surface. 240
Figure 6-46: Shows the ring crack radius for smooth polished surface as a function of the fracture load for P-II and Cr-II specimen using alumina indenter. The uncertainty in the ring crack radius is 1.48 μm and 1.34 μm for P-II and Cr-II samples respectively. 241
Figure 6-47: Shows the stress intensity factor against the defect size after normalized by the radius of the contact region at (ν=0.24) for P-II specimen. 243
Figure 6-48: The distribution for the small defect size was used using Gumbel distribution against the crack length for a) Normal crack size and b) Normalised crack size. 245
Figure 6-49: Shows the maximum (r_{max}) minimum (r_{min}) and radii at which $K_I=K_{IC}$ versus applied load. The crack depth is 2.24 μm and 2.23 μm, the sphere radius is 2.5 mm.

Poisson's ratio is (0.24), Young modulus 390 GPa and the fracture toughness of the substrate is 3.5 MPa.$m^{1/2}$ and 2.9 MPa.$m^{1/2}$ for P-II and Cr-II specimen respectively..... 246

Figure 6-50: Shows flaw density determined from the searched area for the sphere radii of (2.5 mm) for the P-II and Cr-II specimens for a) Normal flaw density distribution and b) Normalised flaw density distribution (i.e. flaw size normalised by the grain size and flaw density normalised by the number of grains per unit area). The flaw density axes use a logarithmic scale. (Flaw size represents crack depth)..... 249

Figure 6-51: Comparison flaw density plots between the Warren's data at different sphere radii (r = 2.5, 5, 10, and 20mm) [79] and the experimental data at sphere radius (r = 2.5 mm). 250

Figure 7-1: Show a simple sketch of the effect of threshold on the length of a strain feature at different increment applied strain. 253

Figure 7-2: Pole figures for the grain boundary plane, G12 of the common facet plane in the polycrystalline alumina (P-II and Cr-II samples) in grains G1 (dark) and G2 (light) for the upper hemisphere. The boundary plane is near the basal facet plane (0001) in the G1 for strain feature A in P-II sample and the G2 in strain feature B in sample P-II and the strain feature in Cr-II sample. a) Strain feature A in the P-II sample, b) Strain feature B in the P-II sample, and c) Strain feature in the Cr-II sample..... 256

Figure 7-3: Pole figures for the grain boundaries plane, G23 and G13 of the common facet plane in the P-II and Cr-II samples respectively. The boundary plane is not near the basal facet plane (0001) in the G1, G2 nor G3 for a) Non cracked boundary close to the strain feature A in the P-II sample, b) Non cracked boundary close to the strain feature B in the P-II sample, and c) Non cracked boundary close to the strain feature in the Cr-II sample. 258

Figure 7-4: Schematic image of the grain G1 and grain G2 in bulk C to show the grain size, dG and displacement, ΔdG for G1 and G2 perpendicular to the grain boundary. This also, shows the shrinkage for the grains G1 and G2. 260

Figure 7-5: Shows the maximum thermal expansion (a) and minimum thermal expansion (b) in the hexagonal structure..... 261

Figure 7-6: Shows the coefficient of the thermal expansion perpendicular to boundary as a function to the angles between the (0001) and boundary pole..... 262

Figure 7-7: The maximum thermal expansion coefficient against the grain boundary for a) P-II sample and b) Cr-II sample. (Hollow bars show the cracked boundaries). 264
Figure 7-8: The net thermal displacement perpendicular to the boundary against the grain boundary for a) P-II sample and b) Cr-II sample. (Hollow bars show the cracked boundaries). 265
Figure 7-9: Prediction of thermal stresses with uncertainties using a simple model, for the thermal stress at boundary (effective stress) versus the grain boundary for the a) P-II sample and b) Cr-II sample. (Hollow bars show the cracked boundaries). 266
Figure 7-10: The finite element model to measure the stress across the boundaries a) The thermal stress versus the grain boundary plane area, b) The intergranular stress against the (0001) pole misorientation for the grains neighbouring, c) The stress as a function of the basal plane pole misorientation for one grain or both grain adjacent, and d) The stress against the (0001) pole misorientation and the boundary pole for the neighbouring grains. The thin grey line shows the cumulative number of the grain boundaries which was covered the large number of grain and the number of grain boundary more than (5000 boundaries) [55]. 269
Figure 7-11: Shows the stressed area in a) Digital image correlation experiments and b) Hertzian test for an individual ring crack radius. 273
Figure 7-12: Shows the flaws population for the P-II and Cr-II samples using DIC experiments. 274
Figure 7-13: a) Shows the flaw density distribution and b) Shows normalised flaw density distribution for the Hertzian indentation and digital image correlation in the P-II and Cr-II samples. 275
Figure 8-1: Shows the viewed area location on the polycrystalline alumina sample surface near to the edge of the sample. 280
Figure 8-2: Shows the coarse alumina with equiaxed grain and average grain size is about 99 μm [33]. 280
Figure A-1: Optical images for the polycrystalline alumina samples, a) P-I Specimen, and b) Cr-I Specimen after thermal etching. 293
Figure A-2: Scanning Electron Microscope images for the polycrystalline samples a) P-I Specimen, and b) Cr-I Specimen after thermal etching and gold coating. 294

Figure A-3: Scanning Electron Microscope images for showing the microcrack in the P-I sample.....294

Figure A-4: Electron Back Scattered Diffraction, EBSD maps for the polycrystalline alumina samples a) P-I Specimen, and d) Cr-I Specimen at step size (0.2μm) and the level of indexing achieved about (60% to 70%).....295

Figure B-1: Pole figures for the grain boundaries plane, G34 and G45 of the common facet plane in the polycrystalline alumina and the grain boundary plane is not near the (0001) facet plane in the G3, G4 or G5 for a) Non cracked boundary in region of the strain feature A in the P-II sample, b, c) Non cracked boundary in the region of the strain feature B in the P-II sample, and c) Non cracked boundary in the region of the strain feature in the Cr-II sample.....298

Figure B-2: Shows the misorientation between grains as a function of the grain boundary for a) stain feature A and strain feature B in P-II sample and b) strain feature in Cr-II sample. (Hollow bars show the crack boundaries).....299

Figure C-1: a) Shows the minimum (r_{min}) and maximum (r_{max}) ring crack radius at stress intensity factor is equal to the fracture toughness versus of applied load. The sphere radius is 2.5 mm sphere radius is 2.5 mm and crack depth is 4 μm. The mechanical properties for this test are $\nu = 0.24$, E = 390 GPa and $K_{IC} = 2MPa.m^{1/2}$ b) shows the correlation of the ring crack radius between the Warren's data and Warren's equation [109].....306

Figure C-2: Shows cumulative probability of failure at different sphere radius against failure load in the Hertzian indentation experiment [109].....307

Figure C-3: a) Shows the flaw density calculated from the searched area at different radii against the flaw size for the Warren's data and Warren's plot. B) shows the correlation of the flaw density between the Warren's data and Warren's plot [109].....308

Figure D-1: Shows the atomic force microscope for measuring the depth of the thermal groove for the a) strain feature A in P-II sample and b) strain feature B in P-II sample.....310

List of Tables

Table 2-1: Describes the phases for the alumina and also shows their mechanical and physical properties at different melting temperature [9]. 41

Table 2-2: Shows the high purity alumina grades, porosity, density, and applications and their purity at least (99% alumina) [21-23]. 46

Table 2-3: Shows the lower purity alumina, porosity, density, and their applications. The purity for this group between 80% to 90 % alumina [21]. 46

Table 2-4: Shows the thermal properties for the higher and lower purity alumina at the 25°C [21-24]. 48

Table 2-5: Describes the Young Modulus, Shear modulus, Poisson ratio, and the porosity at 25°C in α-Al_2O_3 [21-23]. 52

Table 3-1: Shows the Grinding and Polishing Procedure 86

Table 3-2: Shows the coating type and the experiments that used at this kind of coating.. 87

Table 3-3: Shows the lineal intercept procedure for one micrograph of the pure alumina specimen. 90

Table 3-4: Describes the noise level (RMS) for the displacement vector at different interrogation subimages [67] 102

Table 4-1: Shows a summary of the experiments performed and the average grain size for alumina samples. 112

Table 4-2: Shows the noise level (RMS) at magnification (X100 and X50) and at different window sizes and overlaps for the P-II specimen (1 pixel is 0.0046 μm at magnification X100 and 1 pixel is 0.092 μm at magnification X50). 123

Table 4-3: Shows the noise level (RMS) at magnification (X100) and at different window sizes and overlaps for the Cr-II specimen. 123

Table 4-4: Shows the scatter level at magnification X100 and also, at different window sizes and overlaps for the P-II and Cr-II specimen. The scatter data was measured using polytool function in Matlab. 125

Table 5-1: shows the dimensions and expected gradient of surface crack opening displacement for slot A and slot B 183

Table 5-2: The surface crack opening displacement gradient data using different procedures for the slot A in glass specimen. 185

Table 6-1: Shows the average true angles (α and β) for strain features A and B in P-II sample and also for strain feature in Cr-II sample. 235

Table 6-2: Shows the minimum load and the fracture toughness for P-II and Cr-II specimens at different surface finishes. 242

Table 6-3: Shows the defect sizes, number of defects, searched area, and flaw density for the P-II specimen (i.e. Defect size represents crack depth). 247

Table 6-4: Shows the defect sizes, number of defects, searched area, and flaw density for the Cr-II specimen. 248

Table 6-5: Shows the Arithmetic mean and standard deviation of the distribution for the P-II and Cr-II samples. 248

Table 7-1: Relationships between grain orientations and observations of cracking: Data for the angles between the grain boundary poles and the pole for the facet planes and the misorientation between the basal poles of adjacent grains are given for the P-II sample. 267

Table 7-2: Relationships between grain orientations and observations of cracking: Data for the angles between the grain boundary poles and the pole for the facet planes and the misorientation between the basal poles of adjacent grains are given for the Cr-II sample.268

Table B-1: Shows the angles between the grain boundary pole and the pole for the facet plane (0001) at alpha angle, α (76°, 87°) and beta angle, β (86°, 89°) for the strain feature A and strain feature B respectively in the P-II sample.....300

Table B-2: Shows the angles between the grain boundary pole and the pole for the facet plane (0001) at alpha angle, α (76°, 87°) and beta angle, β (82°, 85°) for the strain feature A and strain feature B respectively in the P-II sample.....301

Table B-3: Shows the angles between the grain boundary pole and the pole for the facet plane (0001) at alpha angle, α (70°, 83°) and beta angle, β (82°, 85°) for the strain feature A and strain feature B respectively in the P-II sample.....302

Table B-4: Shows the angles between the grain boundary pole and the pole for the facet plane (0001) at alpha angle, α (70°, 83°) and beta angle, β (86°, 89°) for the strain feature A and strain feature B respectively in the P-II sample.....303

Table B-5: Shows the angles between the grain boundary pole and the pole for the facet plane (0001) at alpha angle, α (107°) and beta angle, β (71°) for the strain feature in Cr-II sample.....303

Table B-6: Shows the angles between the grain boundary pole and the pole for the facet plane (0001) at alpha angle, α (107°) and beta angle, β (65°) for the strain feature in Cr-II sample.....304

Table B-7: Shows the angles between the grain boundary pole and the pole for the facet plane (0001) at alpha angle, α (99°) and beta angle, β (65°) for the strain feature in Cr-II sample.....304

Table B-8: Shows the angles between the grain boundary pole and the pole for the facet plane (0001) at alpha angle, α (99°) and beta angle, β (71°) for the strain feature in Cr-II sample.....304

Abstract

Recrystallised alumina is used as a high performance crucible material. Its thermal shock resistance is known to be affected by component shape, and also by processing variables, since the defects and internal stress at both the microscale (i.e. between grains due to anisotropic crystal properties) and macroscale (i.e. due to differential shrinkage during sintering) influence the fracture strength. The aim of this thesis is to study the nucleation and growth of defects in pure alumina and Cr-doped alumina, and to investigate how their behavior is affected by residual stresses, such those introduce by thermal expansion of the crystal grains.

In this thesis, digital image correlation is applied to polycrystalline aluminas (i.e. Cr-doped alumina and pure alumina with average grain 3.6 μm and 1.5 μm respectively) that are stressed in an optical microscope. The defect size and the surface crack opening displacement were measured using digital image correlation. The distribution and population of crack nucleating defects were obtained by in-situ observation of the stressed surface and by analysis with digital image correlation. These data are then compared with independent measurements of the defect population using Hertzian indentation, from which defect populations are derived for the pure and Cr-doped alumina samples.

Grain boundary plane and grain orientations in the vicinity of crack nuclei were characterised by electron microscopy. Crack nuclei were shown to develop at boundaries predicted to have high tensile thermal strains, caused by the orientation of the grain boundary plane relative to the adjacent grains, such as basal plane grain facets. The techniques of focused ion beam (FIB) milling and electron backscatter diffraction (EBSD) characterization of the crystallographic orientations and structure of cracked grain boundaries were used to provide data for a model to explain the cracking of these boundaries as a result of the thermal strains and the anisotropic thermal expansion behaviour of alumina.

Declaration

No portion of the work referred to in the thesis has been submitted in support of an application for another degree or qualification of this or any other university or other institute of learning.

Copyright Statement

Dedication

Firstly, thanks to Allah Almighty for giving me the strength, patience and will to finish this project.

This thesis is dedicated in honour to my beloved parents, my brothers, and my sisters for their prayers, understanding and never-ending support and encouragement during my studies.

Also, this thesis is dedicated to my lovely wife for her patience and companionship to complete this Ph. D study. This thesis is dedicated to my beloved baby for bringing a great joy to me and my wife.

Mohsin

Acknowledgment

I would like to thank my supervisor Professor James Marrow for his advice, suggestions and continuous support. I am really happy and feel extremely lucky to work under his supervision. I would like to thank Dr. Colin Leach for his advices.

I would like to express my deepest sense of gratitude to my sponsor the Ministry of Higher Education and Scientific Research in Iraq and Iraqi Culture Department in London for financial support. I would like to thank the Almath Crucibles Ltd, Newmarket, UK for providing the fine alumina samples.

I would like to thank Mike Faulkner for his assistance and training in SEM and EBSD and Ken Gyves for his help with sample preparation. I would like to thank Dr. Jonathan Duff for his assistance in digital image correlation, DIC. I thank all my friends for their support during my PhD.

Finally, I would like to thank my brother Abo Ali and his family during these four years in Manchester, I have been glad with them outside the study environment.

List of Abbreviations

BSE	Back Scatter Electron
CCD	Charge Coupled Device
CTE	Coefficient of Thermal Expansion
DCT	Diffraction Contrast Tomography
DIC	Digital Image Correlation
EBSD	Electron Back Scatter Diffraction
ε_{xx}	Background Strain Parallel to Loading Direction
ε_{yy}	Background Strain Perpendicular to Loading Direction
FCC	Face Centred Cubic
FEG-SEM	Field Emission Gun – Scanning Electron Microscope
FEM	Finite Element Model
FFT	Fast Fourier Transform
FIB	Focused Ion Beam
G1, G2	Grain One, Grain Two ...etc
G12	Grain Boundary between Grain One and Grain Two
GBP	Grain Boundary Plane
HCP	Hexagonal Close Packed
HF	Hydrofluoric Acid
OIM	Orientation Imaging Microscopy
OM	Optical Microscope
PECS	Precision Etching Coating System
RMS	Root Mean Square
SCOD	Surface Crack Opening Displacement
SEM	Scanning Electron Microscope
SE	Secondary Electron
SIF	Stress Intensity Factor
TEM	Transmission Electron Microscope

Chapter 1

1 Introduction

Polycrystalline alumina has good mechanical properties and these properties provide alumina with significant applications [1]. The melting temperature for α-alumina is about 2050 ± 4 °C. It has a good creep resistance due to alumina being stable at high temperature and it also has excellent compressive strength [1]. Polycrystalline alumina is used in medical and high temperature applications (for example, crucible applications) and electronics applications.

There is a relationship between the failure stress and average grain size in polycrystalline alumina (i.e. when the average grain size is large the failure stress is reduced) [2]. Larger crack sizes result in higher stress intensity factor values. These cracks are initiated from the defects on the surface [3].

Polycrystalline alumina surface has a residual stress which can protect its surface from the direct micro-cracking. These residual stresses are equilibrated in the ceramic surface when there is no external load. Polycrystalline α-alumina has a residual stress at boundaries during the change of temperature from the sintering or processing temperature to room temperature. The thermal stresses are produced from the anisotropy in the coefficient thermal expansion and crystallographic directions and this behaviour will provide micro-cracking at boundaries [4].

The polycrystalline ceramic surface was prepared with grinding and polishing and that will produce defects. The ceramic strength will be reduced due to the surface cracks and these cracks are produced from the surface preparation. The Hertzian technique is used to measure the crack size and population for these cracks on the ceramic surface and also fracture toughness was measured at the minimum fracture load [5-8].

This Thesis investigates the fracture and residual stress in polycrystalline alumina. Predicting the development of the intergranular cracking requires knowledge of the short crack growth. The crack nucleation is studied to understand and avoid the sudden fracture and to design the crack path in alumina. A new experimental method for the examination of

the early stages of crack growth during load application by four point bending was applied, with Digital Image Correlation (DIC) used to observe and quantify short crack behaviour. Measurements of the grain boundary plane and grain orientations at the locations of crack nuclei by Electron Backscatter Diffraction (EBSD) and trace analysis of Focused Ion-Beam (FIB) milled cross-sections were used to calculate the relative thermal displacements normal to the grain boundaries. A simple model was developed that assumes the anisotropic grain pairs were embedded in an isotropic medium. Higher tensile strains are predicted when the basal plane (0001) is closer to the grain boundary plane pole. The predicted stresses were compared with the observed behaviour of boundaries to verify the model.

Aims of the Project:

- To find and observe the intergranular cracks in polycrystalline alumina using digital image correlation experiments.
- To observe the defect density and size and also, to calculate the fracture toughness using a Hertzian indentation test.
- To understand the criteria for the crack nucleation, in terms of the grain boundary plane and grain orientation.
- To verify whether the grain boundaries with poles close to the basal plane (0001) tend to crack due to the predicted higher tensile residual stress.

This PhD thesis is organised into the following sections:

- 2D Observation of Intergranular Cracking
  - Digital Image Correlation, DIC
  - Destructive analysis of Grain Boundary Planes
- Modelling of Intergranular Strains
  - Image-based Finite Element Modelling
  - Experimental Validation of the Model
- Indirect Observation of Defect Size and Density
  - Hertzian Indentation Test

For this purpose, experiments were carried out in the sequence illustrated in Figure 1-1. Two materials have been studied in this work, pure alumina with average grain size of 1.5 µm and Cr-doped alumina with average grain size of 3.6 µm.

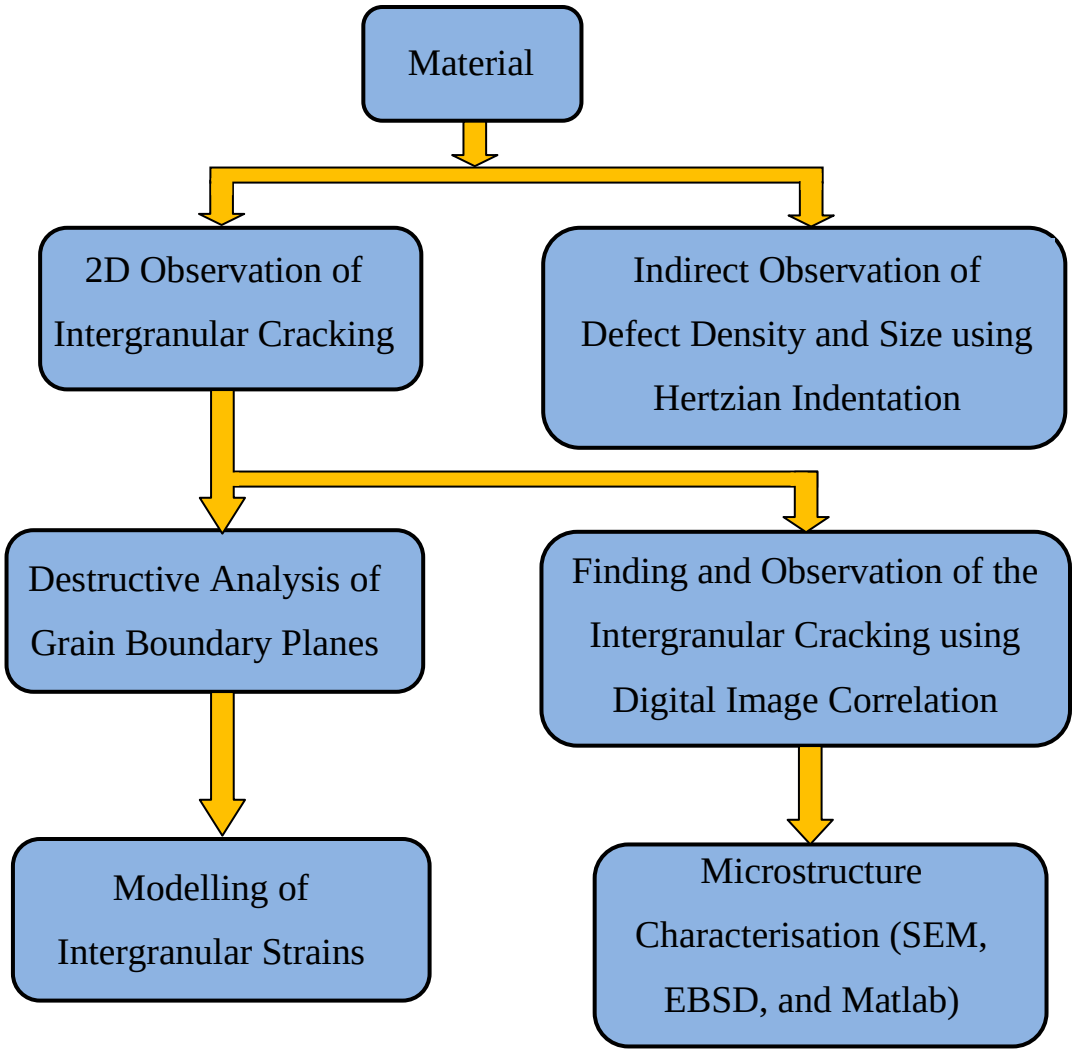

Figure 1-1: The flowchart of the main aims for this thesis.

Chapter 2

2 Literature Review

2.1 Crystal Structure of Alumina

Polycrystalline alumina, Al_2O_3 is a ceramic material. The alumina exists with different phases depending on the alumina purity and its mechanical and physical properties [9]. Alumina (α–phase) is a thermodynamically stable phase, which can be used as a coating to keep the material surface safe from wear. Alumina has other properties for example, mechanical properties, chemical inertness, and thermal stability and these properties provide useful applications for the alumina [10]. Polycrystalline alumina was used as catalyst and catalyst support due to the alumina having a small grain size and high surface area [9, 11]. The alumina phases were explained in this chapter.

The alumina phases are γ, θ, and α phase which represent the crystalline phases that are important in the alumina structure. The α–phase is stable at high temperature (i.e. melting temperature for this phase is 2051 °C) but the other phases do not always exist in the alumina.

The polycrystalline alumina α–phase, is formed at the high temperature of about 1000 °C. The properties for the α–alumina are not the same for other phases, which gives the alumina phases a wide range for applications [9]. Table 2-1 shows the mechanical properties for the alumina phases and also shows the melting temperature for these phases. The α–alumina has a hexagonal structure but the γ–alumina has a spinel structure.

Table 2-1: The phases for the alumina and their mechanical and physical properties at different melting temperatures [9].

Alumina	Selected Properties			
	Density, kg/m^3	Elastic Modulus, GPa	Hardness, GPa	Melting Temperature, °C
α–Alumina	3980	409	28	2051
γ–Alumina	3200	—	—	γ→δ: 700–800
θ–Alumina	3560	—	—	θ → α: 1050

The α–phase alumina is stable at high temperatures and also, other phases are transformed to α–phase at high temperature. At the specific temperature the γ and θ phases are transformed to the corundum phase as shown in Figure 2-1. The α–alumina does not change to the γ and θ phases and the α–phase is thermodynamically stable at 1000 °C [9, 12].

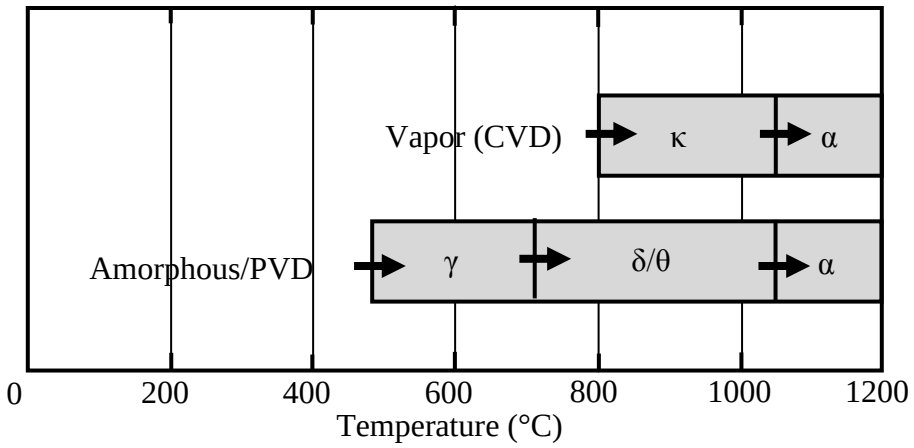

Figure 2-1: The alumina phases (i.e. *α, γ,* and θ phases) and the transition stages at different temperatures [9].

2.1.1 Crystalline Phase of θ–Alumina

The θ–phase is one of the alumina phases, this phase is not a stable phase and it is transformed into the α–phase at high temperature of about 1050 °C [9]. The density value for the α–alumina phase is higher than for the θ–alumina phase as shown in Table 2-1

(i.e. the density for the α–alumina is about 4000 kg/m^3 but for the θ–alumina phase is about 3600 kg/m^3) [9].

The close packed oxygen lattice shows the structure for α, γ and θ phases. The α–alumina has Hexagonal Close Packed (HCP) structure and the Face Centre Cubic (FCC) oxygen lattice shows the structure for the θ–phase [13]. Figure 2-2 shows the oxygen lattice with blue large spheres and the aluminium lattice with two arrangements to form this lattice. The first arrangement is octahedral interstitial locations and the second arrangement is tetrahedral locations. The band gap is about 7.4 eV to provide this phase with insulating properties with high ionic conductivity [14].

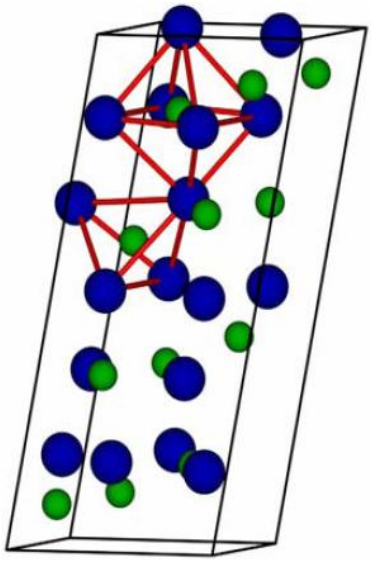

Figure 2-2: Shows a unit cell for the θ–alumina phase. The oxygen atoms show with large blue circles and aluminium atoms with the small green circles.

2.1.2 Crystalline Phase of γ-Alumina

The γ–Al_2O_3 phase is an unstable phase and it is transformed to the θ–alumina phase at a temperature of 700–800 °C. This phase of alumina was used as a catalyst and catalyst support as the γ–Al_2O_3 unit cell has a large specific area and also has a low surface energy [15]. This phase is not used in the high temperature applications because this phase transforms to the stable phase at high temperature (i.e. α–alumina) [16].

The lattice structure for the γ–Al_2O_3 phase has two different lattices, the first lattice is comprised of aluminium ions and it is formed from octahedral and tetrahedral interstitial

locations and the oxygen lattice is formed with the face centre cubic structure are shown in Figure 2-3 [16].

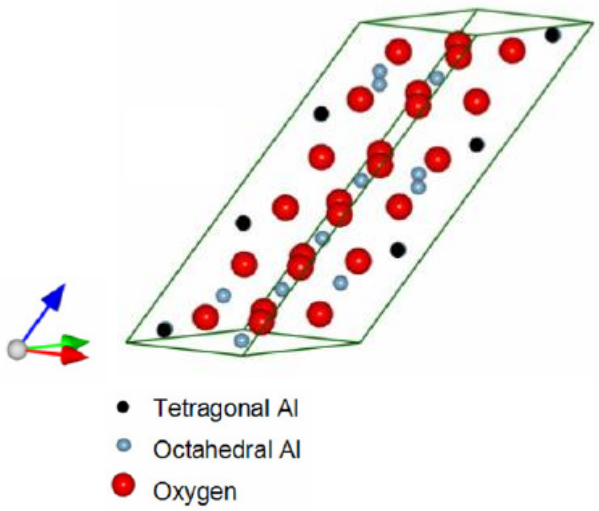

Figure 2-3: The face centre cubic structure for the oxygen lattice and the octahedral and tetrahedral structure for the aluminium lattice. The whole structure forms the γ–alumina phase structure [17].

2.1.3 Crystal Structure of α–Alumina

Polycrystalline α–phase alumina is used as a structural ceramic due it having good mechanical properties and also excellent thermal properties at high temperatures. Polycrystalline alumina has a high strength and these properties are provided during developing, processing, and optimizing the polycrystalline alumina. The alumina was used in parts for many applications instead of the other ceramics due to its high strength. There are many ceramics that have been used as structural ceramics for example titania (TiO_2), zirconia (ZrO_2), magnesia (MgO), yttria (Y_2O_3) and alumina–magnesia spinel ($MgAl_2O_4$). In gas turbine applications, non-oxide ceramics have been used, for example, silicon carbide (SiC), and silicon nitride (Si_3N_4) [12]. When the α–Al_2O_3 phase is single crystal it is called sapphire and has also been used in structural ceramics [12].

The polycrystalline alumina lattice for the α–phase has large oxygen ions with arrangement A–B–A–B to form the HCP sublattice. This arrangement represents the anion structure. The octahedral locations were filled by the cations and also the planes between the oxygen layers, which were represented by close packed planes filled by the cations (i.e. vacancies).

Figure 2-4 shows the basal plane for the α–alumina phase and the arrangement for the oxygen and aluminium layers. The vacant cation location is used to describe the arrangement for the three different types of the cation layers and the cation arrangement in the series a–b–c–a–b–c. The whole arrangement of the anions and cations forming the unit cell for the α–alumina phase is A–a–B–b–A–c–B–a–A–b–B–c–A. The lattice parameters for the hexagonal structure are (a_0=4.7589×10^{-8} cm and c_0=12.991×10^{-8} cm) and the ionic radii for the aluminium ion is 0.053 nm and it is 0.138 nm for the oxygen ions [10].

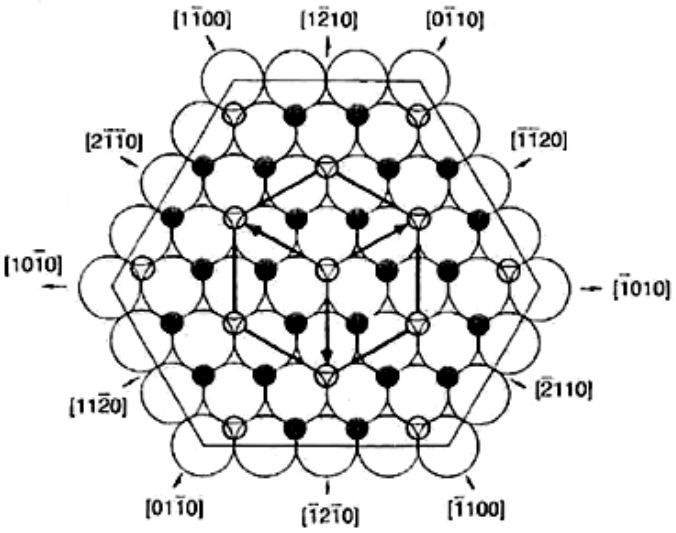

Figure 2-4: Shows the cation and anion arrangement for the basal plane in the α-alumina phase. The large open spheres represents the anion layer and the small filled and open spheres represent the aluminium and vacant octahedral interstices respectively [18].

Figure 2-5 shows the global Cartesian coordinate system for the single grain and the elastic and thermal properties for the polycrystalline ceramics depending on these coordinates with axes x, y, and z [19]. The a- and c-direction represents the crystal coordinate system within the grain (i.e. single grain). The hexagonal directions for the polycrystalline ceramic are the a- and c-directions, which were represented with the crystallographic directions. The elastic and thermal properties for the hexagonal structure depend on these directions (i.e. one direction has a higher value from the thermal and elastic properties which are represented by c-direction and the other direction has a small value for these properties in the a-direction). This behaviour is called anisotropy. In the polycrystalline ceramics, the anisotropy strain produced due to the thermal expansion coefficient was different between

the crystallographic directions (i.e. α_{11} represent the thermal coefficient in a-direction and α_{33} represent the coefficient in c-direction) when the material was cooling from the sintering temperature to the room temperature (i.e. temperature change (ΔT)) [19].

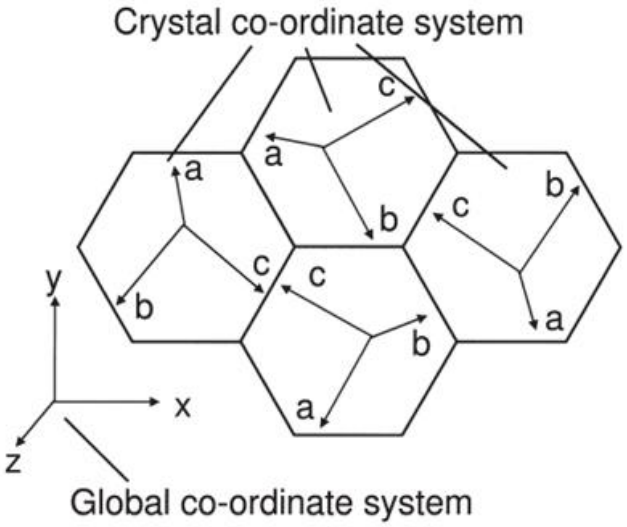

Figure 2-5: The basal plane in the hexagonal structure and the global Cartesian and crystal coordinate system for this structure [19].

2.1.3.1 Applications of α–Alumina

Polycrystalline alumina has good properties for use in mechanical and electronic applications and this represents the main applications for alumina. The minor applications for this material are in the thermal and chemical applications [10]. Polycrystalline alumina is used to fabricate high pressure sodium lamps, specifically from translucent alumina, as this type of alumina has a higher chemically stability and high heat resistance [20].

There are two sets of polycrystalline alumina and these groups depend on the alumina purity and the applications. Table 2-2 shows the high purity alumina, which represents the first group for the polycrystalline alumina and the purity is at least 99% alumina.

Table 2-3 shows the second group, which represents the low purity alumina and this group has purity from 80 % to 99 % alumina. For each group there are many grades as shown in these tables [21]. Some materials were added to the alumina during the processing in order to provide these groups and grades. Sometimes these materials do not affect the mechanical properties. The high purity alumina (i.e. the first group as shown in Table 2-2) has a density (> 3.75 g/cm^3) and this value was obtained at the high temperature between

(1500–1900 °C). The low purity alumina (i.e. the second group as shown in Table 2-3) has good properties for these material applications. Also these grades are easy to fabricate.

Table 2-2: The high purity alumina grades, porosity, density, and applications and their purity at least (99% alumina) [21-23].

Grade	Al_2O_3 Content,%	Kind of product and applications	Porosity %	Density g/cm^3	Applications
A1	> 99.6	Electrical and Engineering	0.2–3	3.75–3.95	Structural
A2	> 99.8	Translucent	<1	3.90–3.99	Sodium lamp
A3	> 99.5	Hot-pressed	<1	3.80–3.99	Machine tools
A4	> 99.6	Sintered Recrystallised	3–6	3.75–3.85	Refractory
A5	99.0–99.6	Low dielectric	1–5	3.76–3.94	Microwave

Table 2-3: Shows the lower purity alumina, porosity, density, and their applications. The purity for this group is between 80% to 90 % alumina [21].

Grade	Al_2O_3 Content,%	Kind of product and applications	Porosity %	Density g/cm^3	Applications
A6	99.5–99.0	Electrical and Engineering	1–5	3.71–3.92	Mechanical and Electrical
A7	94.5–96.5	Electrical and Engineering	2–5	3.60–3.90	Insulators and Wear parts
A8	86.0–94.5	Electrical and Engineering	2–5	3.40–3.90	Insulator, Wear parts, Refractory
A9	80.0–86.0	Electrical and Engineering	3–6	3.30–3.60	Insulator, Wear parts, Refractory

The polycrystalline alumina with high purity is more than 99% alumina and it is a thermodynamically stable phase, which was used for high temperature applications.

Figure 2-6 shows crucible products, which are fabricated from recrystallised high purity alumina. These have high thermal shock resistance due to the high average grain size for polycrystalline alumina of about 200 μm [22]. The corrosion strength was measured after the decrease in the glassy phases of the polycrystalline alumina surface when these phases are attacked by the chemical media. The high purity alumina caused to increase the dielectric and electrical properties.

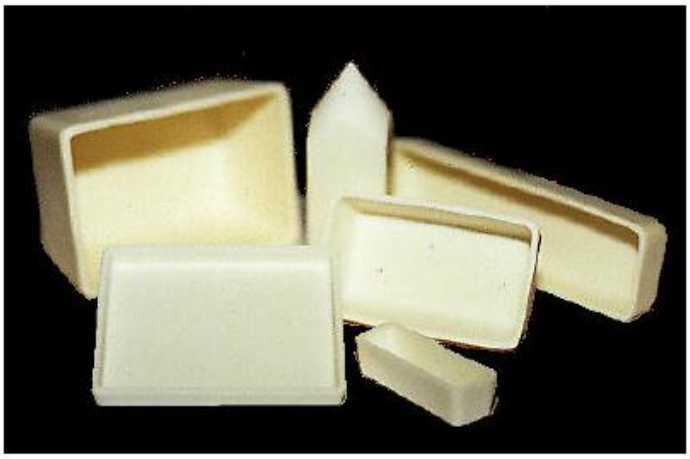

Figure 2-6: Shows the crucibles which were made from the high purity re-crystallised alumina of about 99% alumina [22].

2.1.3.2 Physical properties of α–Alumina

Polycrystalline α–alumina has good physical properties, which provide the technical and structural applications in the single crystal and polycrystalline α–alumina. These properties are shown below:

2.1.3.2.1 Thermal properties

Table 2-4 describes the thermal expansion coefficient, specific heat, enthalpy and the thermal conductivity properties for higher and lower purity polycrystalline alumina. The thermal expansion coefficient was measured from the sample size change, divided by the temperature in the a- and c-direction for the alumina.

Table 2-4: The thermal properties for the higher and lower purity alumina at 25°C [21-24].

Grade	Thermal Expansion Coefficient 10^{-6} (1 / K)	Specific Heat (J / g.K)	Enthalpy at 25 °C, (J / g)	Thermal Conductivity (W / m.K)
A1	5.4	0.775	0	30–40
A2	5.4	0.775	0	30–40
A3	5.4	0.775	0	27–40
A4	5.4	0.775	0	25–35
A5	5.4	0.780	0	30–40
A6	5.1–5.4	0.780	0	25–30
A7	5.1–5.4	0.760–0.780	0	20–30
A8	4.9–5.5	0.755–0.785	0	15–20
A9	4.9–5.5	0.750–0.785	0	15–20

The change in the sample size to the original size (ΔL/L) describes the thermal expansion and after the thermal expansion is divided by the temperature change to obtain the thermal expansion coefficient (α). (C_p) represents the specific heat, (ΔH) represents the enthalpy and (λ) represents the thermal conductivity and all these properties depend on the temperature (K) and also, these properties are related by the equations below [21].

$$\Delta L/L = -0.180 + 5.494 \times 10^{-4} T + 2.252 \times 10^{-7} T^2 - 2.894 \times 10^{-11} T^3 \quad \text{(A1–A4, 25-1600 °C)} \quad (1)$$

$$\alpha = 5.494 \times 10^{-4} + 4.504 \times 10^{-7} T - 8.682 \times 10^{-11} T^2 \quad \text{(A–A4, in 1/K, 25-1600 °C)} \quad (2)$$

$$C_p = 1.0446 + 1.742 \times 10^{-4} T - 2.796 \times 10^{4} T^{-2} \quad \text{(A1–A4, in J/g.K, to 1500 °C)} \quad (3)$$

$$\Delta H = -412.86 + 1.0446 T + 0.872 \times 10^{-4} T^2 + 27960 T^{-1} \quad \text{(A1–A4, in J/g, 25-1500 °C)} \quad (4)$$

$$\lambda = 5.5 + 34.5 \exp [-0.0033 \times (T - 273)] \quad \text{(A1–A4, in W/m.K, 25-1300 °C)} \quad (5)$$

The thermal expansion coefficient (α) in Equation (2) is measured by the differentiation of the thermal expansion as described in Equation (1). The enthalpy (ΔH) in the Equation (4) is calculated by integrating the specific heat in Equation (3) divided by the temperature (i.e. C_p / T) at (25°C) to temperature (T).

2.1.3.2.2 Thermal expansion coefficient (α)

The high temperature will cause crystal dimensions to change due to the anisotropy in different crystallographic directions [25]. The thermal expansion coefficient for the polycrystalline alumina and single grains are increased with increasing temperature as shown in Figure 2-7 a, b. This figure shows the (α) at 25 °C and also at a high temperature of 1200 °C for the polycrystalline alumina with average grain size of about 23 μm. This alumina has porosity ranging from 4% to 49% and there is no relationship between the porosity values and the value of (α). Figure 2-7 a shows the thermal expansion coefficient for the single alumina grain at the low and high temperature of about 100 °C and 1100 °C respectively and also shows (α) in this range from the temperature for the polycrystalline alumina. There are two values for the thermal expansion coefficient in the hexagonal structure one of them is parallel to the c-direction and another one is parallel to the a-direction. The thermal expansion coefficient in a- and c-direction was measured at this range of the temperature, between 100 °C and 800 °C and the results for the value of (α) in c-direction is higher by about 10% than the value of (α) in the a-direction [10].

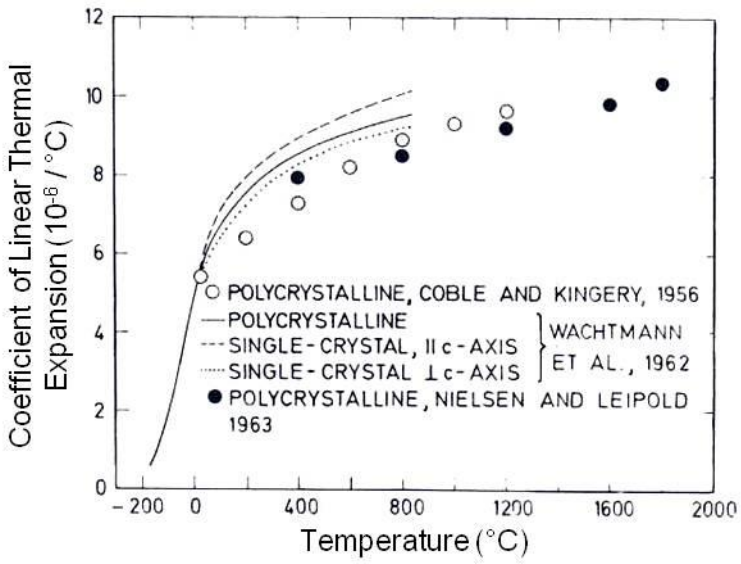

a)

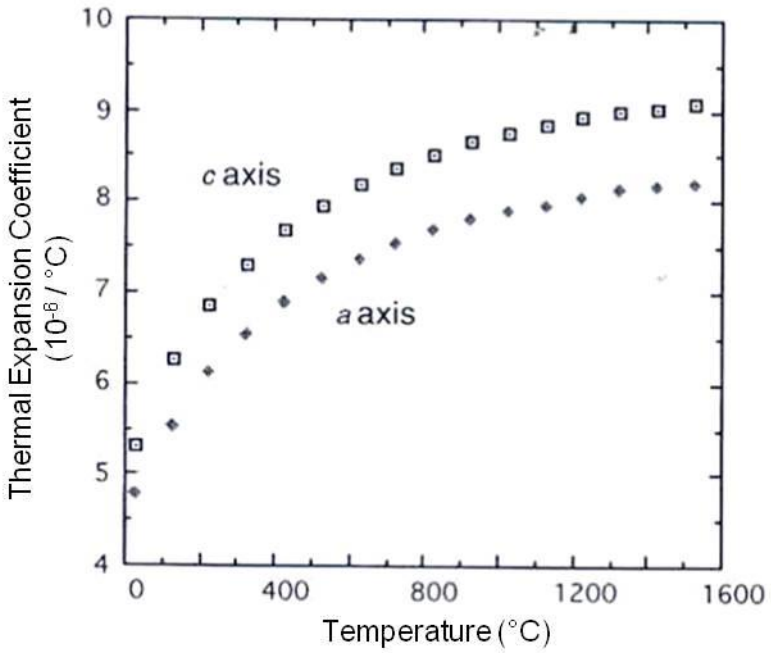

b)

Figure 2-7: a) Shows the (α) for the polycrystalline alumina and individual grain increase with increasing the temperature from various studies [10], whereas b) Shows the values (α) for the individual gains in the α-alumina [26].

2.1.3.2.3 Sintering and grain growth

The sintering method is used to fabricate ceramic materials by the material transferring from the source to the sink of matter. The surface tension was used to assess the driving force for the firing method in the ceramic material. There are different paths to transfer the material from the ceramic surface or from the grain boundary or from the internal sources to the neck which represents the sink of matter, shown in Figure 2-8. There are six paths to show the diffusion or transport between grains [27]:

-The first, second and third paths represent the diffusion from the surface to the neck of the two particles.

-The fourth, fifth and sixth paths represent the diffusion from the crystal boundary to the neck of the two particles.

The firing method is divided into types and these types depend on the shrinkage behaviour. The first type causes the shrinkage (i.e. methods from fourth to the sixth path which caused the shrinkage) and the second type does not cause shrinkage (i.e. methods from first to the third path which do not cause shrinkage) [10].

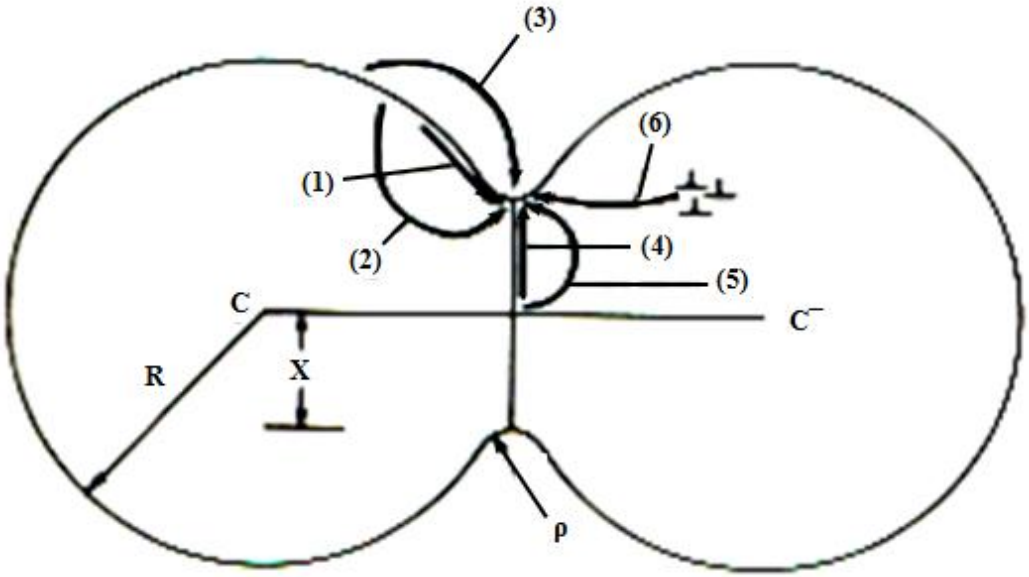

Figure 2-8: The firing mechanism with the six paths to describe the material transfer to the sink [10].

Some impurities were added to polycrystalline alumina during the firing method [28]. The magnesium oxide was added about (0.05 wt%) to polycrystalline alumina during the sintering and that controls the growth of the grains during the sintering procedure and these materials resulting a porosity is about 0.5 % [22]. There are other impurities that have a harmful affect on the sintering procedure, for example calcium oxide and silicon oxide [22].

2.1.3.3 Mechanical properties of α–Alumina

2.1.3.3.1 Elasticity

The mechanical applications and behaviour for the polycrystalline alumina depend on the elastic properties for Al_2O_3 (i.e. high and low purity alumina). The Young modulus and Poisson's ratio were used to describe the lattice strain and also the strain energies. The crystallographic directions for the hexagonal structure are not the same that causes the anisotropy in Young modulus and Poisson's ratio (i.e. anisotropy elastic properties) and the elastic strain was anisotropic for the same reason as above [10].

The crystallographic directions (a- and c-direction) are anisotropic in the single crystal and this occurs at the microscopic scale for the polycrystalline ceramics. The Cartesian coordinates for the macroscopic scale are the same that causes the isotropic behaviour at this scale [10].

Table 2-5 describes the Young modulus, shear modulus, and Poisson's ratio at 25°C. Figure 2-9 shows that these properties are increased with increasing the temperature for the polycrystalline alumina [21].

Table 2-5: This table describes the Young Modulus, Shear modulus, Poisson ratio, and the porosity at 25°C in α-Al_2O_3 [21-23].

Grade	Al_2O_3 / Porosity, %	Young's Modulus, GPa	Shear Modulus, GPa	Poisson's Ratio
A1	≥ 99.6 / 0–2	410–370	164–158	0.27–0.24
A2	≥ 99.8 / < 1	405–380	164–161	0.25–0.22
A3	≥ 99.5 / < 1	400–370	163–140	0.26–0.23
A4	≥ 99.6 / 3–6	380–340	150–140	0.26–0.24
A5	≥ 99.0 / 1–5	380–340	145–130	0.26–0.24
A6	96.5–99.0 / 1–5	375–340	140–120	0.25–0.24
A7	94.5–96.5 / 1–5	370–300	140–110	0.25–0.23
A8	86.0–94.5 / 2–5	330–260	130–100	0.25–0.22
A9	80.0–86.0 / 3–6	330–260	130–100	0.25–0.22

$$E = E_o \times [1 - \eta_E \times (T–298)] \quad \text{with} \quad \eta_E = 1.2\times10^{-4}\ 1/K \quad (6)$$

$$G = G_o \times [1 - \eta_G \times (T–298)] \quad \text{with} \quad \eta_G = 1.4\times10^{-4}\ 1/K \quad (7)$$

$$\nu = \nu_o \times [1 - \eta\nu \times (T–298)] \quad \text{with} \quad \eta_\nu = 6.9\times10^{-5}\ 1/K \quad (8)$$

Where: (E) represent the Young modulus, (G) is the shear modulus, and (ν) is the Poisson's ratio and they depend on the temperature (T) in Kelvin (see Equations 6, 7, and 8). (E_o), (G_o), and, (ν_o) represent the elastic properties at room temperature of Young modulus, Shear modulus, and Poisson's ratio as described in Table 2-5.

Figure 2-9 shows the Young modulus applies correctly at this temperature range (750–1000 °C), Shear modulus applies correctly at this temperature range (650-800 °C) and Poisson's ratio applies correctly at this temperature range (650–700 °C) [21].

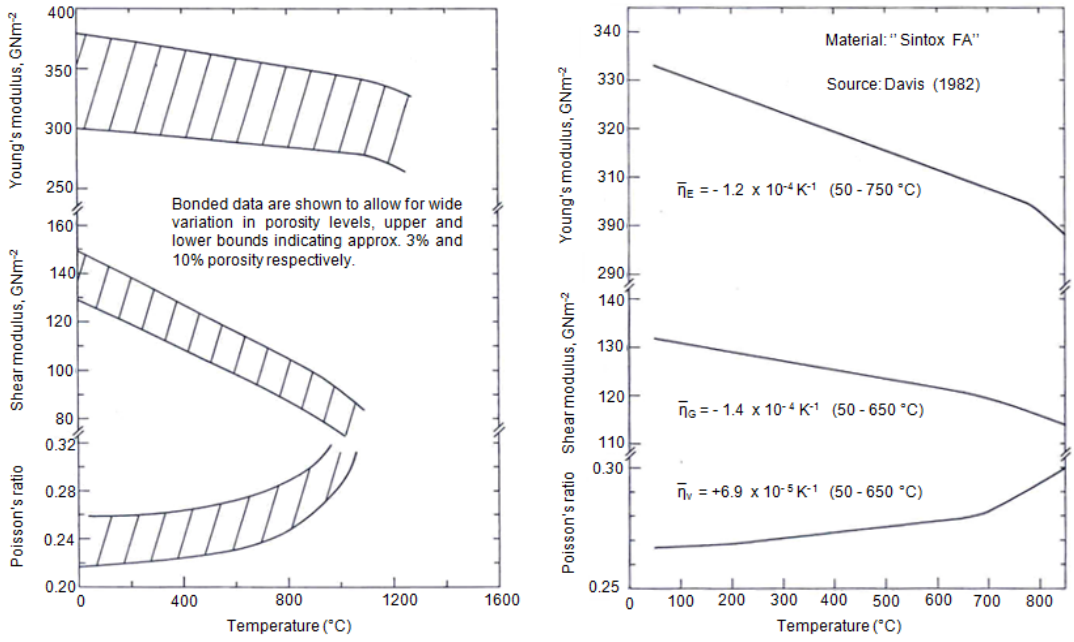

a) b)

Figure 2-9: Describes the elastic properties (E, G, and ν) against the temperature for the α-Al_2O_3 for the group a) high-purity alumina for grade A4 and this alumina has porosity with range 3% to 10% b) low-purity alumina for grade A7 in the polycrystalline alumina [21].

2.1.3.3.2 Crack behaviour in polycrystalline α–Alumina

Polycrystalline alumina surface has cracks, which were initiated by different external sources. These cracks can propagate and grow when the polycrystalline alumina surface is subjected to the external load (for example bending stress). Polycrystalline alumina was used in many applications due to the alumina having good mechanical and thermal properties. The grinding and polishing technique was caused to provide many cracks on the alumina surface and these cracks will have an effect of reducing the sample strength. The polycrystalline alumina surface has another kind of crack; these are hidden cracks, their location is subsurface and they will also reduce the sample quality. The surface residual stresses are very important to study the fractures on the sample surface (i.e. the unexpected failure will occur on the sample when the external stress was higher than surface residual stress). The apparent fracture toughness is affected by these residual stresses (i.e. the fracture toughness was higher at large crack length) [29, 30].

The type of cracking that commonly happens for the polycrystalline alumina is intergranular. The intergranular cracks are propagated between the grains and also this kind of crack will separate the neighbouring grains. If there is a bridge at the crack tip that will stop the crack growing and also affect the surface crack opening [31].

A high applied load was provided from the indentation test and this behaviour will introduce a crack on the polycrystalline alumina surface, as shown in Figure 2-10a. These cracks were observable due to the sample surface being prepared using polishing and the thermal etching procedure for the sample of interest (i.e. sample with cracks). The grain boundary was observed, the thermal etching will release the energy at the grain boundary that will cause problems to see the crack (i.e. the intergranular crack is similar to the grain boundary) and also the crack has no coating due to the crack opening and it is charging under SEM. Figure 2-10a shows the indentation location on the top left of this image and also shows the crack tip, which is not easy to observe but the main crack was seen under SEM with many branches (i.e. A, B, C, and D). Figure 2-10b shows the grains and grain boundary orientation using Orientation Imaging Microscopy (OIM) [32].

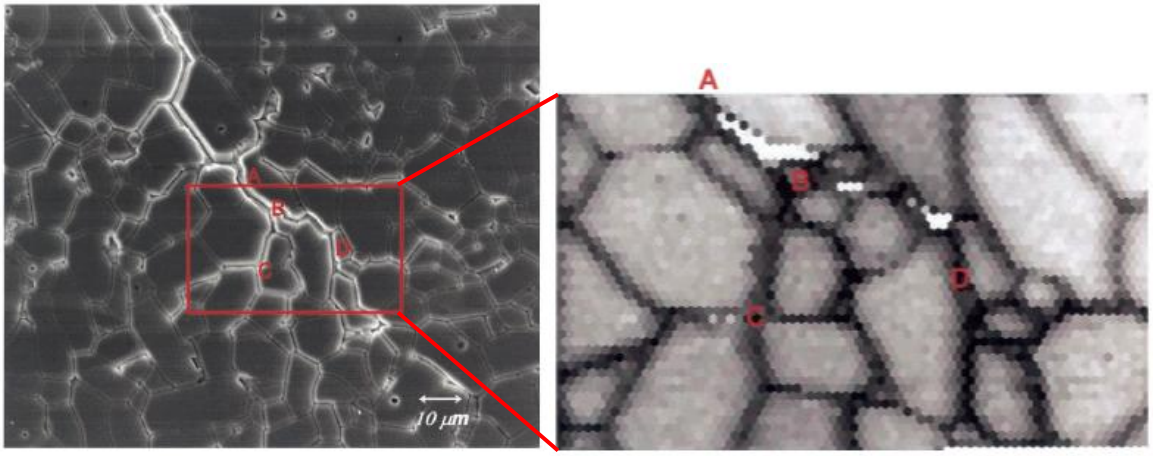

a) b)

Figure 2-10: Images showing a) the scanning electron microscopy for the Al_2O_3 with crack which was produced by indentation b) the grain orientation map for the polycrystalline alumina using (OIM) [32].

The coarse grain size alumina with average grain size 104 μm has intergranular residual stress due to the anisotropic thermal expansion coefficient [33]. Figure 2-11 shows the grains and grain boundary orientation. This figure describes the intergranular cracking along the grain boundaries with higher thermal expansion coefficient for these boundaries [33]. Also, the microcracking was produced in the composite material due to the phases that were different and that introduced anisotropy coefficient thermal expansion [34, 35]. Electron backscatter diffraction was used to study the grains and grain boundary orientation for polycrystalline alumina with different grain size, for example 16 μm and 104 μm. There is a relationship between the average grain size and the step size (for example the step size is 4.8 μm and 0.8 μm for the average grain sizes of 104 μm and 16 μm respectively). The crystal properties represent by the elastic stiffness properties (C_{11} = 496.8 GPa, C_{12} = 163.6 GPa, C_{13} = 110.9 GPa, C_{33} = 498.1 GPa and C_{44} = 147.4 GPa) and the coefficient of the thermal expansion ($\alpha_{11} = \alpha_{22} = 8.62\times10^{-6}$ K^{-1} and $\alpha_{33} = 9.38\times10^{-6}$ K^{-1}) [33]. The thermal stresses at the grain boundaries are measured when the polycrystalline alumina is cooling from the sintering temperature (i.e. change of temperature from 1900 °C to 25°C) [33]. The Griffith method is used to build the finite element model for the crack formation and also the crack growing in the polycrystalline alumina [19].

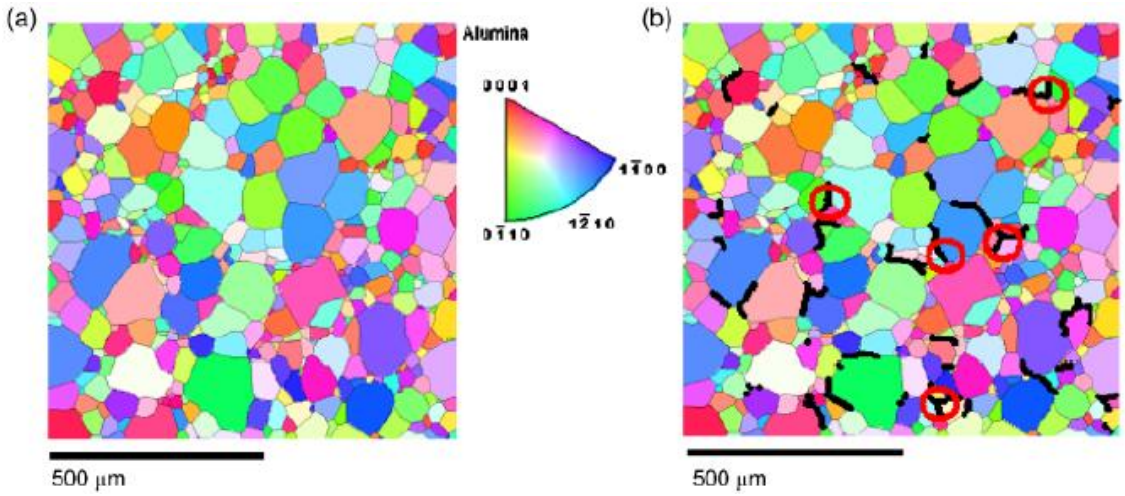

Figure 2-11: a) Shows the grains orientation using EBSD for the alumina has average grain size 104 μm and b) Shows the FEM to study the microcracking distribution in the EBSD map [33].

2.1.3.3.3 Residual stress and initial microcracking in polycrystalline α-Alumina

The residual stress is in the solid material when there is no external applied load. The residual stress was used to protect the material from these external loads due to it being balanced with the external loads [36]. There are other sources which produce these residual stresses for example the plastic deformation (i.e. the residual stress produced during the sample preparation). The residual stresses are introduced from the different phases (for example the composite material) and also from different elements (for example the coating) [37]. The residual stress is used to keep the sample safe from failure when this kind of residual stress is compressive [38].

There are three kinds of the residual stresses and these groups depend on the residual stress range (i.e. small or big range for these stresses) [39]:

The first type of the residual stress is with large length scale and these stresses are found in the compound material or in the pure material, the first type is called macrostresses. The second type of the residual stress has a scale length and this will compare with grain size. This kind of stress will introduce the anisotropy strain in the grains (i.e. this kind of stress is called microstresses). The third type of residual stress is introduced within the sub-crystal (i.e. the scale size for the third type is smaller than the grain size) and also from some of the

defects (for example dislocations, and vacancies) and it is also called microstresses and causes the anisotropy strain [40].

The residual stresses were used to keep the material from cracking due to the balancing between theses residual stresses and the externally applied load. The residual stress will also be introduced due to the anisotropy crystallographic directions in the polycrystalline ceramics and these directions will cause the anisotropy thermal expansion coefficient during the cooling from the processing temperature to room temperature (i.e. change of temperature). The residual stress depends on the distribution of the grain boundary orientation (i.e. texture) and also on the average grain size [41].

The ceramic materials will provide anisotropy thermal expansion coefficient and also the misfit strain due to change of temperature. These thermal strains will introduce the microcracking at the grain boundary and these cracks will initiate when the crack size is larger than the critical grain size. The crack does not occur when the crack size is below the critical grain size. The grain size does not affect the residual stress in a brittle material but the fracture energy was determined from these stresses and this behaviour depends on the average grain size. Figure 2-12 shows the microstructure with the microcracks and also, shows the residual magnitude of the stresses at the same region of interest [42]. The EBSD was used to study the grains and grain boundary orientation and also to describe the high stresses along the boundary which introduced the microcracking [43] as shown in Figure 2-12.

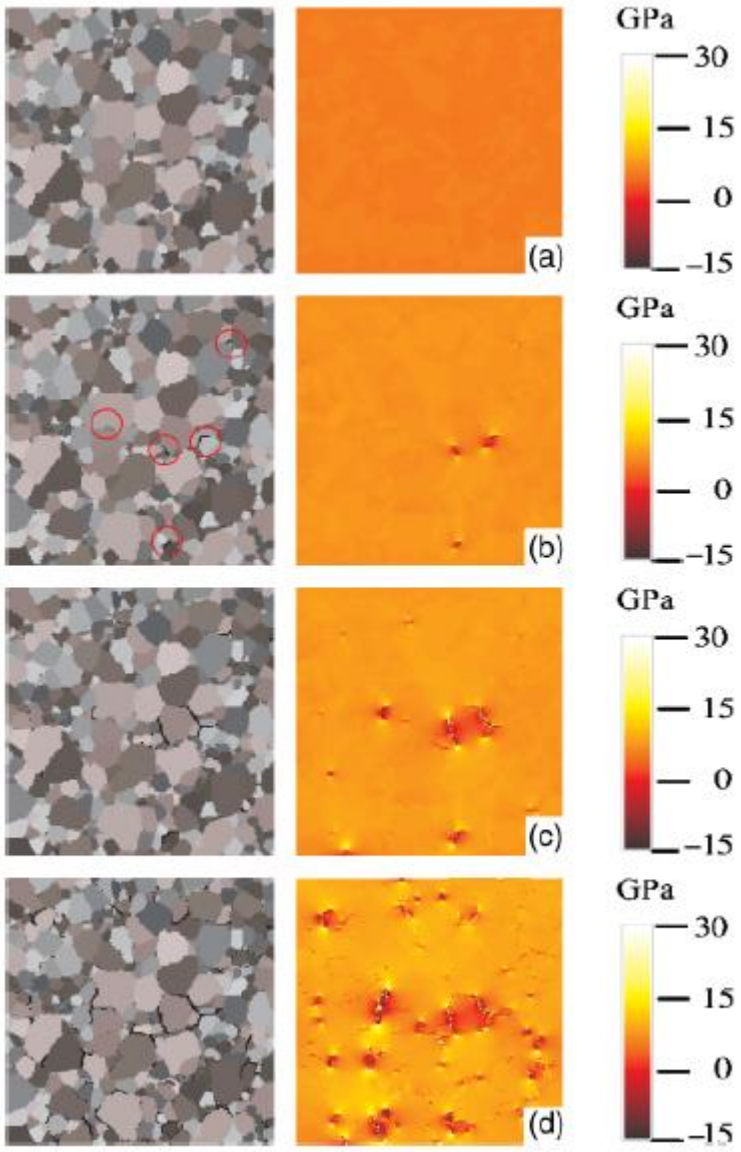

Figure 2-12: A coarse ceramic with average grain size 104 µm with the microcracks as marker with red circles and the distribution residual stress in x- and y-direction (σ_{xx}+ σ_{yy}) map to show the high residual stress at the same location for these microcracks at different temperatures changes , a) ΔT=–450 °C, b) ΔT=–950 °C, c) ΔT=–1150 °C and d) ΔT=–1550 °C [33].

The polycrystalline ceramics are cooled from the processing temperature [44-46]. The residual stresses are introduced from the anisotropic thermal contraction and these stresses are the cause of the microcracks. A simple model predicts that the stresses depend on the grain facet length and they have a maximum value when the grains have a normal direction for their facet length (A, B, C and D). The range of the residual stresses is compared with

the scale size of the facet length for the grains and the residual stress is changed from the tension to the compression between the neighbouring gains, as shown in Figure 2-13 [46].

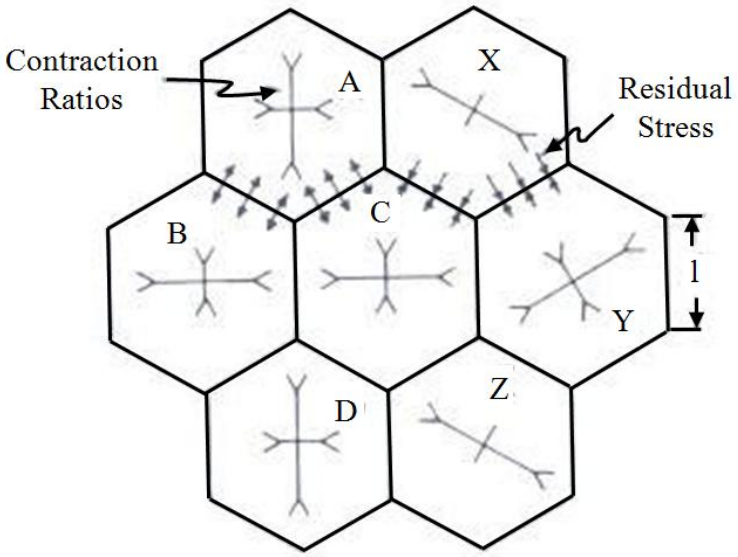

Figure 2-13: Shows the tension and compression residual stresses along the facet length for the grains [47].

The residual stress at the facet grain is calculated using Equation 9.

$$\sigma(x) \approx E \times \Delta\alpha \times \Delta T \times [1 + a \times \ln(l / x)] F(\theta, \phi) \qquad (9)$$

Where: (E) represents the Young's modulus of the polycrystals brittle material, (Δα) represents the coefficient of the thermal expansion difference (i.e. the change between high and low thermal expansion coefficient) (ΔT) represents the change of temperature (i.e. cooling from sintering temperature to the room temperature), (l) represents the facet length for the grains, (x) represents the distance from the grain edge to the region stress, (a) is a constant, and (F) represents the function for the adjoining crystals and (θ, Ø) represents the misorientation for the neighbouring crystals.

The residual stresses are allowed at the scale ln (l / x) and they also increase with increasing the grain size. These residual stresses are the cause of the microcracks in the large grain size [46]. The failure occurs when the facet grain length is higher than the critical facet length (l_c) as shown in Equation 10 [44]:

$$l_c = 3.1\left(K_b / E \times \Delta\alpha \times \Delta T\right)^2 \quad (10)$$

Where: (K_b) represents the grain boundary fracture resistance when the facet size is larger than the critical facet length (l_c) [48].

The microcracking can be produced in the material due to the anisotropy thermal expansion and also these microcracks are initiated when the external load was applied [48]. Equation 9 describes the overlay between the residual stresses and the stress intensity factor at the uniform applied load. The compression residual stresses are caused to stop the microcracks and the neighbouring grains are not affecting by these microcracks, due to the compression at these adjoining grains, as presented in Figure 2-14.

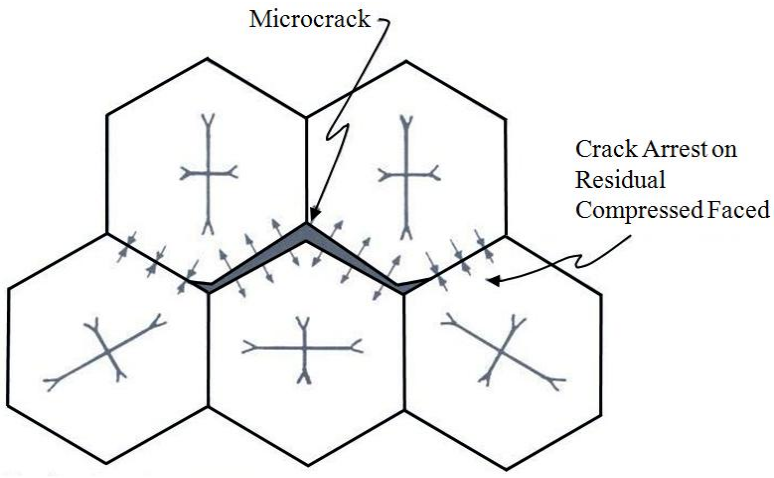

Figure 2-14: Shows microcracks opening at the tension residual stress and these microcracks are closed at the compression residual stresses [49].

2.1.3.4 Structure of Grain boundaries in α-Alumina

The facet planes presented the gain boundaries planes in the brittle samples [50]. The basal and rhombohedral planes, {0001} and $\{01\bar{1}2\}$, respectively, represent the low index planes which describe the facet planes in the polycrystalline alumina [51]. The surfaces for each grain were formed from the low index planes during the cooling from the firing temperature [50].

The grain boundaries structure and the grain's orientation are studied by using (TEM) and (EBSD) for the polycrystalline alumina [50]. The basal plane has a higher value of the stacking fault energy and the {0001} and $\{1\bar{2}10\}$ planes have been observed to form at the high temperature between 1300 °C–1400 °C in the creep testing under tensile loading [52].
The grains and grain boundary orientations and the misorientation between the grains are used to study the structure for the polycrystalline alumina grain boundaries [53]. The facet planes for the polycrystalline alumina are basal plane (C) (0001), pyramidal plane (P) $\{11\bar{2}3\}$, structural Rhombohedral plane (S) $\{01\bar{1}1\}$, Rhombohedral plane (R) $\{01\bar{1}2\}$ and there is plane with low energy and this plane is called a prismatic plane (M) $\{01\bar{1}0\}$ [51].

2.2 Diffraction Contrast Tomography of Polycrystalline Alumina

Figure 2-15 a, shows the microstructure for the alumina with coarse average grain size of about 100 μm [33]. Diffraction contrast tomography (DCT) is used to study the grains orientations as shown in Figure 2-15 b. The three-dimensional microstructure was observed and the intergranular porosity is determined by using DCT are shown in Figure 2-15 c [54]. The intergranular cracking in the coarse grain size along the grain boundary is propagated under a compressive stress as shown in Figure 2-15 d [54].
The grain boundaries planes or facets planes have low index energy and the facets planes are in the same direction for the low index plane. The stereographic projection was used to assess the grain boundary planes and also the grain boundary poles distribution. The grain boundary planes poles are studied relative to the crystal axes (for example a- and c-direction for the hexagonal structure). Figure 2-16 shows the facet planes poles distribution for the polycrystalline alumina [51].

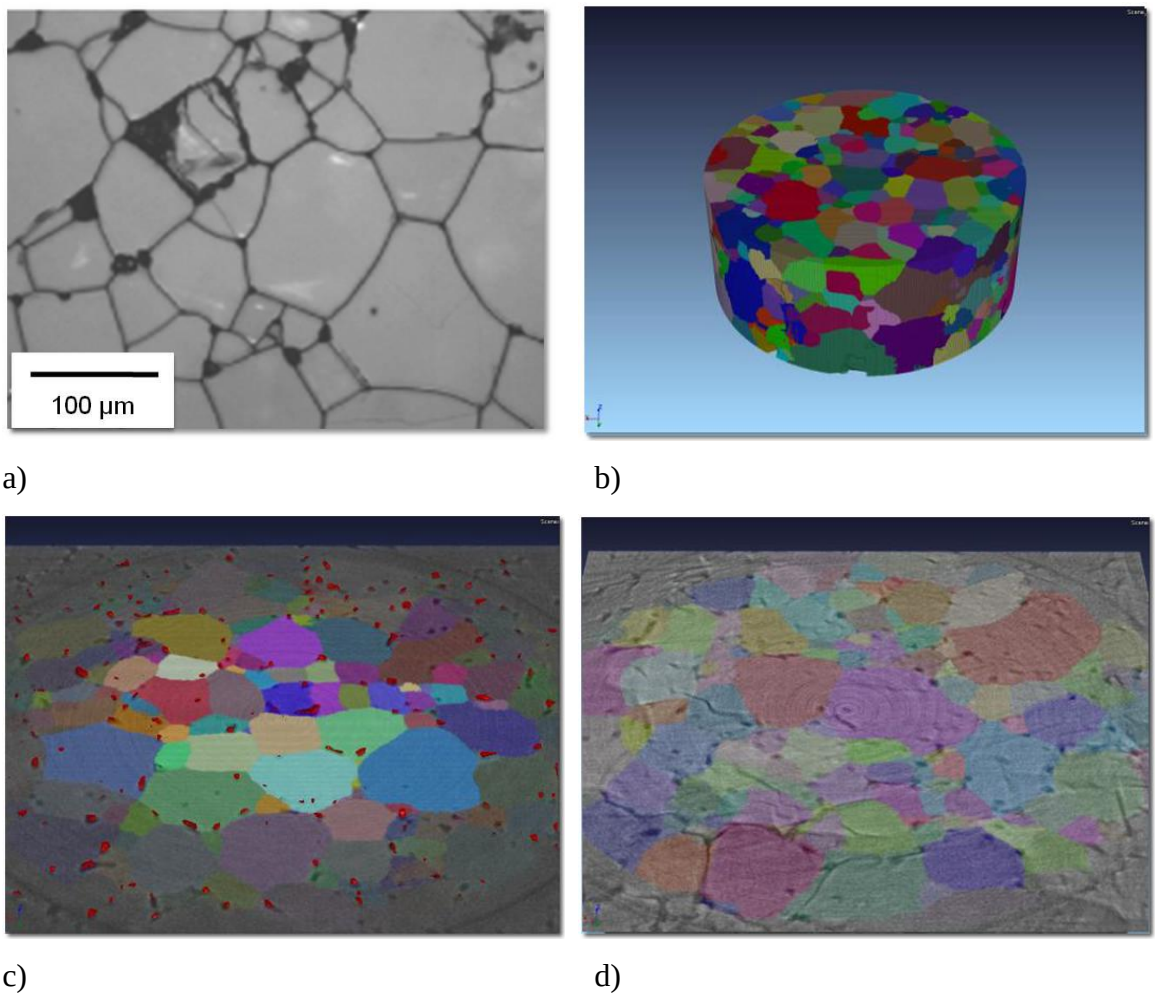

Figure 2-15: a) Shows the microstructure for the coarse alumina with average grain size of 100 µm [33], b) Shows the three dimensional structural for the alumina with a volume of about 1 mm diameter and 0.5 mm high [54], c) Shows the intergranular porosity in the coarse alumina [54] d) Shows the intergranular microcracks which are observed under the compressive stresses [54].

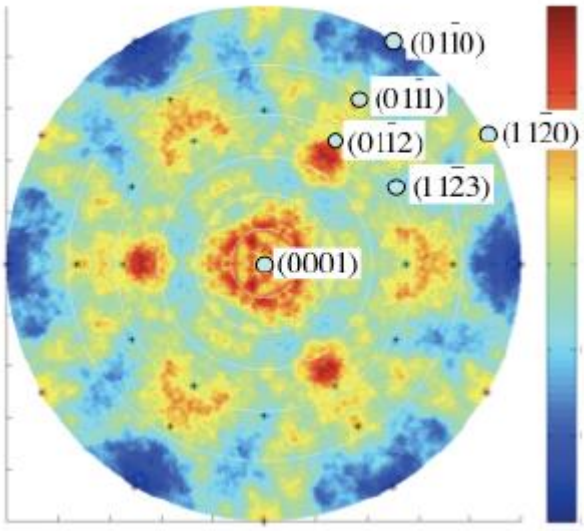

Figure 2-16: Shows the facets planes poles distribution using the stereographic projection for the (α-Al_2O_3) [51].

David Gonzales has written a finite element model (FEM) to predict intergranular strain [55]. The intergranular stresses are measured along the grain boundary and stress variation across the grain, after the polycrystalline alumina was cooled from 1900 °C to room temperature. Figure 2-17 shows the results for the FEM, which was used to calculate the thermal stresses along the grain boundaries and across the grains in coarse polycrystalline alumina.

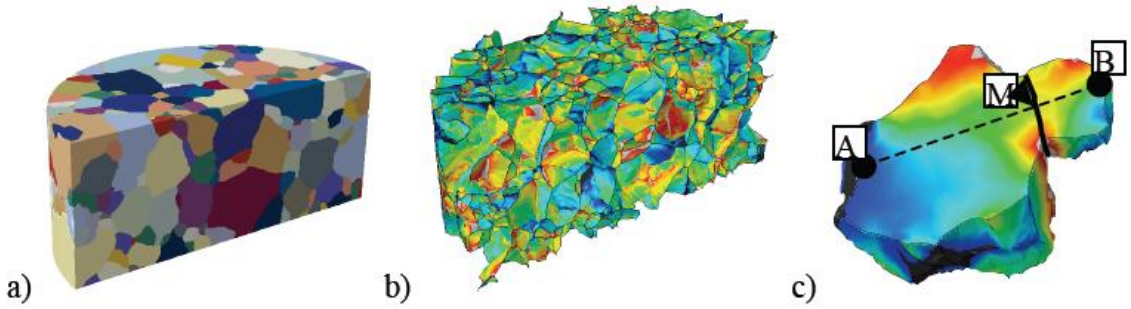

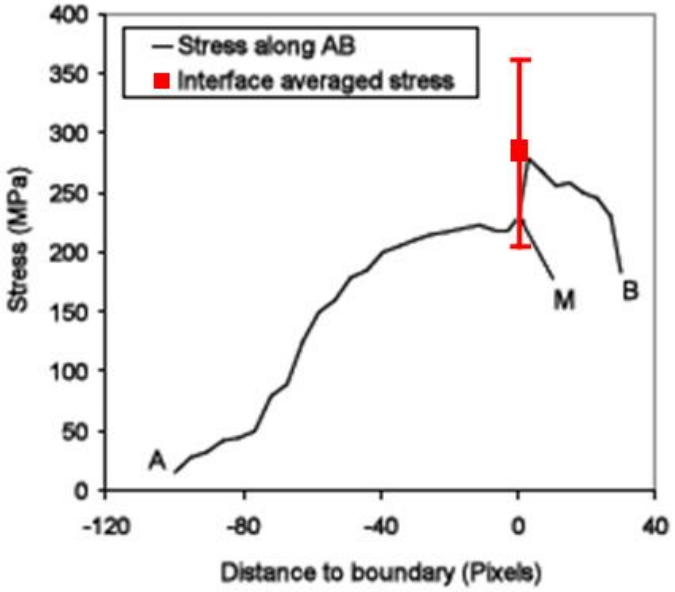

d)

Figure 2-17: The results from FEM, a) The three dimensional for the coarse alumina microstructure using DCT, b) The thermal stresses orthogonal to grain boundaries, c) Shows one grain boundary and the stress variation across the grain and grain boundary, d) The relationship between the intergranular stress as a function of the distance to boundary along the line AB and also the interface averaged stress at the grain interface (at the point M). (1 pixel is 1.8 µm) [55].

Summary

The alumina types are explained with mechanical and physical properties and the alumina crystallographic structure are described in this chapter. The polycrystalline α- alumina is explained in this chapter in detail and the relationship between the properties of the alumina and possible applications is detailed. The crack behaviour in the α-alumina is explained and also the crack sources are described in the literature review. The residual stresses at the grain boundary for the polycrystalline alumina, due to anisotropy thermal expansion coefficient after the cooling from the sintering temperature to the room temperature are described. These stresses introduced microcrack along the grain boundaries, due to the anisotropy crystallographic directions (i.e. a- and c-direction, for the hexagonal structure). The grains and grain boundary orientation was assessed using DCT and also the facet planes are explained for the alumina and these planes found to have low index energy.

2.3 Digital Image Correlation, DIC

Digital image correlation is used to calculate the vector displacement between two images before and after the deformation. The digital image correlation technique does not attach to the sample surface and the resolution from the optical microscope is enough to record the deformation. The digital image correlation does to obtain both uniform and not uniform deformation. The results are obtained directly for digital image correlation (i.e. numerical and modelling analysis do not need for analysis the data). Digital image correlation is used to obtain the vector displacement for the nano and micro applications.

2.3.1 Principle of Digital Image Correlation

Digital image correlation is used to provide the full field displacement in x- and y-direction for a series of the images. The full field displacement in the two dimensions is provided from the single camera, using digital image correlation technique [56-58]. There are many features on the sample surface (i.e. viewed area) and these features are moved in the x- and y-direction, this will provide vector displacement in both directions, but these features do not change in the z-direction.

In the area of interest (i.e. viewed area) there are many lines of pixels per image and also each line has many pixels per line. These pixels describe the light intensity. The South Carolina University 1980s used the digital image correlation for the first time and they modified digital image correlation equipments. The vector displacement was measured from two images before and after applied loads and these images have the same features distribution for the digital image correlation.

Figure 2-18 describes the digital image correlation technique, there are two subimages (S) and (S1) for the non-deformed and deformed cases respectively. The correlation between the deformed subimages (S1) and the non-deformed subimage (S) will provide the vector displacement in x-direction (u_m) and the displacement in y-direction (v_m) at the middle point in the non-deformed subimage (i.e. point M as shown on this figure). The Taylor expansion of the first order is used to determine the coordinates and the vector displacement in both directions (i.e. x-and y-direction) for the non-deformed subimage as shown below [56]:

$$x_{n1} = x_m + u_m + \left(1 + \left.\frac{\partial u}{\partial x}\right|_M\right) \cdot \Delta x + \left.\frac{\partial u}{\partial y}\right|_M \cdot \Delta y \quad (11)$$

$$y_{n1} = y_m + v_m + \left.\frac{\partial v}{\partial x}\right|_M \cdot \Delta x + \left(1 + \left.\frac{\partial v}{\partial y}\right|_M\right) \cdot \Delta y \quad (12)$$

$$C = \frac{\sum_{N \in S} \left[f(x_n, y_n) - f_d(x_{n1}, y_{n1})\right]^2}{\sum_{N \in S} \left[f(x_n, y_n)\right]^2} \quad (13)$$

Where: f(x, y) and f_d(x, y) represent the light intensity for the subimages (S) and (S1) respectively; (C) represents the matching function between the undeformed and deformed subimages. (x_n, y_n) represents the coordinates for the underformed subimage, (x_{n1}, y_{n1}) represents the coordinates for the deformed subimage.

The vector displacements in x-direction (u_m) and the vector displacement in y-direction (v_m) represent the actual displacement after the correlation between the deformed and underformed subimages. There are other displacements derived from the point at the centre of the underformed subimage and these are components in x- and y-direction and also shear components: $\left.\frac{\partial u}{\partial x}\right|_M, \left.\frac{\partial v}{\partial x}\right|_M, \left.\frac{\partial u}{\partial y}\right|_M, \left.\frac{\partial v}{\partial y}\right|_M$. Numerical methods are used to determine theses displacements, for example the Levenburg-Marquardt or Newton-Raphson methods [57, 58]. Figure 2-18 shows the Cartesian coordinates for the non-deformed and deformed subimage for the digital image correlation method.

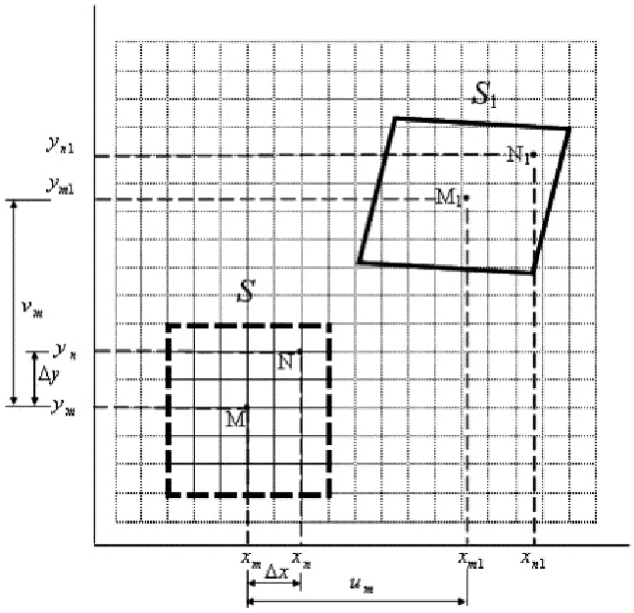

Figure 2-18: The digital image correlation procedure for the undeformed subimage (S) and the deformed subimage (S1) [56].

The displacements are measured after deformation of the sample (i.e. the samples are subjected to mechanical loading). Each sample has enough features on the surface and these features have the same distribution in both images (i.e. deformed and undeformed images) are used for the correction, as shown in Figure 2-19 a [59]. There is relationship between the subset size and the accuracy of displacement and this relationship depends on the features distribution on the sample surface. The strain is measured from the displacement (the change of distance between two features divided by original distance between them) which is calculated from the correlation between the deformed and undeformed subimages, as shown in Figure 2-19 b [59]. The viewed areas for the deformed and underformed subimages have the same features distribution. The samples are undergone deformation in x- and y-direction and also maybe rotation after the applied load and there is an option in the digital image correlation to modify the rotation and translation as shown in Figure 2-20. A number of methods are used for determining the parameters from the correlation, for example least–squares methods [60], Fourier transform methods [61] and Bayesian probability techniques [62, 63].

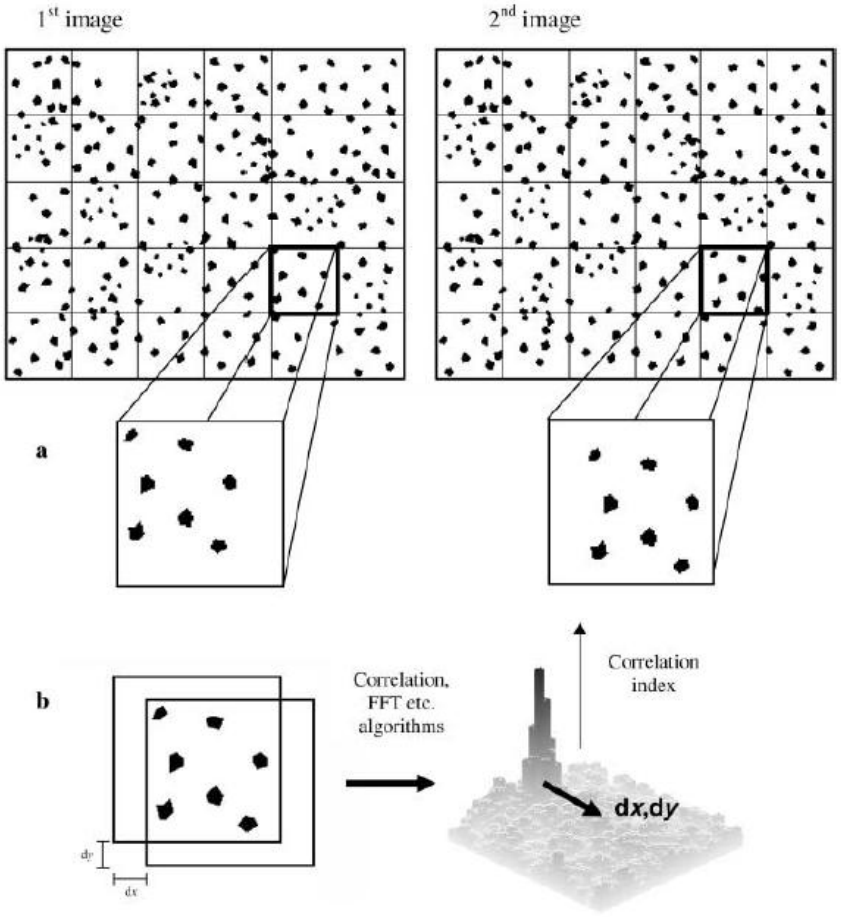

Figure 2-19: a) Shows two images (i.e. before and after the deformation); each one divided into many subimages and each subimage has enough features and the same distribution of features and b) Shows the matching between the deformed and underformed subimages to obtain the displacements in x- and y- direction (i.e. dx and dy) [59].

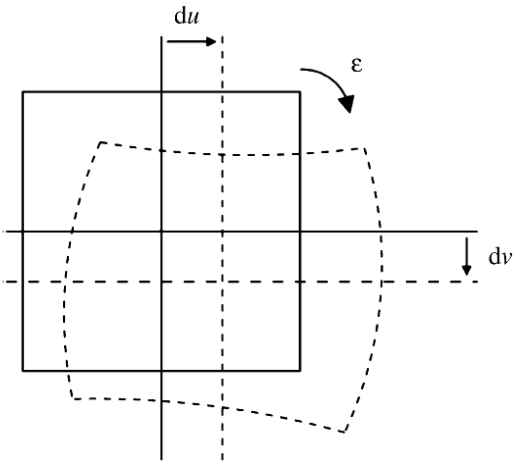

Figure 2-20: The deformation of the interrogation window size after the applied load and that caused the translation and rotation of this window after the deformation [59].

The digital image correlation is used to calculate the vector displacement in the x- and y-direction and also when the sample is rotated during the applied load, a shear component displacement occurred. The observed strains determined from these displacements components (i.e. x- and y-direction and shear components) are described in Equation 14 and the strain was obtained from DIC is different from the mechanical strain. [59].

$$\varepsilon_{xx} = \frac{du}{dx}, \qquad \varepsilon_{yy} = \frac{dv}{dy}, \qquad \varepsilon_{xy} = \frac{du}{dy}, \qquad \varepsilon_{yx} = \frac{dv}{dx}, \tag{14}$$

Where (u, v) represents the real displacement in the x- and y-direction respectively, dx and dy, represent the magnitudes of the vector displacement. The strains are determined from the vector displacement as mentioned in [64].

The vector displacement is calculated from the integer pixels (one pixel). Figure 2-21a, shows that there are two features; the first feature moves a whole pixel but the second one moves just half a pixel and this study is used to explain the peak locking behaviour. The peak locking is described from the probability density plot and this plot is observed from the vector displacement in the x-direction (i.e. du) as shown in Figure 2-21b. The plot shows the peak locking behaviour and the images will need re-treatmeant again to provide them with good features distribution on the sample surface for DIC.

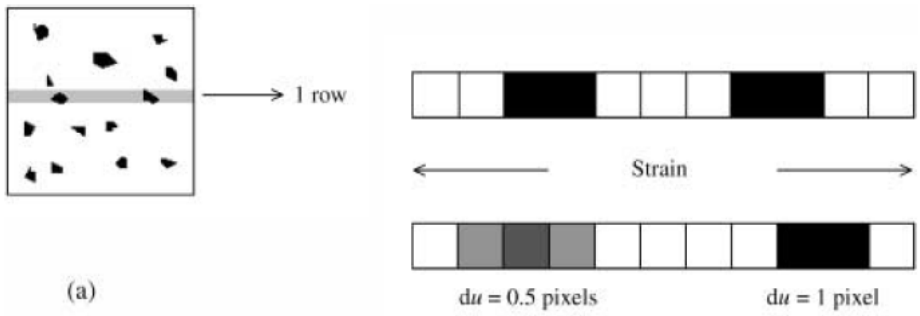

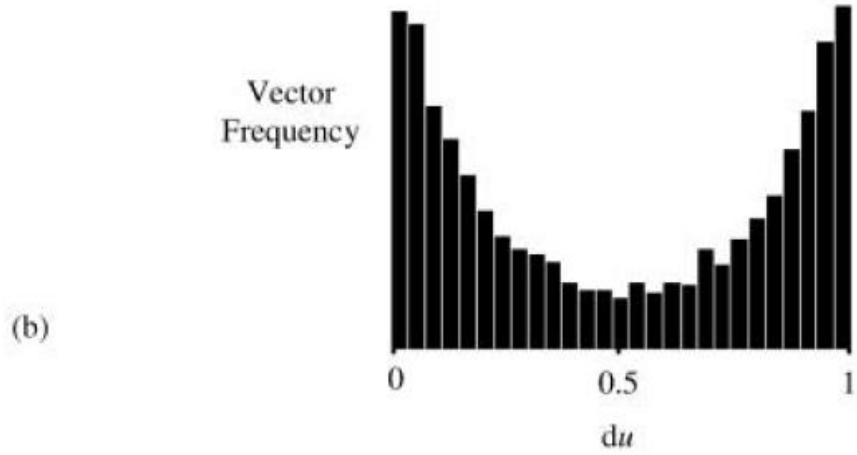

Figure 2-21: a) Shows the viewed area with many features on its surface. One array of pixels has two features; one of them moved one integer pixel but another feature moved half pixel. The first feature is strong for determining the displacement but the second feature is not very clear on the charge coupled device; b) Shows the peak locking behaviour from the probability density plot [59].

2.3.2 Digital Image Correlation Requirement

The area of interest for digital image correlation analysis has many features with suitable size. These features are deformed under applied load (i.e. the surface was prepared for digital image correlation correctly). The chemical etching or thermal etching is used to finish the area of interest for DIC in this project.

The sample surface is prepared for digital image correlation and then these features on the viewed area are checked by measuring the vector displacement accuracy. When the features sizes are small, there are two methods were used to improve the vector displacement accuracy, one of them using high magnification to observe many features on the viewed area (i.e. improve the image quality) and another method is used to provide the surface with other features for DIC. When the feature sizes are large, there are two methods were applied to reduce the vector displacement error (i.e. noise level). The first method is using a large interrogation window size that results in obtaining small errors in the vector displacement and the resolution is reduced for the strain features in the strain map. The second method uses a small magnification to cover a large number of the features within

the viewed area [65]. There is another method to prepare a large sample for the digital image correlation; using spray painting as shown in Figure 2-22.

The interrogation window size of 2×2 pixels is used for the feature size in the theory technique but the subset is 3×3 pixels for the experimental technique which is used for digital image correlation [59]. There is relationship between the interrogation window size and the accuracy of displacement (i.e. when the large interrogation windows size is used to obtain the high accuracy but the small window sizes provided the lesser accuracy) [66].

Figure 2-22: Shows the white and black spray paint for the large deformation; large viewed area and the feature sizes are measured [67].

2.3.3 Application of Digital Image Correlation

Haiyan Li *et al*. have applied DIC to study the crack initiation in the nuclear graphite as shown in Figure 2-23. These cracks were not observed using the optical microscope but digital image correlation is used to detect these cracks from the strain map. The observed strain is provided from the relative displacement [68]. These cracks are normal to the applied load and that caused the cracks to open. The crack lengths and openings are measured from the digital image correlation and the surface crack opening displacement equation is used to determine the crack depth. The failure stresses for the nuclear graphite depend on the crack size. The distribution of the fracture stresses in this material is studied relative to the cracks [68].

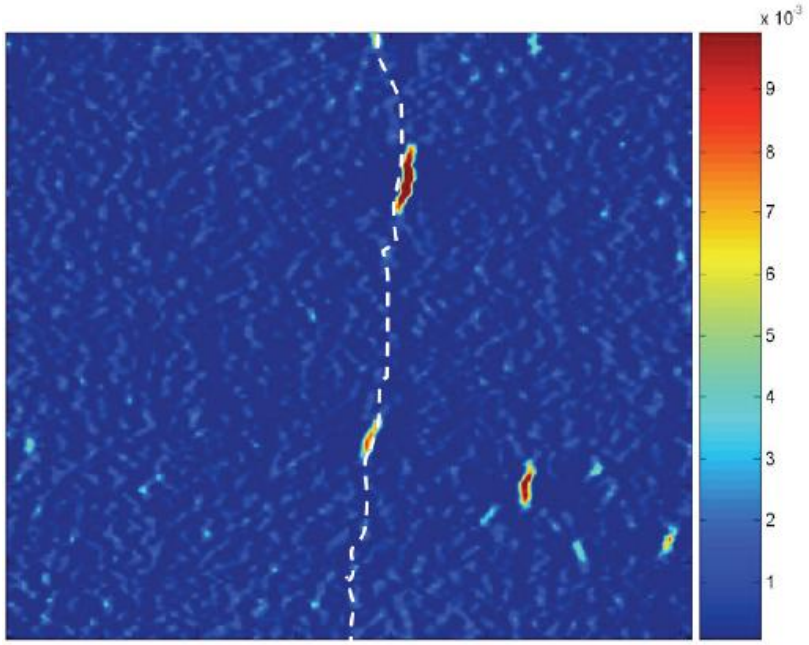

Figure 2-23: Shows the strain map which is used to observe the microcracks on the nuclear graphite surface and the white line describes the failure path [68].

M Mostafavi has also studied the defect development in the ceramics sample and specifically in a graphite specimen using DIC. The DIC is used to assess the crack creation and growing in the graphite samples and the applied biaxial flexural stress. This load caused the strain features to open. The surface crack opening displacement is measured from the displacement map after crack depth and length are measured. This experiment is used to understand the relationship between the applied load and the fracture stress [69]. Figure 2-24 shows the crack's development in the graphite sample under the flexural stress [69].

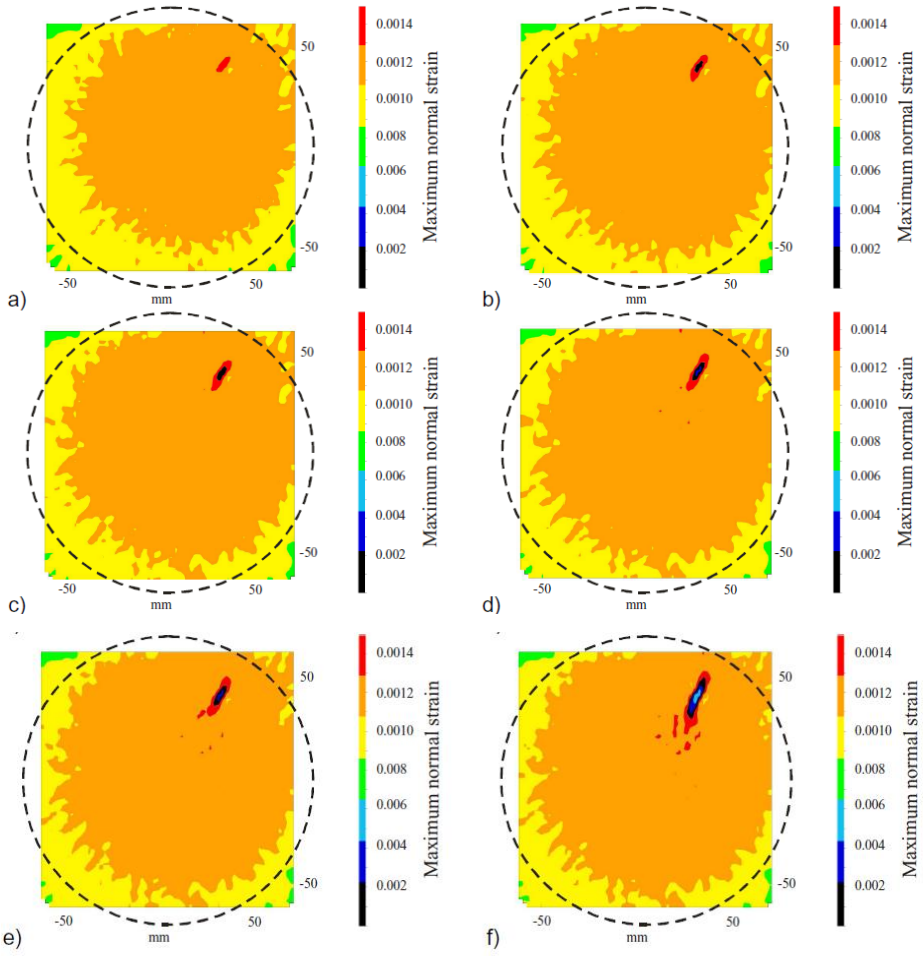

Figure 2-24: Shows a defect growing in the graphite sample when the sample is subjected to the flexural stress. The strain is analysed using DIC; the maximum normal strain for the area of interest a) σ_b=11.60 MPa, 2c= 1.5 mm, b) σ_b =22.80 MPa, 2c= 3.5 mm, c) σ_b = 22.90 MPa, 2c= 10.0 mm, d) σ_b = 23.00 MPa, 2c= 13.7 mm, e) σ_b = 23.05 MPa, 2c= 16.3 mm, f) σ_b = 23.10 MPa, 2c= 16.9 mm [69].

Jonathan Duff *et al*. have studied the intergranular cracking along grain boundaries under corrosion media (i.e. this kind of cracking is called intergranular stress corrosion cracking). The sample is used for this test is the stainless steel type 304H and also three point loading is used to apply the loading. The surface crack opening displacement is measured on each side of the cracks using DIC. Large cracks are detected in the stainless steel sample under applied load and these samples treated with 0.1 M potassium tetrathionate solution to induce stress corrosion cracking. This large intergranular stress corrosion cracking is shown in Figure 2-25 [70].

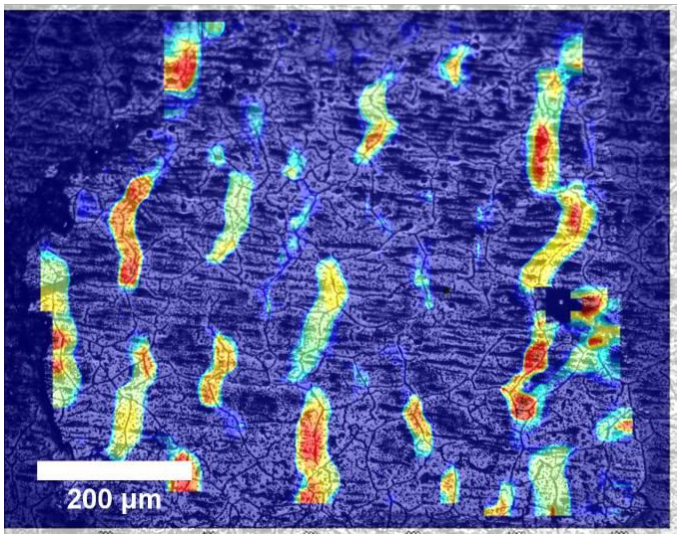

Figure 2-25: Shows the intergranular stress corrosion cracks with overlaying a stain map on the optical image after 48 hours and the red strain features show the cracks at the grain boundary [70].

S. Rahimi *et al*. have studied the stress corrosion cracking for the austenitic stainless steel in a test solution (0.1 M $K_2S_4O_8$) using a three point bending test. Figure 2-26 shows the crack development under these conditions using digital image correlation. The stainless steel sample surface is assessed using EBSD before the stress corrosion experiment. The sample is etched at 950 °C and this temperature provides the sample surface with the Σ3 grain boundary [71].

The optical microscope is used to collect the images at different times under the conditions above and then digital image correlation is used to observe the crack development in the strain map. The cracks are observed to arrest at the boundaries close to the Σ3 grain boundary which was observed from the electron back scatter diffraction map [71].

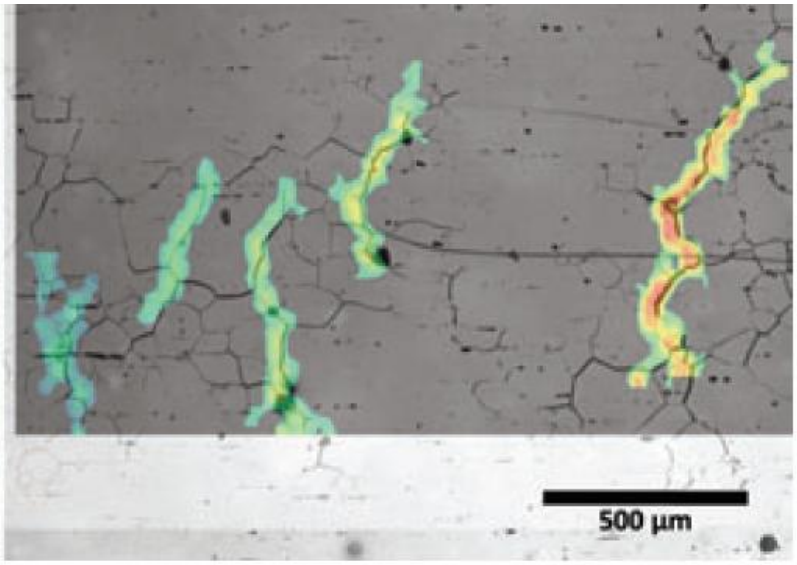

Figure 2-26: Shows the overlaid stain map with cracks at 24 hrs on the stainless steel microstructure at the same time [71].

A.A. Khan *et al*. have studied the localised strain for the cast magnesium alloy Elektron WE43 using DIC. This sample surface is assessed using EBSD for studying plastic deformation (for example twinning) and also to study the grain boundary orientation before DIC test. The magnesium sample is loaded using fatigue loading at different cycles to increase the plastic deformation and that causes the failure, as shown in Figure 2-27. The electron backscatter diffraction map is compared with the strain map from DIC for the same area of interest. The twinning is observed on the area of interest using EBSD map which was represented the source to initiate the plastic strain (i.e. the same region has twinning deformation using EBSD and localised strain using DIC). The failure occurred from the brittle phase [72].

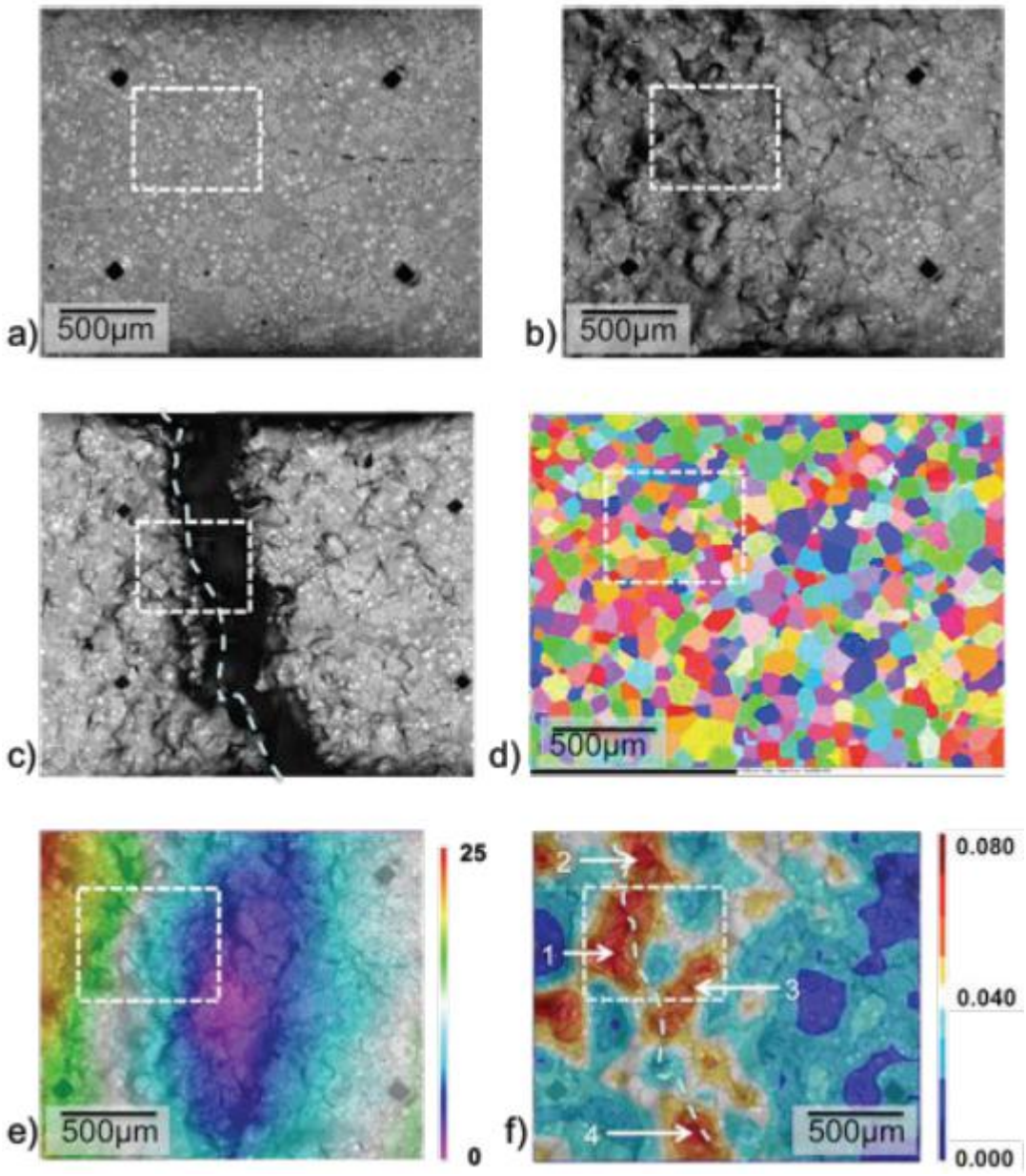

Figure 2-27: a) The initial image for the microstructure of the magnesium allay, b) The microstructure after fatigue test at 1510 cycles, c) The failure path in microstructure of the magnesium allay at 1513 cycles, d) The EBSD map for the sample before fatigue test. e, and f) The map of the displacement and the strain respectively from DIC after fatigue test at 1510 cycles [72].

V. Srinivasan *et al*. have prepared the samples using spray painting but the natural features are used for the alumina sample to obtain an accurate distribution of features. DIC is used to determine the coefficient of thermal expansion for polycrystalline alumina samples. The

normal features are used to obtain a good correlation and there is an option in the DIC to measure the thermal expansion coefficient. The thermal chamber is used to heat the alumina sample and that caused expansion of the sample dimensions and then the DIC software is used to provide the results for the CTE [73].

Stephane Roux *et al*. have used digital image correlation to assess the defect development in the silicon carbide ceramic. The DIC is used to study the surface crack opening displacement on each side of the defect and also, the crack length and crack depth were obtained from DIC. The sandwich beam (i.e. the initiated cracks are introduced on the sample surface) is used for this experiment for studying the crack development on the SiC surface. The 3-point bending technique is used to apply the load on the silicon carbide surface and that allowed the crack to propagate in the direction normal to the applied load. The stress intensity factor and fracture are measured using FEM data and these parameters depend on the displacement from DIC [74].

Summary

The DIC is used to assess and provide important information for the material on macroscales, microscales, and nanoscales. The DIC has a good resolution at these scales and can capture the deformation in the x- and y-direction at these scales. In this thesis the surface preparation using thermal etching for digital image correlation have been investigated. The crack's propagation in polycrystalline alumina is detected by using DIC and these cracks are not observed by using other techniques, for example optical and scanning electron microscope. The strain feature opening in the polycrystalline alumina provides the possibility to observe the cracks.

2.4 Hertzian Indentation

The failure description (i.e. the crack size and distribution) in a brittle material can be studied using Hertzian indentation mechanics [75, 76]. This test needs a level surface and a spherical indenter.

The grinding and polishing techniques are used to prepare the ceramic surface for the Hertzian test. These techniques initiate cracks on the brittle ceramic surface which cause the failure. The strength of material depends on the cracks, for example the wear strength is affected by these cracks. The crack lengths are determined at the applied load and these defects will propagate to form the ring crack during a Hertzian test [5-7, 77-80]. The Hertzian test is used to measure (K_{IC}) at the lower value from the applied load on the coarse surfaces [81].

A Hertzian test is used to determine the cracks sizes and crack distribution [78]. A solid indenter is used to apply the load on the ceramic surface to initiate the cracks on the surface. Wilshaw's method is used to calculate the crack densities [7]. The Hertzian test provides one failure force (P_F) and one ring crack radius at the specific defect length.

2.4.1 Contact stress field

The flat or level surface is used for the Hertzian test and there is no friction between the sample surface and the indenter, as shown in Figure 2-28. The contact region radius is measured using a Hertzian test with different elastic properties for the indenter and the sample as described in Equation 15 and the peak pressure (P_o) is calculated using Equation 17:

$$a = \left(\frac{3RP}{4E^*} \right)^{1/3} \tag{15}$$

$$\frac{1}{E^*} = \frac{1-\nu_1^{\,2}}{E_1} + \frac{1-\nu_2^{\,2}}{E_2} \tag{16}$$

$$P_o = \frac{3P}{2\pi a^2} \tag{17}$$

Where: (a) is the contact region radius, (R) is the indenter radius, and (P) is the applied load. The elastic properties are described by the Poisson's ratio ($\nu_{1)}$ and (ν_2) and Young's modulus (E_1) and (E_2) for the hard sphere and flat surface respectively.

There are two important stress components in the Hertzian test; the first stress component is the radial tensile stress at the contact region and this stress causes defects to develop on the ring cracks radius. The second stress component is the compressive stress that determines the final depth point of the crack and this stress is produced due to the radial stress decrease with the crack depth and that will provide the compressive stress as described in Figure 2-28 [82-84].

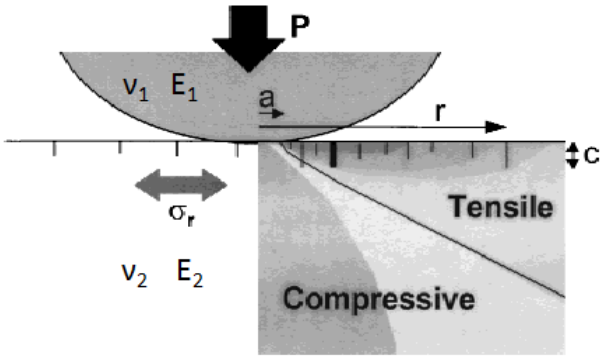

Figure 2-28: Shows the contact between the level ceramic surface and the indenter at the applied load (P) and the produced defect size (c) using Hertzian test. Also, the stresses field around the contact region is shown [85].

2.4.2 Evaluation of Hertzian Cone Crack

The solid and not sharp indenter is applied on the flat sample surface and this technique is used to produce the cracking, as shown in Figure 2-29. The defects are created and grow on the brittle material surface at the critical applied load; these defects propagate to the ring crack radius.

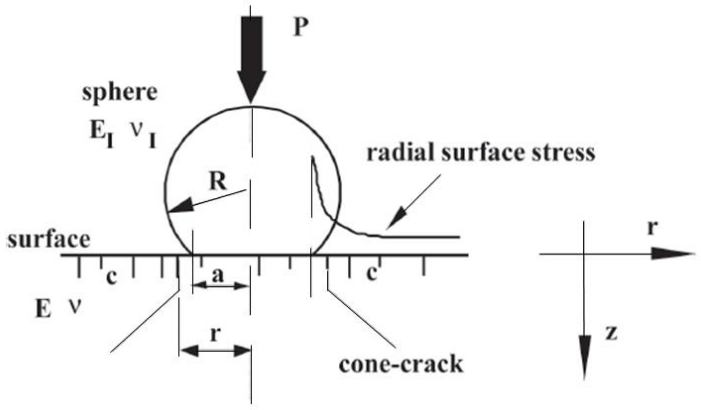

Figure 2-29: The cone crack development after the applied load (P) and the radial surface stress around the contact region [86].

The Hertzian test is used to form the cone cracks on the brittle ceramic surface as shown in Figure 2-29. The area around the contact region is the source to initiate these defects due the stress in this region being a radial tensile stress. Figure 2-30 shows the development of the ring crack radius to the cone crack after the applied load and also shows the cone crack closing after the removal of the load from the sample surface [75].

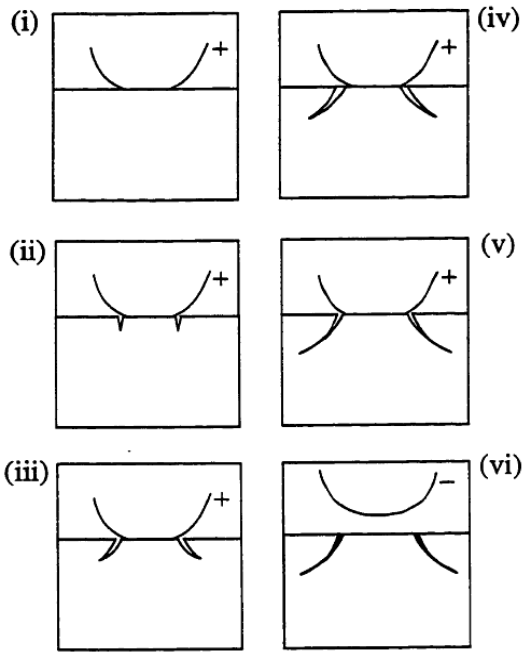

Figure 2-30: The development of the cone crack under applied load and these cracks closing after removing the load from the sample surface. This test is done using Hertzian indentation test [75].

2.4.3 Hertzian Cone Crack Mechanics

The defect formation mechanics is not easy and there are two methods to start the development of flaws [83]. The first method is that the defects are initiated from the sample surface around the contact region due to the radial stresses at this region and this stress causes these defects to develop into cone cracks.

The second method is the cone defect development in the downward direction due to K_I (the stress intensity factor) at the defect tip, allowing a small crack size around the contact region to the ring crack radius to develop. These defects are grown and they follow a path normal to the applied load [7, 83, 87, 88].

The (K_I) is divided by $P_o(\pi a)^{1/2}$ to provide the normalised value for the stress intensity factor as shown in Figure 2-31. The stress intensity factor value for the small crack size is positive due to this kind of crack being close to the radial tensile stress region. The stress intensity factor value is negative for large defect size due to these types of defects being in the compression stress. When the fracture toughness is more than the stress intensity factor the failure will not happen. When the fracture toughness is equal to the stress intensity factor there are two kinds of defects; small and large defects. For the large defect size in the compression area, a defect is not developing and the failure is stable. For the small defect size in the radial stress area; this kind of defect is developing due to the failure at this type is not stable and this defect propagates to the ring defect radius [86].

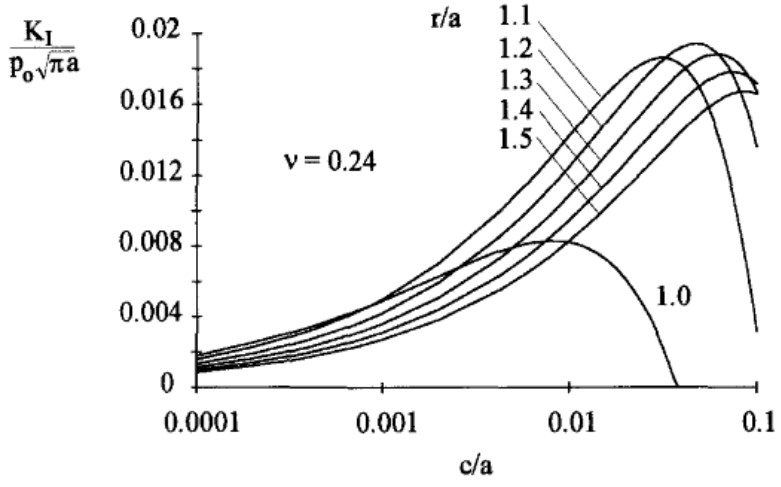

Figure 2-31: Shows (K_I) increases with increasing the defect length at different ring defect radius. (K_I) and defect size are normalised by the contact region radius [80].

Summary

The Hertzian test is used to study the fracture properties for brittle materials. The crack sizes and densities are assessed using a level sample surface and a solid indenter. The fracture toughness is measured at the minimum load in the coarse ceramic surface due to the densities of defects in these materials being larger than in the fine ceramic surface. The stress around the contact area is the radial tensile stress and this type of stress will propagate the defect size to ring defect size and this stress will decrease with the defects depth and will become a compressive stress. In this thesis the fracture toughness was determined at the minimum observed fracture load and also, the flaw size and density were studied for the polycrystalline alumina sample.

Aims of Thesis

The aims of this thesis are to observe and find the intergranular microcracks in polycrystalline alumina samples using digital image correlation experiments. The defect density and size was observed and also, the fracture toughness was calculated at the minimum load using the Hertzian indentation test for the alumina samples.

Chapter 3

3 Experimental Methods

3.1 Introduction

This chapter covers the experimental work details including the experiments to determine the most suitable design for the samples. The aim of this thesis is to examine the crack behaviour using digital image correlation (DIC) for observation of cracks that would otherwise be invisible, and to obtain microstructural data to estimate the thermal stress at the microscale, such as measurement of the grain boundary planes. The orientation of the grain boundary and microcracks were observed using SEM and EBSD respectively. The fracture toughness for the polycrystalline alumina sample was measured using Hertzian indentation. The Hertzian test was used to measure the flaw size and density. A graphical overview of the work that has been done for this thesis is shown in Figure 3-1.

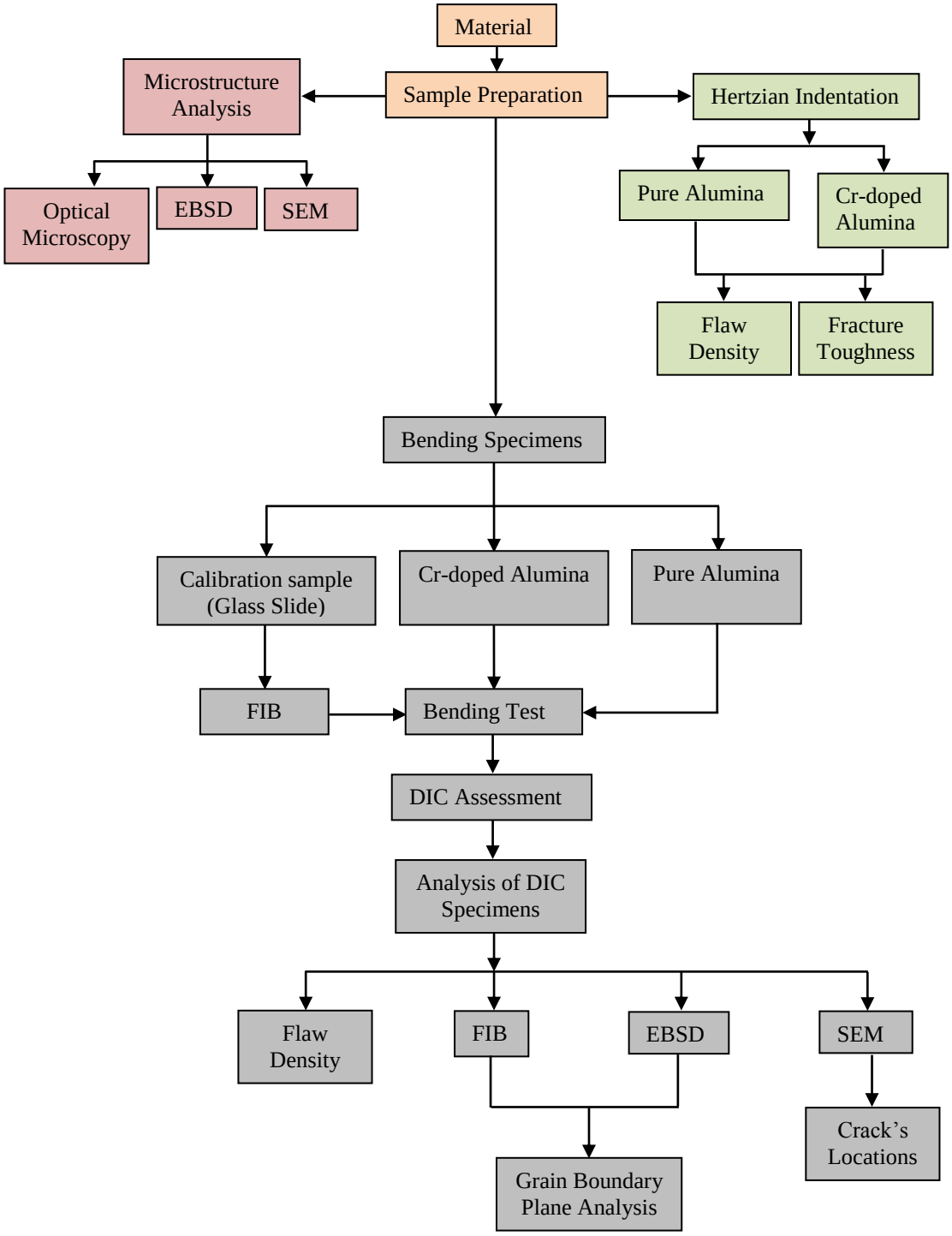

Figure 3-1: Flowchart illustrating the overall sequence of the experimental work carried out in this thesis.

3.2 Microstructural Analysis

This section comprises four investigation methods. Firstly, optical microscopy was used to observe the microstructure for the pure alumina and Cr–doped alumina. Secondly, a scanning electron microscope was used to show microstructure features and also to show the crack location in the microstructures. Thirdly, EBSD was used to observe the orientation of grains in the microstructure. The lineal intercept method was used to calculate the average grain size from the Scanning Electron Microscope (SEM).

3.2.1 Materials and Specimen Preparation

3.2.1.1 Grinding and polishing

The materials used were pure alumina (99.8% Al_2O_3) and Cr–doped alumina (99.8% Al_2O_3 and 0.1%Cr). Both were supplied in a slip cast and extruded condition and sintered by Almath Crucibles[1].

Specimens requiring dimensional change were cut using a Struers Accutom–5 Precision Cutter with a low concentration diamond cutting wheel of diameter (125 mm) and thickness (0.5 mm). The feed rate was 0.020 mm/s to introduce minimal strain and the disc rotation was 3000 rpm. The sample dimension was (7 mm wide, 10 mm long and 3 mm thick) for the optical microscope, scanning electron microscope and electron backscatter diffraction experiments.

The hot mounting is used to mould the polycrystalline alumina samples because all the pores and the cracks was filled by the resins in the ceramics materials [89].

Diamond powders ranging in particle size from 75 μm to 1 μm with low nap–polishing pads were used for polishing. The powders were employed for polishing with water based diamond polishing lubricant. The specimen was finally polished to a mirror finish using a colloidal silica solution. The grinding and polishing steps as shown in Table 3-1 and between each step, they were cleaned in water and methanol and dried in hot air.

[1] Samples provided by Almath Crucibles Ltd, Newmarket, UK

Table 3-1: Shows the Grinding and Polishing Procedure

Grinding	Materials	Grit (µm)	Lubricant	Time (min)
Step 1	Diamond	75	Water	30
Step 2	Diamond	40	Water	30
Step 3	Diamond	20	Water	30
Step 4	Diamond	10	Water	30
Polishing				
Step 5	Diamond	6	Water	60
Step 6	Diamond	1	Water	60
Step 7	Colloidal Silica			180

3.2.1.2 Thermal Etching

The polycrystalline alumina samples are etched using a thermal etching technique to remove the energy from the boundary. The thermal etching temperature was lower than the firing temperature [89]. The polycrystalline alumina microstructure was detected using an optical device.

The sintering temperature of the alumina specimens was about 1610 °C [22]. The alumina samples were etched at a temperature of 150-200 °C below the sintering or firing temperature. Thermal etching steps have been shown in Figure 3-2.

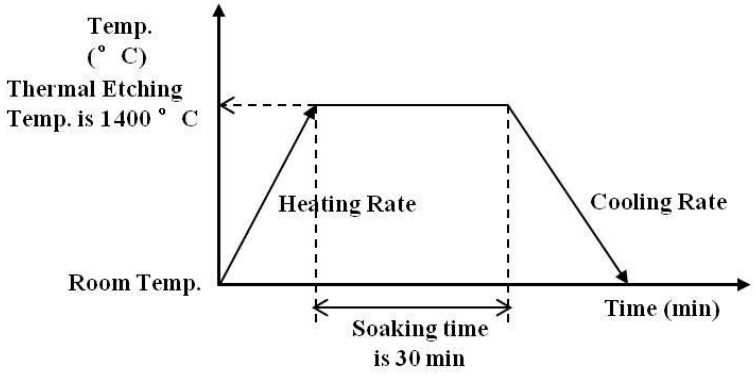

Figure 3-2: Shows the thermal etching procedure.

Where:

1. Heating rate is about 500 °C per hour.
2. Thermal etching temperature is about 1400 °C for 30 minutes.
3. Cooling rate is about –300 °C per hour.

3.2.1.3 Gold and Carbon Coating

Alumina specimens were coated with gold and carbon. SEM imaging required gold coating by sputtering for 3 minutes using an Edwards S150B sputter coating whereas, EBSD used carbon coated by sputtering for 2 seconds using an Edwards E603A sputter coating. Table 3-2 shows the coater that was suitable for each experiment.

Table 3-2: Shows the coating type and the experiments that used at this kind of coating.

Coating Type	Experiments			Time
	SEM	EBSD	DIC	
Carbon Coating		√		2 seconds
Gold Coating	√		√	3 minutes

3.2.2 Instruments

3.2.2.1 Optical Microscope (OM)

The microstructure of the as–received specimens of both materials (pure alumina and Cr–doped alumina) was characterized using an optical microscope. The Olympus–BH2–UMA microscope was used for collecting the optical images.

3.2.2.2 Scanning Electron Microscope (SEM)

The SEM is used to achieve good quality images to observe the detail of the microstructure for example, microcracks, porosity, and features on the sample surface. The level of the

magnification is higher and the image resolution is good for the scanning electron microscope (SEM).

A Philips XL30 SEM, device was used to study the crack and fracture surface with higher resolution in the polycrystalline alumina. The aperture was 50 μm diameters (lens modulation), the working distance is (10 mm) and spot size 3–4 was used for SEM. The SEM is used to provide the information about the surface or the structure of surface [90]. Figure 3-3 shows the details for the SEM.

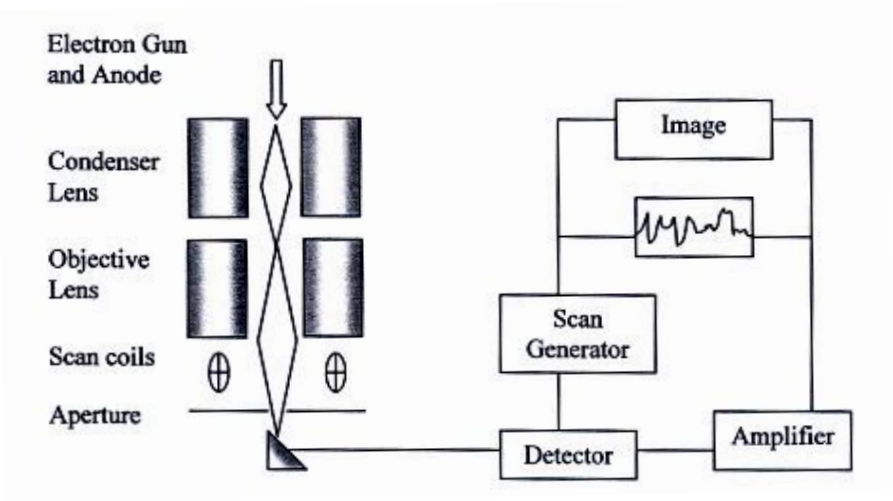

Figure 3-3: Shows the details of the SEM to provide the beam of electron which was used to observe the detail of the microstructure [90].

The polycrystalline alumina samples were mounted on the aluminium stubs with adhesive carbon tabs. The carbon or gold coating was used to ensure the samples are electrically conductive.

3.2.2.2.1 Electron backscatter diffraction (EBSD)

The electron backscatter diffraction is used to observe the grains and grain boundary orientation. The alumina samples were tilted to about (70°) toward the camera which is used for the diffraction [91]. The XL30 microscope is used for the electron back scatter diffraction and the electron beam is interacting with sample surface and then the electrons move from the sample surface to the camera of diffraction. The output data are assessed using Tango software to plot the orientation maps and the pole figure. The voltage used for

the EBSD is 20 kV, with spot size 3 or 4 and working distance of 20 mm. Figure 3-4 shows the EBSD components.

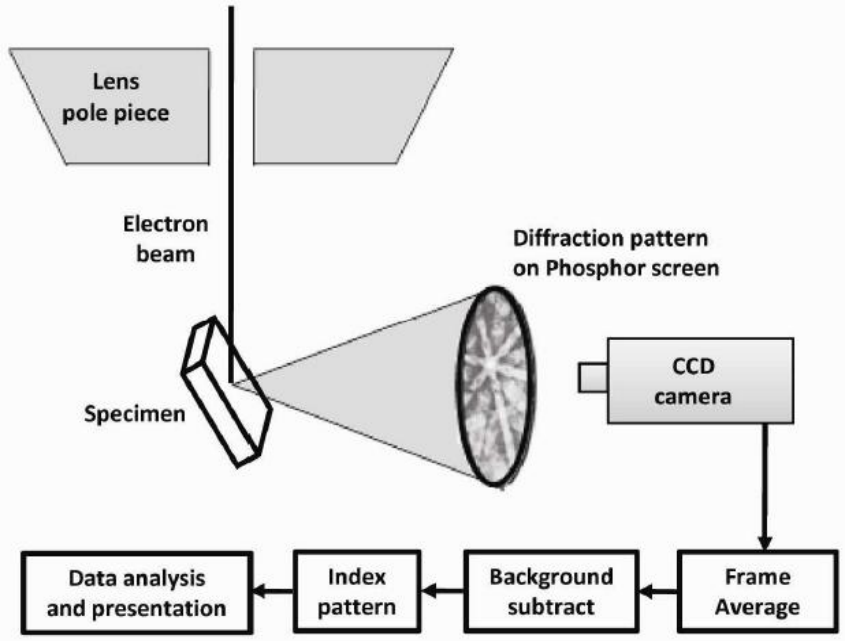

Figure 3-4: Shows the stages for the electron backscatter diffraction system [91].

3.2.2.3 Determining Average grain Size using Lineal Intercept Procedure

This method is used to estimate the average grain size for the polycrystalline alumina samples by counting the grains number in the SEM images. Three images or more were used for this method with two vertical lines, two horizontal lines, and two diagonal lines and these lines are intercepted with each grain. The (1/2) grain is intercept with these lines for each grain and the interception of these lines with the triple points of the grains are (1 ½) grains [92]. Equation 18 is used to measure the average grain size [93] for the polycrystalline alumina samples.

$$\overline{D} = 1.56 \frac{C}{MN} \qquad (18)$$

The test line length is (C), the intercept number between the vertical, horizontal, and diagonal lines with the grains represented by (N), the microstructure magnification is (M), and the proportionality constant is (1.56) [93].

Figure 3-5 and Table 3-3 shows the lineal intercept procedure and the average grain size is determined for polycrystalline alumina surface. The five micrographs were used to determined the ($\overline{D}$) and it is about 8.21±0.93 μm.

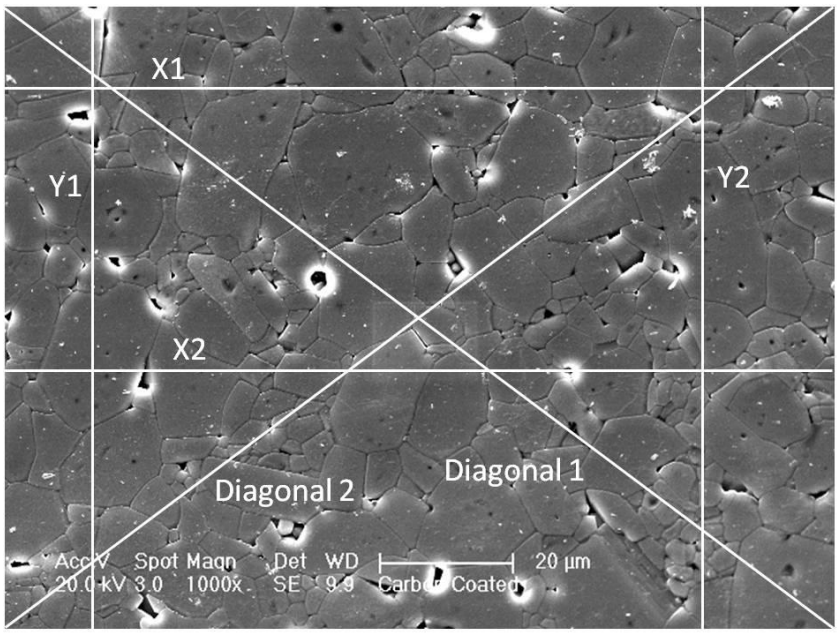

Figure 3-5: Shows the lineal intercept method to determine the average grain size for the pure alumina specimen.

Table 3-3: Shows the lineal intercept procedure for one micrograph of the pure alumina specimen.

Test Line	Total Length of test line (mm)	No. of intercepts	Conversion (mm) to (μm)	Grain Size (μm)
X1	120	19	1.6	6.15
X2	120	16	1.6	7.31
Y1	152	15	1.6	9.88
Y2	152	22	1.6	6.73
Diagonal 1	251	30	1.6	8.15
Diagonal 2	251	36.5	1.6	6.70

3.3 Digital Image Correlation Analysis

The DIC is not destructive technique and does not contact the sample surface [94, 95]. DIC is used to calculate the displacement in x- and y-direction after the initial image match with the image after the deformation and also the strain was determined of the displacement to obtain the strain map. The intergranular microcrack on the alumina sample was observed on these strain maps.

3.3.1 Preliminary Calibrations

The primary objective of this experiment is to predict the deflection at the centre for the glass and alumina specimens against applied load as shown in Figure 3-6. This was necessary as the later experiments were conducted under displacement control, with monitoring of strains by a strain gauge bonded to the sample. The strain gauge (632–124) (these numbers show the Rs stock number) was fixed on the centre of the sample surface. The strain gauge length was 2 mm and the strain gauge resistivity was about 120 Ω is per unit length. The strain gauge was calibrated using software Lab VIEW Signal Express before the experiment was started, and the error was (0.01 milli–strains).

Simple beam theory applied for a rectangular cross section gives in Equation 19 in the region between the inner rollers [96].

$$\sigma = \frac{3P(L-l))}{2td^2} \tag{19}$$

This surface stress (σ) corresponds to the applied load calculable by the Equation 20.

$$P = \frac{2\times\sigma_f \times d^2 \times t}{3\times(L-l)} \tag{20}$$

The deflection at the centre of the sample for this geometry can be calculated by the Equation 21.

$$\delta = \frac{P\times D}{48EI}\times\left[3L^2 - 4D^2\right] \tag{21}$$

$$I = \frac{d\times t^3}{12} \tag{22}$$

$$D = \frac{(L - l)}{2} \qquad (23)$$

Where:

L = the outer span.

l = the inner span.

d = the sample thickness.

t = the sample width.

E = Young's Modulus.

P = the load.

δ = the deflection at centre of the sample.

I = Second moment of area, m^4.

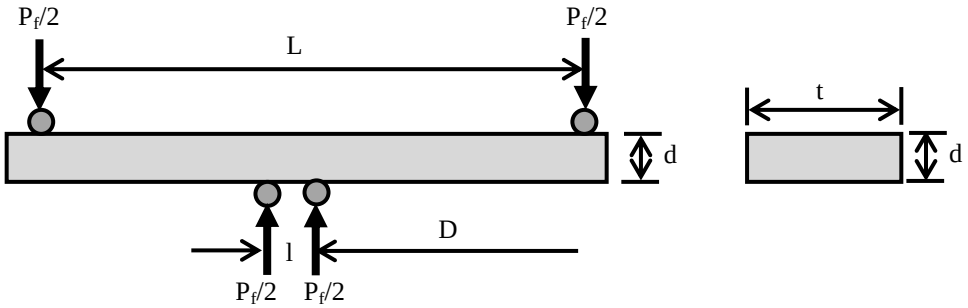

Figure 3-6: Four point bending sample and the sample's dimensions.

The effect of the applied displacement on the surface stress was obtained from the strain gauge values and also, the elastic modulus (E).

3.3.2 Digital Image Correlation for calibration specimen (glass specimen)

3.3.2.1 Preparation of the Glass Surface for DIC

The purpose of this experiment was to assess the optimum surface finishes for DIC observations of glass. The glass sample would later be used to measure the opening displacements of a small slot by DIC. The glass surface was abraded by grinding and then

the surface was etched using Hydrofluoric Acid (HF) at different concentrations (50% and 95%) as shown in Figure 3-7. The glass surface was examined using an optical microscope at different magnifications (X10 and X20).

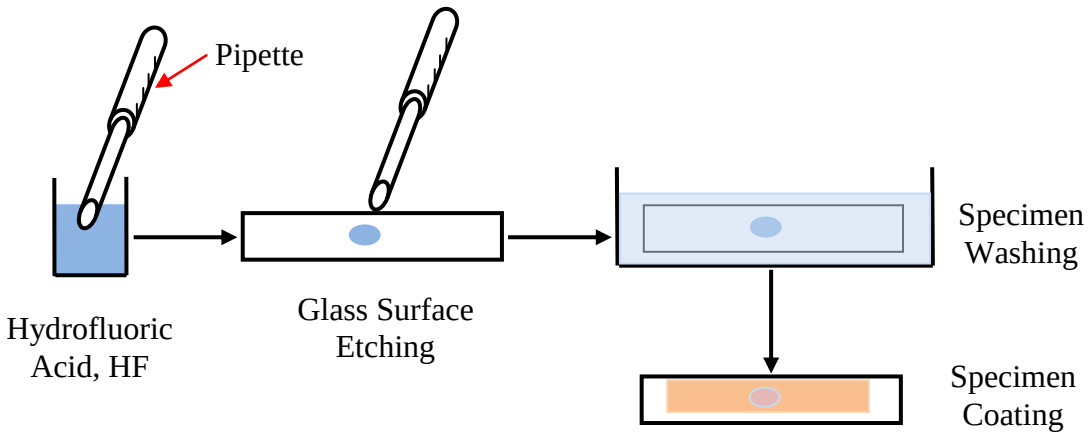

Figure 3-7: Shows the steps for the surface preparation of the glass specimens for DIC.

There are two procedures for preparing the glass surface for digital image correlation as shown below:

The First Method

The glass specimens were abraded using diamond paste (10 µm) and then the surface was etched using chemical etching (95% HF) for 3 mins and after that the surface was coated using gold coating for 4 mins.

The Second Method

The glass slide was abraded using diamond paste (10 µm) and then the surface was etched using chemical etching from (50% HF) for 3 mins and after that the surface was coated using gold coating for 4 mins.

3.3.2.2 Focused Ion Beam for producing notches on the glass specimen

Figure 3-8 shows the Focused Ion Beam (FIB) equipment and the ion beam used in FIB is (i.e. Ga^+ ions) [97]. The Ga^+ ions attack the alumina surface and that will produce the secondary electrons to provide more details about the alumina surface.

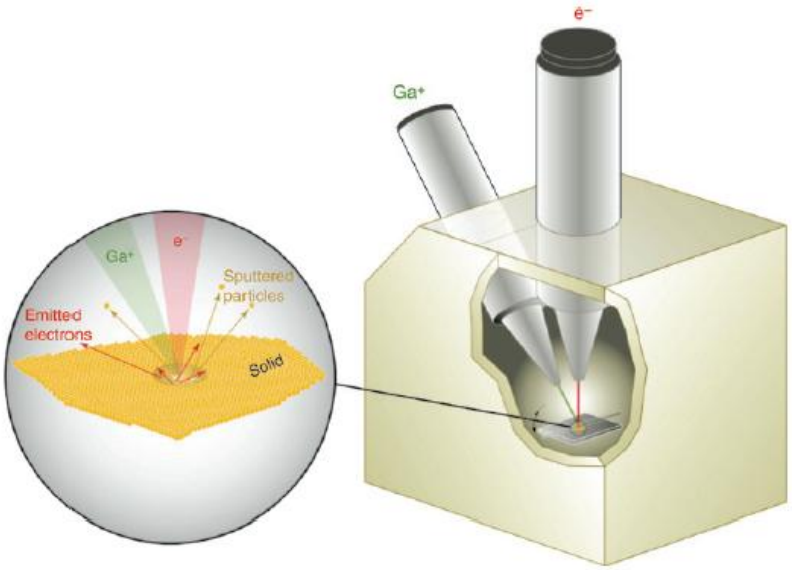

Figure 3-8: Shows FIB–SEM equipment and the interaction the ion beam with the sample surface as shown in the magnified view [97].

Small slots were created using FIB Nova NanoLab 600 Focused Ion Beam / Field Emission Gun on the glass specimen surface. Figure 3-9 shows the slots location marked with a yellow line. The slot length was 40 µm and 20 µm and the depths were 20 µm and 15 µm for slots A and B respectively. The slots were created using a focused ion beam of 20 kV accelerating voltage, with current 9.5 nA and working distance about 4.9 mm and tilt angle was about (52°).

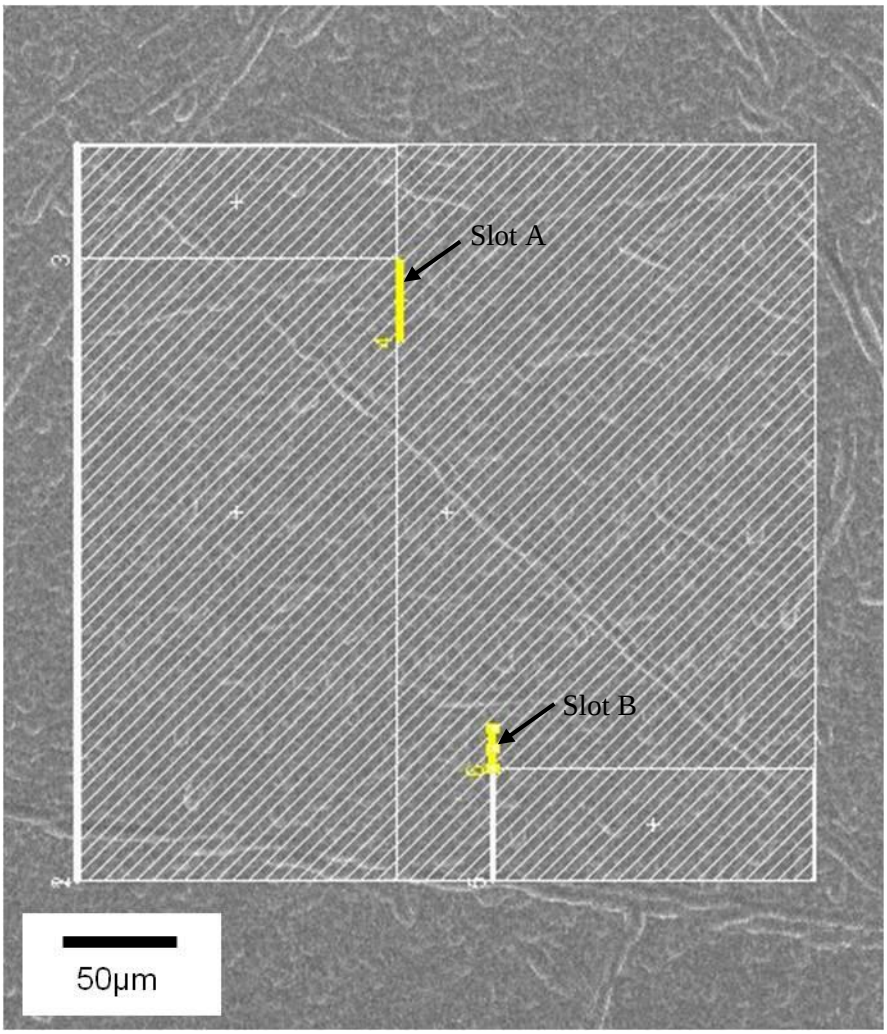

Figure 3-9: Schematic for the slots location (slot A and B) on the glass slide.

3.3.2.3 Strain Measurements

The strain gauge (632–124) was fixed on the centre of the sample surface as shown in Figure 3-10. The strain gauge length was 2 mm. The strain gauge resistivity was about 120 Ω is per unit length. The strain gauge was calibrated using software Lab VIEW Signal Express before the experiment was started, and the error was 0.01 milli–strains. The strain gauge was mounted on the upper surface of the glass specimen using Cyanoacrylate, close to the region of interest, and located completely between the inner supporting rollers.

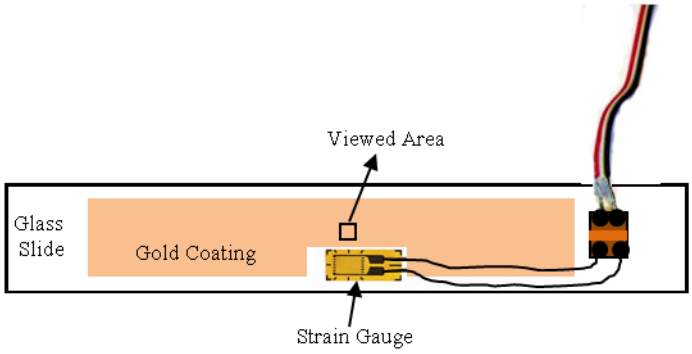

Figure 3-10: Sketch of the glass specimen and shows the strain gauge location on the upper surface of the specimen.

3.3.2.4 Four Point Bending Test

The 4-point bend experiment was conducted with the strain gauge adhered to the sample surface before the sample was deformed. The sample was observed using an optical microscope with X20 lens and with the working distance about 38 mm. The load was increased between images by using a micrometer to apply displacements. The viewed area was (2048 pixels ×2048 pixels) corresponding to 450 µm by 450 µm at magnification X20. Images were recorded using an Image Pro X CCD camera (12 bit, 2048×2048 pixels). Digital Image Correlation was then carried out on a networked Dual Processor PC (2×2.8 GHz Processor, 2 GB RAM) with Davis Strain Master 2D software for acquisition visualisation (LA Vision, Germany). The interrogation window size was used 128×128 pixels and overlap 50%

The dimensions of the glass samples were (48×10.6×2.05 mm). The edges of the samples were prepared by polishing to reduce any cutting damage. The outer and inner spans were 48.0 mm and 5 mm respectively. The stiff rig is self-aligning to the sample using a ball bearing. Figure 3-11 shows the digital image correlation setup and four point bending rig.

After the machine was set up, the load was increased using the micrometer. Before the load was applied an initial image was taken without deformation (initial image) using the digital camera. The displacement was then incremented by intervals of 0.015 mm at 30 minute intervals as shown in Figure 3-11a. A 12–bit Image Pro X CCD digital camera (2048×2048 pixels) was used to record 20 images at each location at each increment, covering a total

area of approximately (450×450 μm). Typically several increments were required to break the sample.

a)

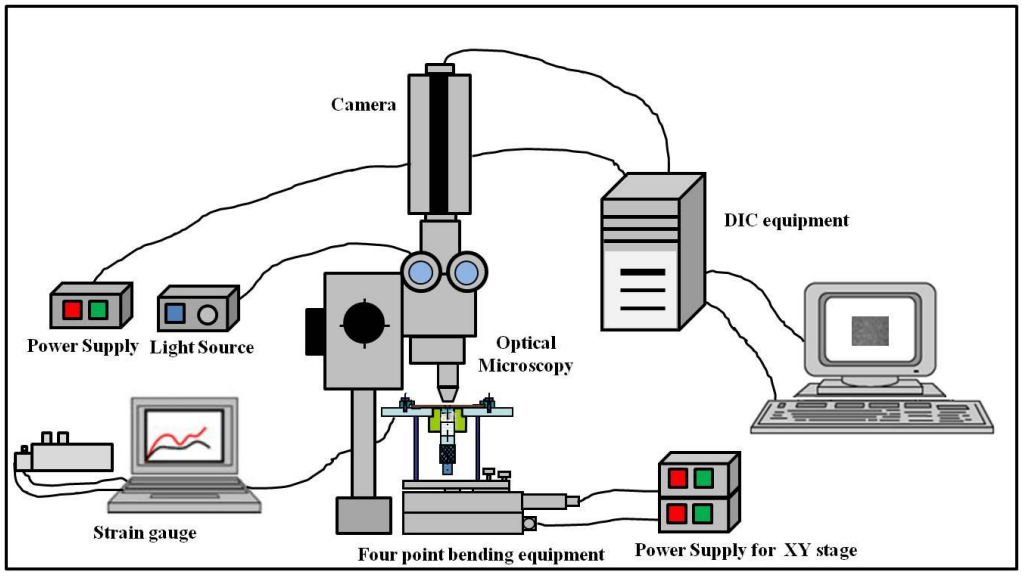

b)

Figure 3-11: a) Shows digital image correlation set up, b) Schematic image for DIC set up.

3.3.2.5 Finite Element Model Description for Glass Specimen

A finite element simulation was carried out ABAQUS/Standard Ver. 6.9 [98] to analyse the displacement and strain fields near the slot which was created using FIB in the four point loading condition Figure 3-12. This finite element model was constructed by a postdoctoral research associate, Mahmoud Mostafavi. One quarter of the specimen is normalised due to the symmetry and suitable conditions of boundary were applied. 45,000 quadratic (20–node) decreased integration brick elements were employed. The material was considered to be linearly elastic with elastic constants, E = 70 GPa and Poisson's ratio ν = 0.25 [81]. To apply the load, a set of nodes which were assumed to be in contact with lower support were constrained in the vertical direction and constant displacement was applied on the nodes which were in contact with the upper support. To reduce the computational time, small elements were used near the FIB slot (nominal size 0.001 mm) and larger elements (nominal size 2 mm) far from the region of interest; the mesh is shown in Figure 3-13. Strains and displacements were extracted from the model along the paths as shown in Figure 3-12 were compared with the results obtained from DIC analysis. The FIB slot was modelled as having a depth of 11.64 µm and a surface length of 40 µm with elliptical shape. The depth was chosen to confirm the defect dimension using DIC and FEM, and hence confirm that the calculation of defect depth from opening displacement is sufficiently accurate.

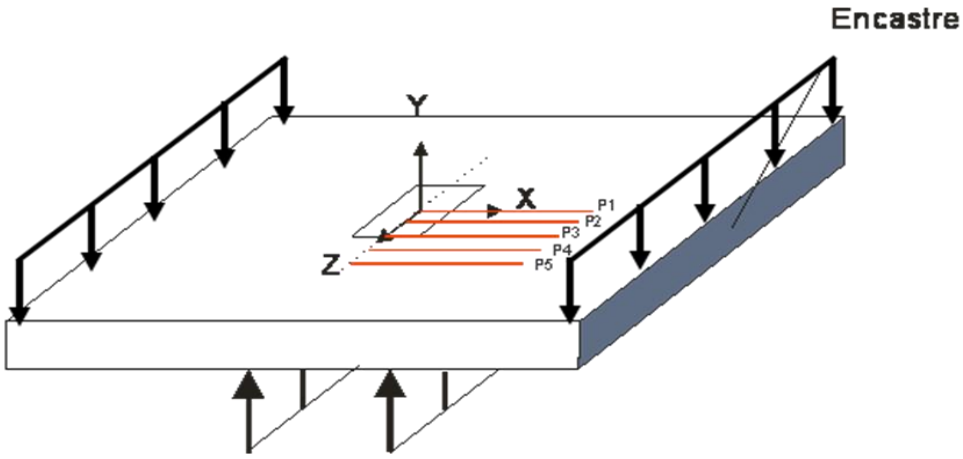

Figure 3-12: Shows the slot position and the loading direction.

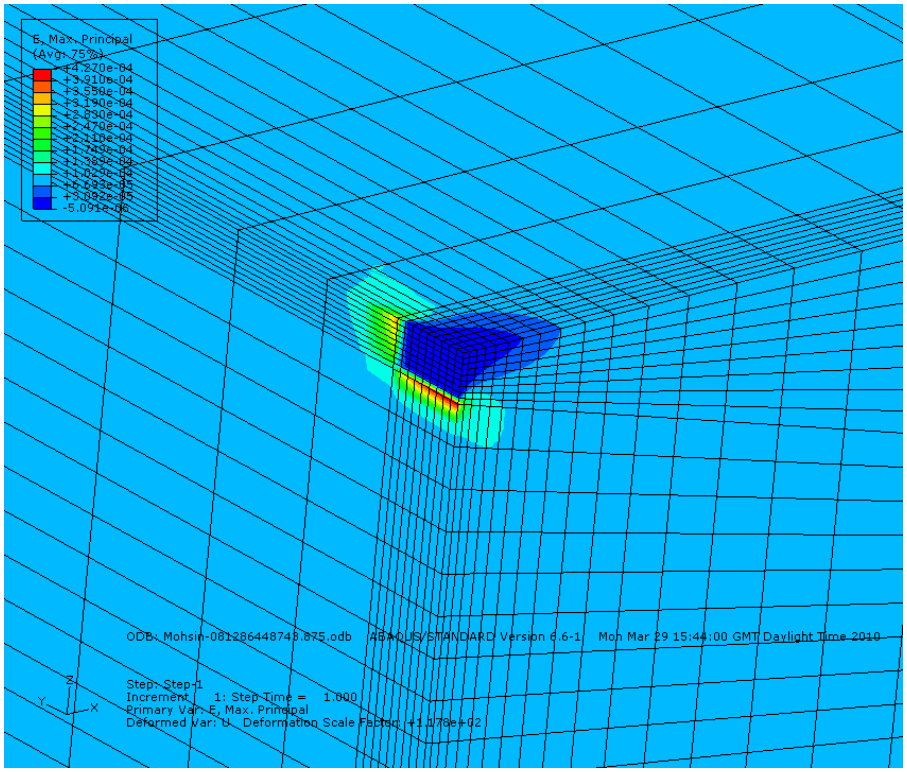

Figure 3-13: Shows the mesh used close of the FIB slot (nominal size 0.001mm) and large elements (nominal size 2mm) far from the FIB slot.

3.3.3 Image Correlation to study of the crack nuclei in alumina

3.3.3.1 Surface Preparation and Fracture test for DIC

The objective was to observe crack nucleation in polycrystalline alumina microstructures. Four point bend fracture tests were conducted under displacement control; with samples of nominal dimensions of 48×10.6×2.05 mm. Figure 3-14 shows the digital image correlation setup (Imaging Suite). The edges of the samples were polished to remove cutting damage, which would reduce sample strength. The outer and inner spans were 48.0 mm and 5.0 mm. Steel rolling pins were used to minimize contact friction, and self–aligned to the sample using a ball bearing. The compressive strength for the polycrystalline alumina is high and that will resist the contact damage.

The alumina surface has a stain gauge and it is attached using M–Bond 200 catalyst and the adhesive will harden without the catalyst. The strain gauge was adjacent to the observed region, measuring the applied strain as shown in Figure 3-14d. The displacement was

incremented by intervals of 0.02 mm (equivalent to a strain increment of approximately 0.0001) at 60 minute intervals as shown in Figure 3-14a. A 12–bit Image Pro X CCD digital camera (2048×2048 pixels) was used to record 20 images to improve the image quality at each of 25 locations at each increment, covering a total area of approximately (500×500 μm). The twenty images are then averaged tighter to remove any transient variations that have occurred during collection.

The load is applied to the pure alumina and Cr-doped alumina sample, the position of the observation region relative to the microscope changes. In order to track the same area of the specimen, the position of the sample under the microscope is controlled by two movable platforms. The first one enables the movement of the specimen in the x- and y- directions shown in Figure 3-14b. It is used to position the same area at different applied strain and it is used to cover a large area of approximately (500×500 μm). For fast and accurate movement of the X–Y stage (Thorlabs), two motor drives were used for both directions. The second stage used is a tilting stage which was used to modify the pure alumina and Cr-doped alumina samples (i.e. the sample was not necessarily level and this tilt stage was used to put the samples in the level position, to ensure the observed surface remained orthogonal to the camera axis).

An oil immersion lens with X100 magnification was used with a working distance of 0.25 mm and immersion oil (Fractoil) of 1.517 refractive index [99] as shown in Figure 3-14c. The analysed field of view of each image was 100×100 μm. Improvements in the optical path during the project gave resolutions of 0.046 μm / pixel for pure alumina and Cr-doped alumina samples, since a larger fraction of the CCD array could be employed.

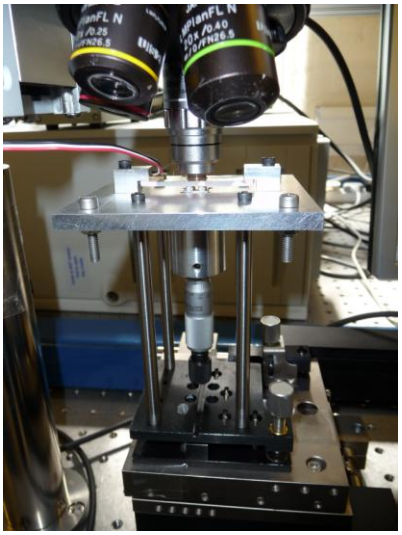

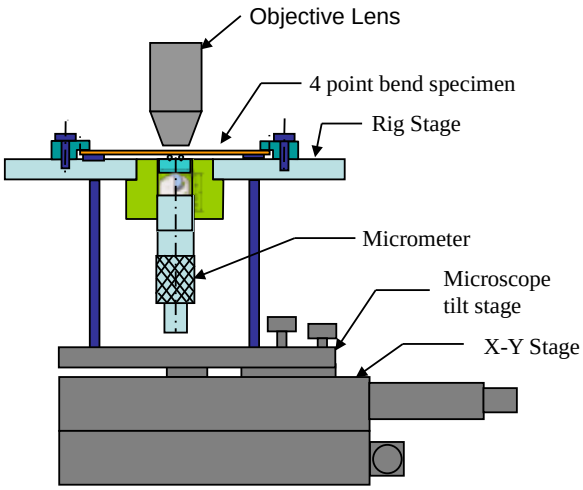

a) b)

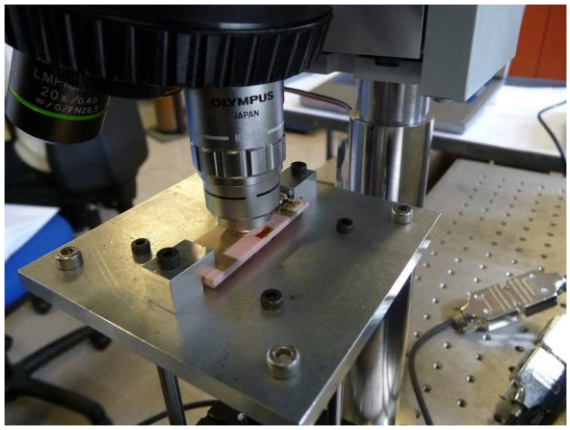

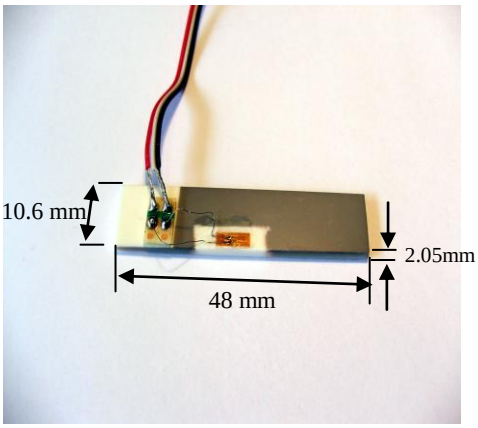

c) d)

Figure 3-14: a) Rig for in–situ optical observation of the tensile surface during four point bend loading, b) Schematic illustration of experimental setup, c) Specimen under the lens (X100), and d) Sample for digital image correlation.

A surface with suitable random features for DIC analysis was achieved by thermal etching at 1400 °C in air for 10 hours and gold coating with an Edwards S150B sputter coating at an exposure time of 3 minutes. Images were analysed using the LAVision Davis Image Correlation software (version 7.2). A subset of 64×64 pixels and overlap 50% was used for analysis of the pure alumina, and 128×128 pixels with a 50% overlap for the Cr-doped alumina. These parameters were selected as the feature density within the grains and feature size for the Cr-doped alumina structure was larger than for pure alumina.

3.3.3.2 Digital Image Correlation (DIC) Procedure

The optical images of the cracked alumina samples at different applied loads were assessed using DIC. The DIC is used to calculate the surface displacement, microcracks growth, and the surface crack opening displacement. The RMS (i.e. noise level) is used to assess the displacement accuracy for each optical image at different surface preparation for DIC and that was done using Davis version 7.2 for a range of window sizes. The objective was to demonstrate that thermal etching and gold coating gave adequate surface feature characteristics for the pure alumina and Cr-doped alumina specimens. Table 3-4 shows the relationship between the window sizes and the displacement accuracy [67].

Table 3-4: Describes the noise level (RMS) for the displacement vector at different interrogation subimages [67].

Size of Interrogation Window (pixels)	Accuracy of Calculated Vector
128×128	0.01 to 0.03 pixels
64×64	0.02 to 0.05 pixels
32×32	0.05 to 0.2 pixels

3.4 Grain Boundary Plane Analysis

The purpose of this experiment was to obtain the crystal orientation for the grains and grain boundaries of interest. The EBSD and FIB techniques were used for the grain boundary planes.

3.4.1 Preparing the Surface

The alumina surface was prepared (i.e. remove the gold coating and thermal etching layer after the fracture test) for EBSD using different methods. The gold coating and thin layer of the thermal etching were removed using FIB equipment for 4 min. Also, using Gatan machine, Model 682, Precision Etching Coating System (PECS) was used to clean the alumina surface from the gold coating and thermal etching layer for (30 min.). The alumina

sample was tested to check the indexing (Kikuchi Patterns) using Scanning Electron Microscope CAMSCAN but the indexing did not find at these conditions.

Also, mechanical polishing was used to remove the gold coating and thermal etching layer from the same pure alumina and Cr-doped alumina specimens used for fracture tests. This used diamond paste 6 μm and 1 μm for 30 min each. The specimen was finally polished to a mirror finishing surface using a colloidal silica solution for 3hrs to make the surface more suitable for EBSD.

3.4.2 Electron Backscatter Diffraction of selected regions

The FIB equipment was used to position the region of interest using slots as reference markers and then work out the position of the feature relative to these markers. The region of interest was polished using mechanical polishing to achieve Electron Backscatter Diffraction, EBSD map. The sample was tested to check the indexing (Kikuchi Patterns) using Scanning Electron Microscope CAMSCAN. Typically the indexing was about (50%-60%) with a step size of (0.5 μm).

3.4.3 Focussed Ion Beam, FIB Milling

The selected strain features associated with their grain boundaries were examined using DIC. FIB and EBSD were used to determine the adjacent grain crystal orientations relative to the grain boundary orientation. Trenches about 10 μm in width with depth up to 10 μm were cut across the selected grain boundaries using FIB equipment. The boundaries of interest were analysed by using backscatter diffraction (EBSD) analysis and focused ion beam (FIB) milling.

The grain boundary planes were determined using the grain boundaries of interest in the FIB (the trace analysis method) [100]. The trench across the boundaries of interest was created using focussed ion beam milling and the boundary of interest was deposited by a micron layer of platinum.

Figure 3-15 shows the trench milled across the grain boundaries of interest and also the trace of the grain boundary. The projected angles were measured using Photoshop software

by looking at enlarged pictures at large magnification. Figure 3-16 a, b shows the project alpha angle ($\bar{\alpha}$) and the projected beta angle ($\bar{\beta}$) for the three dimensional of the grain boundary of interest and (θ) is the tilting angle. The true angles alpha (α) and beta (β) were calculated using Equations (24) and (25).

$$\tan\alpha = \frac{\tan\bar{\alpha}}{\cos\theta} \tag{24}$$

$$\tan\beta = \frac{\tan\bar{\beta}}{\cos(90-\theta)} \tag{25}$$

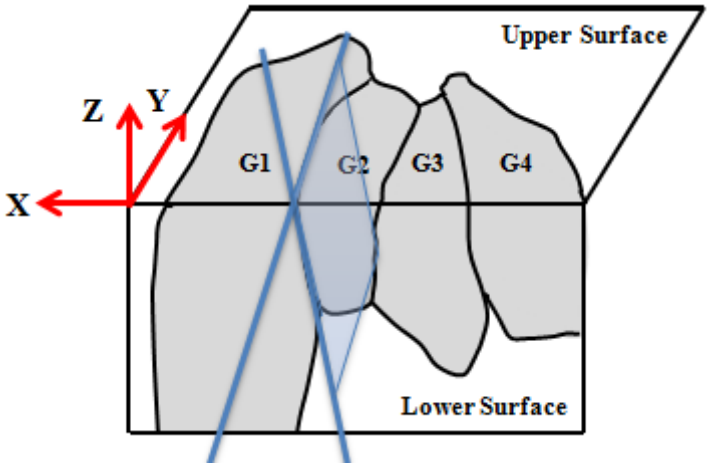

Figure 3-15: Shows the traces of a grain boundary on two adjacent specimen surfaces (Upper Surface, Lower Surface) and these surfaces are orthogonal in the alumina sample. The specimen axes are XYZ and the tilting is about 52° for the alumina surface.

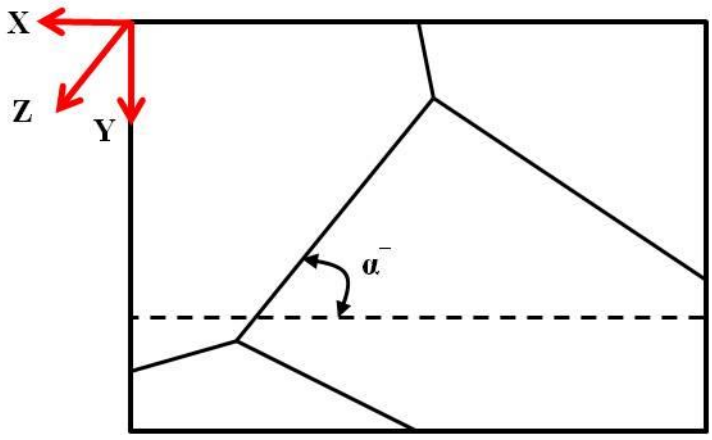

a)

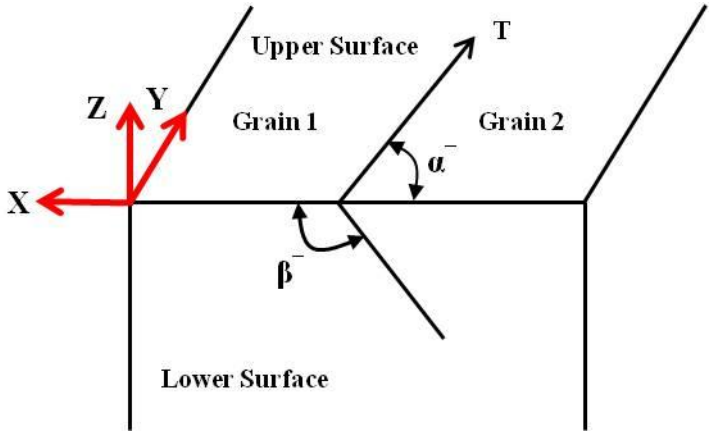

b)

Figure 3-16: Shows the grain boundary plane in the 3-D for the polycrystalline alumina sample, a) Shows the schematic for the upper surface which is used to determined the projected alpha angle in the xy-plane, b) Shows the upper and lower surface and the lower surface is used to measure the projected beta angle in the xz-plane.

3.5 Hertzian Indentation

Hertzian indentation was used to assess of the surface damage of polycrystalline alumina. The Hertzian test is used to study the cracks sizes, densities, and the fracture toughness for the alumina samples.

3.5.1 Surface Preparation for Hertzian test

Hertzian indentation was used to determine the surface cracks sizes and densities. Polycrystalline alumina specimens of 48 mm length, 10.6 mm width, and 2.05 mm thickness were prepared as shown in Figure 3-17. The surface of sample was ground using diamond paste 40 μm and 20 μm to prepare the surface for Hertzian testing. There are two methods to prepare the polycrystalline alumina samples surfaces for the Hertzian indentation test for:

1- The polycrystalline alumina surface is prepared by 6 μm diamond paste and 1 μm diamond paste for 1 hr and then colloidal silica on the soft cloth for 3 hrs. This method is provided fine surface.

2- The polycrystalline alumina surface is prepared by 10 μm diamond paste for 15 min. This method is provided the coarse surface and the surface quality is not good due to there are many voids (i.e. pullouts the grains).

For each procedure, the samples were finally cleaned in water and methanol and dried in hot air.

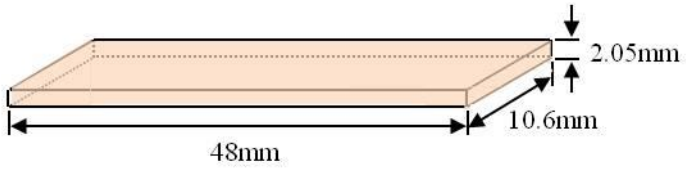

Figure 3-17: Sketch of a Hertzian test specimen

3.5.2 Hertzian Indentation test

An Engineering System (NOTTM), CK10 Acoustic Sensing, 10 KN Testing Machine is used for this experiment as shown in Figure 3-18. The Young modulus (390 GPa) and Poisson's ratio (0.24) [101] and the radius (2.5 mm) for the alumina indenter were used for Hertzian analysis. The ring crack radius is detected by the transducer of the acoustic emission. The tests number is used for this test between 30 and 40 indentations and these indents were applied on the smooth and rough surface with 0.25 mm/min of the load speed. The ring crack radius is detected by using optical device.

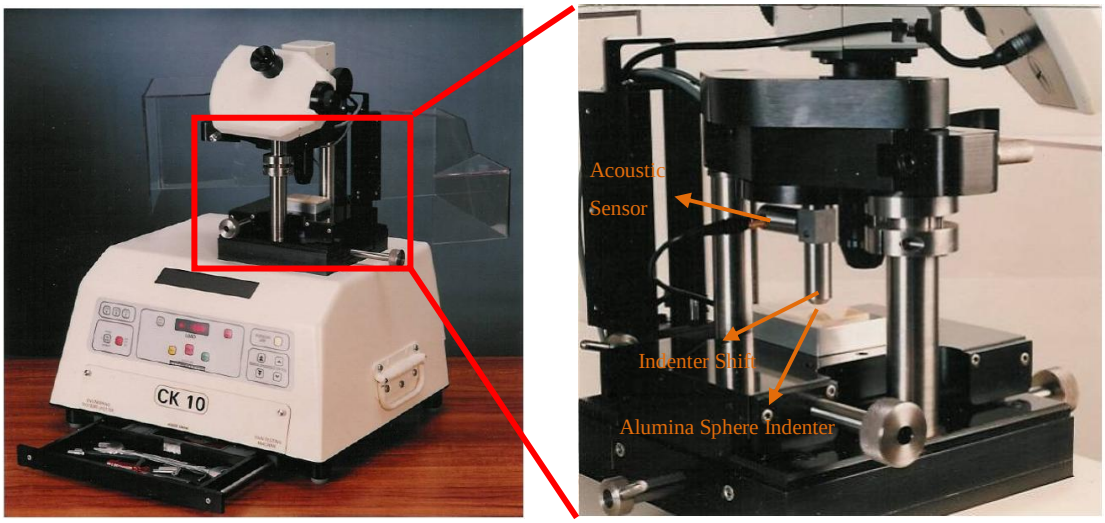

Figure 3-18: Shows the Hertzian indentation equipment, CK10 and also shows the acoustic sensor, indentation shift and alumina indenter.

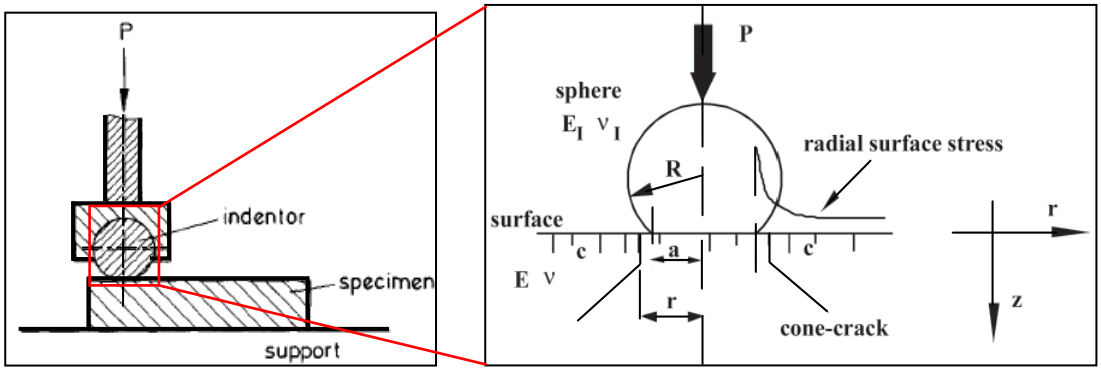

Figure 3-19: Shows the Hertzian indentation diagram to observe the crack size, contact region, and radial tensile stress [102].

3.5.3 Surface Preparation for Microstructural Examination

The polycrystalline alumina surfaces with ring cracks are not easy to measure after the Hertzian test. The alumina crucible was fine for etching the samples for showing the ring crack radius on the Hertzian samples as shown in Figure 3-20. The fine samples are etched using (50 % KOH) with temperature 300 °C for 3 mins and then the samples are polished using 1 µm diamond paste to take out the material from the surface which produce after etching and after that these cracks were observed using optical microscope. The coarse surface with cracks are etched using the same conditions which were used for the fine surface but the temperature 400 °C for 4 mins and then polished the surface using the same method which is mentioned for the fine samples to observe the cracks on the coarse surface.

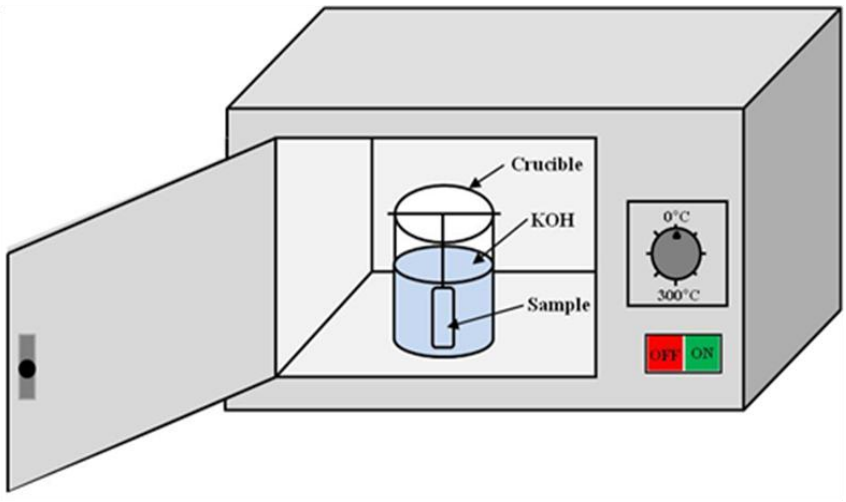

Figure 3-20: Schematic image of the chemical etching in potassium hydroxide (50% KOH) at different temperatures and exposure timed for this solution.

3.5.4 Stress Intensity Factor calculations

The Equation 26 was used to calculate the stress intensity factor and this value normalised by $(1/P_o(\pi a)^{1/2})$ [103]. These equations were used to measure crack size and also to decide the small cracks were the main source to form the ring crack [80]. The elastic properties were similar for the specimen and the indenter which were used to measure the crack size [103].

$$K = \frac{K_I}{P_o \times \sqrt{\pi \times a}} \tag{26}$$

$$\frac{K_I}{P_o \times \sqrt{\pi a}} = \mu \times \left(\frac{c}{a}\right)^{1/2} \tag{27}$$

$$\mu = \left[1.12 \times \frac{(1-2\nu)}{3(r/a)^2} - \frac{2\alpha}{\pi}\left(\frac{c}{a}\right)\right] \tag{28}$$

$$\alpha = \frac{-1}{\sqrt{u}}\left[\frac{1-\nu}{1+u} \times u + (1+\nu) \times \sqrt{u} \times \tan^{-1}\left(\frac{1}{\sqrt{u}}\right) - 2\right] \tag{29}$$

$$u = \left(\frac{r}{a}\right)^2 - 1 \tag{30}$$

Equation 31 was used to measure the peak pressure (P_o) at the contact circle.

$$P_o = \frac{3P}{2\pi \times \left(\frac{3RP}{4E^*}\right)^{2/3}} \tag{31}$$

Where:

P, represents the fracture load (N).

a, represents the contact area radius (μm).

c, is the defect size (μm).

r, is the ring crack radius (μm).

ν, represents the Poisson's ratio

The equations were used in the Hertzian indentation study depending on the crack size initiation value (c) when the Goal seek (function from Excel) was used to get a high or lower solution of crack size as there is a peak in the curve (i.e. the normalized stress intensity factor versus normalized crack size). As mentioned in 2.4.3, the smaller solution is that of the unstable crack that forms the detected cone crack.

3.5.5 Statistical Analyses

The extreme value statistics were used to distribute and assess the defect size population [104]. This extreme value analysis was used to compare the crack size distribution for the pure alumina and Cr-doped alumina values using the Gumbel extreme value distribution (Y) (see Equation 32). The cumulative probability of the defect size (P_i) is calculated from the ranking of the defect size is divided by the total number of the defects sizes [104].

The Gumbel extreme value distribution is calculated using the moments method and the accuracy for this method is about (95%) as shown in Equation 36 [104].

$$Y = -\ln(-\ln(P_i)) \tag{32}$$

Moments Methods:

$$\alpha_{moments} = \frac{\sqrt{6}}{\pi} S \tag{33}$$

$$\lambda_{moments} = X - 0.5772\alpha_{moments} \tag{34}$$

Standard Error:

$$SE_{moments} = \alpha_{moments}\sqrt{\left(1.168 + 1.1y^2 + 0.191y\right)/n} \tag{35}$$

95% Confidence:

$$X \pm 2SE_{moments} \tag{36}$$

The number of the defects is about 26 defects in the pure alumina and Cr-doped alumina samples; the total number of the defects is 26. The standard deviation for the total number of the defect sizes (S) and the average value for the number of the defects (X) were calculated using the equations 35 and 36.

3.5.6 Determination of surface crack densities

The densities of cracks were assessed using defect location and the distribution for the defects. The cracks densities were measured using searched area A (P_i, c_i) [7]. The Hertzian test provided information for the defects densities and each failure load was introduced one ring defect radius at the defect size is obtained at this load. The minimum radius (r_{min}) and the maximum radius (r_{max}) for the ring defect within the fracture toughness is less than the stress intensity factor and they were calculated for each defect size. The maximum ring crack radius is introduced at the farthest location from the alumina sphere (i.e. indenter). The minimum ring crack radius is provided from the minimum load and (Y) is a constant for the plane defects and it is about (1.12). The flaw densities were calculated using Equation 42 [79].

$$\alpha = \frac{2\sqrt{\pi} \times K_{1C}}{Y \times (1-2\nu)} \tag{37}$$

$$r_{\max} = \left(\frac{P_i \times \sqrt{c_j}}{\alpha} \right)^{1/2} \tag{38}$$

$$r_{\min} = \frac{3R}{4E^* \left(\frac{9R^2}{16E^{*2}P_i} \right)^{1/3}} \tag{39}$$

$$K_{1C} = \frac{Y\alpha(1-2\nu)}{2\sqrt{\pi}} \tag{40}$$

$$A(c) = \pi \times \left(r^2{}_{\max} - r^2{}_{\min} \right) \tag{41}$$

$$\rho(c) = n(c) \Big/ \sum\nolimits_i A_i(c) \tag{42}$$

Chapter 4

4 Results I

4.1 Microstructural Analysis

In this section the microstructure for the alumina samples was observed using an optical microscope. The microcracks and the orientation of the grains and grain boundary were observed using a scanning electron microscope (SEM) and electron backscattered diffraction (EBSD) respectively. The average grains sizes were calculated using the lineal intercept method.

Four sets of microstructures were investigated, but not all tests were applied to all microstructures. The pure alumina (P-I) specimen and Cr-doped alumina (Cr-I) specimen as shown in Table 4-1 were only available with dimensions smaller than the dimensions necessary for four point bending samples that were used for the digital image correlation experiments. A summary of the experiments performed is given in Table 4-1 and the microstructure and the electron backscatter diffraction results for P-I and Cr-I specimens are shown in appendix A.

4.1.1 Grain Size

The average grain sizes were calculated by lineal intercept procedure and this method was described in Experimental chapter in section (3.2.2.3). The results have been shown in Table 4-1. This shows that the Cr-doped aluminas have a grain size of around 3 μm, whereas the pure alumina samples exhibit grain size of either 8.2 μm (P-I) or 1.5 μm (P-II).

Table 4-1: Shows a summary of the experiments performed and the average grain size for alumina samples.

Samples	Compos-ition	Average Grain Size (μm)	Experiments					Reference Name
			SEM	EBSD	DIC	FIB	Hertzian	
Cr-doped Alumina I Slip Cast	99.80% Al_2O_3+ 0.1% Cr	2.73±1.08	√	√				Cr-I
Cr-doped Alumina II Extruded	99.80% Al_2O_3+ 0.1% Cr	3.60±0.81	√	√	√	√	√	Cr-II
Pure Alumina I	99.80% Al_2O_3	8.21±0.93	√	√				P-I
Pure Alumina II	99.80% Al_2O_3	1.50±0.82	√	√	√	√	√	P-II

4.1.2 Optical Microscopy

Figure 4-1 shows images taken by optical microscope after sample preparation, as described in section (3.2.1) for specimens (P-II, and Cr-II specimen). The images of the P-I and Cr-I samples are in appendix A (Figure A-1).

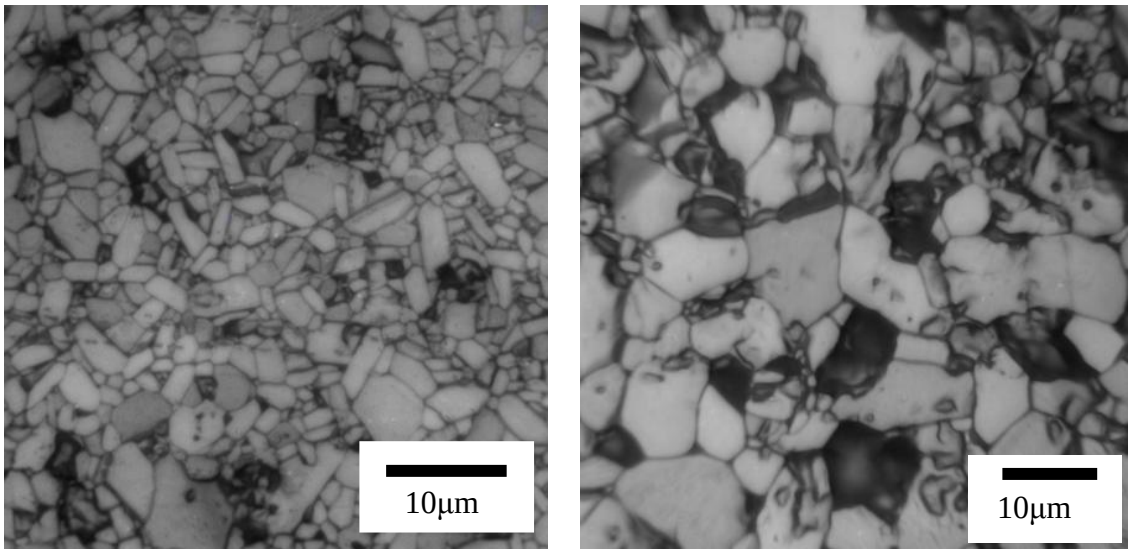

a) **b)**

Figure 4-1: Optical images for the specimens a) P-II specimen, and b) Cr-II specimen after thermal etching.

4.1.3 Scanning Electron Microscopy

Figure 4-2 shows images taken by a scanning electron microscope for thermally etched and gold coated samples. The microstructure shows pores, labelled with yellow arrows and non-equiaxed grain shapes. The images of the P-I and Cr-I samples are in appendix A (Figure A-2).

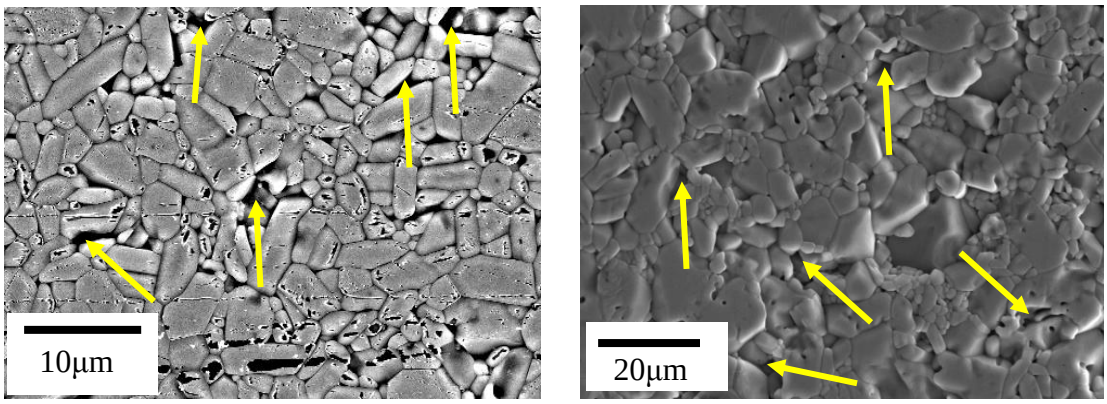

a) **b)**

Figure 4-2: Scanning electron microscope images for the samples a) P-II specimen, and b) Cr-II specimen.

4.1.4 Electron Backscatter Diffraction, EBSD

The objective of this work was to confirm that EBSD maps could be obtained from these samples (P-II, and Cr-II specimen), to confirm that the sample preparation techniques were satisfactory, and to establish the time and mapping parameters required to obtain maps of representative areas of microstructure. Using the Tango software the EBSD maps were cleaned using a medium level of noise reduction. The step size was 0.2 µm for high quality orientation EBSD maps. The level of indexing achieved was about 60% to 70%. The mis-indexed points are represented with their closest neighbouring pixel orientation (for example, grain boundaries, porosity, and surface scratches during the sample preparation). The local orientation map for different samples is shown in Figure 4-3. The pole figures for the P-II and Cr-II samples were done on the stereographic projection for the upper hemispheres as shown in Figure 4-4. These do not show any strong texture, although the number of grains sampled is not large. The EBSD maps of the P-I and Cr-I samples are in appendix A (Figure A-3).

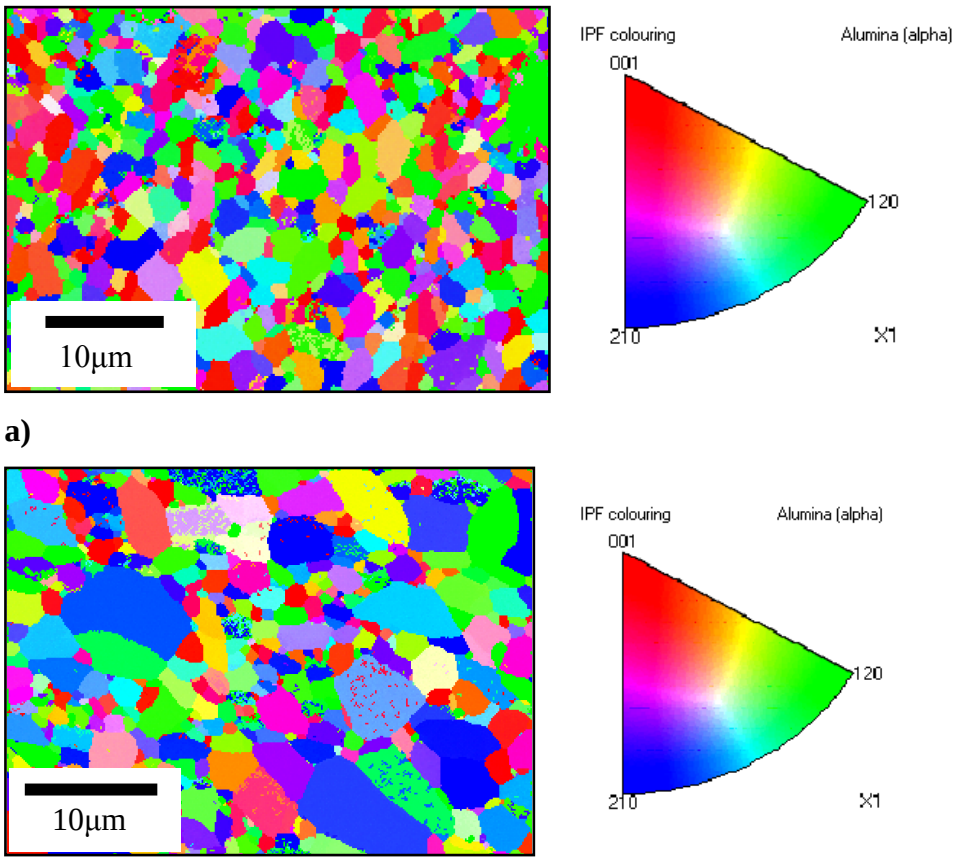

Figure 4-3: Electron Back Scattered Diffraction (EBSD) maps for the samples a) P-II Specimen, and d) Cr-II Specimen. EBSD for both samples have been done at step size (0.2µm) and the level of indexing achieved was about (60% to 70%).

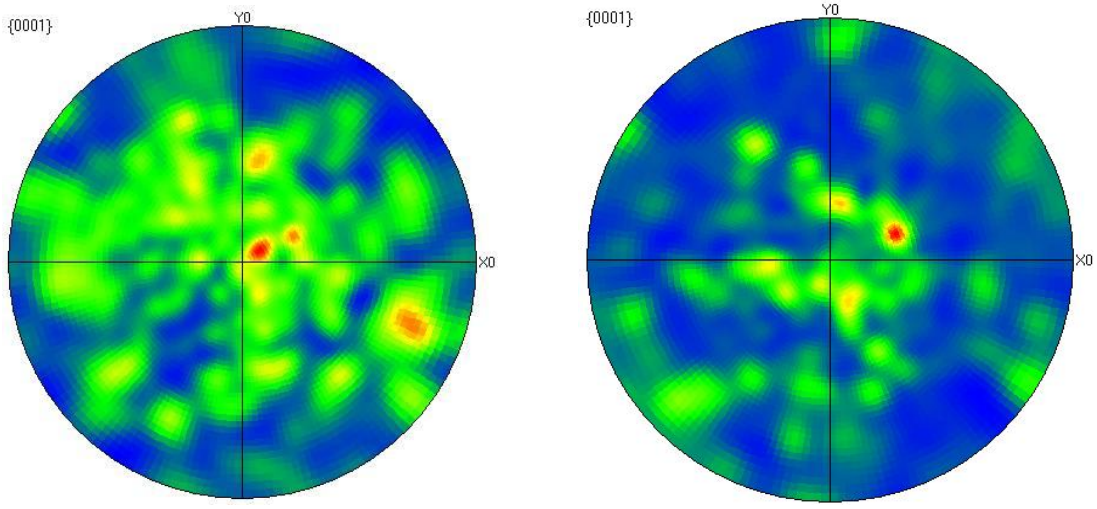

a) P-II Sample b) Cr-II Sample

Figure 4-4: Shows the pole figures for the a) P-II sample and b) Cr-II sample

4.2 Digital Image Correlation Analysis

4.2.1 Influence of the window size and surface finish on DIC noise on the Glass specimen

The purpose of this experiment was to assess the surface finishes in glass, as prepared in section (3.3.3.1). The effect of Hydrofluoric Acid (HF) at different concentration 50% and 95% is shown in Figure 4-5 and Figure 4-6 respectively. The surface was observed at different magnifications X10 and X20 and the surface was assessed using DIC at different window sizes 32×32, 64×64, and 128×128 pixels and overlaps 50% and 75%. The RMS noise measured is shown in Figure 4-7. This shows the lowest noise for 50% concentration at 50% overlap when viewed under X10 magnification. The condition used in the DIC experiment to measure surface crack opening displacement is 50% HF and 50% overlap when viewed at X20 magnification. Those conditions were used for the glass specimen as the FIB-milled slots were too small for magnification X10 to be used. The measured noise level was higher than the theoretical level achievable [67].

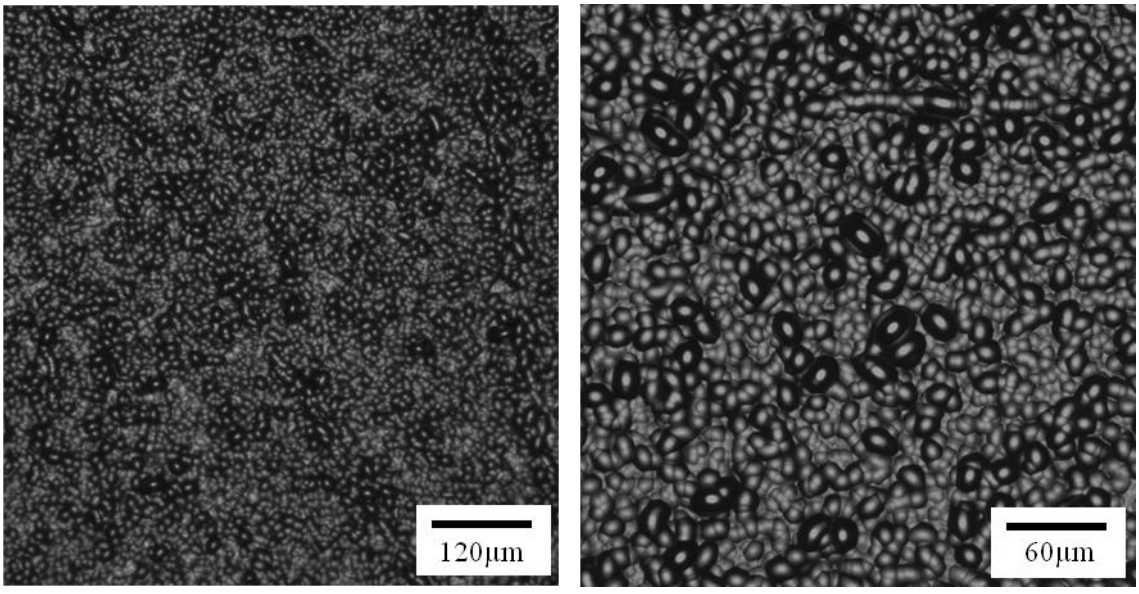

a) **b)**

Figure 4-5: Shows the microstructure for the features distribution on the glass surface using chemical etching at concentration (50% HF) for (3 min.) and gold coating for (4 min) at different magnifications a) X10 and b) X20.

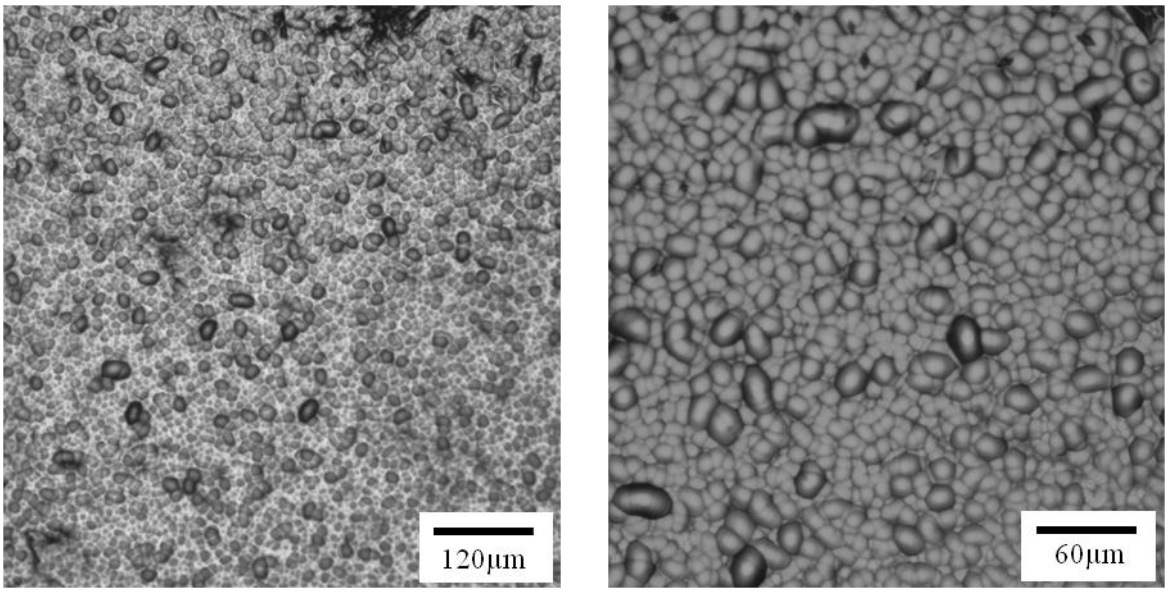

a) **b)**

Figure 4-6: Shows the microstructure for the features distribution on the glass surface using chemical etching at concentration (95% HF) for (3 min.) and gold coating for (4 min) at different magnification a) X10 and b) X20.

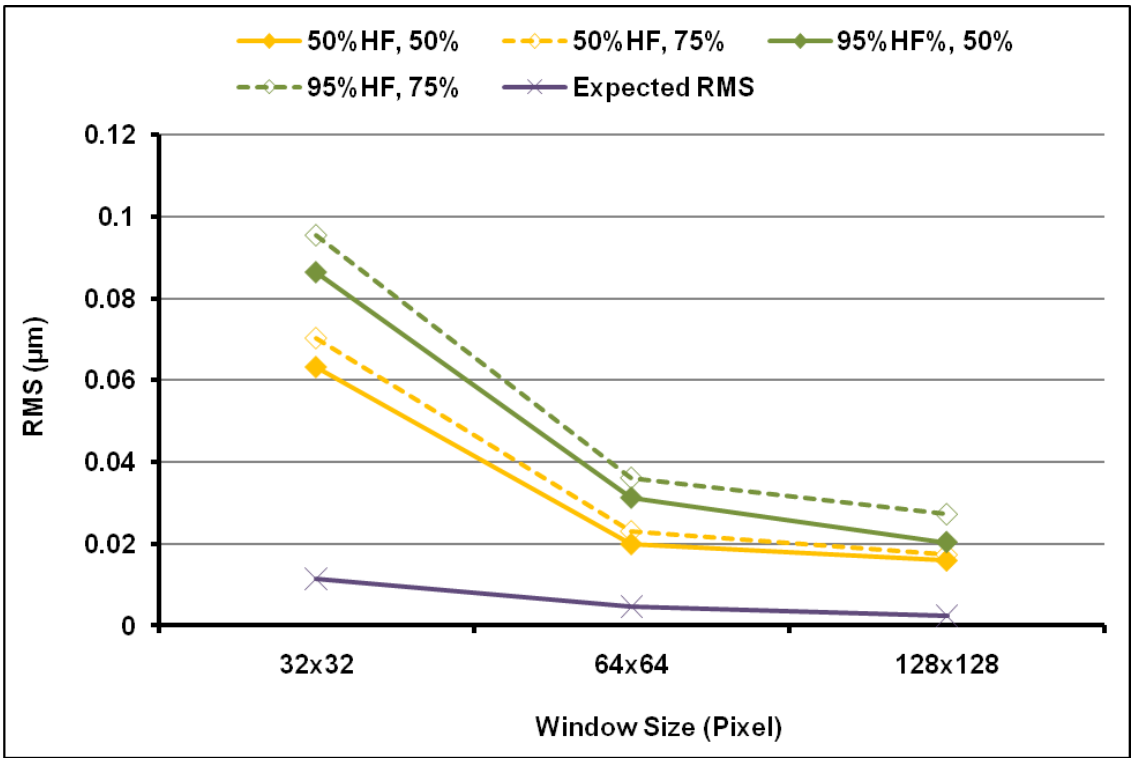

a)

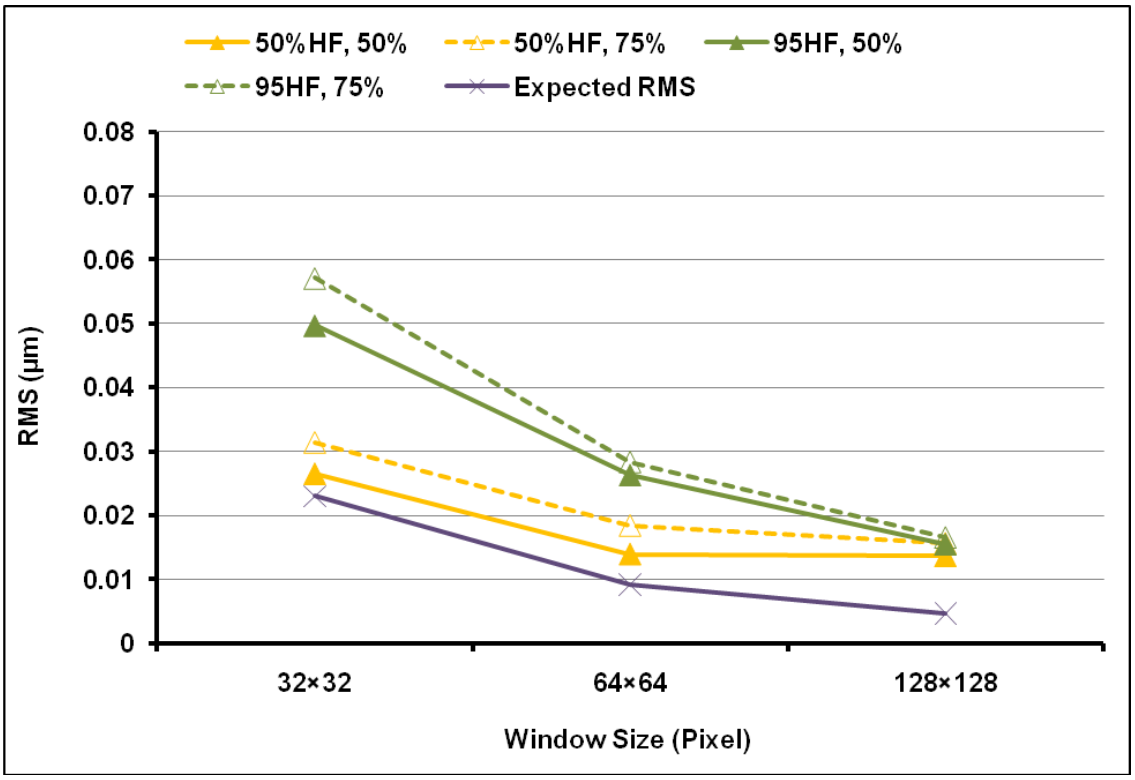

b)

Figure 4-7: The relationship between the noise level (RMS) as a function of the window size for the glass specimen a) magnification X20 and b) magnification X10. Legend shows different concentrations (50%HF and 95%HF) and different overlaps (50% and 75%) and theoretical RMS.

4.2.2 Influence of the window size and surface finish on DIC noise on the P-II and Cr-II specimens

4.2.2.1 Surface Finish

Grinding, polishing, thermal etching and gold coating were carried out to produce a surface with suitable random features with sufficient contrast for DIC analysis for the P-II and Cr-II specimens. The sample surface was prepared for the digital image correlation using different surface finish techniques as shown in Figure 4-8 (see section 3.3.4.1 for a description of the methods). Gold coating, after polishing and thermal etching allow for a good optical image of the microstructure.

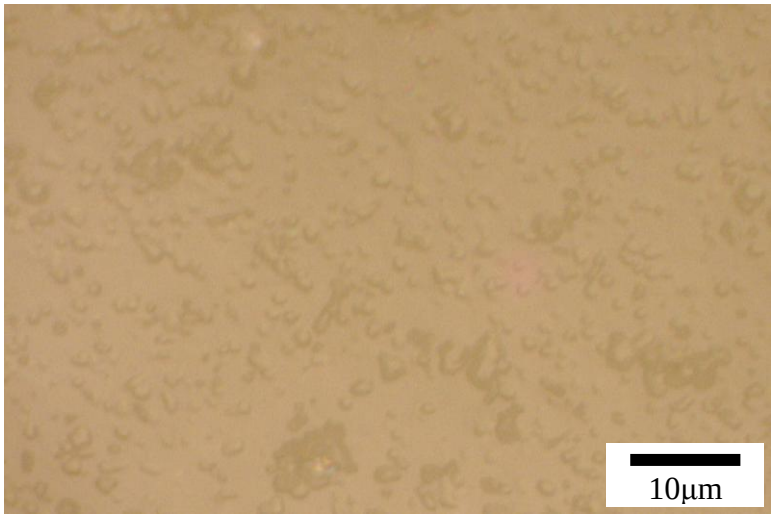

a) Grinding and Polishing

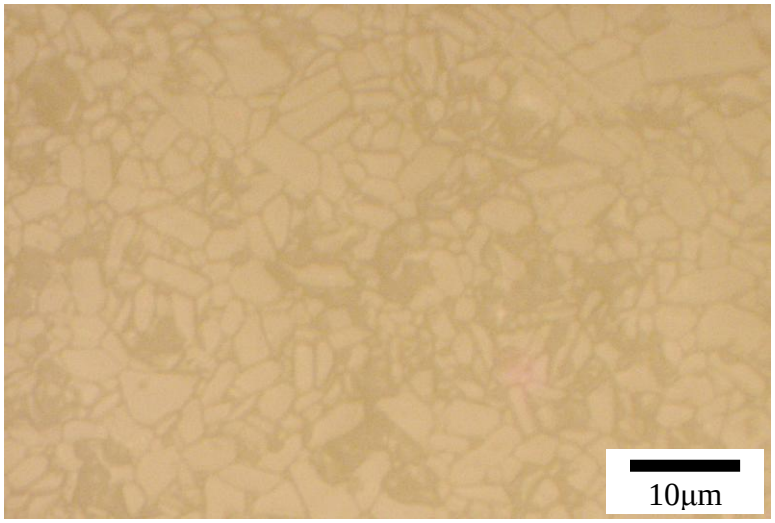

b) Grinding, Polishing, Thermal etching, and Carbon Coating

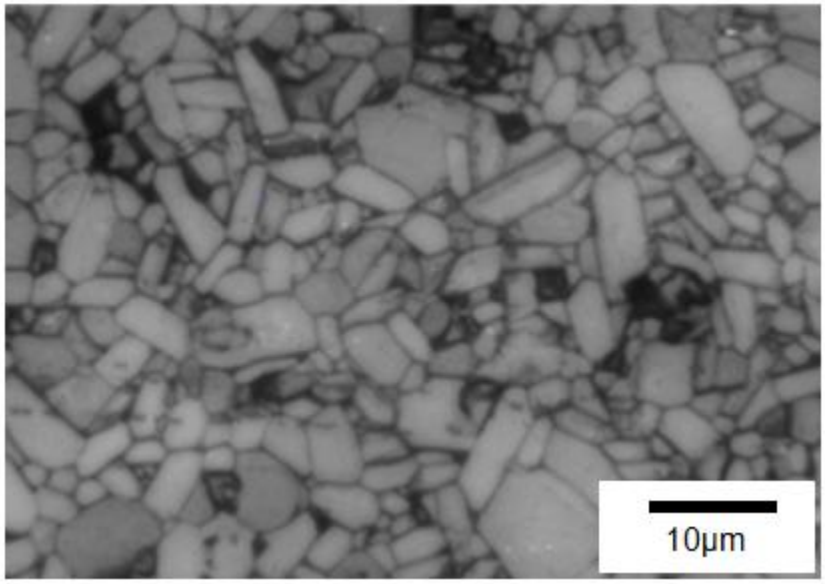

c) Grinding, Polishing, Thermal etching, and Gold Coating for P-II specimen

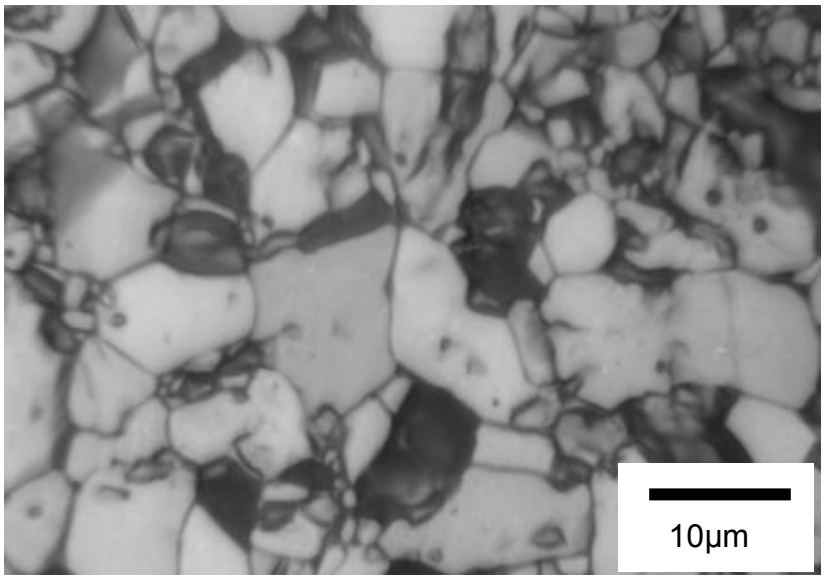

d) Grinding, Polishing, Thermal etching, and Gold Coating for Cr-II specimen

Figure 4-8: Shows the surface of alumina samples, prepared for digital image correlation at different surface finish techniques a) Grinding and polishing of the sample surface b) Grinding, polished, thermal etching and carbon coating of the sample surface c) Grinding, and polished, thermal etching and gold coating of the P-II sample surface d) Grinding, and polished, thermal etching and gold coating of the Cr-II sample surface.

The noise level was measured at magnification of (X100) for different surface finishes on the P-II sample as shown in Figure 4-8 for 50% overlap. The noise level (RMS) results are shown in Figure 4-9 against the interrogation window (the window size is affected by the

subimages as discussed in more information in the following section). Similar data were obtained for the Cr-II sample Figure 4-9b.

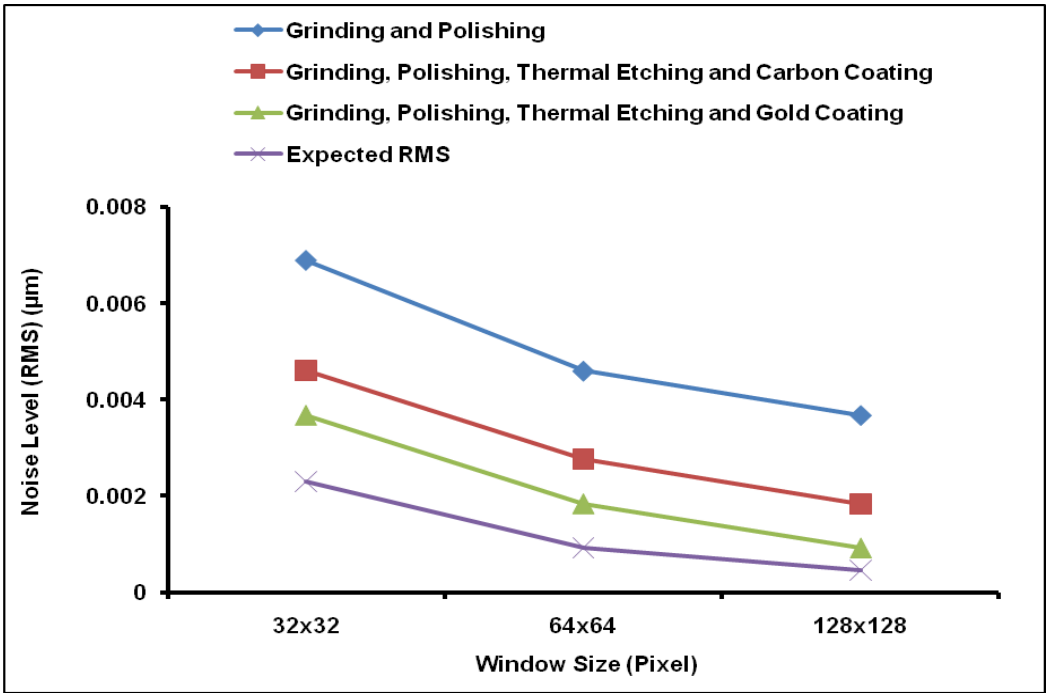

a)

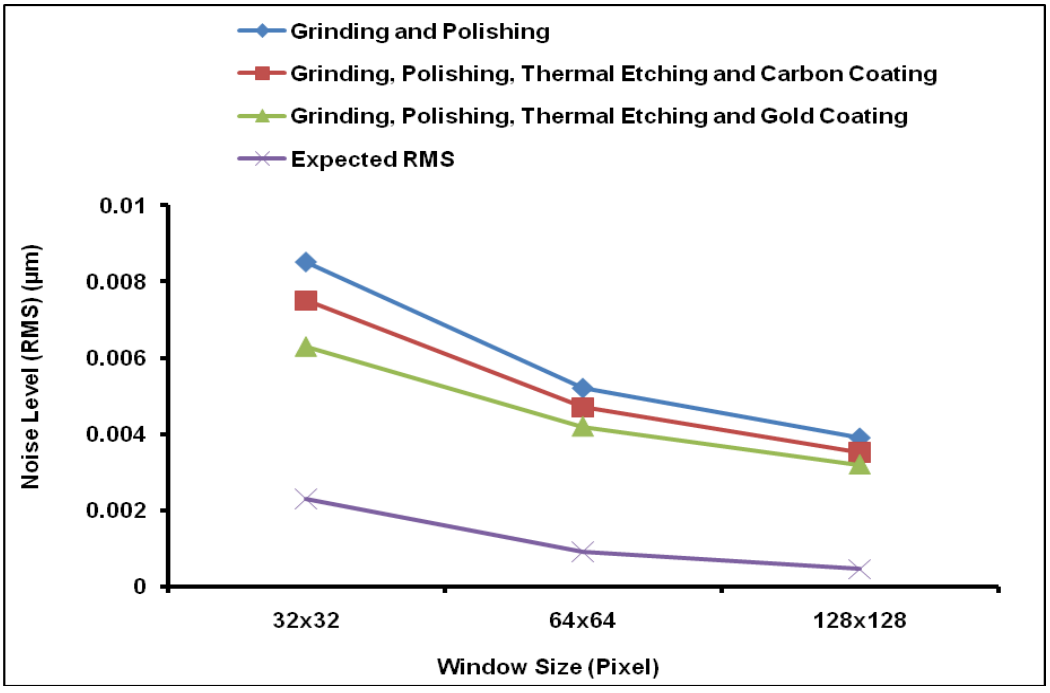

b)

Figure 4-9: The relationship between the noise level (RMS) as a function of the window size at magnification (X100) and overlap (50%) for a) P-II sample and b) Cr-II sample.

4.2.2.2 Window Size and Overlap

The displacement accuracy in DIC affects by the interrogation window size. The noise level of the DIC decreased with increasing the interrogation window size and number of feature size [105]. The accuracy was studied using two methods. The first method is used to apply small movement between the first image and the second image which were used to determine displacement accuracy. The displacement map was used to provide the displacement vector using digital image correlation. The noise level was measured for the single pass at different interrogation window size, magnification and overlaps. The large interrogation window size was provided large displacement accuracy and the results are shown in Table 4-2 and Table 4-3 and Figure 4-10 and Figure 4-11 for samples P-II and Cr-II respectively.

The second method used at the multi-pass to measure the displacement of the horizontal direction in the displacement vectors (i.e. the vector displacement was determined in the X-direction from the left to right of the image in the region at the centre of the viewed area). The displacement accuracy was calculated at different overlaps and interrogation window size for the stressed specimen at magnification X100. The displacement accuracy for the interrogation window size (128×128 pixels) and overlap 50% was much smoother. The interrogation window size 64×64 pixels has more scatter data than window size 128×128 pixels are shown in Figure 4-12 and the scatter data for P-II and Cr-II samples are shown Table 4-4. The magnitude of scatter data for P-II and Cr-II samples in Table 4-4 are higher than the RMS noise for both materials in Table 4-2, Table 4-3.

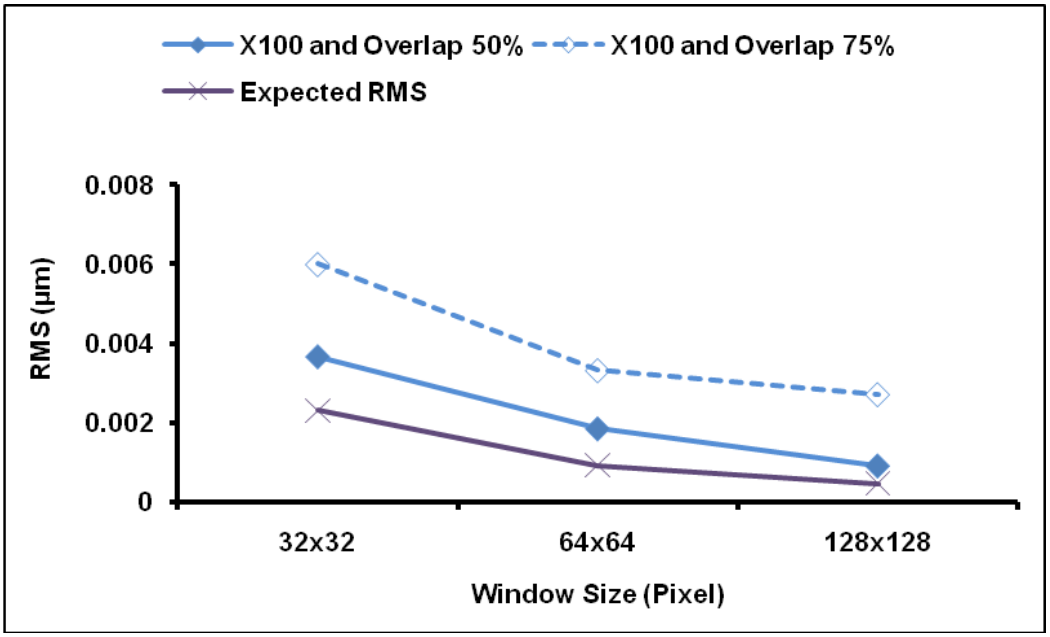

a)

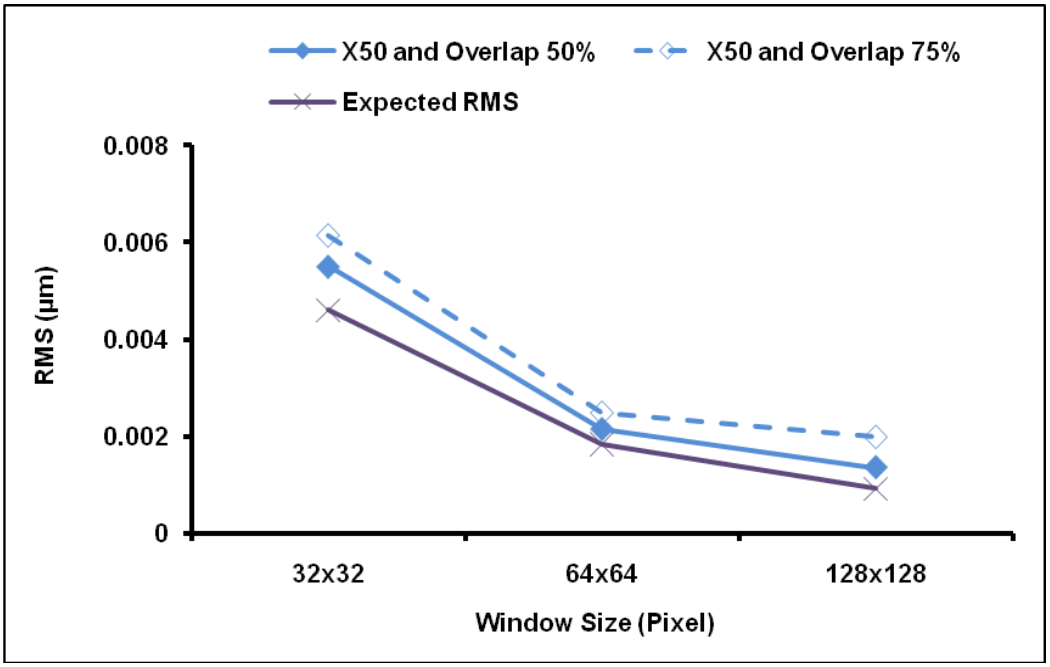

b)

Figure 4-10: The noise level (RMS) against the window size and also, at different overlaps for the P-II sample a) at magnification X100 and b) at magnification X50. First method was used.

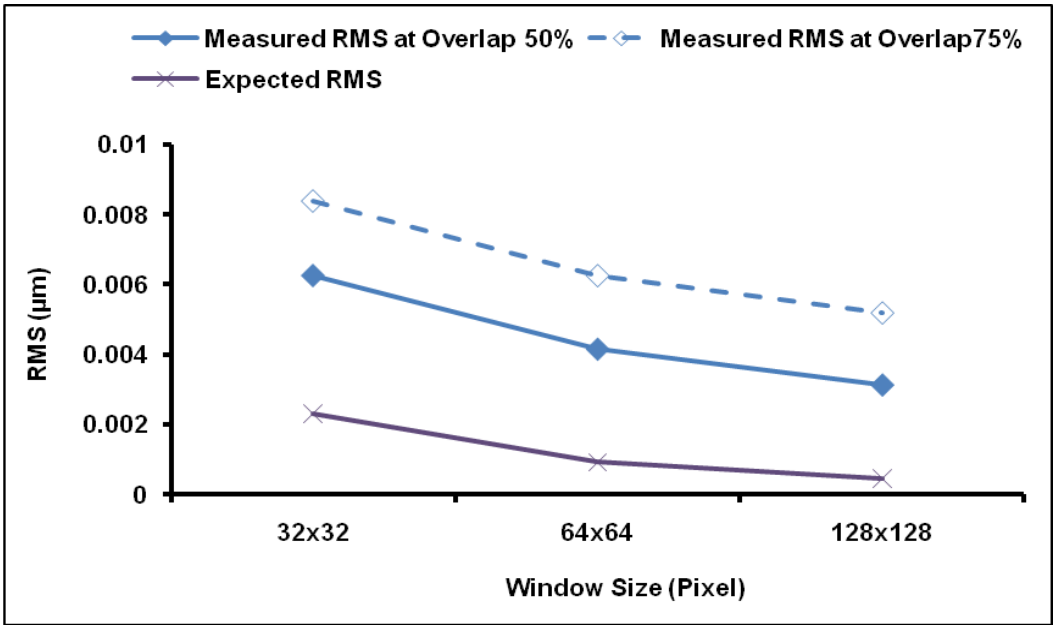

Figure 4-11: The noise level at magnification X100 against the window size and at different overlaps for the Cr-II sample. First method was used.

Table 4-2: Shows the noise level (RMS) at magnification (X100 and X50) and at different window sizes and overlaps for the P-II specimen (1 pixel is 0.0046 µm at magnification X100 and 1 pixel is 0.092 µm at magnification X50).

Magnification	Window size (pixels)	RMS (µm)	
		overlap 50%	overlap 75%
X100	32×32	0.0037	0.006
	64×64	0.0018	0.0033
	128×128	0.00091	0.0027
X50	32×32	0.0055	0.0062
	64×64	0.0022	0.0025
	128×128	0.0014	0.0019

Table 4-3: Shows the noise level (RMS) at magnification (X100) and at different window sizes and overlaps for the Cr-II specimen.

Magnification	Window size (pixels)	RMS (µm)	
		overlap 50%	overlap 75%
X100	32×32	0.0063	0.0084
	64×64	0.0042	0.0063
	128×128	0.0032	0.0052

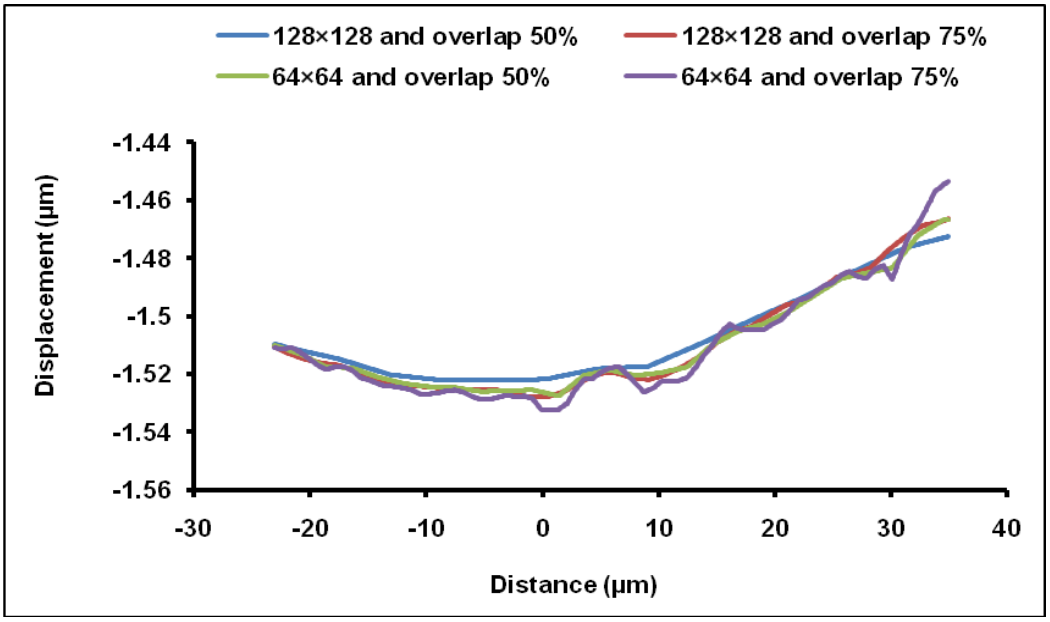

a)

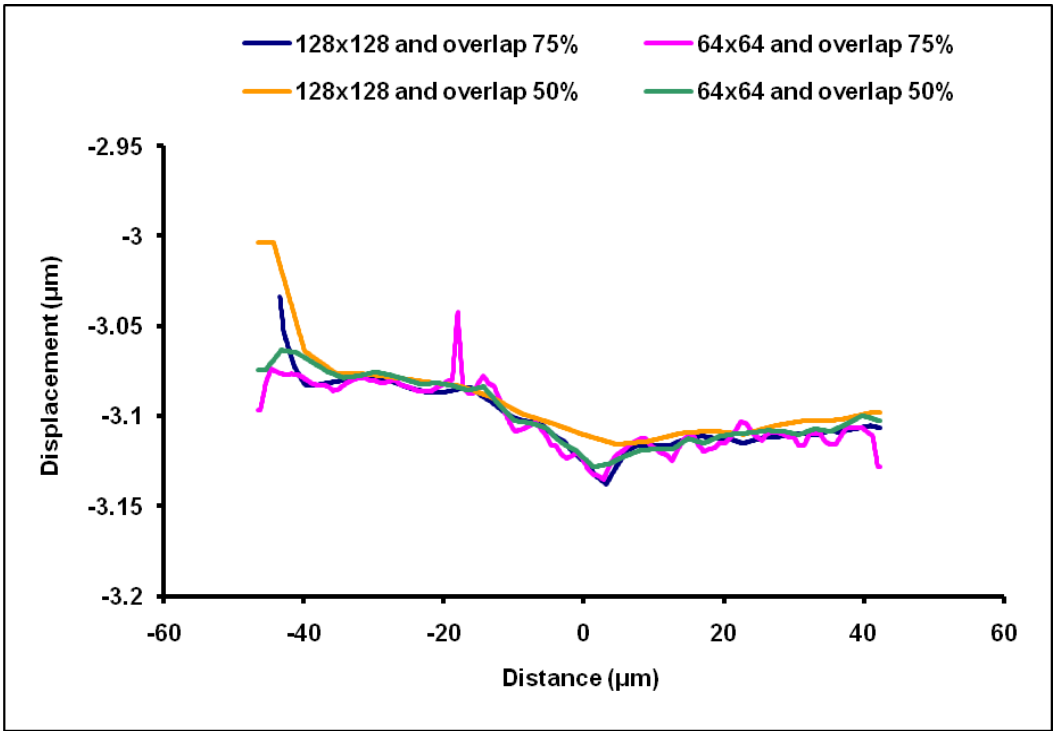

b)

Figure 4-12: Line profiles of displacement in the x-direction along a line across the image (viewed area) at magnification X100. The subset of 128×128 pixels and 64×64 pixels are compared and also different overlaps of 50% and 75% for a) P-II specimen and b) Cr-II specimen. Line profile of displacement was in the region outside the cracked region. Second method was used.

Table 4-4: Shows the scatter level at magnification X100 and also, at different window sizes and overlaps for the P-II and Cr-II specimen. The scatter data was measured using polytool function in Matlab.

Windows Size (Pixel)	Overlaps %	Scatter or noise (μm)	
		P-II	Cr-II
64×64	50	0.033	0.022
	75	0.035	0.023
128×128	50	0.029	0.031
	75	0.033	0.034

4.2.3 Comparison DIC data between Glass and P-II and Cr-II Specimens

The purpose of this experiment is to show how the experiment performs in reducing the magnitude of the necessary shift corrections and avoiding errors due to peak locking and also for improving the intensity distribution. The intensity distribution is important to achieve sufficient grey scale variation in the DIC images. The digital image correlation data were compared between the Glass, P-II, and Cr-II specimens. The comparisons between these data were used to find the better set up for the optical microscope and sample preparation for digital image correlation. The methods were used for comparing between the data as shown in the section below:

4.2.3.1 Interrogation Window Size

The purpose of this experiment was to show the typical features evident in windows of different sizes. The windows are labelled with a yellow marker. The interrogation window sizes that were achieved for the DIC experiment on the raw images at different interrogation window sizes 64×64 pixels for the specimen P-II and 128×128 pixels for Cr-II and glass specimen respectively, is shown in Figure 4-13.

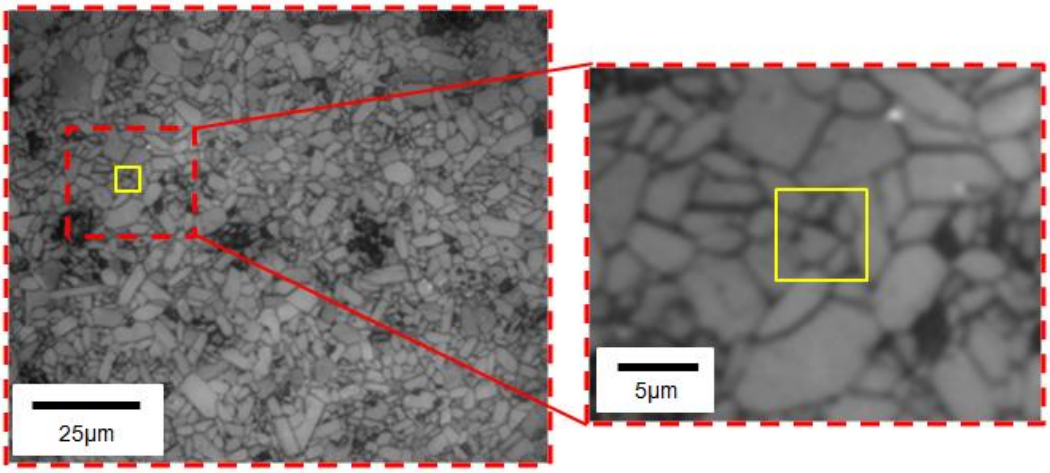

a)

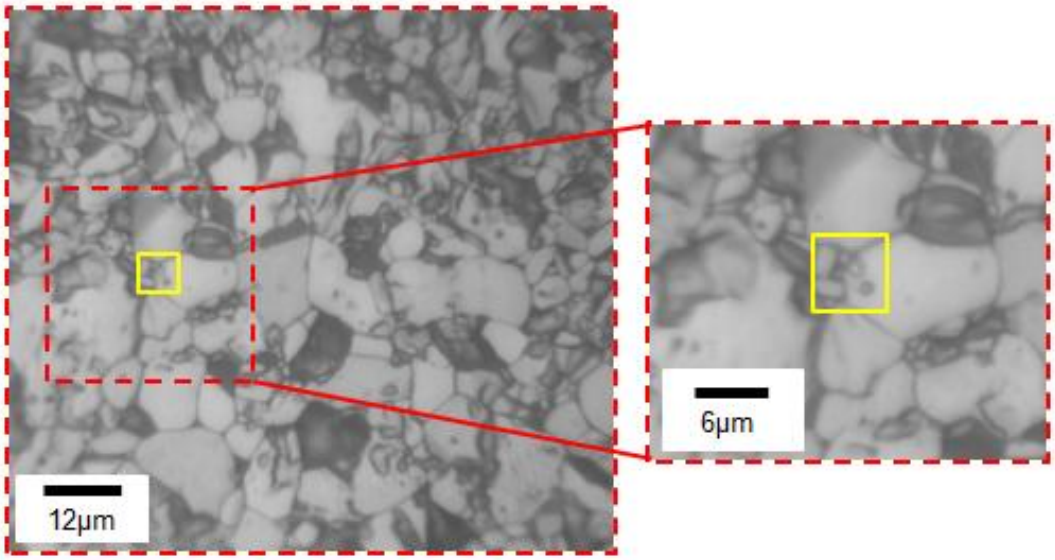

b)

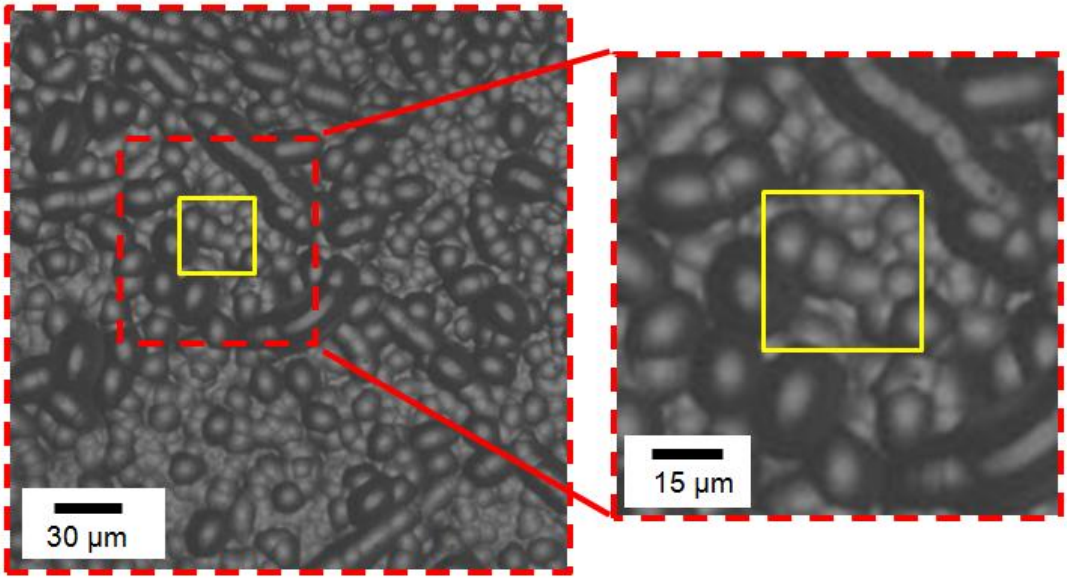

c)

Figure 4-13: The window size for the specimens a) P-II specimen, the window size used was (64×64) pixels on the viewed area b) Cr-II specimen, the window size used was (128×128) pixels on the viewed area and c) Glass specimen, the window size used was (128×128) pixels on the viewed area.

4.2.3.2 Shift Correction

The purpose of shift correction is to remove rigid body movements between images. The correction window size was chosen depending on the movement and deformation between the images during the test. The shift correction for P-II and Cr-II specimens and the glass specimen were compared by determining the shifting of the features in the X-axis and Y-axis between images recorded at each strain increment (micrometer displacement) during the loading experiment. This is the actual shift during the experiment. The shift correction was done using a Batch processing using the Davis software for the raw images and then the shift correction and rotation correction was done for a series of the recorded images. Correction window size depends on the movement between the images (the correction window size is 512×512 pixels if the deformation is large and the window size is 32×32 if the deformation is small). There is another correction if the sample was rotated during applied load and the process for this case is called rotation correction. The rotation window size depends on the rotation between the images during the experiment. The shift correction

and rotation correction process are shown in Figure 4-14. Although this procedure is intended to remove bulk movements, it is generally considered that accuracy of experiments is improved if the necessary shift corrections are minimised by good experimental control.

The result of the shift correction for P-II, Cr-II, and glass specimens in both directions x- and y-direction at window size 512×512 pixels for shift correction and window size 128×128 pixels for rotation corrections have been shown in Figure 4-15. The shift correction was reduced by using XY-stage and the purpose from this stage to keep the features on the processed and live image on the same locations. The features on the live image are compared with the processed image. When the coordinates for these features on the live image not the same on the processed image, the XY-stage was used to move the features on the live image to the same location on the processed image.

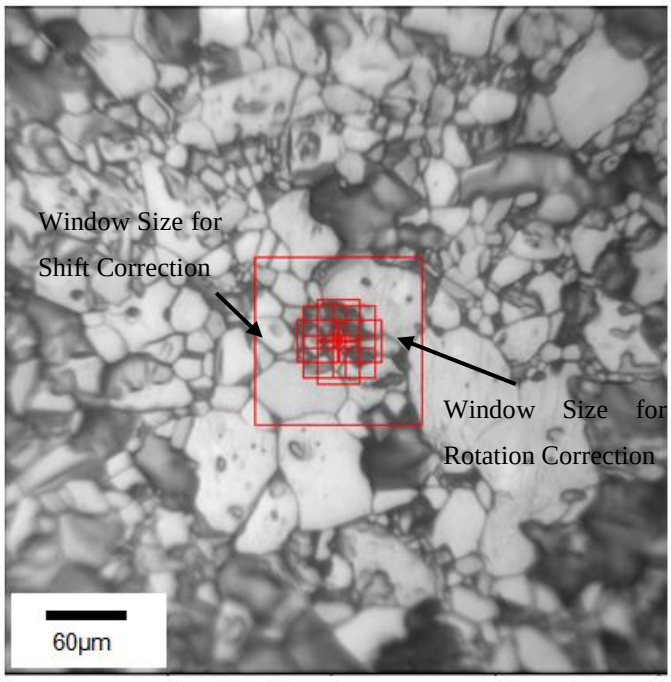

Figure 4-14: Shows the shift correction and rotation correction procedure using window size (512×512 pixels) for shift correction and using several windows size (128×128 pixels) for rotation correction for Cr-II specimen.

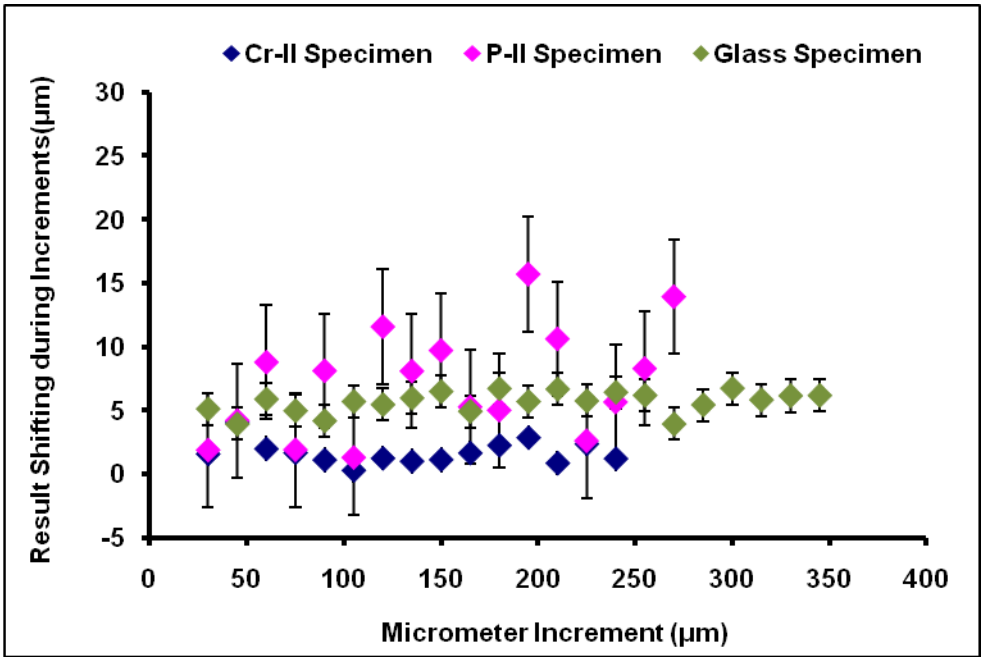

Figure 4-15: The relationship between the result of the movement (shifting) of the features during increasing the applied strain at different micrometer displacements for P-II, Cr-II, and Glass specimen. Interrogation window size of 512×512 pixels for shift correction and using several windows size 128×128 pixels for rotation correction was used for this case.

4.2.3.3 Peak Locking

The surface preparation was important to assess the accuracy of the displacement in the viewed area for the digital image correlation. When the features sizes are too small (the feature size is less than one pixel) that will cause peak locking problem. The vector field displacement in X-direction (Vx) was used to calculate the Probability Density Function (PDF). The interrogation window size used for the P-II specimen was 64×64 pixels and overlap 50%, window size for Cr-II and glass specimen was 128×128 pixels and overlap 50%. Figure 4-16 shows there is pixel locking for the P-II specimen but there is no pixel locking for Cr-II and glass specimens. The peak locking in the P-II specimen due to the deformed region in this sample have different features with different displacements (see Figure 4-16a). After deformation one feature moves 0.5 pixels and the second one will move a whole pixel. The second feature looks unchanged but the first feature is not clear on the CCD and the vector displacement was determined from the correlation of the two

features. The image processing in Davis software was done for the P-II sample to improve the image equality and the observed pixel locking did not affect on the P-II sample results.

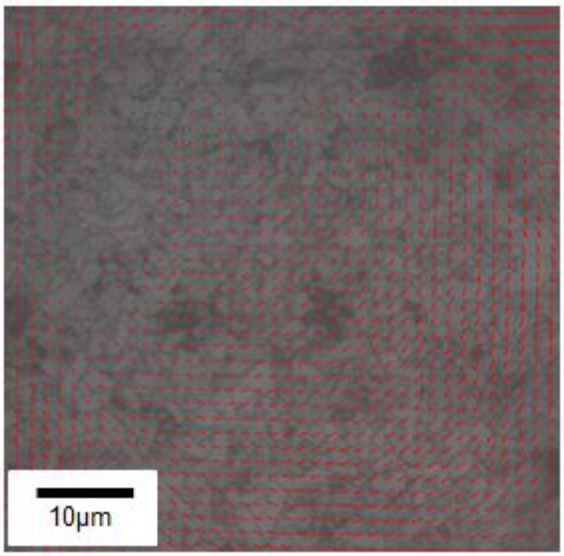

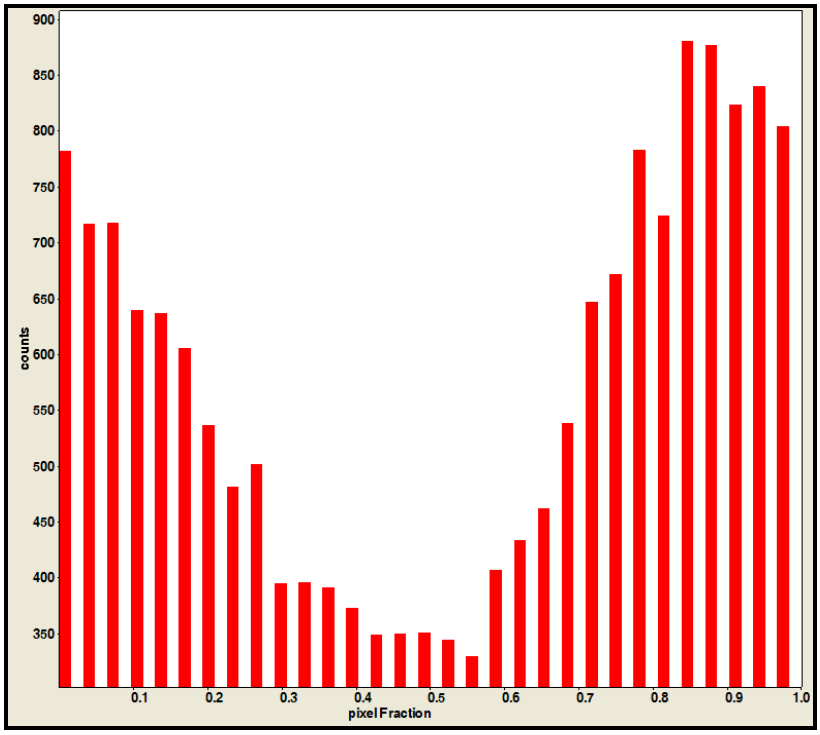

a)

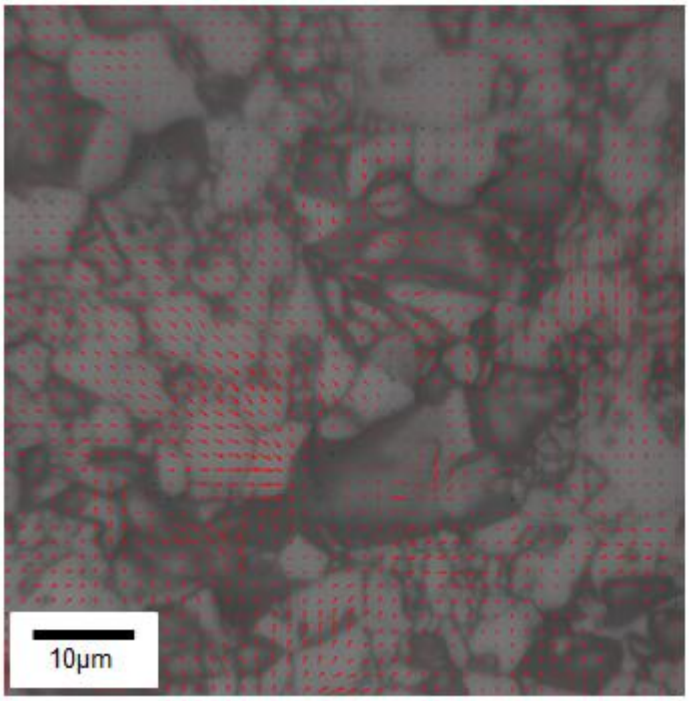
10µm

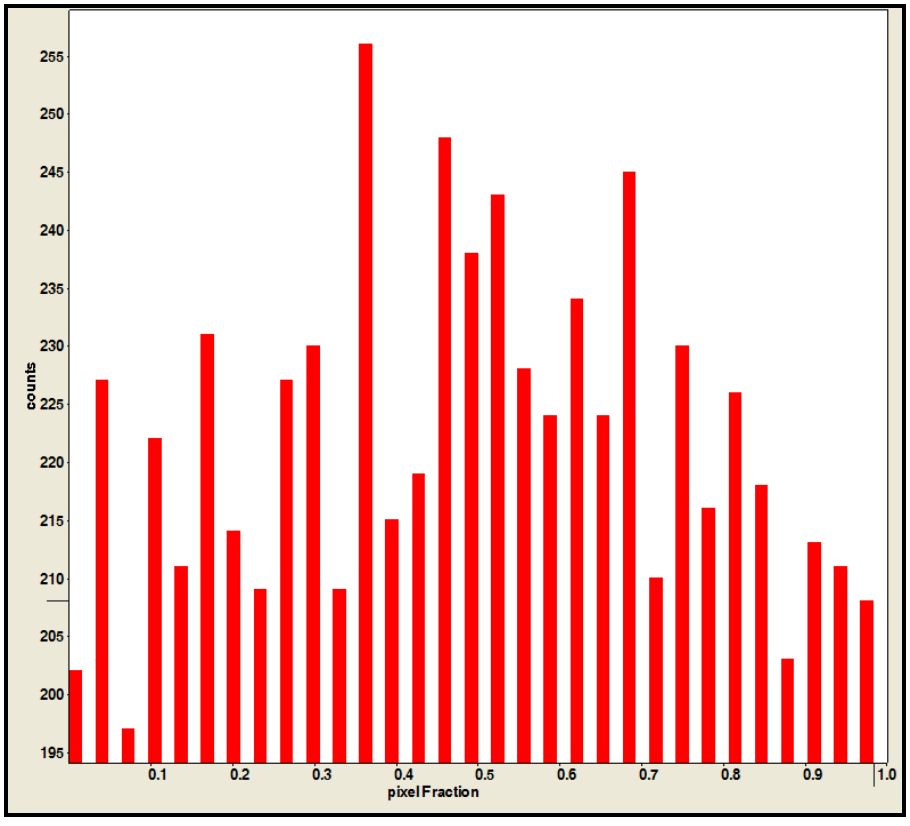
counts
255
250
245
240
235
230
225
220
215
210
205
200
195
0.1
0.2
0.3
0.4
0.5
0.6
0.7
0.8
0.9
1.0
pixel Fraction

b)

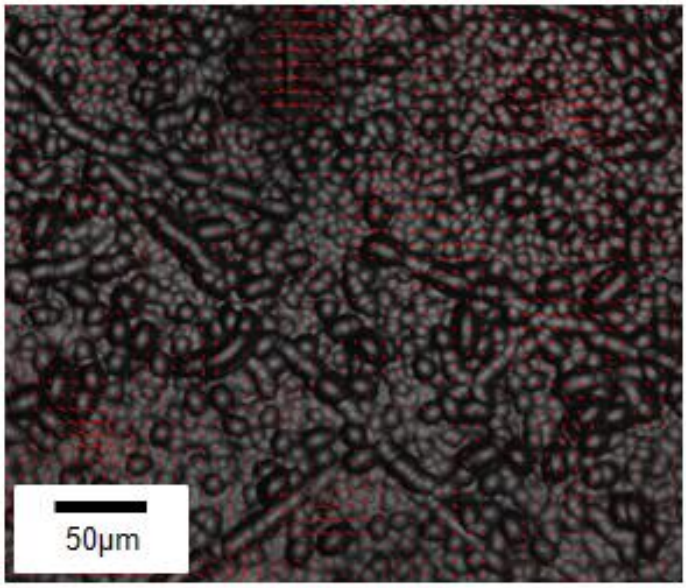

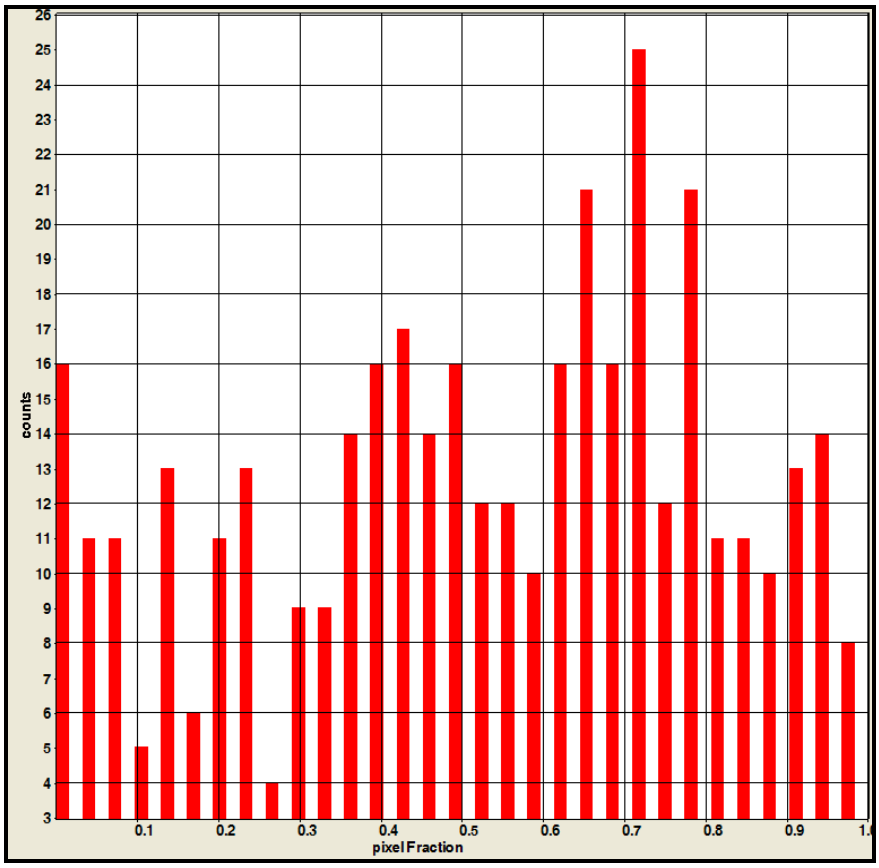

c)

Figure 4-16: Shows the images with different features have different displacement using interrogation window size 64×64 pixels and overlap 50% for P-II, 128×128 pixels and overlap 50% for Cr-II, and Glass specimen; this is shown by the probability density plot of the displacement vector.

4.2.3.4 Intensity Distributions of P-II, Cr-II, and Glass specimens

The light intensity introduced from the CCD which was provided many pixel arrays and there are many lines of the pixels per image and also many pixels per array. The light pixel is produced from the light intensity and the reading is (100) and the reading for the black pixel is (0). The intensity pattern was used for the matching between the series images for digital image correlation. Figure 4-17 shows the comparison intensity distribution between the P-II and Cr-II specimen at magnification X100, and Glass specimen at magnification X20 at the red line. Figure 4-18 shows the relationship between the grey scale intensity as a function of the distance for the P-II, Cr-II, and Glass specimen. This procedure has done using Image-J software using the Plot Profile option and it can be seen that the intensity distribution in the P-II sample does not have as large a variation in the grey scale. This is a reason for pixel locking due to the feature variation during the deformation.

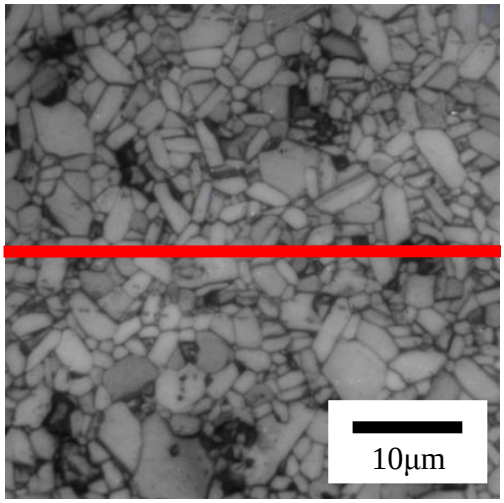

a) P-II Specimen

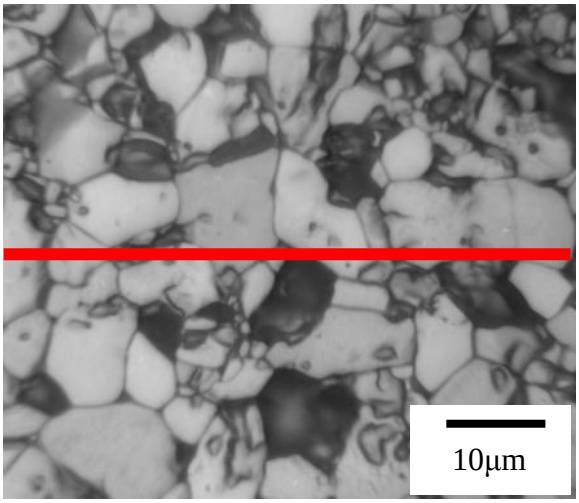

b) Cr-II Specimen

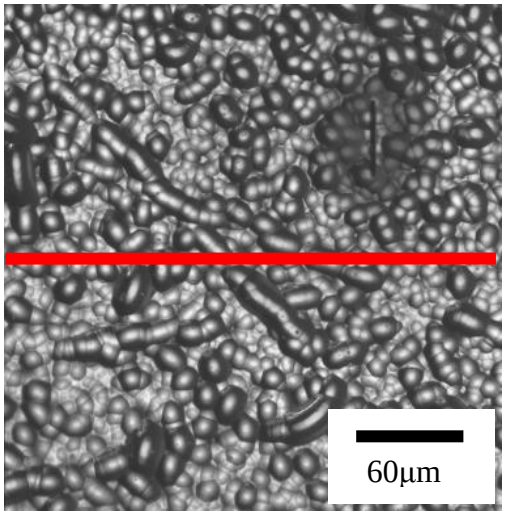

c) Glass Specimen

Figure 4-17: Shows the microstructure data for the raw reference images which are used to observe the intensity distribution using Image-J software for a) P-II specimen b) Cr-II specimen c) Glass specimen. Figure represents for P-II and Cr-II specimens at magnification X100 and glass specimen at magnification X20.

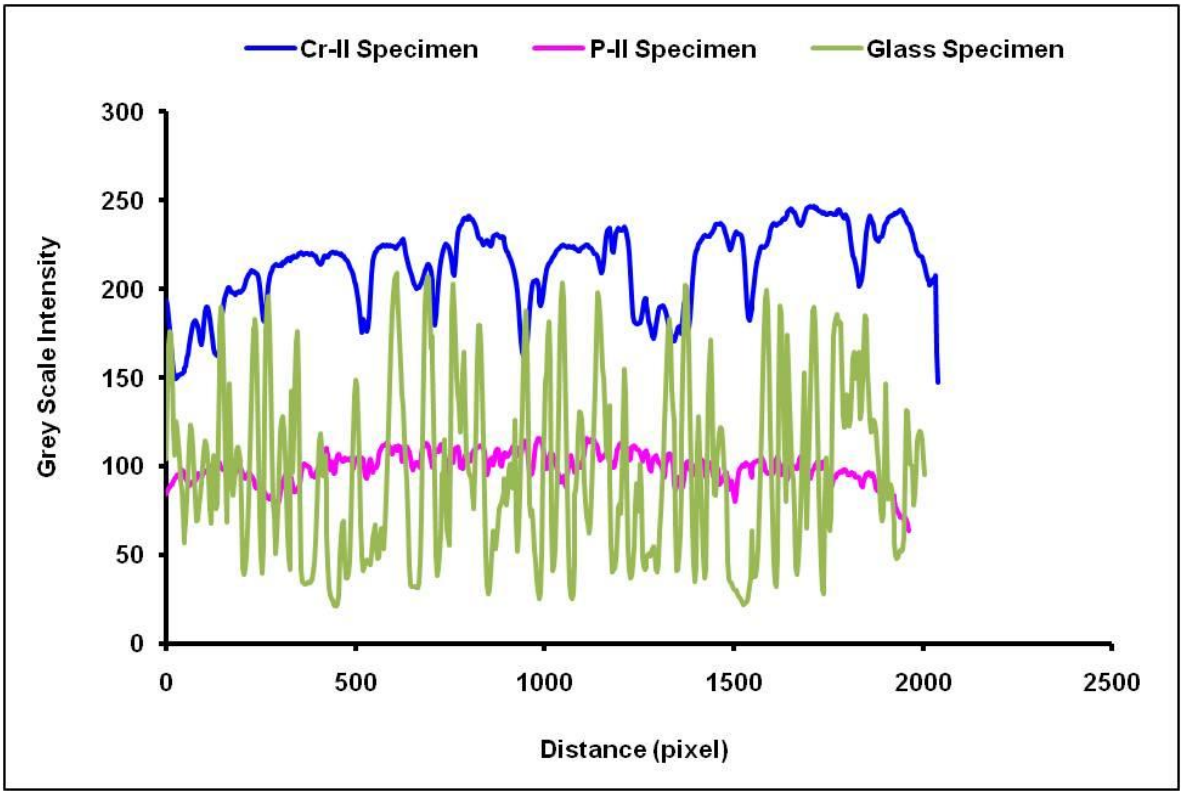

Figure 4-18: Typical intensity distribution plot for P-II and Cr-II specimen at magnification X100 and Glass specimens at magnification X20.

4.2.4 The accuracy of DIC to measure bulk strain on the calibration specimen (glass specimen)

4.2.4.1 Curvature Calibration Test

This test was to estimate the apparent strain that could arise from sample curvature. This was done by first calibrating the relationship between defocus distance and apparent strain by changing the vertical displacement between the lens and the specimen surface (change in focus) in the positive direction range (0 to 5µm) and negative direction range (0 to -5µm). The change in vertical displacement was measured between the lens and the sample surface using a Dial Test Indicator. The apparent strain was measured from Davis calculation at interrogation window size 128×128 pixels and overlap 50% as shown in Figure 4-19. A glass specimen was used, prepared as in section (3.3.3).

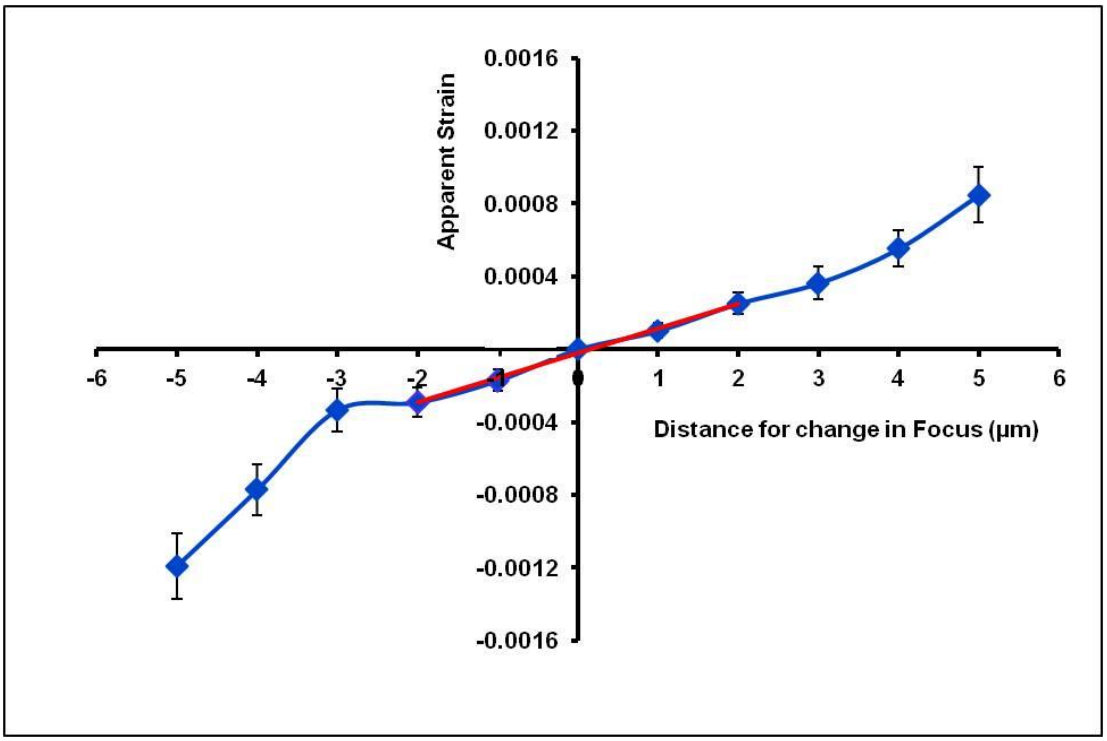

Figure 4-19: Evolution of average strain (apparent strain) along the X - axis with the distance moved toward the camera in the positive and negative direction. Interrogation window size was 128×128pixels and overlap 50%.

The error bars represented in Figure 4-19 use the RMS values for strain for this surface. The gradient was calculated from the apparent strain values and it was 0.0001 per µm. The red line is simply a fit to the central region where the behaviour is more linear.

4.2.4.2 Comparing between the strain gauge outputs and measured strain (DIC strain)

The position of the strain gauge on the glass calibration sample is shown in Figure 4-20. The distance between the region of the strain gauge and viewed area was about 5 mm. The sample contained two slots (slot A and slot B) as described in section (3.3.3.2) which were within the observed area and the slot B was closer to the strain gauge region as shown in Figure 4-20.

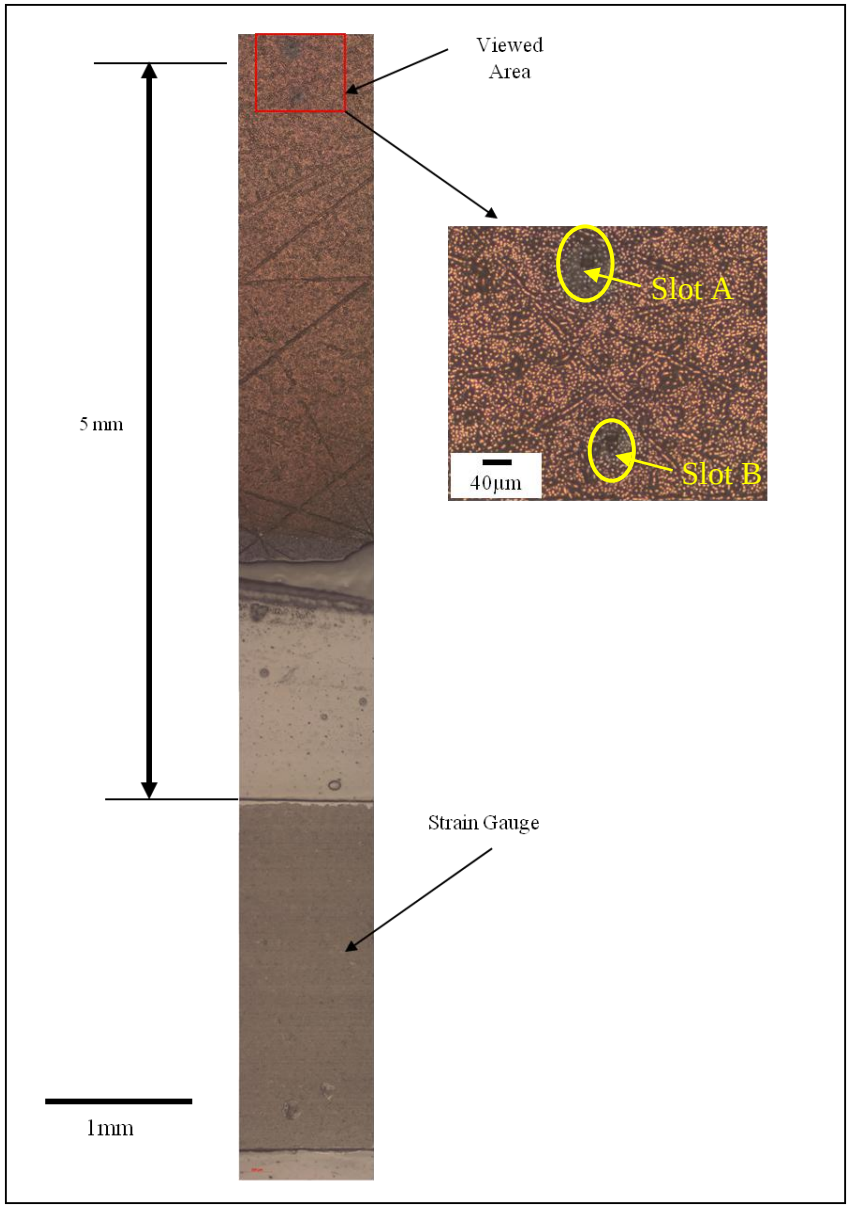

Figure 4-20: Optical image showing the distance between the viewed area (FIB-milled slot A and slot B are marked) and the strain gauge position for the glass specimen is shown.

Figure 4-21 shows the analysed or viewed area using digital image correlation and also, shows the loading direction (X-axis). The analysed area used for digital image correlation was approximately (460×460µm).

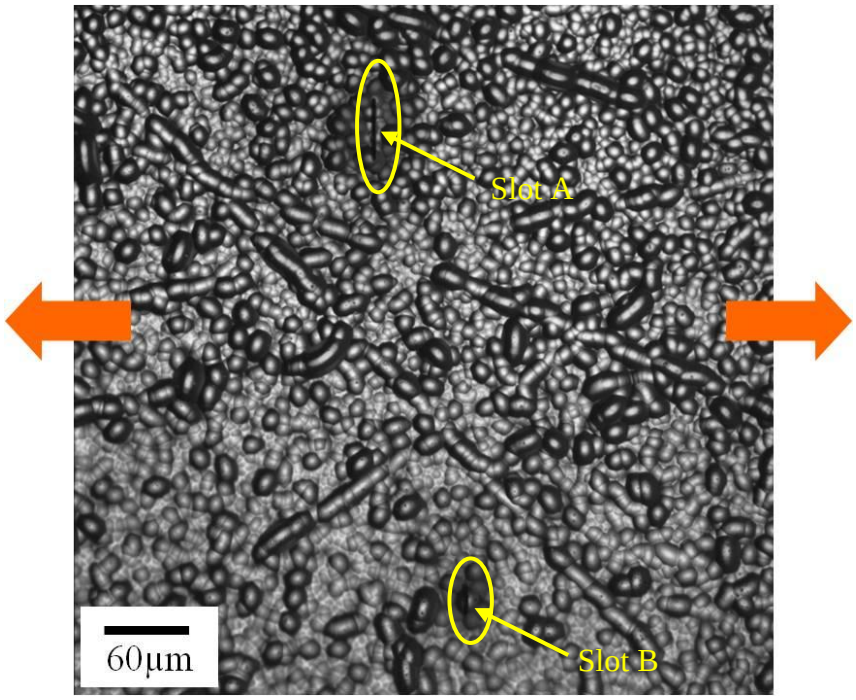

Figure 4-21: Shows the analysed or viewed area which used for digital image correlation and also, the arrows show the loading direction in X-direction.

The average strains in the X-direction (ε_{xx}) and Y-direction (ε_{yy}), with an window size of 128×128 pixels and overlap 50% are shown in Figure 4-22 as a function of the strain gauge output. The average strain is the digital image correlation mean strain value along a line through the centre of the viewed area (i.e. a region with no slots). The DIC strain in the X-direction increases with applied strain, but the increase is significantly less than the strain gauge output. The gradient of DIC mean X-strain and DIC mean Y-strain are about 0.403 and 0.067 respectively.

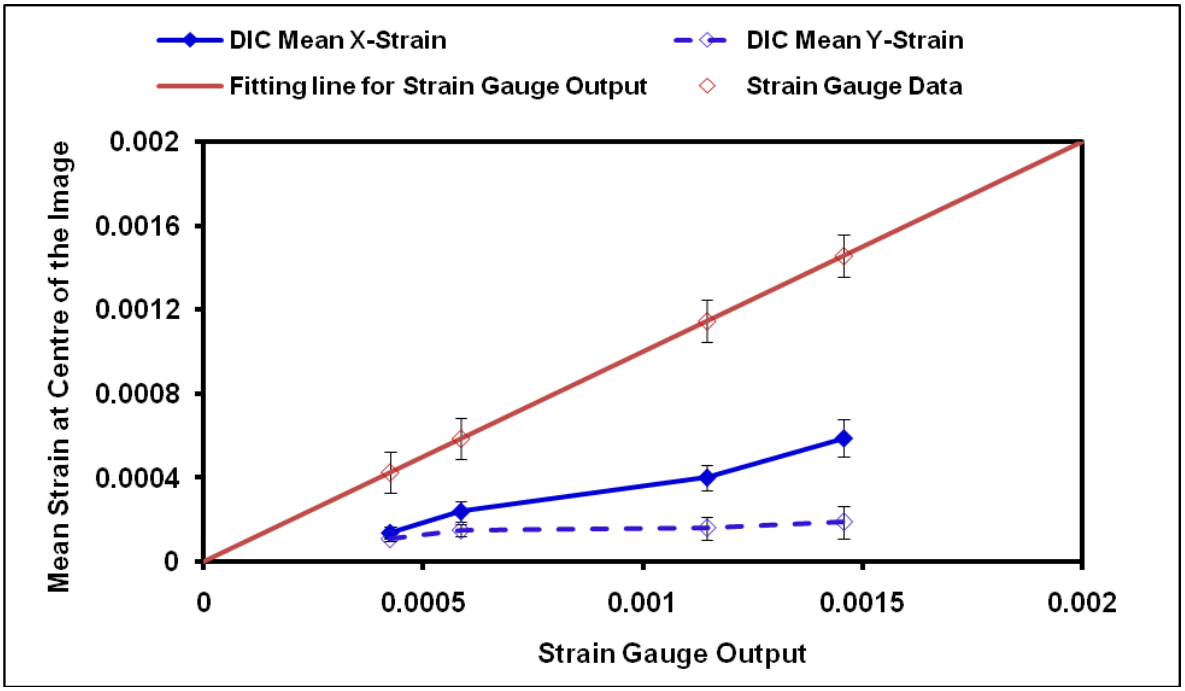

Figure 4-22: Shows the digital image correlation mean strain at the centre of the image (viewed area) at interrogation window size of 128×128 pixels and overlap 50% against the strain gauge output for the glass specimen. DIC mean strain is measured at the centre of the viewed area with no slots.

4.2.4.3 Variation of Displacement across the image

The displacement variation across the image (viewed area) in both the X and Y-direction was examined. For example, Figure 4-23 a and b show the displacement maps in X and Y-axis at window size 128×128 pixels and overlap 50%. The line profile (white lines as shown in the same Figure) was used at a different position within the viewed area. The displacement maps are for an applied strain of 0.00059 from strain gauge.

The displacement plots at different applied strain were analysed to obtain the average digital image correlation strain along each line. This was measured by dividing the total displacement by the line length in either the X- or Y- direction. Figure 4-24 shows the X-strain increase with applied strain. The DIC strain in X-direction was larger than DIC in Y-direction, both the X and Y strains increase across the image.

The mean DIC strain and DIC strain slope in X- and Y-direction was measured from Figure 4-24 a and b. The average digital image correlation strain was measured at different line positions across the viewed area as a function of the applied strain. The measured strain

gradient (DIC strain gradient) is calculated from the measured strain (at different line positions and strain increments) divided by the line position as shown in Figure 4-24 a and b. The digital image correlation strain and DIC strain slope results have been shown in Figure 4-25. The interrogation window size used for this case was 128×128 pixels and overlap was 50%.

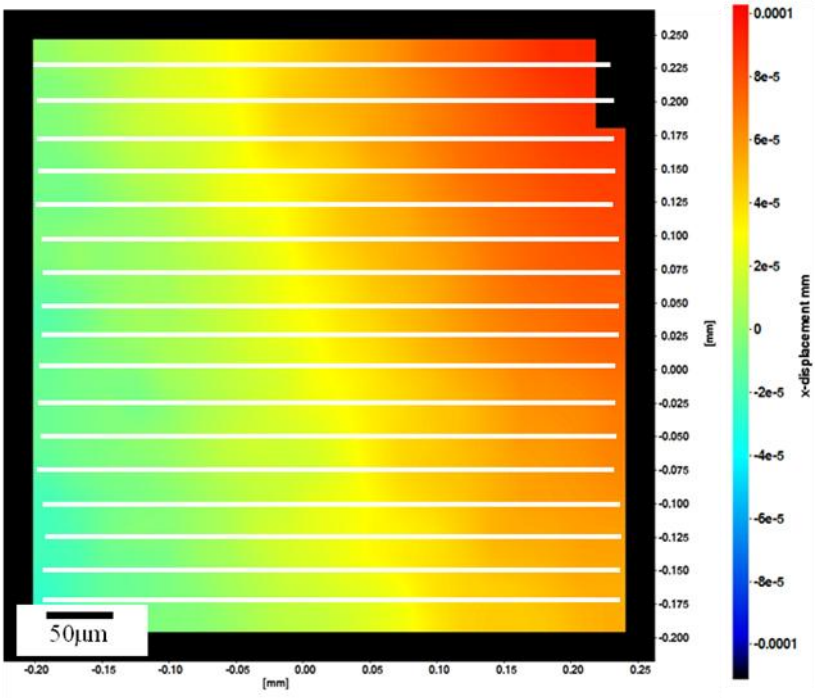

a) X-direction

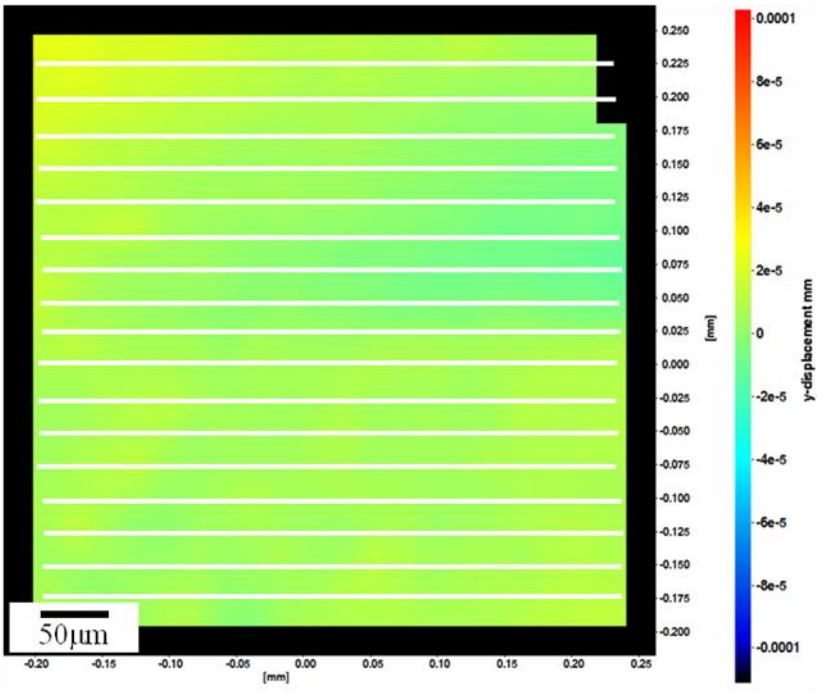

b) Y-direction

Figure 4-23: Shows the displacement map at interrogation window size 128×128 pixels and overlap was 50% and also shows the line profile across the viewed area at different positions and at applied strain 0.00059 for the glass specimen at a) X-displacement, and b) Y-displacement. The white lines describe the line profile using DIC (i.e. the location for measuring the displacement).

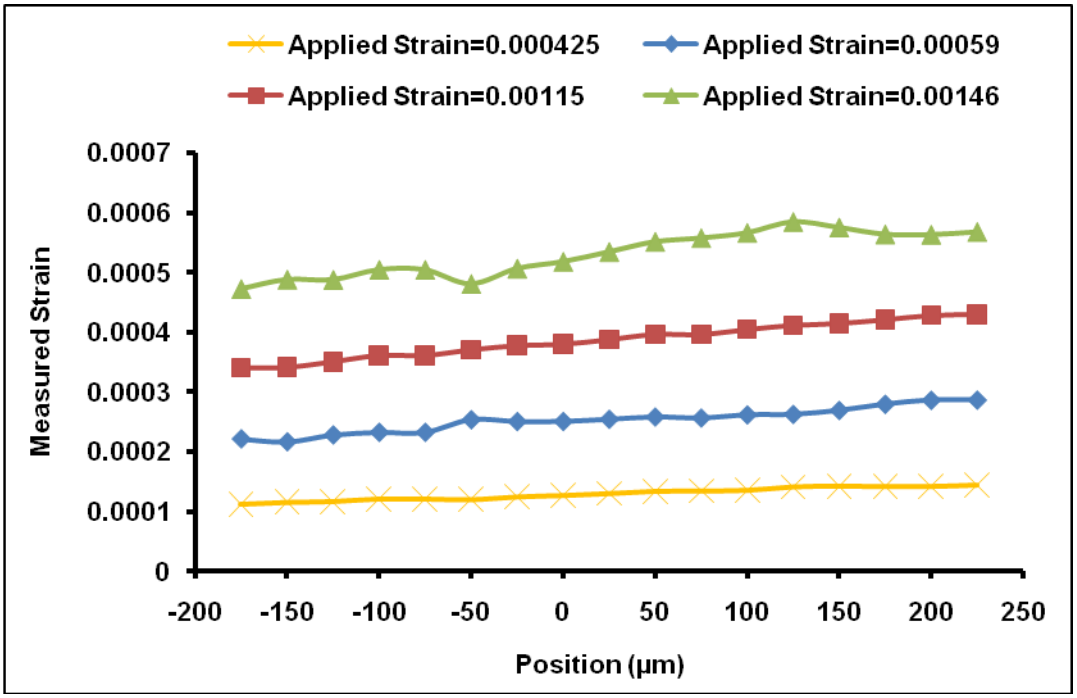

a) X-direction

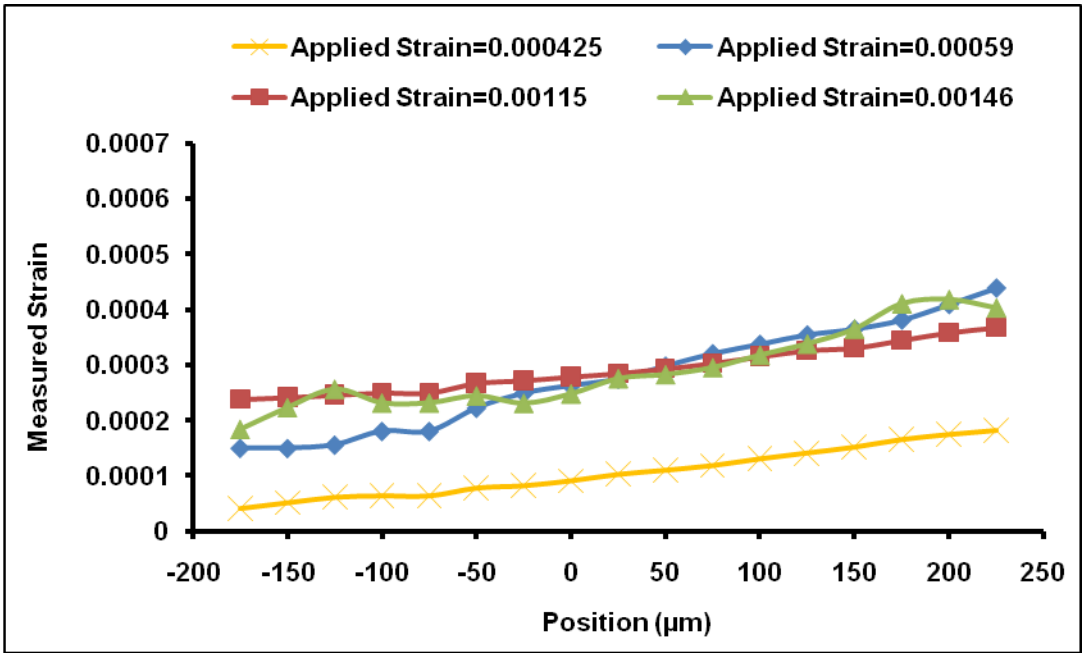

b) Y-direction

Figure 4-24: The relationship between the digital image correlation strain (i.e. the strain was measured from the relative displacement) as a function of the distance at different line position across the image and also, at different applied strains a) ε_{xx} and b) ε_{yy}. Interrogation window size was 128×128 pixels and overlap was 50%.

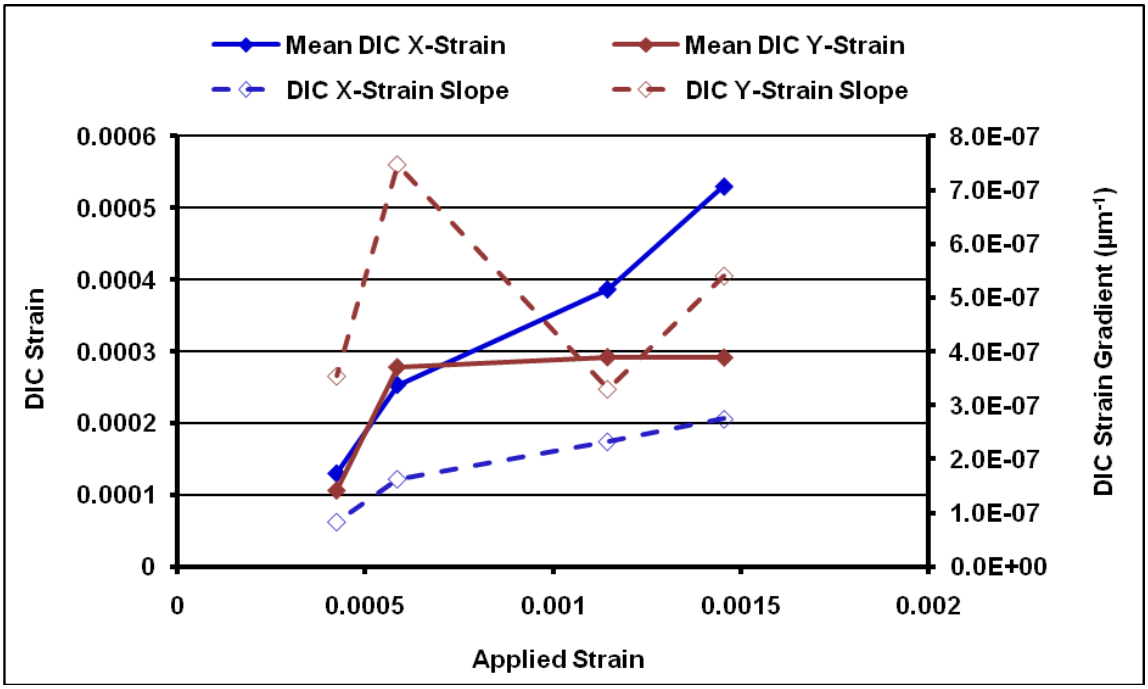

Figure 4-25: Shows the mean measured strain (Mean DIC strain) and DIC strain gradient at different positions as a function of the applied strain in the X and Y-directions. Interrogation window size was 128×128 pixels and overlap 50%. Mean DIC strain and slope show the strain which was measured from the relative displacement for whole viewed area at different line profile positions.

4.2.4.4 Variation of Strain across the Image

Figure 4-26 show the strain map using window size 128×128 pixels and overlap 50% and also, shows the line profile (white lines as shown in same Figure) at different positions at applied strain 0.00145. After processing using the Davis Batch process the deformation field underwent further processing to obtain the strain field in X and Y-direction, which is shown in Figure 4-26 and the colour bar for both X and Y-directions was from zero to maximum. The variation of strain along the series of lines is shown in Figure 4-27 and they show that the strain in X-direction increases towards the centre of the sample, whereas the strain in the Y-direction shows no pattern. The analysis was done at an applied strain of 0.00145.

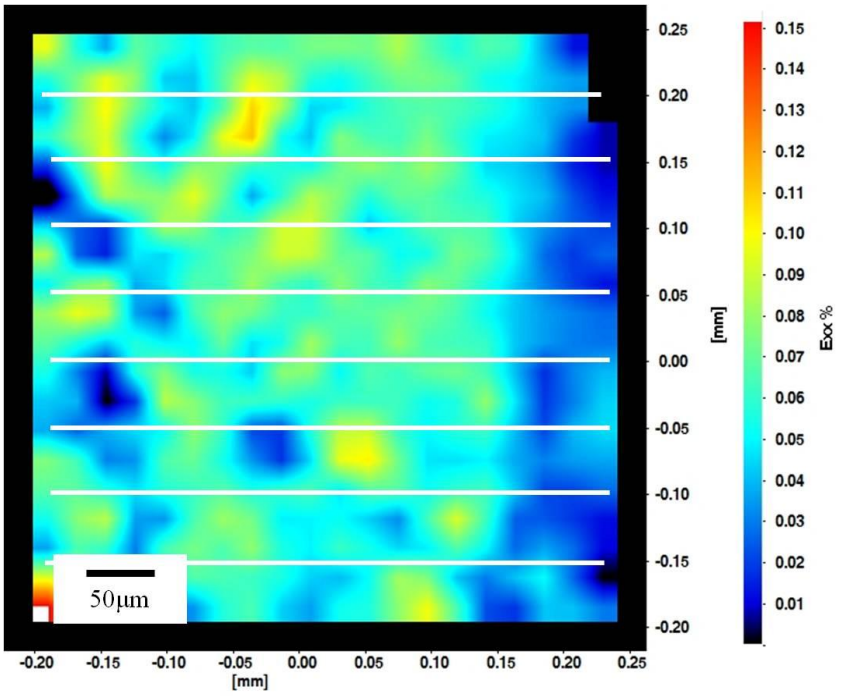

a) X-direction

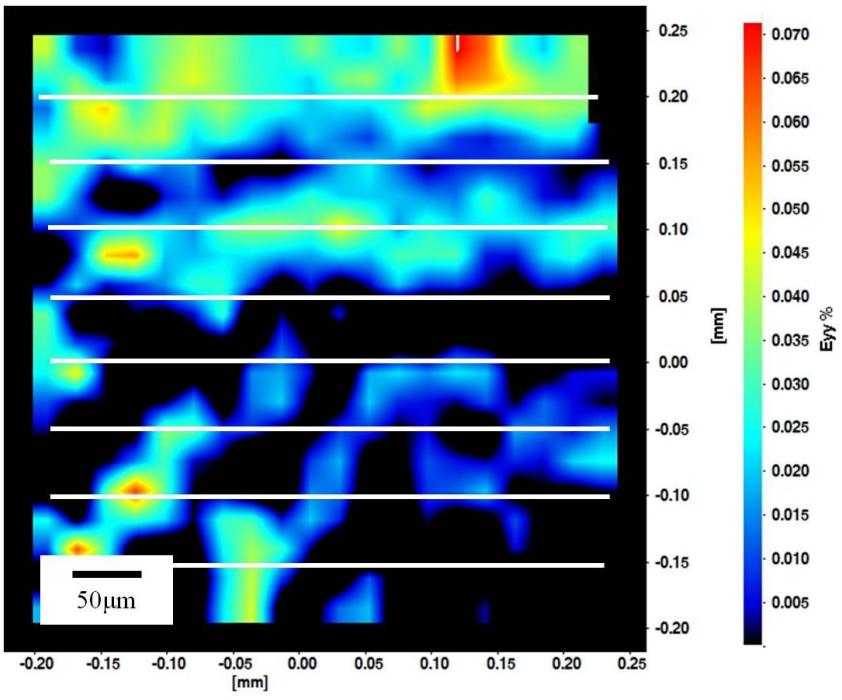

b) Y-direction

Figure 4-26: Shows the strain map and also, the line profile across the viewed area at different positions at applied strain 0.00145 for the glass specimen at a) ε_{xx}, and b) ε_{yy}. Interrogation window size used was 128×128 pixels and overlap 50%. The white lines describe the line profile using DIC (i.e. the location for measuring the strain).

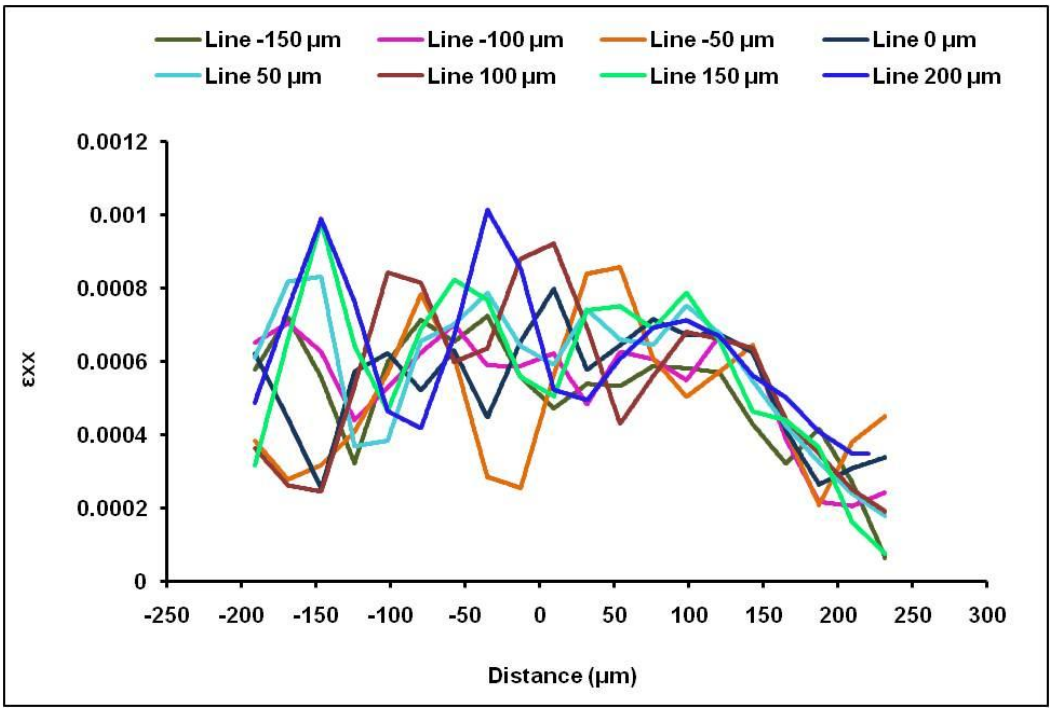

a) X-direction

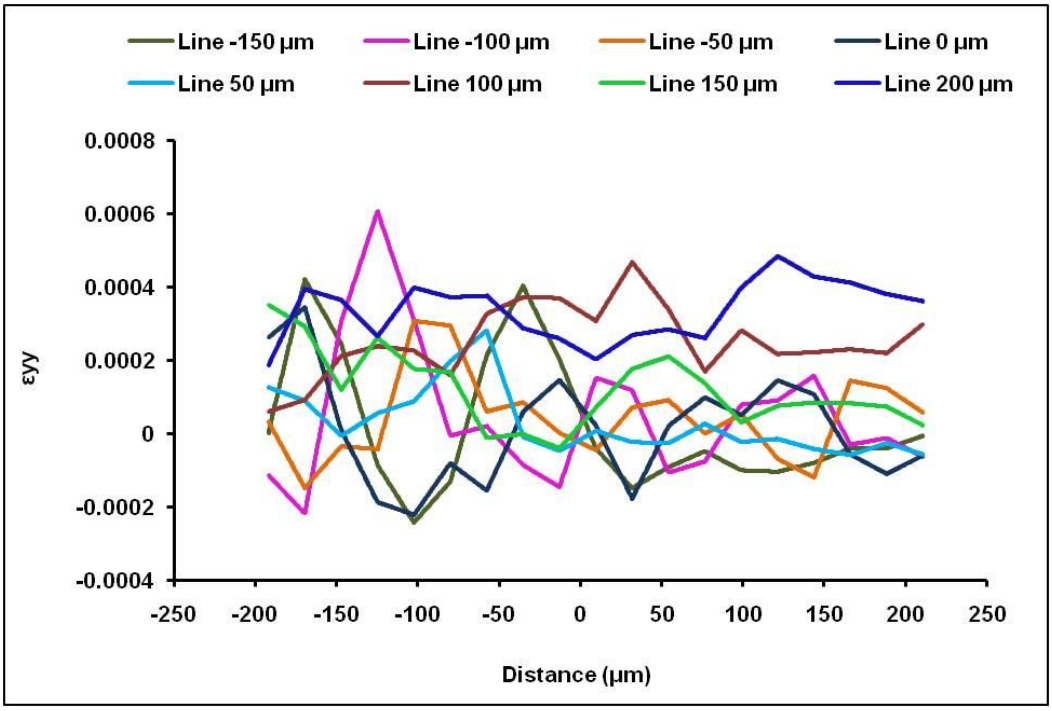

b) Y-direction

Figure 4-27: Shows the digital image correlation strain at different line positions across the analysed area as a function of the distance from the left of the viewed area for a) ε_{xx} (strain at X-direction), and b) ε_{yy} (strain at Y-direction). Interrogation window size was 128×128 pixels and overlap 50% at an applied strain of 0.00145.

4.2.4.5 Comparing the applied strain using FEM and strain gauge outputs

The purpose of this experiment was to test the agreement between the strain gauge outputs and strain predicted by the finite element model (see section 3.3.2.5). The applied vertical displacement (micrometer increments) was used to calculate the strain in the FE model. The results are shown in Figure 4-28. The error bar was obtained using the calibration data of the strain gauge. The agreement is quite good, with a difference between the gradients of 0.0934.

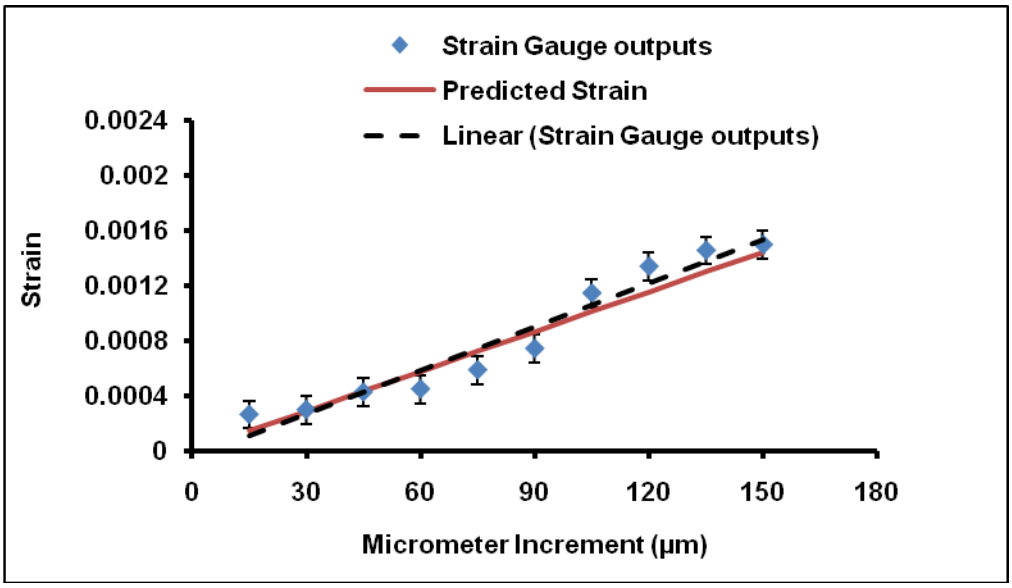

Figure 4-28: The relationship between the strain gauge outputs and the predicted strain (FEM strain) as a function of the micrometer displacement for the glass specimen.

4.2.5 The accuracy of DIC to measure bulk strain on the P-II specimen

Figure 4-29 shows the analysed area (viewed area) using DIC and also, shows the loading direction in the X-direction (the arrows on the viewed area show the loading direction). The interrogation window size used was 64×64 pixels and overlap 50% for measuring the DIC strain.

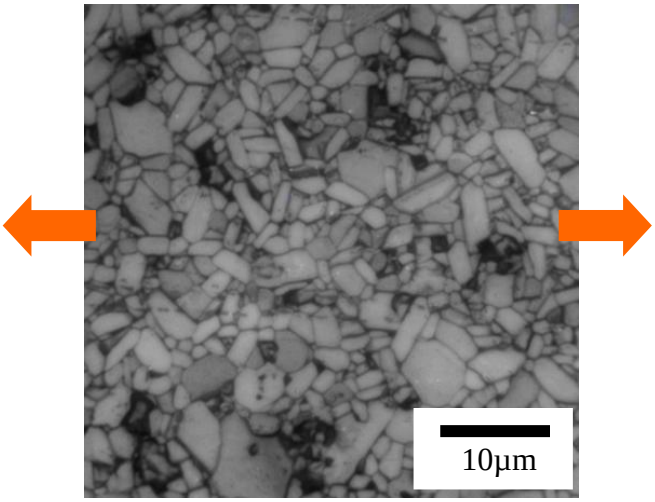

Figure 4-29: Shows the analysed area using digital image correlation and also, showing the loading direction in the X-direction for the P-II specimen.

The average strains in the X-direction (ε_{xx}) and Y-direction (ε_{yy}), with interrogation window size 64×64 pixels and overlap 50% are shown in Figure 4-30 as a function of the strain gauge output. The average strain was the digital image correlation mean strain values along a line through the centre of the viewed area with no cracks. The gradient of DIC mean X-strain and DIC mean Y-strain are about 0.815 and 0.467 respectively.

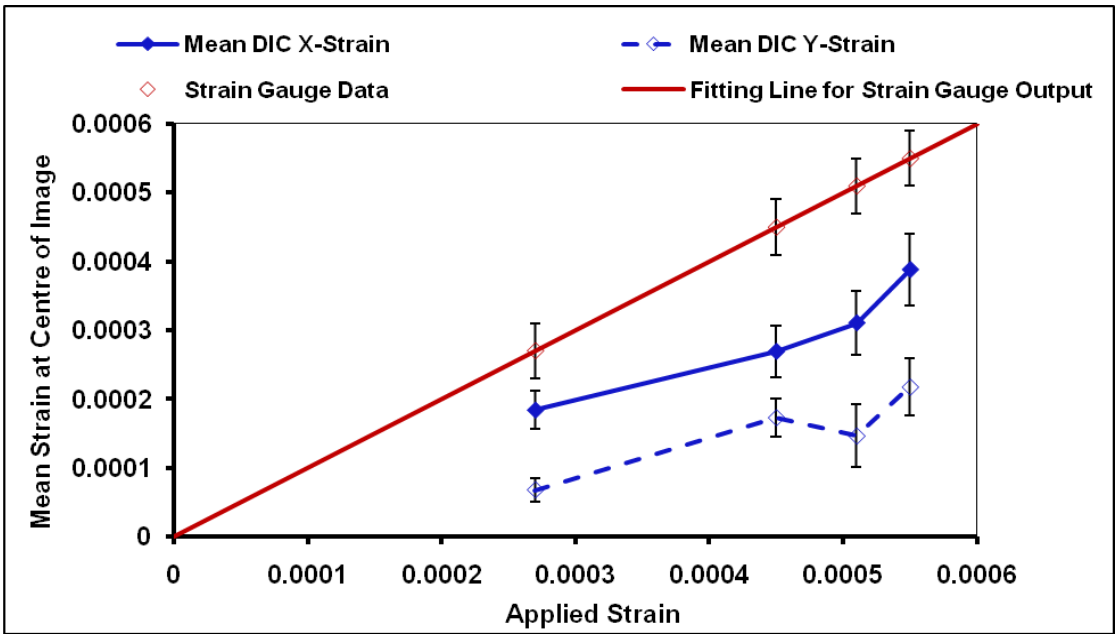

Figure 4-30: Shows the digital image correlation mean strain at the centre of the image (viewed area) at interrogation window size 64×64 pixels and overlap 50% against the applied strain for the P-II specimen. DIC mean strain is measured at the centre of the viewed area with no cracks.

4.2.5.1 Variation of Displacement across the image

As with the glass sample, the displacement varies across the image. For example, Figure 4-31 a and b shows the displacement maps in X and Y-directions at window size 64×64 pixels and overlap 50%. The line profile (white lines as shown in same Figure) was used at different positions of the viewed area and at applied strain 0.00027, as measured by the strain gauge).

The displacement plots at different line positions and applied strain and then the average digital image correlation strain across the image was measured as before in the section (4.2.4.3). The DIC strain results for the X and Y-directions have been shown in Figure 4-32 a and b respectively. Figure 4-32 shows the X-strain increase with applied strain and also varies in a consistent way from one side of the specimen to the other and also, shows the DIC strain in X-direction was larger than the DIC strain in the Y-direction and Y- strain is almost constant. The average digital image correlation strain and DIC strain gradient were measured at different line positions across the viewed area as a function of the applied strain, as mentioned before and the results are shown (Figure 4-33).

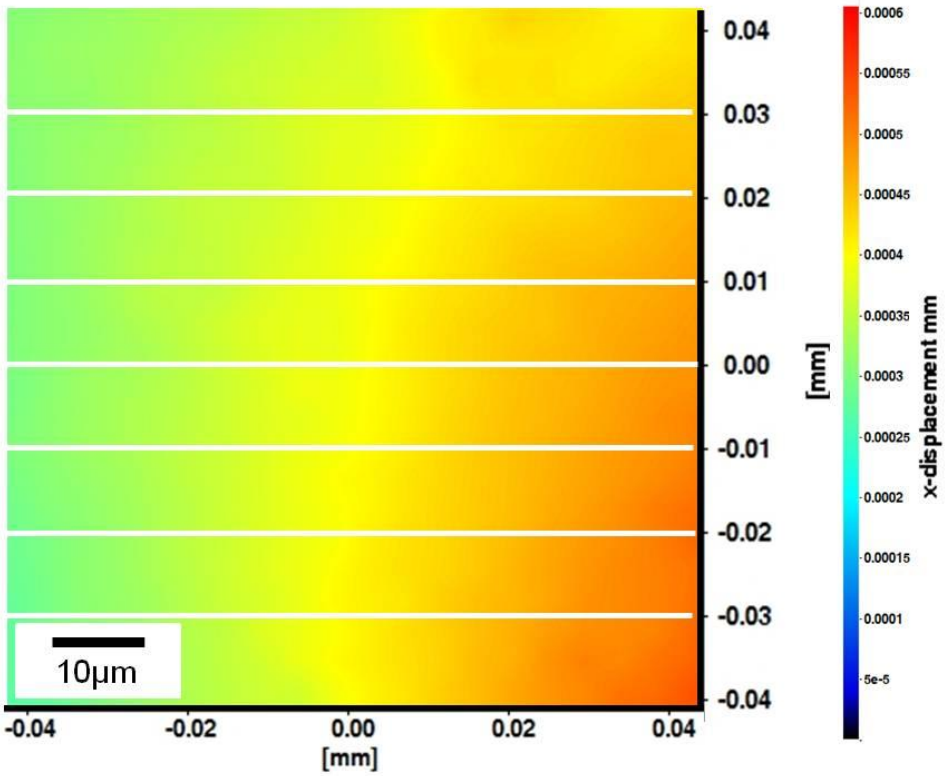

a) X-direction

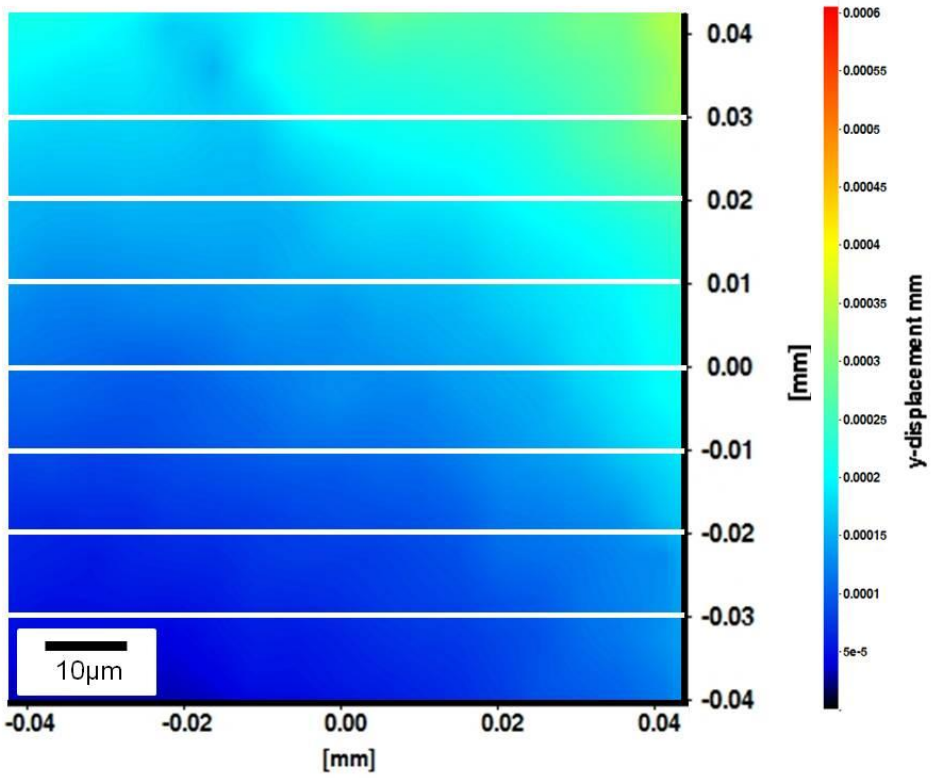

b) Y-direction

Figure 4-31: Shows the displacement map at interrogation window size 64×64 pixels and overlap 50%. It also shows the line profile across the viewed area at different positions and at applied strain of 0.00027 for the P-II specimen at a) X-displacement, and b) Y-displacement. The white lines describe the line profile using DIC (i.e. the location for measuring the displacement).

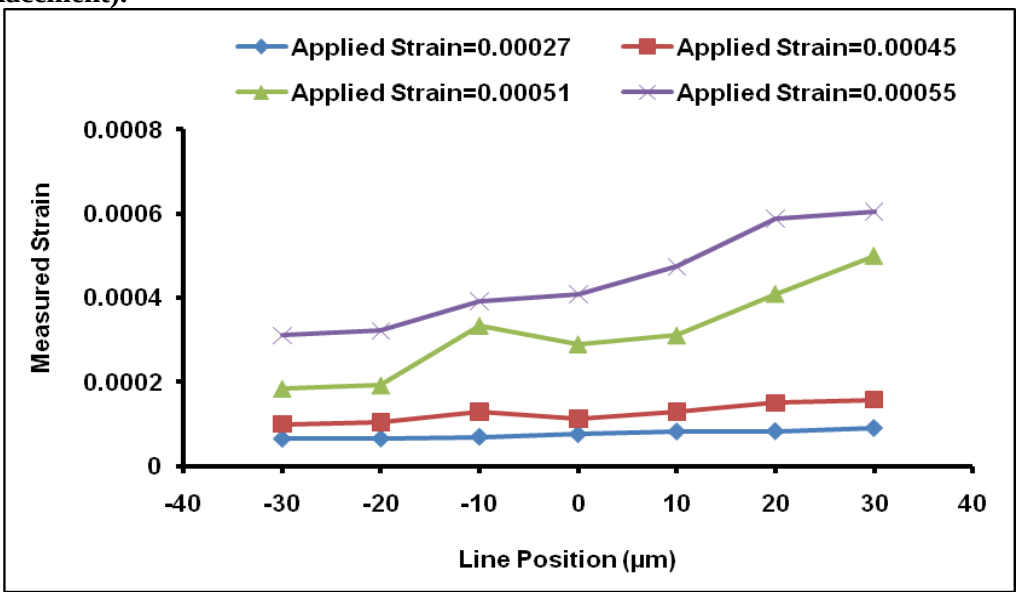

a) X-direction

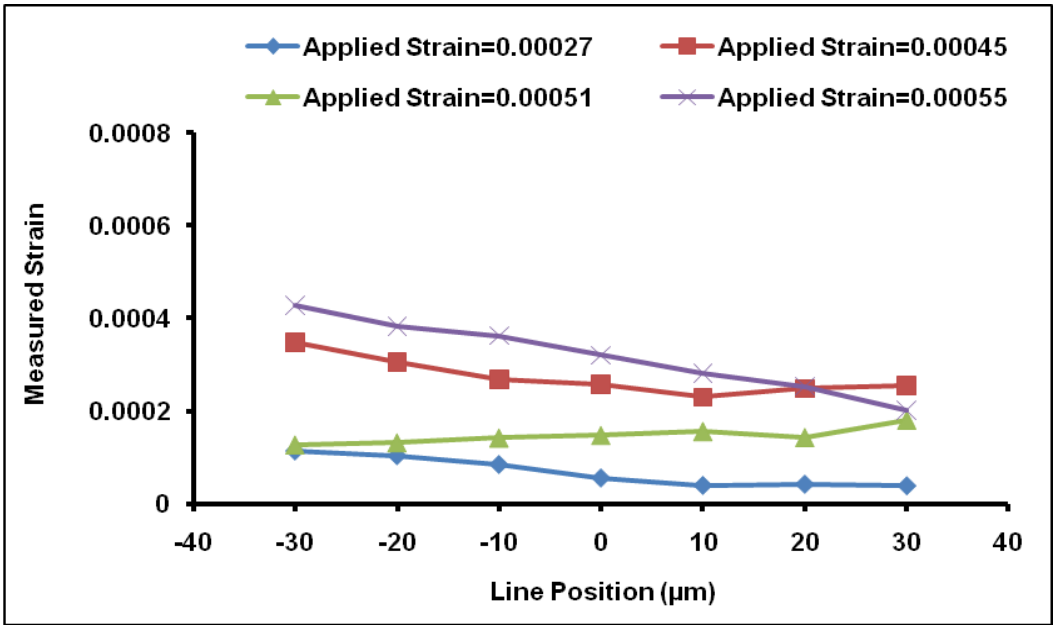

b) Y-direction

Figure 4-32: The relationship between the digital image correlation strain (i.e. the strain was measured from the relative displacement) as a function of the position at different line positions across the image and at different applied strains a) ε_{xx} and b) ε_{yy}. Interrogation window size was 64×64 pixels and overlap 50%.

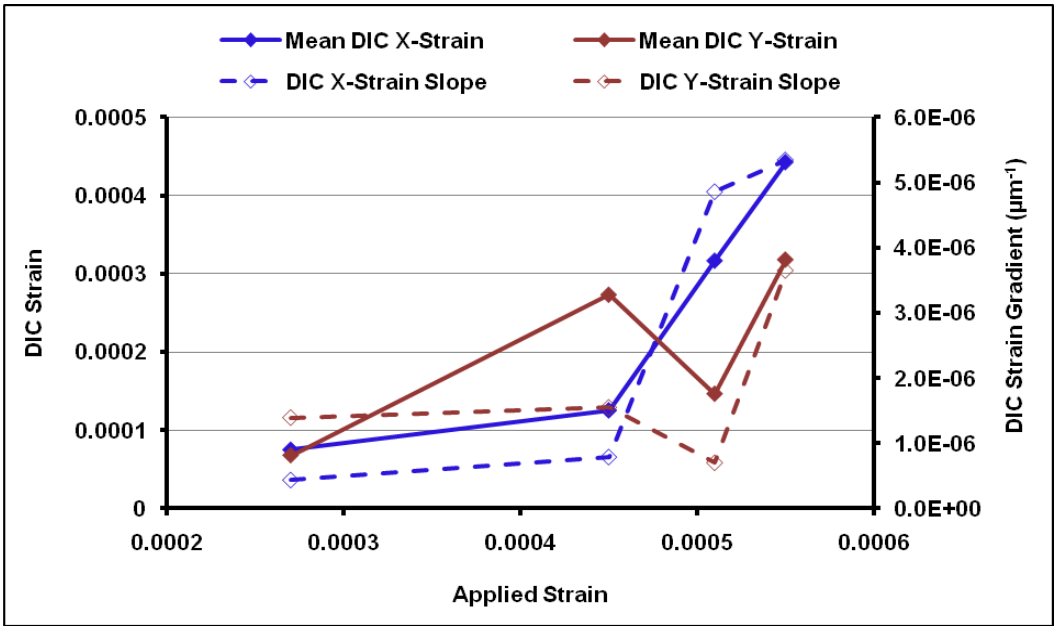

Figure 4-33: Shows the mean measured strain (Mean DIC strain) and DIC strain gradient at different positions as a function of the applied strain in the X and Y-directions. Interrogation window size was 64×64 pixel and overlap 50%. Mean DIC strain and slope show the strain which was measured from the relative displacement for whole viewed area at different line profile positions.

4.2.5.2 Variation of Strain across the Image

Figure 4-34 show the strain map using a window size of 64×64 pixels and overlap of 50% also showing the line profile (white lines as shown in same Figure) at different positions at an applied strain of 0.00027. The digital image correlation strain was measured at different line positions across the analysed area. The results for the variation of strain across the image are shown in Figure 4-35. They show that the strain the in X-direction increases towards the centre of the sample, whereas the strain in the Y-direction shows no pattern.

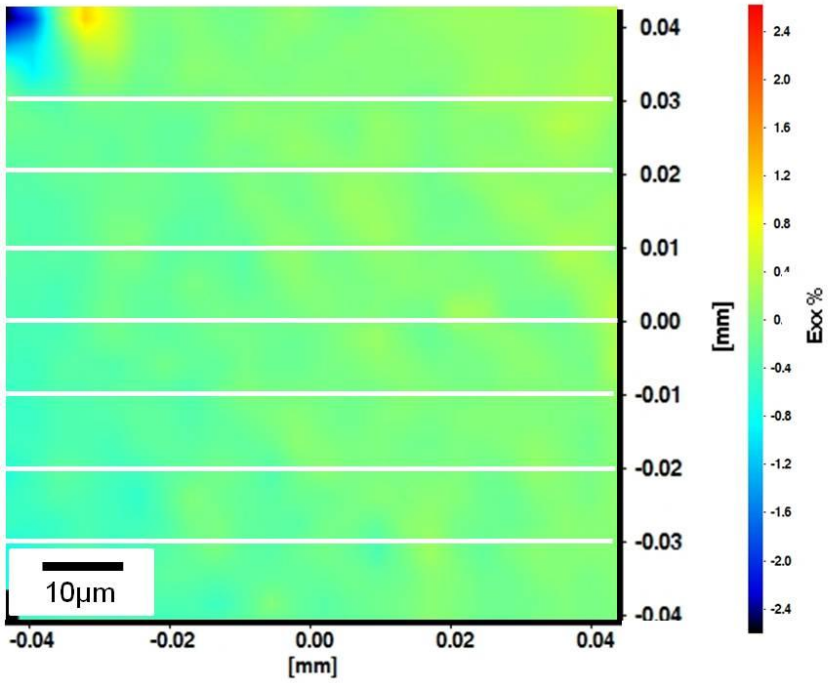

a) X-direction

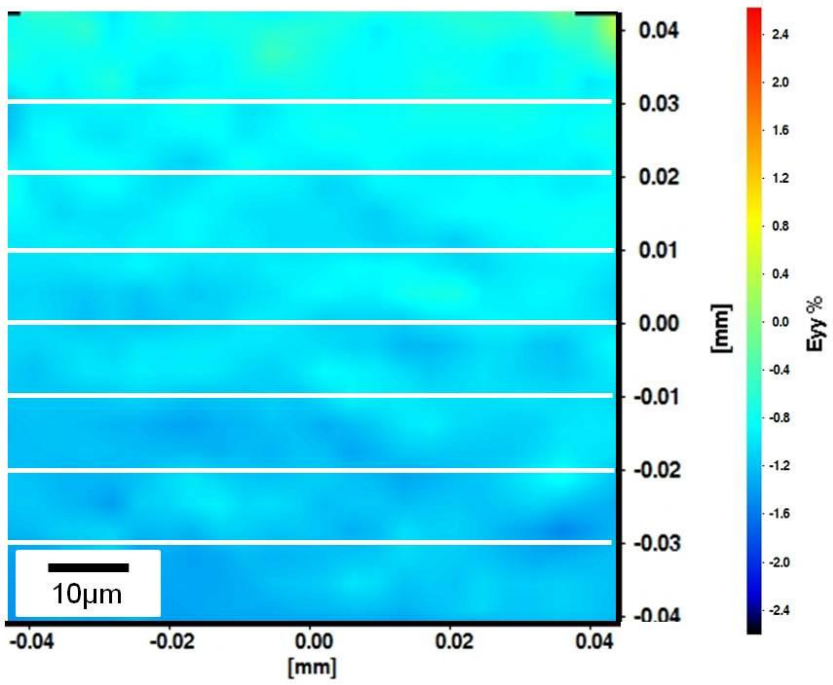

b) Y-direction

Figure 4-34: Shows the strain map and the line profile across the viewed area at different positions at an applied strain of (0.00027) for the P-II specimen at a) ε_{xx}, and b) ε_{yy}. Interrogation window size was 64×64 pixels and overlap was 50%. The white lines describe the line profile using DIC (i.e. the location for measuring the strain).

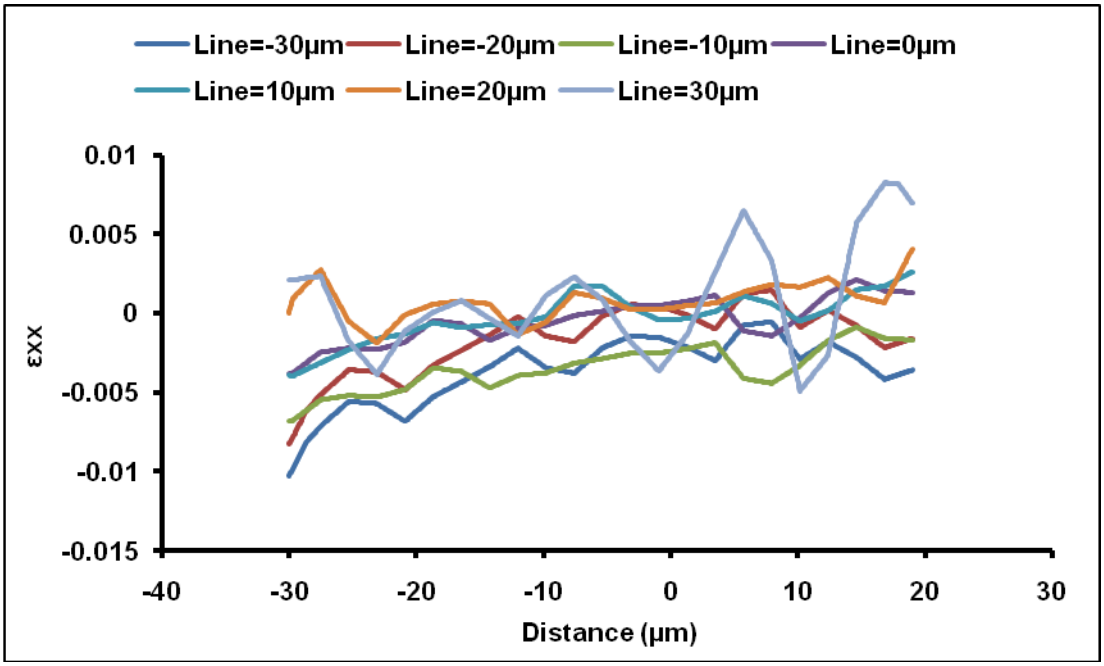

a) X-direction

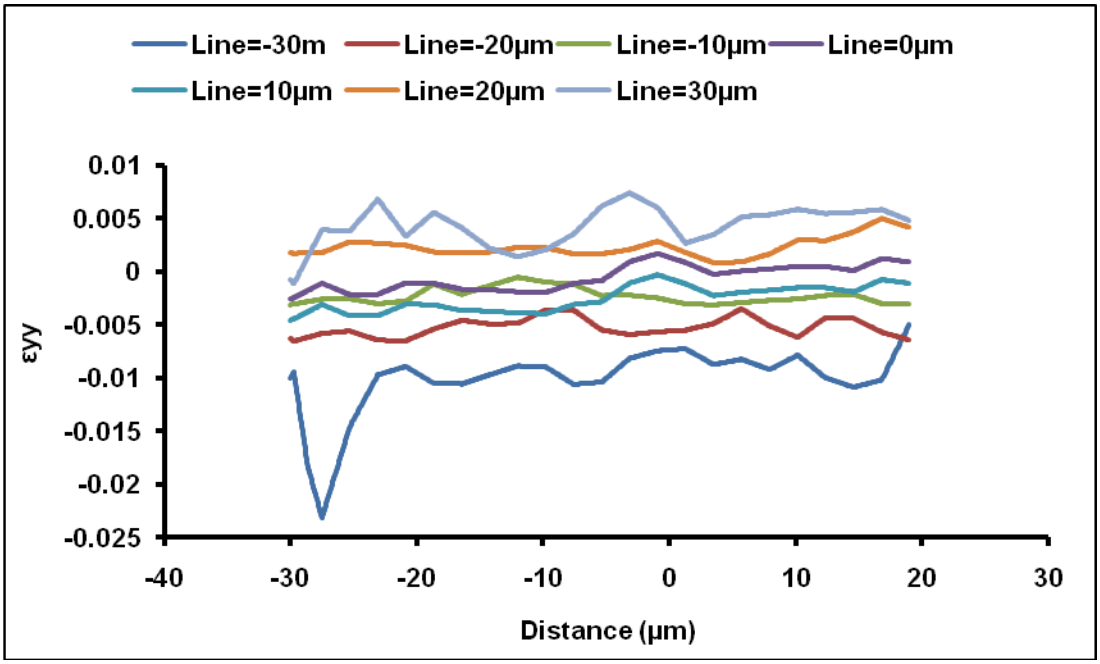

b) Y-direction

Figure 4-35: Shows the digital image correlation strain at different line positions across the analysed region against the distance from the left of the viewed area for a) ε_{xx} (strain in the X-direction), and b) ε_{yy} (strain in the Y-direction). Interrogation window size was 64×64 pixels and overlap 50% at applied strain (0.00027).

4.2.6 The accuracy of DIC to measure bulk strain on the Cr-II specimen

Figure 4-36 shows the analysed area (viewed area) using DIC and also, shows the loading in the (X-axis) (the arrows on the Figure show the loading direction). The interrogation window size used was 128×128 pixels and overlap 50% for measuring the DIC strain.

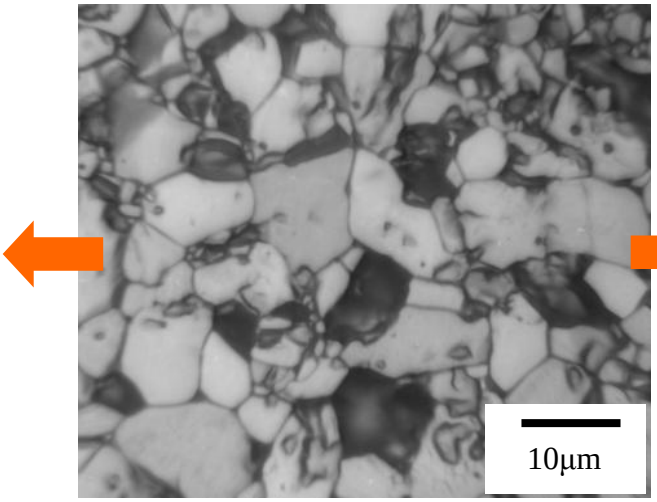

Figure 4-36: Shows the analysed area using digital image correlation and also, showing the loading direction in the X-direction for the Cr-II specimen.

The average strains in the X-direction (ε_{xx}) and Y-direction (ε_{yy}) obtained as before for the P-II sample are shown in Figure 4-37 as a function of the strain gauge output. The gradient of DIC mean X-strain and DIC mean Y-strain are about 0.682 and 0.156 respectively.

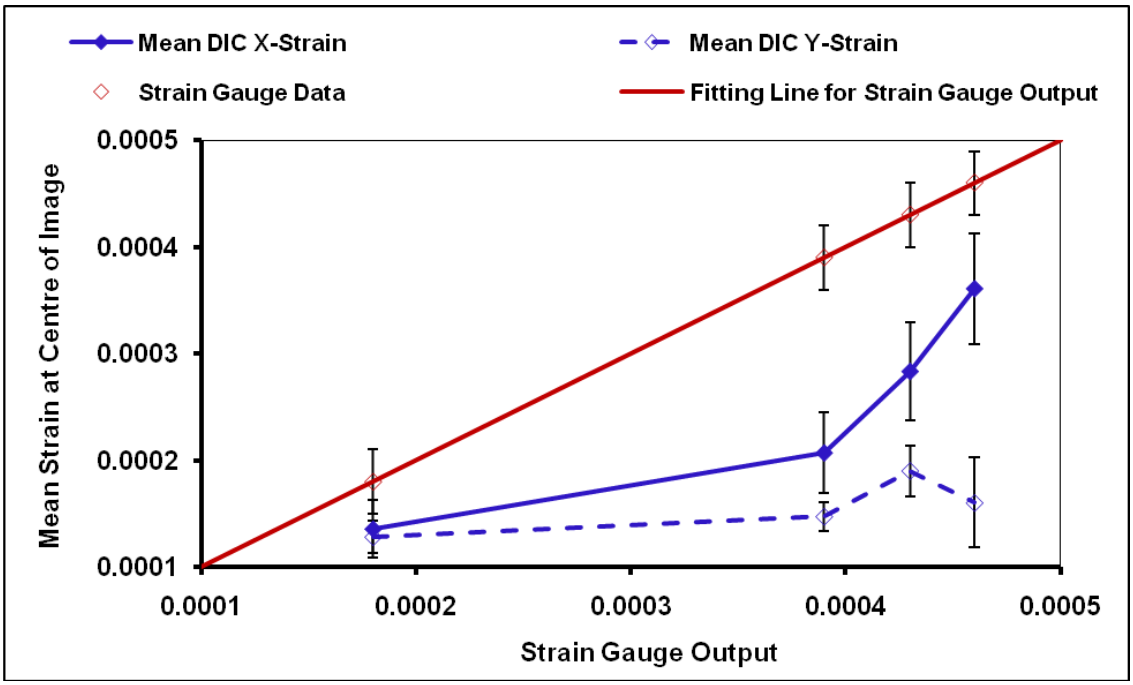

Figure 4-37: Shows the mean strain at the centre of the image (viewed area) at interrogation window size 128×128 pixels and overlap 50% as a function of the applied strain for the Cr-II specimen. DIC mean strain is measured at the centre of the viewed area with no cracks.

4.2.6.1 Variation of Displacement across the image

Figure 4-38 a and b shows the displacement maps in the X and Y-directions at window size 128×128 pixels and overlap 50%. The line profile (white lines as shown in same Figure) was used at different positions within the viewed area and at applied strain of 0.00018 from strain gauge. The DIC strain results in the X and Y-directions obtained as mentioned before in section (4.2.4.3) are shown in Figure 4-39a, b respectively. Figure 4-39 shows the X-strain increases with applied strain and also varies in a consistent way from one side of the specimen to the other; it also shows DIC strain in X-direction was larger than DIC in Y-direction and Y-strain is low and almost constant. The variation of strain and strain gradient with applied strain are shown in Figure 4-40, obtained as mentioned early in section (4.2.5.1).

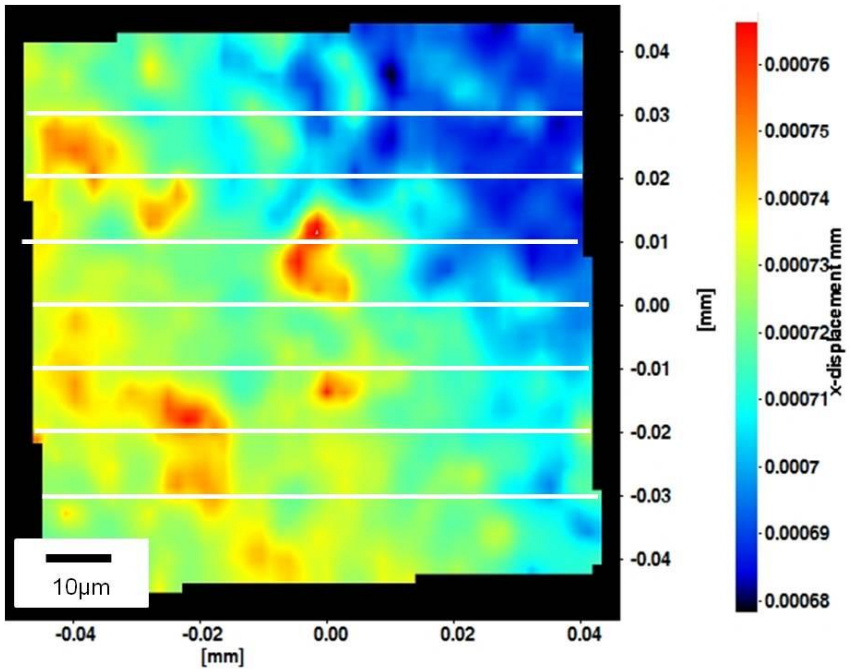

a) X-direction

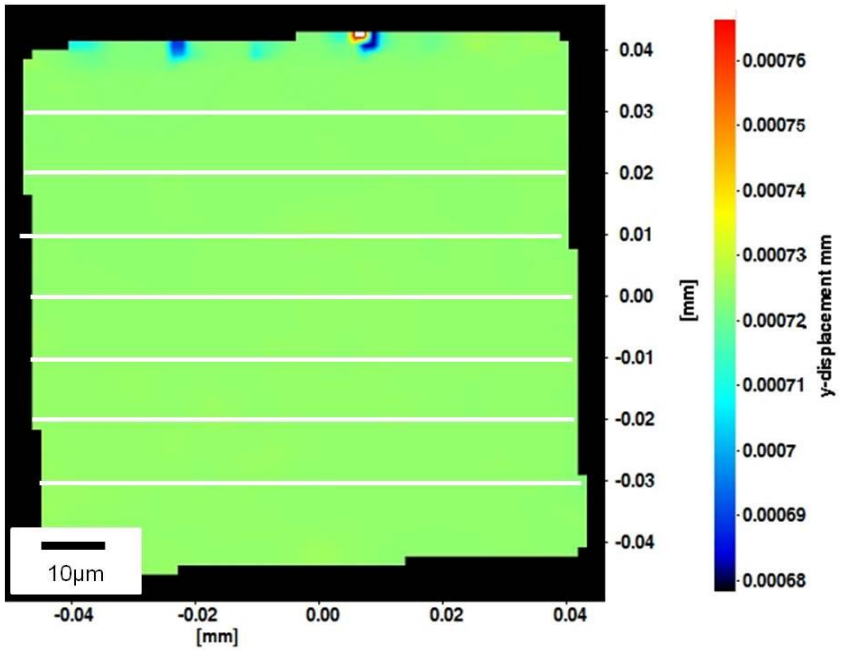

b) Y-direction

Figure 4-38: Shows the displacement map at interrogation window size 128×128 pixels and overlap 50%; the line profiles are also shown across the viewed area at different positions and at applied strain (0.00018) for the Cr-II specimen at a) X-displacement, and b) Y-displacement. The white lines describe the line profile using DIC (i.e. the location for measuring the displacement).

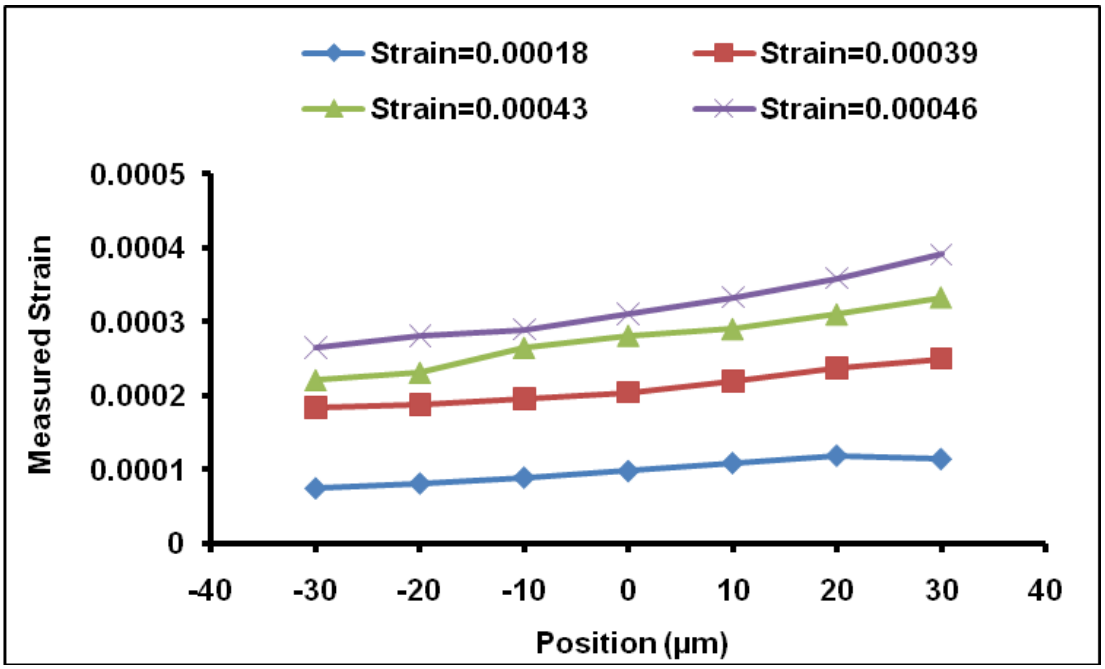

a) X-direction

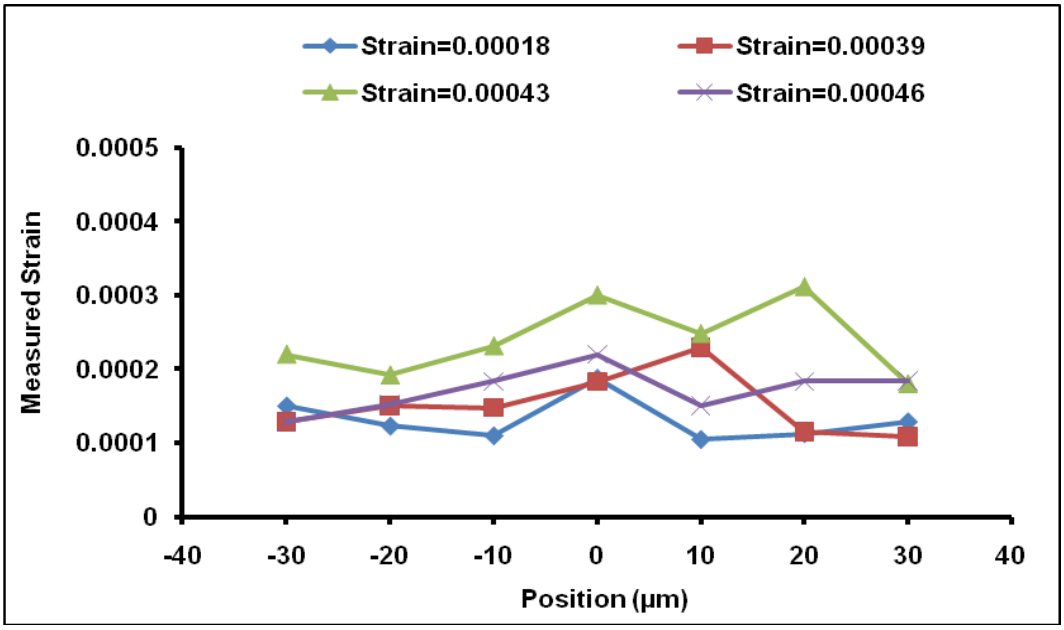

b) Y-direction

Figure 4-39: The relationship between the digital image correlation strain (i.e. the strain was measured from the relative displacement) as a function of the position at different line positions across the image and also, at different applied strains a) ε_{xx} and b) ε_{yy}. Interrogation window size was 128×128 pixels and overlap 50%.

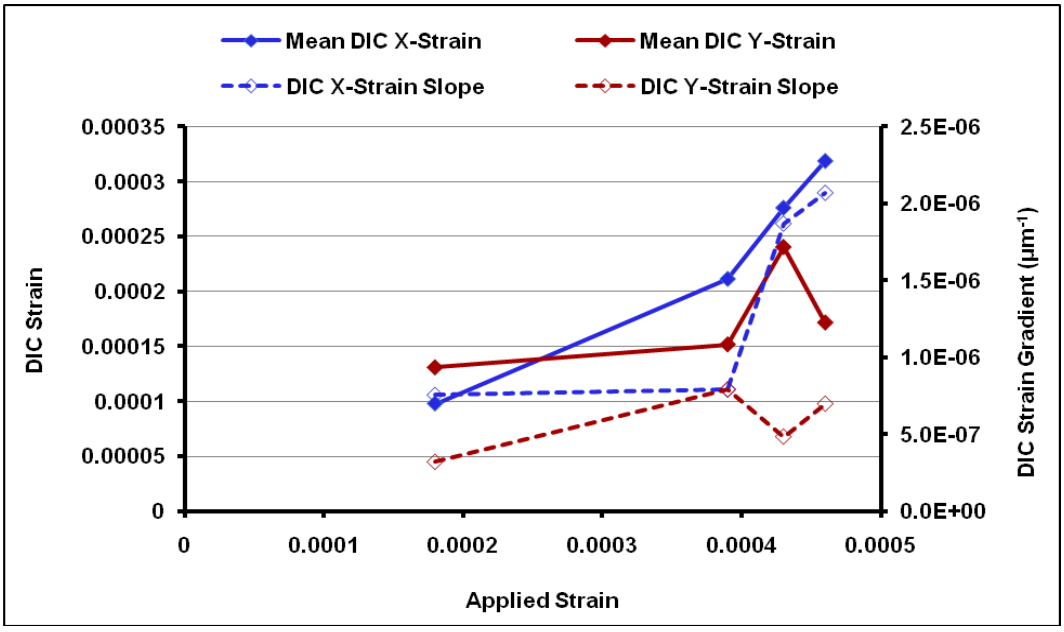

Figure 4-40: Shows the mean measured strain (Mean DIC strain) and DIC strain gradient at different positions as a function of the applied strain in the X and Y-direction. Interrogation window size was 128×128 pixels and overlap 50%. Mean DIC strain and slope show the strain which was measured from the relative displacement for whole viewed area at different line profile positions.

4.2.6.2 Variation of Strain across the Image

Figure 4-41 show the strain map at window size 128×128 pixels and overlap 50% and also, shows the line profile (white lines as shown in same Figure) at different positions at an applied strain of 0.00018. The digital image correlation strain was measured at different line position across the analysed area and also at the applied strain of 0.00018. The results have been shown in Figure 4-42. They show that the strain in X-direction increases towards the centre of the sample, whereas the strain in the Y-direction shows no pattern. The significant dip observed in Figure 4-42 b is due to the strain feature in Cr-II sample that was observed at the same location as the strain feature shown in Figure 4-41a.

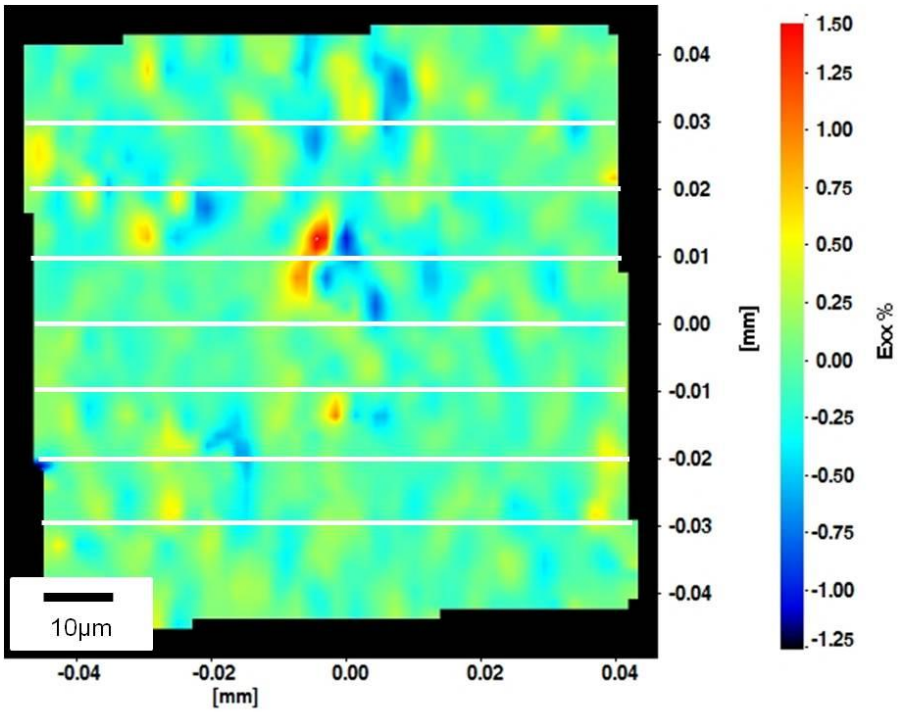

a) X-direction

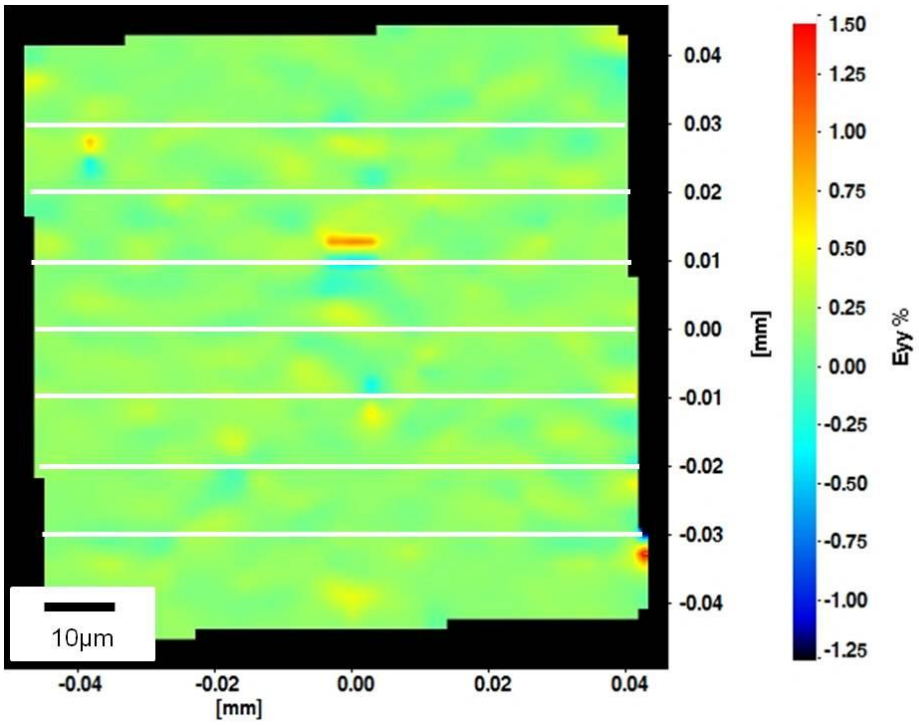

b) Y-direction

Figure 4-41: Shows the strain map and also, the line profile across the viewed area at different position at 0.00018 applied strain for the Cr-II specimen at a) ε_{xx}, and b) ε_{yy}. Interrogation window size was 128×128 pixels and overlap 50%. The white lines describe the line profile using DIC (i.e. the location for measuring the strain).

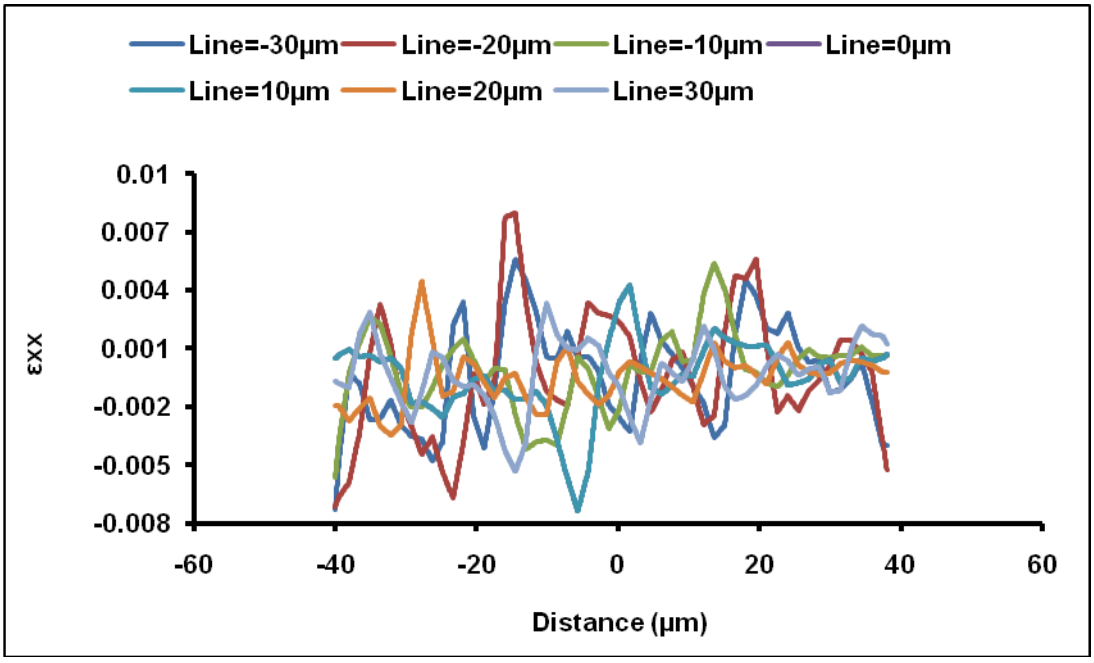

a) X-direction

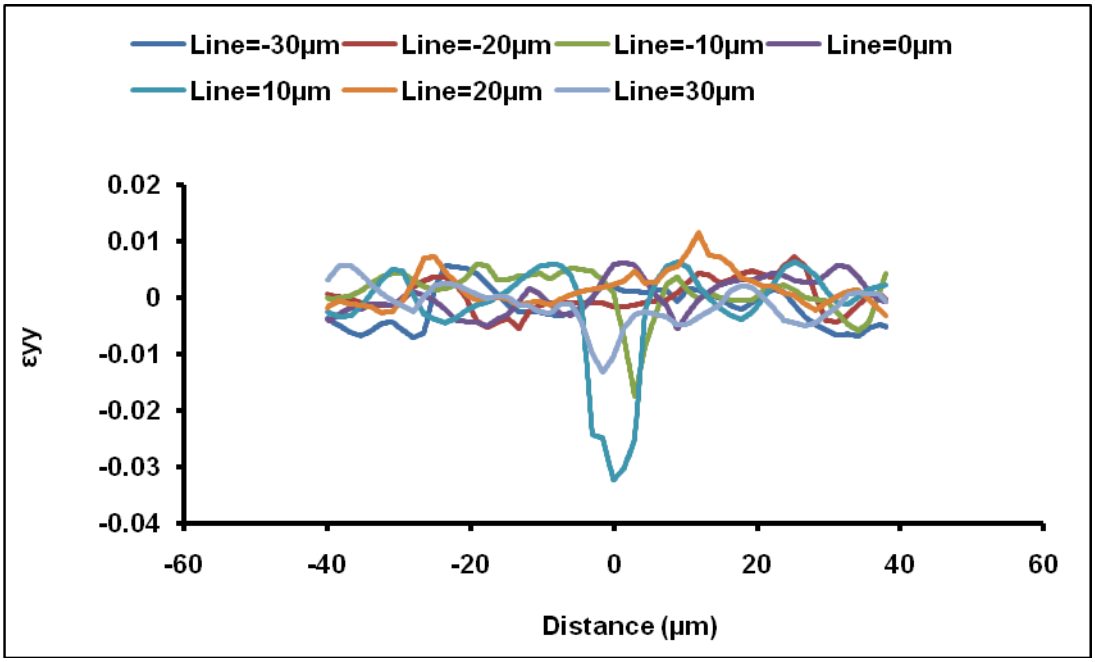

b) Y-direction

Figure 4-42: Shows the digital image correlation strain at different line positions across the analysed area against the distance from the left of the viewed area for a) ε_{xx} (strain in the X-direction), and b) ε_{yy} (strain in the Y-direction). Interrogation window size was 128×128 pixels and overlap 50% at an applied strain of 0.00018.

4.2.7 Using the Finite Element Model to assess the effects of DIC parameters on the measured surface crack opening displacement (SCOD) (glass specimen)

4.2.7.1 Predicting SCOD using the FEM

The aim of this model was to calculate whether the true surface crack opening displacement (SCOD) of a 40 µm long slot, with a depth of 11.64 µm, may be obtained from measurements at locations around it as shown in Figure 4-43. These measurements represent the same data were provided from experimentally by DIC.

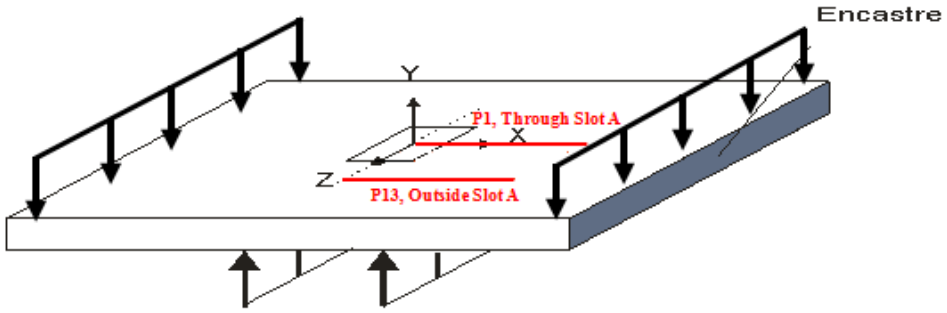

Figure 4-43: Shows the slot A location on the glass slide sample and the line profile for measuring the displacement across the slot A (i.e. P1) and the displacement away from slot A (i.e. P13). The loading direction shows by arrows.

The displacements along two paths (P1 and P13) were calculated using the finite element model on the RHS (i.e. right hand side) of the slot A. The displacement was measured at the location that goes through the slot A (i.e. P1) and also the displacement was measured at a location away from the slot A (i.e. P13) as a function of distance on each side of the slot A as shown in Figure 4-44. Figure 4-45 shows the results for the SCOD measured by the difference between the displacement in paths P13 and P1.

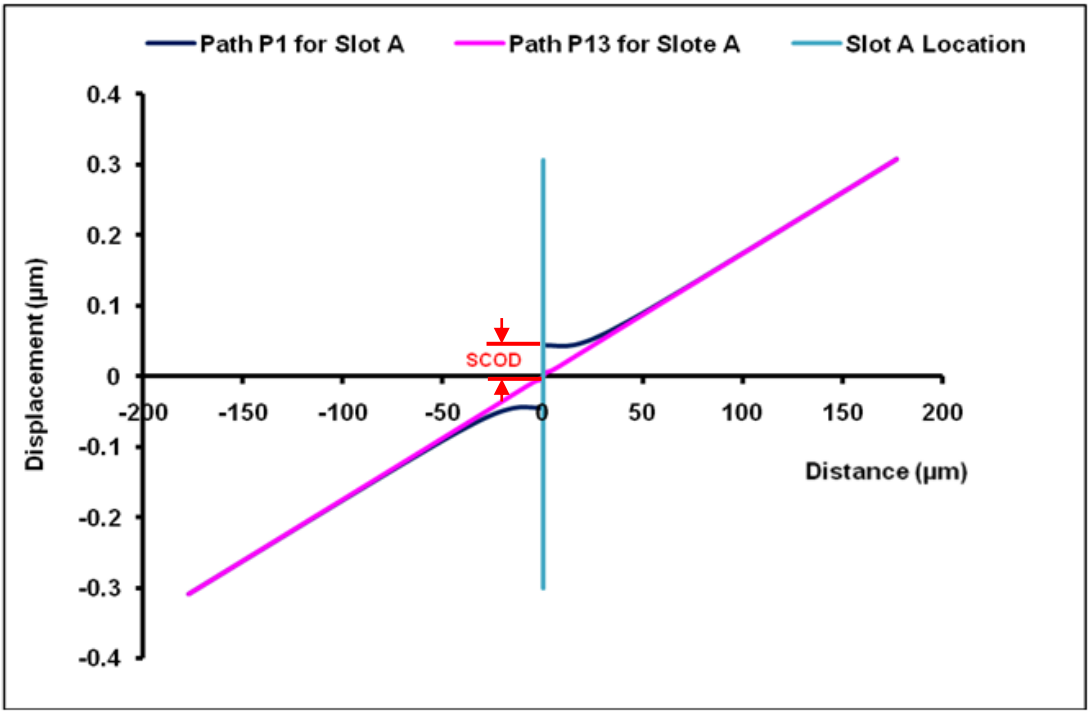

Figure 4-44: Shows the displacement through the slot A, P1 and also, the displacement remote of the slot A (outside the slot A, P13) as a function of the distance in X-axis as shown in Figure 4-43 at an applied strain of 0.00185.

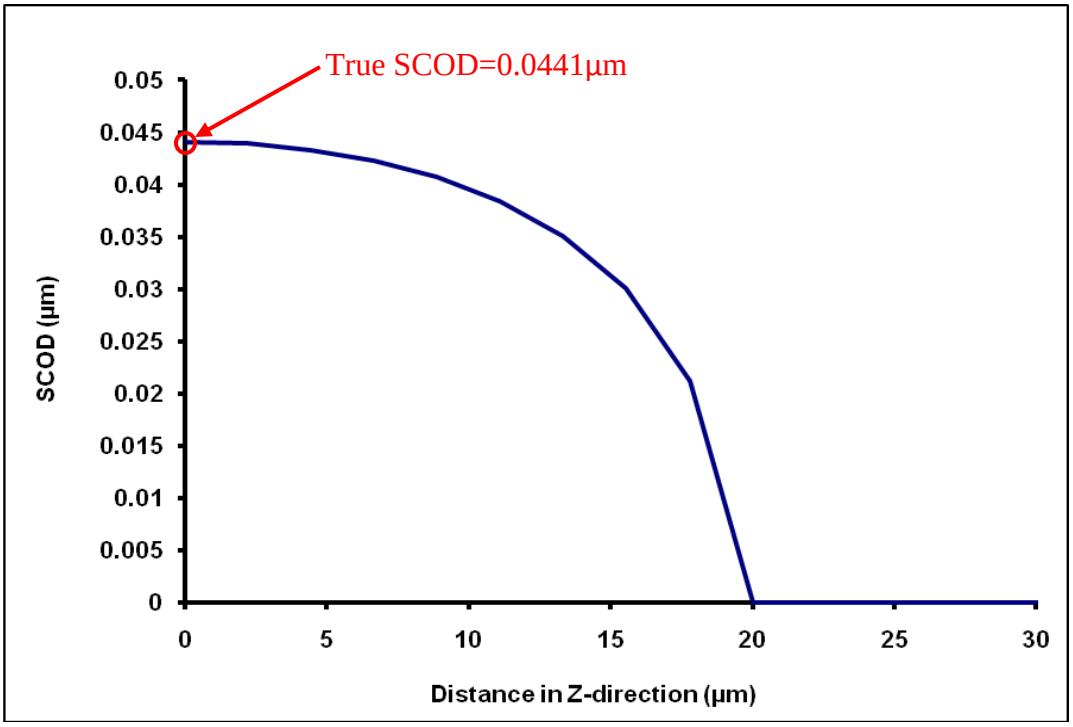

Figure 4-45: The maximum surface crack length (true surface crack opening displacement, SCOD) at the centre of a 11.64 µm deep slot as a function of the slot length at an applied strain of 0.00185, predicted using the FE model.

4.2.7.2 The effect of the Window Size on the measurement of Displacement Difference using FEM data

The aim of this experiment is to show how the measurement of surface crack opening displacement (SCOD) is affected by the window size employed in image correlation. The SCOD for the experimental data was affected by the overlapping of windows with the notch; it is expected to be least accurate when measurements are made close to the notch. As the window size increases, the effect of noise will be reduced, but the overlap at the notch will increase. To approximate this, the FE model data were averaged in groups that represent the effect of window size and a 0% overlap was used for the purpose of illustration. Strictly the Fourier transform analysis may not be identical to this but there was not sufficient time in the project to accurately assess the effect of window size on a simulated data set. Figure 4-46 shows that increasing the window size decreased the apparent opening displacements across the slot. The difference in displacement between paths through and remote to the slot is shown in Figure 4-47. The effect is summarised in

Figure 4-48 as the normalised surface crack opening displacement measurements from around the slot A (divide the measured SCOD by true SCOD). The normalised surface crack opening displacement was calculated using all the values within the window and also the displacement was calculated as an average where the window overlaps the notch at the origin location for slot A. The normalised SCOD was measured as a function of window size after the slot A offset was 16 pixel to the right hand side of slot A and the purpose from this offset is to observe of the effect of overlap window size with the slot A. This shows that increasing window size reduces the apparent opening displacement of the slot by up to 50% for a 128 ×128 window. The effect of shifting the position of the windows relative to the slot is small. For the typical image correlation window size of 64 × 64 pixels, the expected error is (0.02-0.05 pixel) while at 128 × 128 pixels it is (0.01-0.03 pixel) [67]. Note that the effect of image correlation noise has not been included.

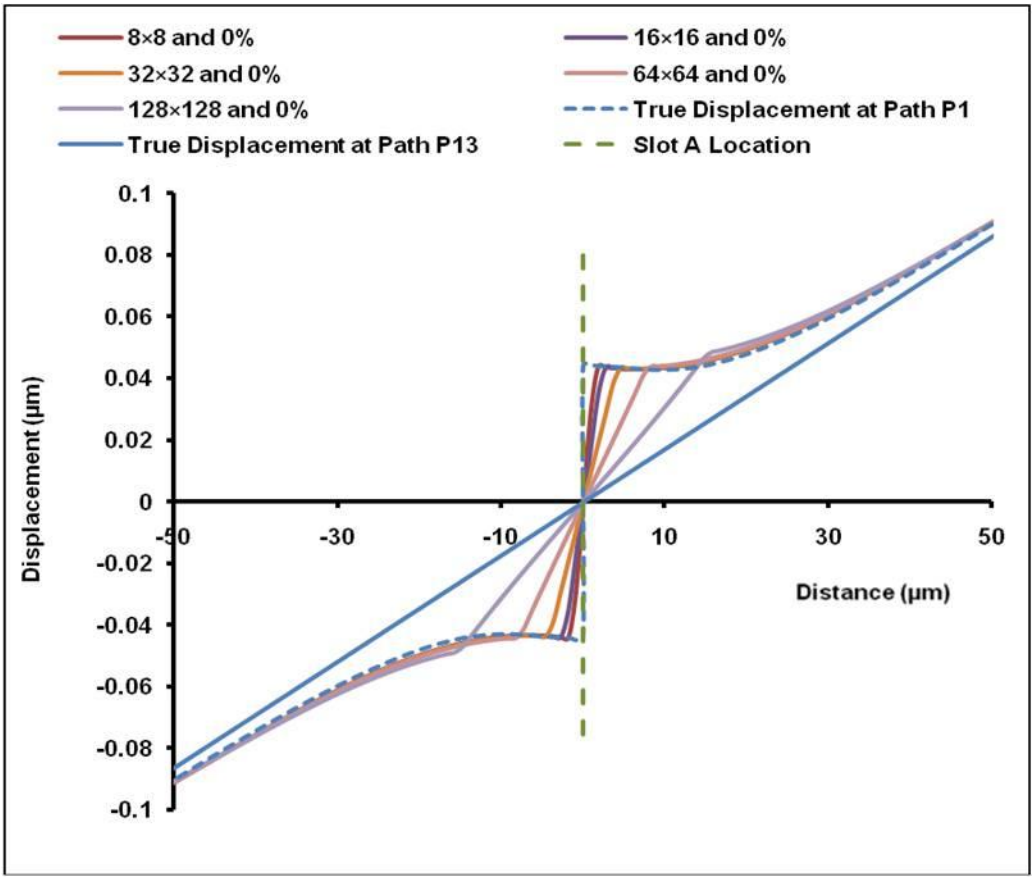

Figure 4-46: The relationship between the predicted displacement from FEM (i.e. true displacement) and measured displacements at different window sizes (i.e. measured displacement was determined using polynomial function) as a function of the distance on each side of the slot A at applied strain of 0.00185.

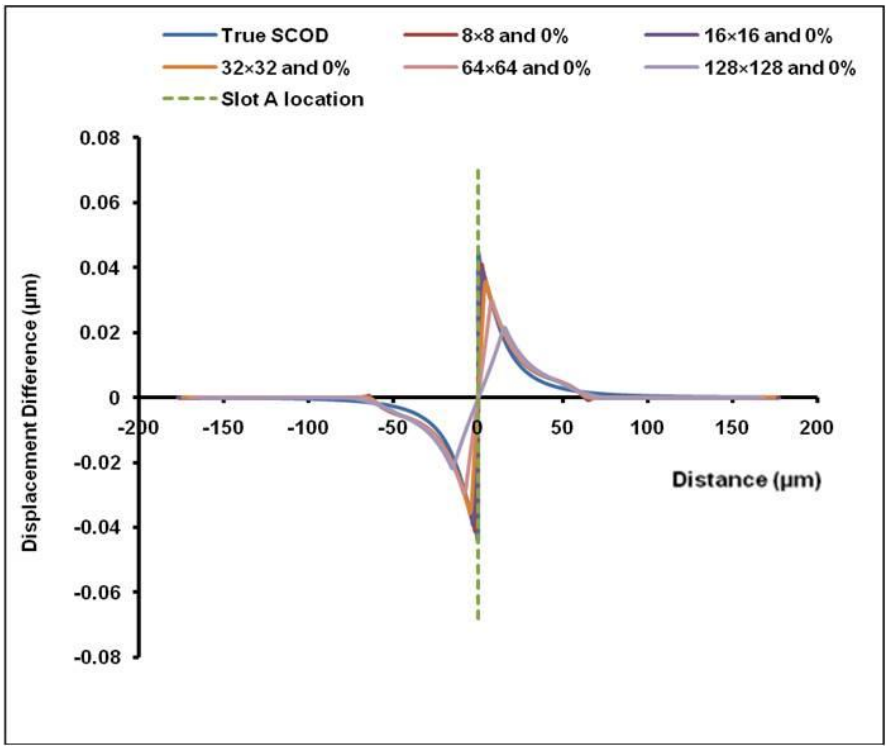

Figure 4-47: The difference between the displacement through (across) the slot A and the displacement remote to (outside) the slot A for the predicted displacement and measured displacement against the distance on each side of the slot A. Applied strain is (0.00185).

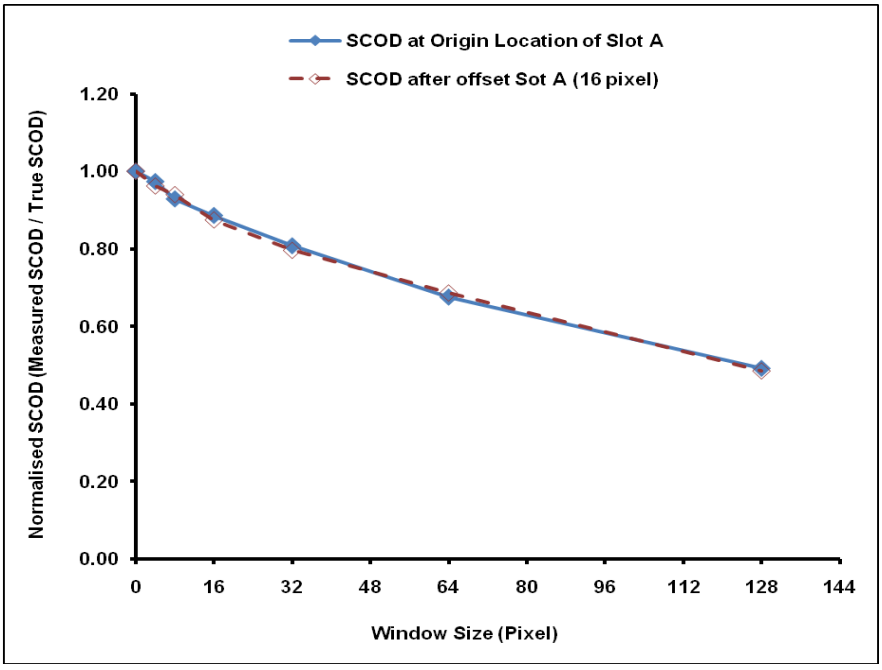

Figure 4-48: The relationship between the normalised surface crack opening displacement (measured SCOD / true SCOD) at the origin location of slot A and normalised SCOD after offset the slot A (16 pixels) against the window size. Applied strain is (0.00185).

4.2.8 Digital Image Correlation (DIC) for measuring surface crack opening displacement (SCOD) for the glass specimen

4.2.8.1 Strain Map for observation the strain features for the glass specimen

The normal strain in the X-direction can be obtained using strain map routines in LA Vision Davis. The optical micrograph for the glass sample, on which a strain map is superimposed, shows that peaks in strain can be associated with the slot's position, as shown in Figure 4-49. The applied strain is 0.00185. The stress axis was in the horizontal (X-direction). The strains associated with the features are of the order of 0.2%, and are large compared to the background strains, which were of the order of 0.08% (see Figure 4-49). The strain maps are useful for the visualisation and detection of defects, but quantitative analysis is best performing using the displacement data, as described in the next section.

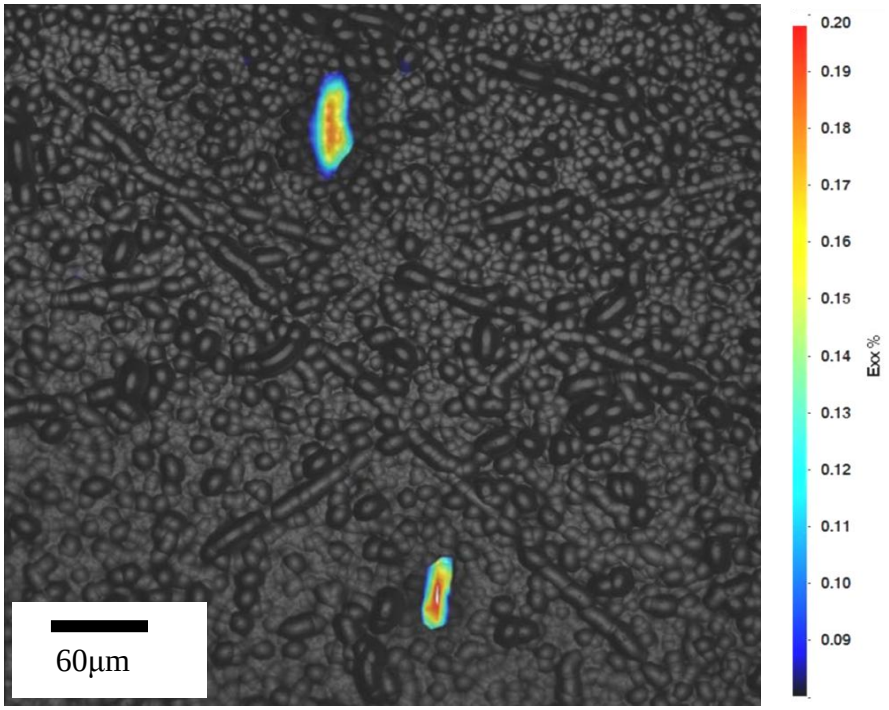

Figure 4-49: The strain features observed from the strain map using DIC overlay on the microstructure image for the glass sample using an interrogation window size 128×128 pixels and overlap 50%. Applied strain is (0.00185) and the threshold strain is 0.08%.

4.2.8.2 Measuring Displacement Difference using DIC

Surface displacements due to the applied load using four point bending test were measured for slot A and slot B on the glass slide by DIC analysis. An X-direction displacement map is overlaid on the optical image to show the locations of slot A and slot B at applied strain is (0.00185) as shown in Figure 4-50.

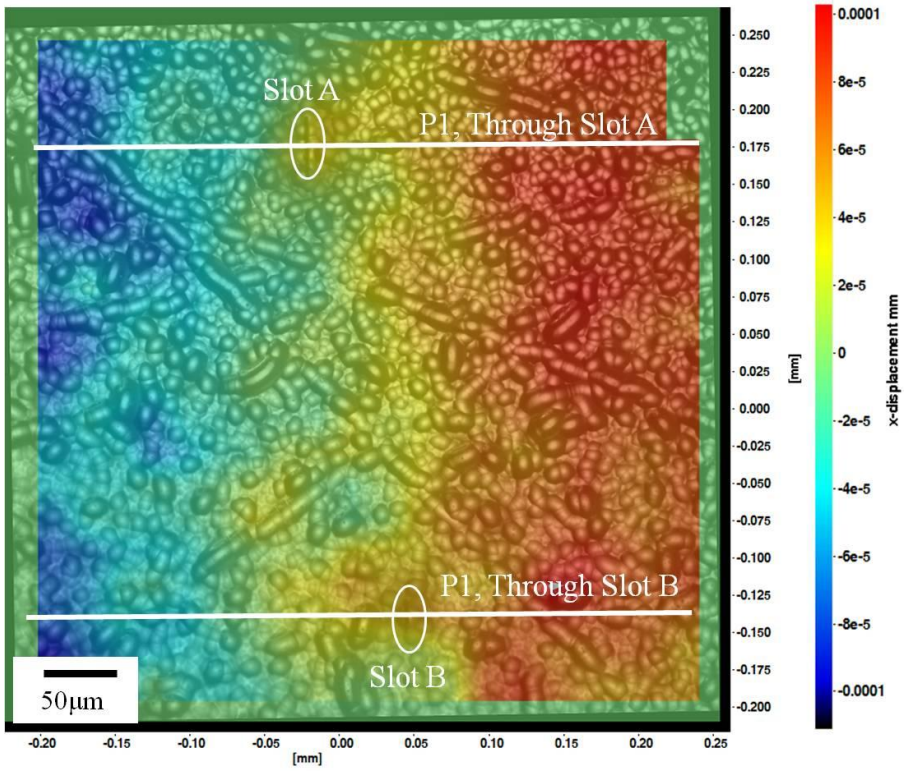

Figure 4-50: The displacement map from DIC overlaid on the optical image for the glass sample using a window size 128×128 pixels and overlap 50%. The applied strain is 0.00185. The slot's location was positioned on the same Figure using a white ellipse marker. The white lines show the line profile through slot A and slot B.

The displacement plots in the X-direction are measured using LA Vision Davis (line profile method) at the location through the slot A and slot B (i.e. P1) and the background trend (P13) (i.e. the displacement through these strain features was normalised using best fit line (i.e.P13) using function SLOPE and INTERCEPT and this method give line of best fit for a set of data point) were compared as shown in Figure 4-50. The displacement results were taken at a window size of 128×128 pixels and overlap 50%. The effects of applied strain (evaluated using the strain gauge) on the displacement are shown in Figure 4-51 and Figure 4-52.

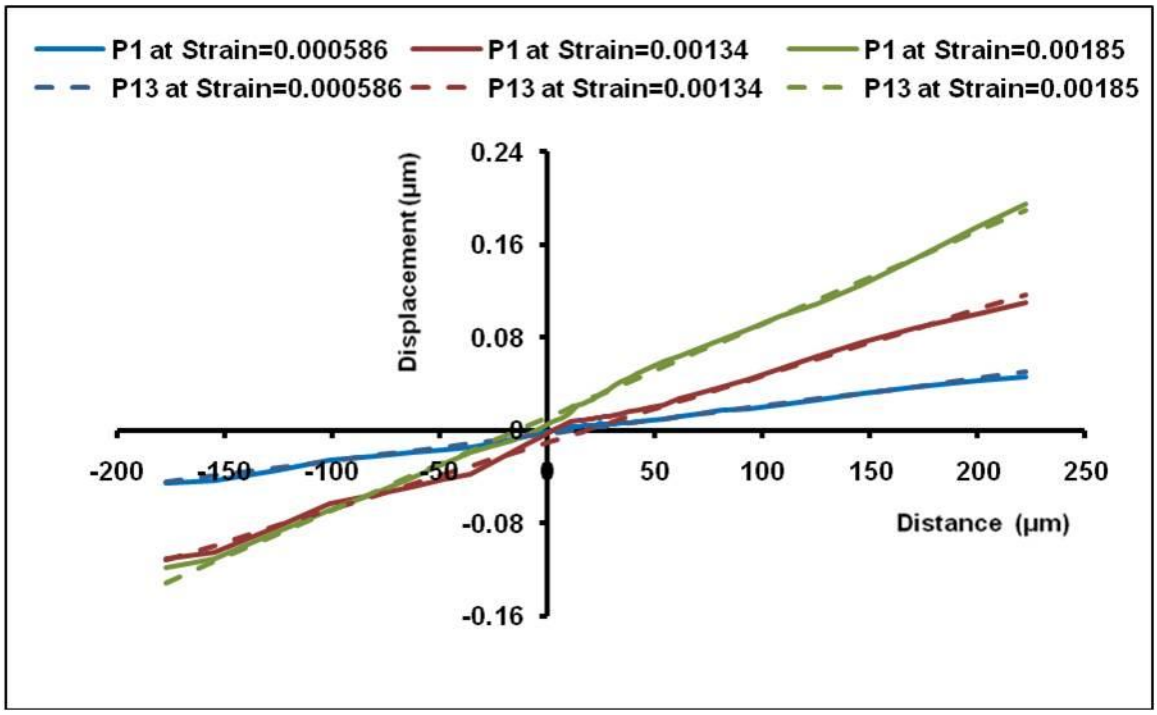

Figure 4-51: Shows the vector displacement against the distance from the left of the viewed area in the X-axis through the slot A (P1) and the fitted displacement through slot A (P13). Interrogation window size used was 128×128 pixels and overlap 50% for slot A.

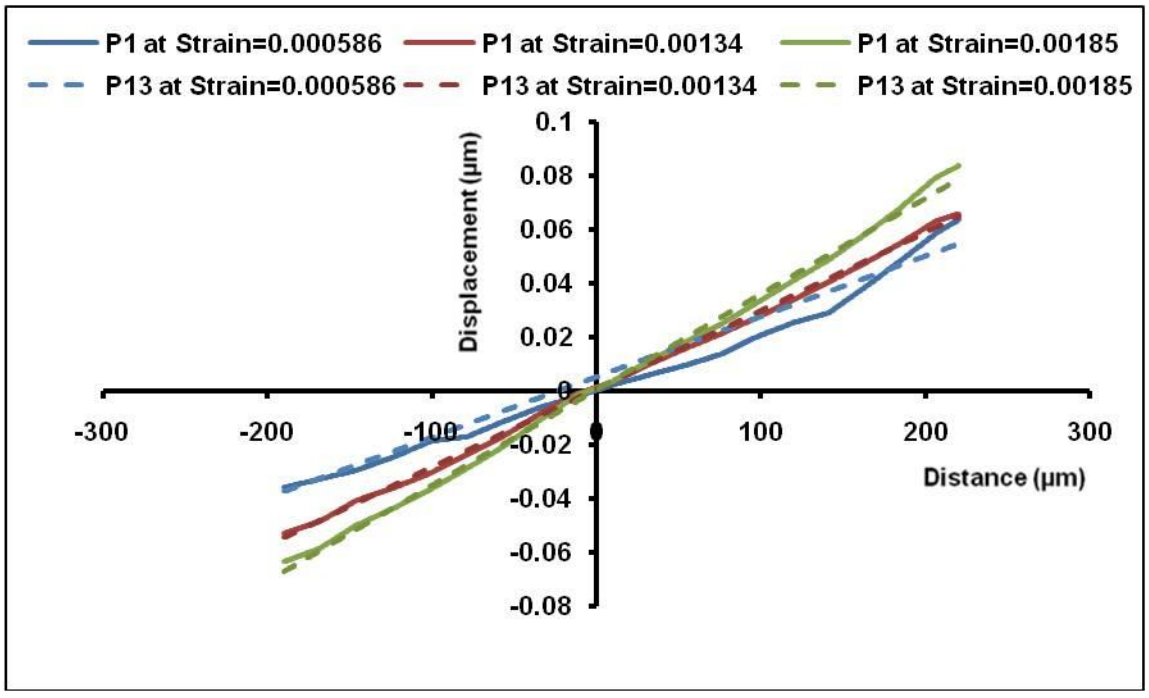

Figure 4-52: Shows the vector displacement against the distance from the left of the viewed area in X-axis through the slot B (P1) and the fitted displacement through slot B (P13). Interrogation window size used was 128×128 pixels and overlap 50% for slot B.

The purpose of these plots was to measure the displacement between points along two lines, the first line (P1) represents the line through the slot and the second line (P13) represents fitted line of the slot. The difference between the displacement in path through the slot and fitted slot is shown in Figure 4-53 a and b, as a function of applied strain. The displacement difference was measured at different applied strains as shown in Figure 4-53. The displacement difference increased with increasing applied strain for slot A (see Figure 4-53a) but the displacement difference did not increase with increasing applied strain for slot B as shown in Figure 4-53b.

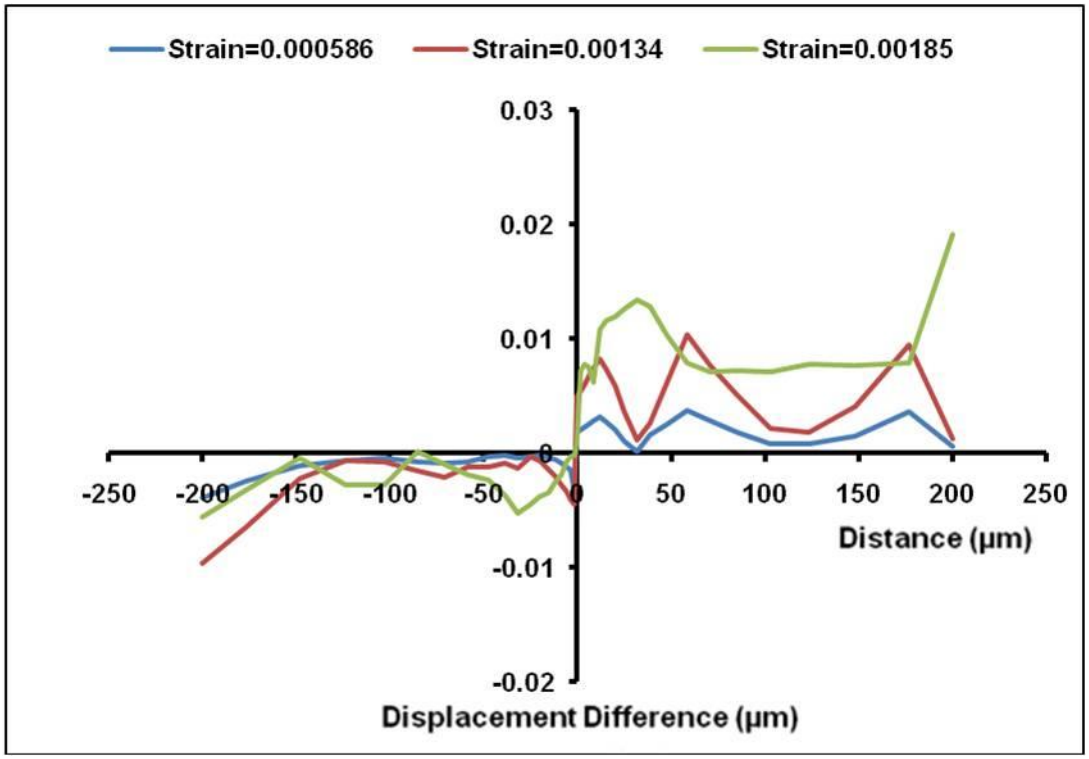

a) Slot A

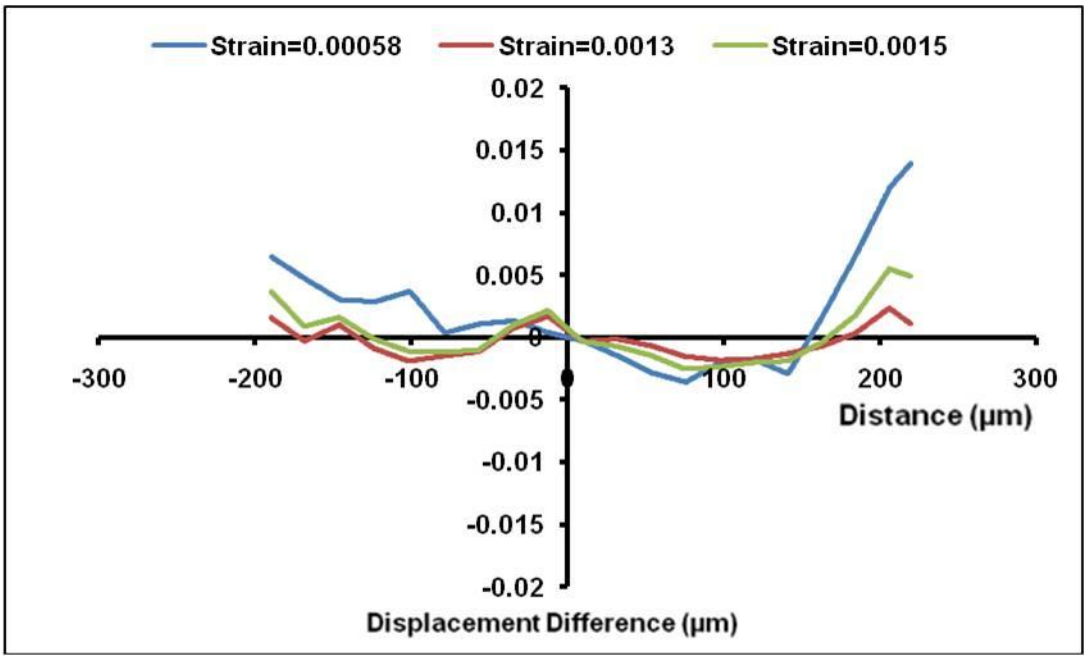

b) Slot B

Figure 4-53: The displacement difference between the displacement through (across) the slot and the fitted displacement through the slot as a function of the distance on each side of the slot. Window size was 128×128 pixels and overlaps 50%. Data for different applied strains are shown for a) Slot A and b) Slot B.

4.2.9 Comparing the FEM and DIC data

The displacement and surface crack opening displacement through the slot A and also, the slot A was fitted and it was compared between the finite element model data and the digital image correlation data. The FE model has the same slot depth and length 11.64 µm and 40 µm respectively as the DIC experiment, for both the FE model and DIC experimental data slot A was used. The finite element model showed there is a displacement difference between the displacements in paths across the slot A compared to a fitted displacement through the slot A as shown in Figure 4-44. The measurement of this displacement by image correlation is expected to be smaller than the true displacement (see Figure 4-46). The digital image correlation data also shows differences between the displacement across slot A and fitted displacement across the slot A (see Figure 4-53a).

Figure 4-54 shows the comparison between DIC displacements data using an interrogation window size of 128×128 pixels and overlap 50% at an applied strain of 0.00185. It also

shows the FEM displacement at a similar applied strain of 0.00185. The simulated effect of image correlation on displacements using the FEM prediction for a window size of 128×128 pixels and overlap 0% was shown on the same plot. The displacements obtained by DIC are smaller than those predicted by the FE model.

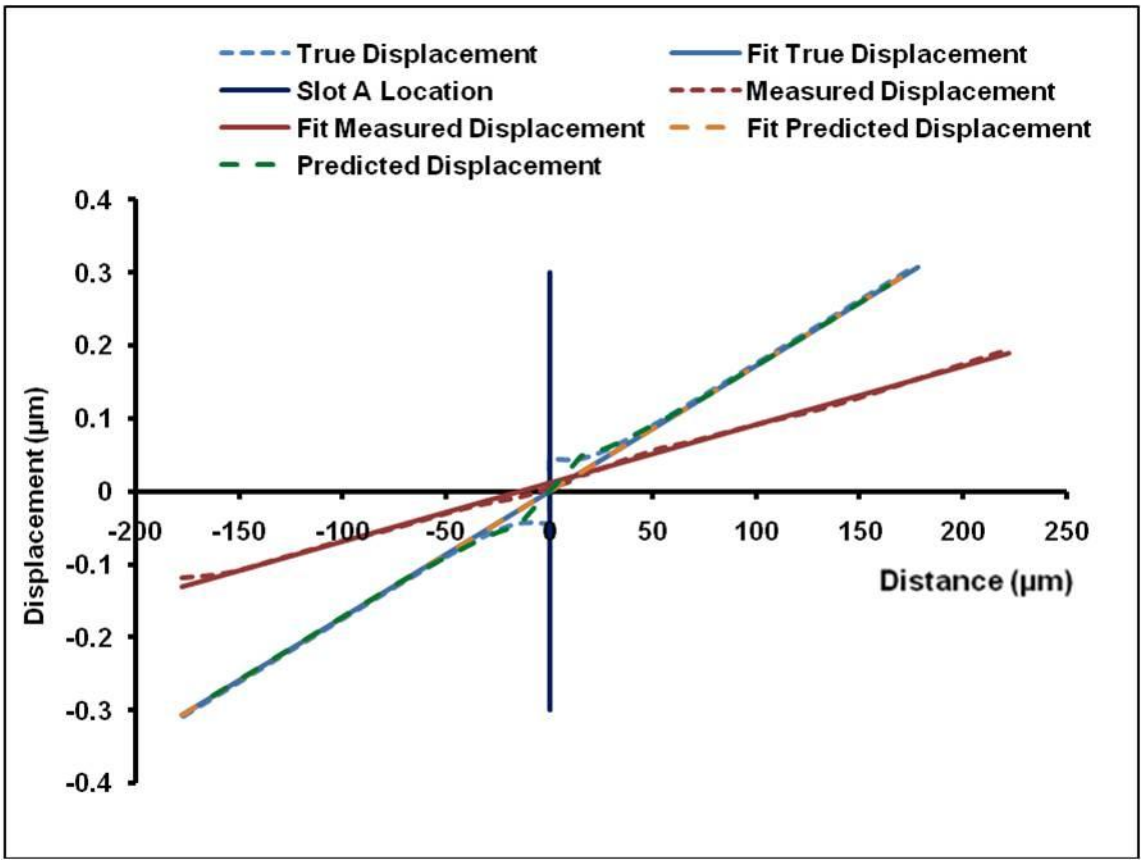

Figure 4-54: The displacement plot for the finite element model data at applied strain (0.00185) and the digital image correlation data. Interrogation window size was 128×128 pixels and overlap 50% at applied strain (0.00185) for DIC. Also showing the measured displacement using FEM prediction data at window size is (128×128) and overlap (0%), as a function of the distance from slot A.

Figure 4-55 shows the displacement difference results obtained from the finite element model at different applied strains, compared with the displacement difference results obtained from digital image correlation data window size 128×128 pixels and overlap 50% as a function of the applied strain. The DIC data is compared with the FEM prediction results using window size 128×128 pixels and overlap 0% at different applied strains. The displacement difference was measured by calculating the difference between the displacement at the line through the slot A (P1) and the fit displacement at a line through

the slot A (P13). Figure 4-55 shows the trend line for the displacement difference for the digital image correlation data and FEM prediction data.

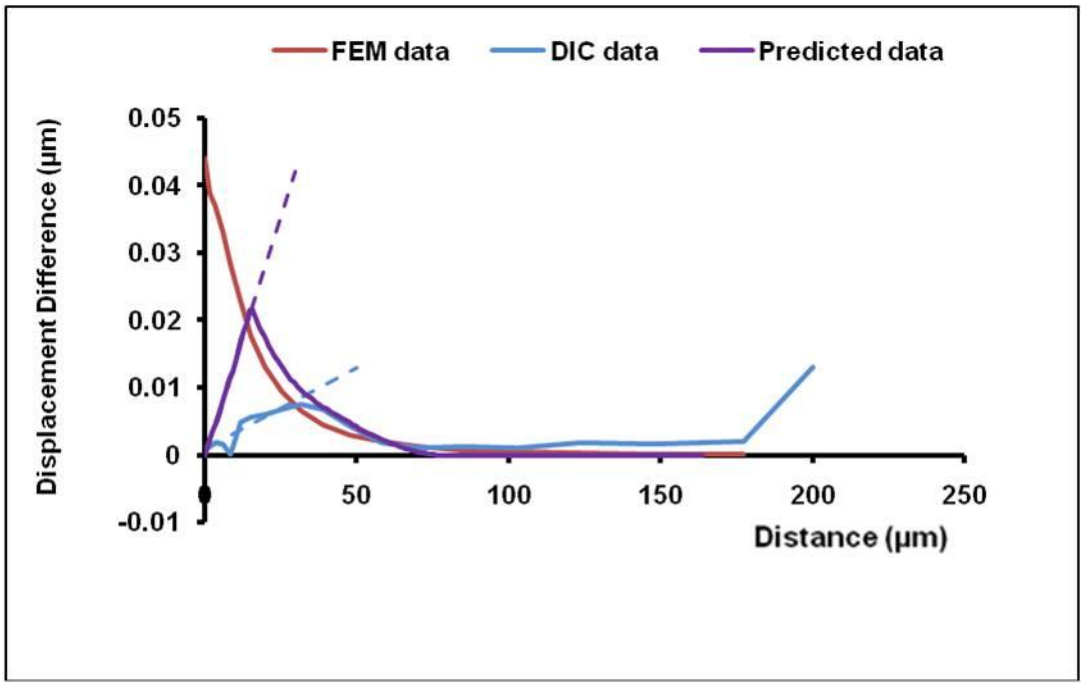

a)

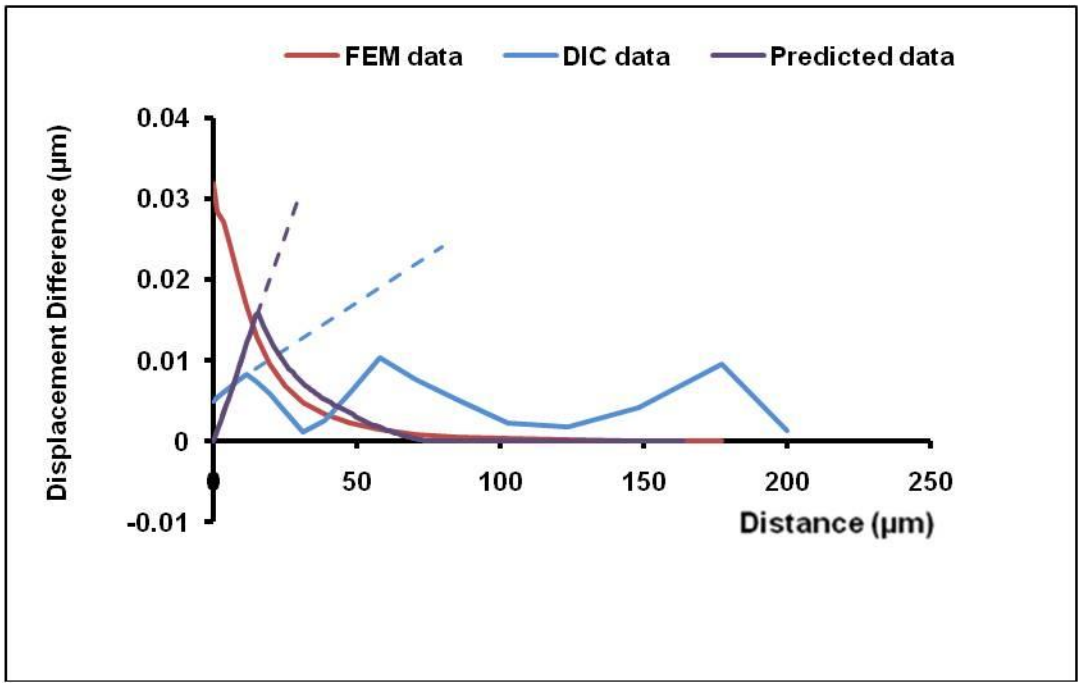

b)

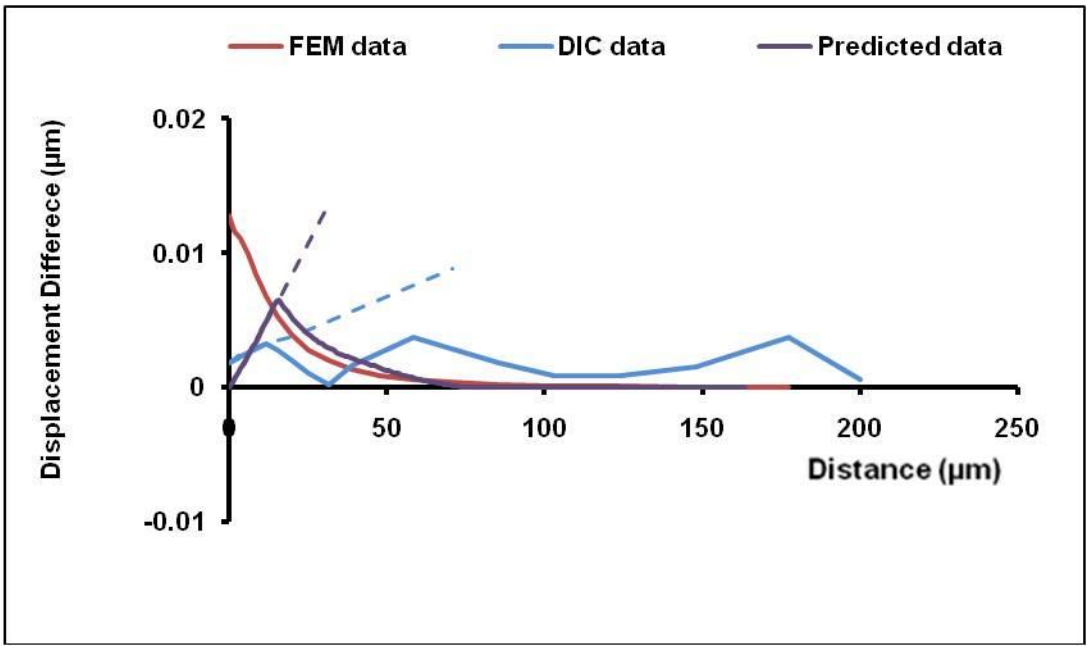

c)

Figure 4-55: The difference between the displacement at the region across the slot A and the fit displacement at the region through the slot A for the finite element model data and for the digital image correlation data. DIC taken with window size 128×128 pixels and overlap 50%. Also the FEM prediction data at window size 128×128 pixels and overlap 0%. The displacement difference was measured at different applied strains a) applied strain was (0.001854) for FEM and predicted data and (0.001849) for DIC data, b) applied strain was (0.00135) for FEM and predicted data and (0.00134) for DIC data, and c) applied strain was (0.000554) for FEM and predicted data and (0.000586) for DIC data.

Figure 4-55 show the trend line for the displacement difference using digital image correlation data at window size 128×128 pixels and overlap 50%. It also shows the trend line for the displacement difference using finite element model prediction data with a simulated window size of 128×128 pixels and overlap 0% at different applied strains. The results for the displacement difference slope are shown in Figure 4-56.

Figure 4-56 shows the strain from digital image correlation analysis of data and the strain from digital image correlation simulation of finite element model data as a function of applied strain. The experimental data show smaller strains than expected, but the strains increase with applied strain. The finite element model has the same notch depth and length 11.64 µm and 40 µm respectively as the experiment.

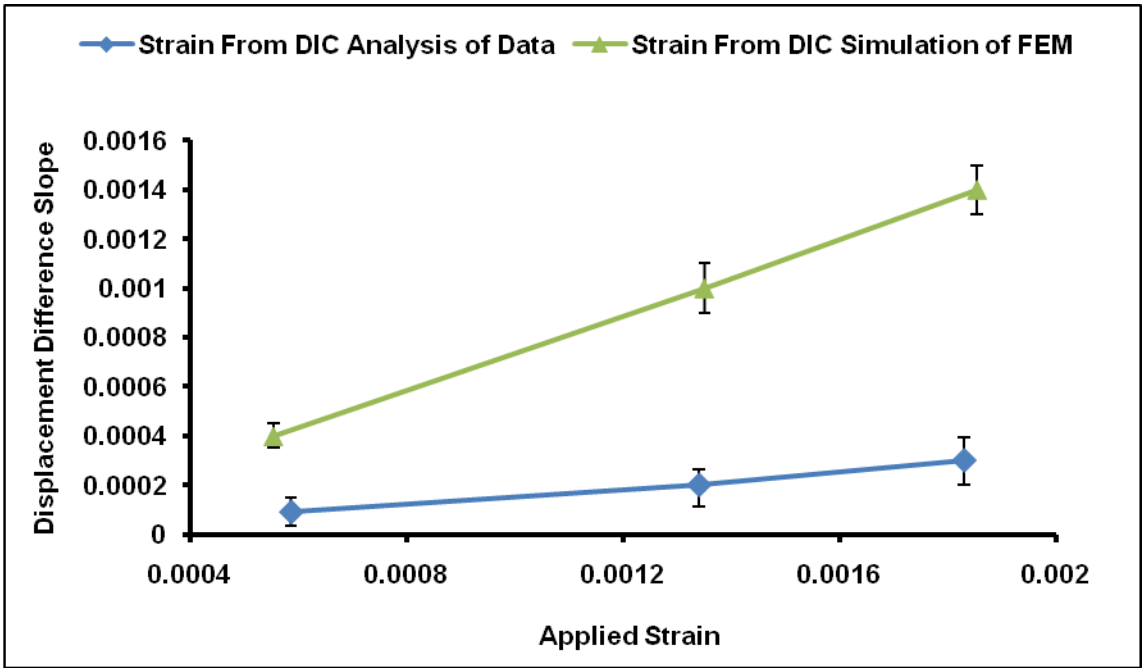

Figure 4-56: Shows the strain from experimental DIC data and the strain from DIC simulation of finite element model data (predicted data) against the applied strain. The experimental data show smaller strains than expected, but the strains increase with applied strain. The finite element model has the same notch depth and length as the experiment.

4.3 Summary

4.3.1 Strain Measurement

The microstructure and the crystal orientation was observed and the average grain size was determined using several techniques for P-I, P-II, Cr-I, and Cr-II specimens. The calibration test on the glass specimen was used to assess the sensitivity of the digital image correlation experiment to defocusing. The glass specimen was prepared using (HF acid) at different concentration (95%) and (50%) for (3 min) at different magnification (X10) and (X20). Then the noise level was measured using DIC at different window sizes and overlaps. The optimum glass specimen conditions for DIC were etching with 50%HF for 4 min and analysis with an interrogation window size 128×128 pixels and overlap 50% at magnification X20.

P-II and Cr-II specimens were prepared for digital image correlation using different procedures at different magnifications and different window sizes and overlaps. P-II and

Cr-II specimen conditions for digital correlation were (polishing, thermal etching, and gold coating to achieve enough features on the surface). The magnification used for DIC was X100 for both specimens due the average grain size being small. The optimum interrogation window size for DIC was 64×64 pixels and 128×128 pixels for P-II and Cr-II specimens respectively with an overlap 50% for both specimens. Data for all three samples were assessed to observe the effects of Features Size, Shift Correction, Pixel Locking, and Intensity Distribution.

The strain gauge data for the glass specimen were compared with the finite element model strain and the agreement was good. The variation of displacement across the viewed area at different positions and applied strains was measured for all samples. Then the average strain was measured from the displacement divided by distance in both X and Y-directions. The mean digital image correlation strain and slope were measured. The variation of strain in X and Y-direction was also measured at different positions as a function of the applied strains. These data will be used in the next section to assess the effects of sample curvature and tilting.

A comparison between DIC strain results for different specimens are shown in Figure 4-57. This shows that the average strains measured by DIC are lower than the expected strains for both glass and alumina samples, with the greatest difference for glass.

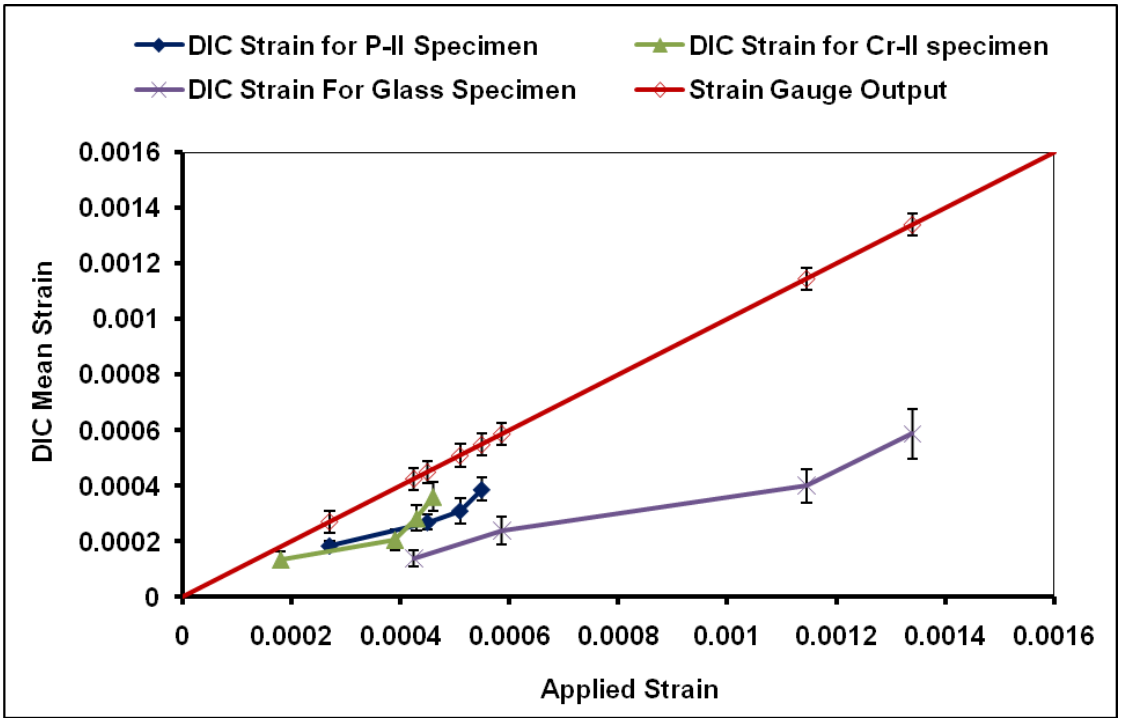

a)

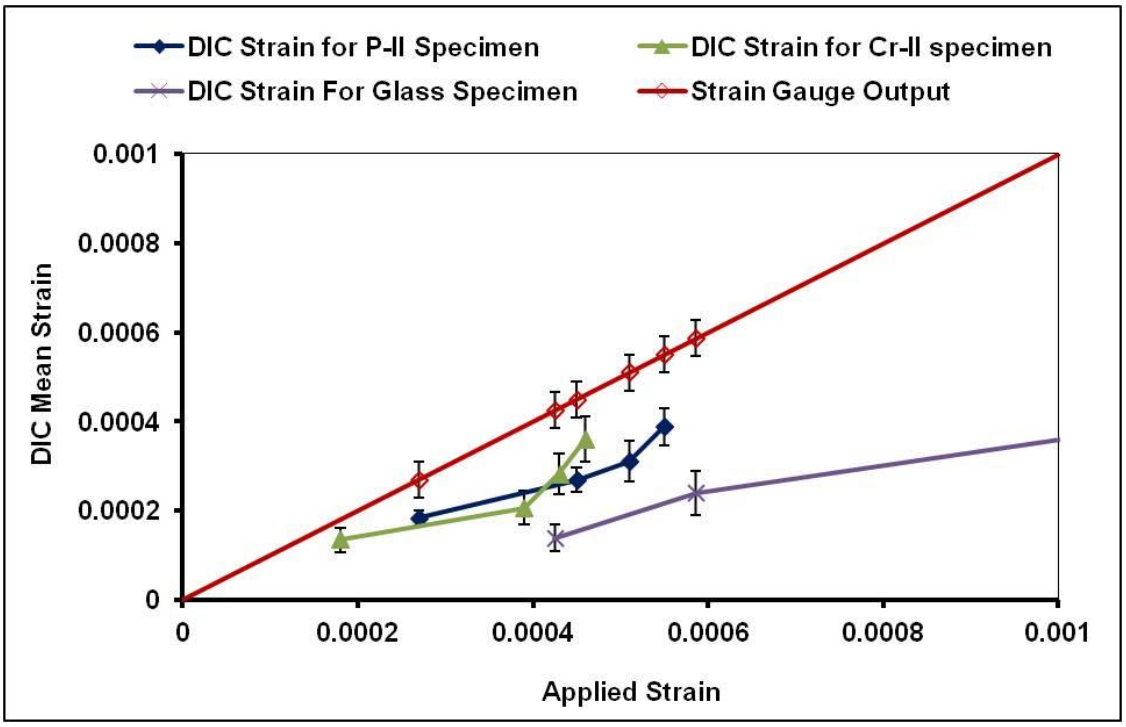

b)

Figure 4-57: a) Comparison digital image correlation mean strain for the P-II, Cr-II, and glass specimens as a function of the applied strain b) Extend the DIC mean strain for P-II and Cr-II samples.

4.3.2 Opening Displacement Measurement

The surface crack opening displacement for slot A was predicted using the finite element model data. The expected opening displacement at the maximum applied strain was 0.044 μm. The true and fitted displacements were measured on the (RHS) and (LHS) of the slot at the region across the slot A and B. The effect of the window size on the measurement of displacement and displacement difference, the displacement difference was simulated at different window sizes (8×8, 16×16, 32×32, 64×64, and 128×128 pixels). The displacement and displacement difference is affected by the overlapping of windows with the slot. It is predicted to be least accurate when measurements are made close to the slot, although as the window size increases the effect of noise will be reduced.

The displacement and displacement difference for slot A and slot B in the glass slide were measured using digital image correlation data, using the same method employed for the FE model data. A variation in displacement across the slot A was observed but not observed for slot B, although it could be seen in the strain map. The displacement and displacement difference across slot A were compared between the finite element data and digital image correlation data at different applied strains. This is represented as an apparent strain arising from the displacement gradient. Both the FEM data and DIC data show an increase in local strain with applied strain, but the effect is smaller in the experimental data and the DIC was used to detect slots/cracks, but not to measure their compliance.

Chapter 5

5 Discussion I

5.1 Quantitative measurement of strains for Glass Specimen using DIC

The average background strain can be represented by the digital image correlation mean strain, determined along a line across the centre of the viewed area, as a function of the applied strain. The line avoided the FIB slots and this evaluation is important in order to determine the influence of each component in the global strain calculation during a loading test. Figure 4-22 shows the digital image correlation strain in the stress direction increased with applied strain, but the measured values are less than strain gauge outputs. The ratio of the digital image correlation strain to the applied strain was about 0.403.

The measured strain in the direction of the applied stress (X-direction) increased with applied strain as shown in Figure 4-24a. However, the measured strain in the Y-direction was less than in the X-direction, as shown in Figure 4-24b.

The strain also varies across the viewed area at different positions. The strain variation in the X-direction increased with applied strain as shown in Figure 4-27a, but the strain variation in the Y-direction remained small as shown in Figure 4-27b. The focus calibration (see Figure 4-19) shows that there is an apparent strain of 0.0001 per μm of vertical displacement. Out of plane movements due to curvature or tilting of the sample could therefore cause a variation of the measured strain. To estimate the possible vertical movements arising from the background strains, the mean strain at the centre of the image (the position where the focus was held) was subtracted from the measured strain at each position. The vertical displacement was calculated using the defocus calibration method as mentioned in section (4.2.4.1). The results (see Figure 5-3) indicate that there is a tilt of 0.029° at applied strain 0.00042 and the sample appeared to be curved during the bending test.

The expected displacements due to sample curvature were calculated from the predicted radius of curvature. The elastic strain depends on the radius of curvature and the small angle approximation was used to calculate the change in the displacement within the

viewed area. The predicted vertical displacement due to the sample curvature at a strain of 0.000586 is shown in Figure 5-2, and is 0.017 μm at the centre of the image relative to the edges of the image. This was compared with the predicted change in vertical position due to the variation of strain across the image (see Figure 5-2). The expected vertical displacement is more than that obtained from the analysis of the digital image correlation strains, by a factor of approximately (15.4).

$$R = \frac{h}{2\varepsilon} \tag{43}$$

$$V_d = R \times \left(1 - \cos\frac{a}{R}\right) \tag{44}$$

Where the (h) is sample thickness, (ε) represents the surface strain (applied strain), (R) is the radius of curvature, (θ) is the tilting angle, (a) is the half length of the viewed area (distance) and (V_d) represents the vertical displacement using Equation 44 as shown in Figure 5-1.

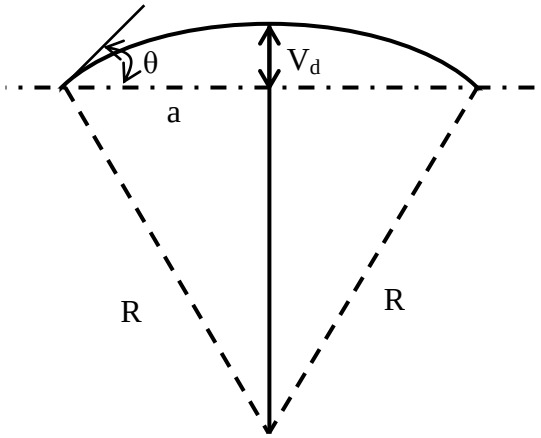

Figure 5-1: Shows the radius of curvature (R) and the vertical displacement (V_d) and the tilt angle (θ).

The strain gauge output agrees with the FE model, suggesting that there is no significant twisting of the sample. The vertical displacement (from the micrometer) was used to

calculate the strain and observe the correlation between the strain gauge outputs and the strain from the FE model (see Figure 4-28). This shows the strain gauge is reliable, since its values agree with prediction of the FE model (i.e. the strain gauge is properly positioned).

The surface gradient was measured by multiplying the digital image correlation strain slope (see Figure 4-25) by the apparent strain slope (from calibration test) (see Figure 4-19) and then obtaining the tilt angle by simple trigonometry. The background strains also show an apparent tilting of the sample relative to the microscope axis, which increases as the load is applied (Figure 5-3). That tilt would be reproducible from experiment to experiment since it is due to the compliance of the microscope set-up, and it is perhaps therefore unavoidable. It will given a background displacement gradient that increase with applied strain.

The tilting and bending will affect both the strains in the X and Y directions. The fact that the calculated displacements are much less than the expected displacements shows that the DIC analysis is not very sensitive. The effect on the X-strains may be evidence of bending, but it appears that the effect is only seen when the measured strains are large. Its effect on the Y-strains is small. The calibration test using simple vertical displacements is not sufficient. This is yet more evidence that the DIC data should only be regarded as qualitative, not quantitative.

In summary, these analyses show that patterns of background strains develop which are consistent with curvature and tilting of the sample. The background strains measured by digital image correlation are less than those predicted, which suggests that DIC is not sufficiently sensitive to the small displacements. The trends in the DIC data are consistent with expectation, but the magnitudes are approximately 50% of these expected. This suggests that under the conditions of these experiments, digital image correlation significantly under measures the small displacements, and may not be relied on to accurately measure relative displacements of features. This will be significant when assessing the opening displacements of the focused ion beam, FIB notches.

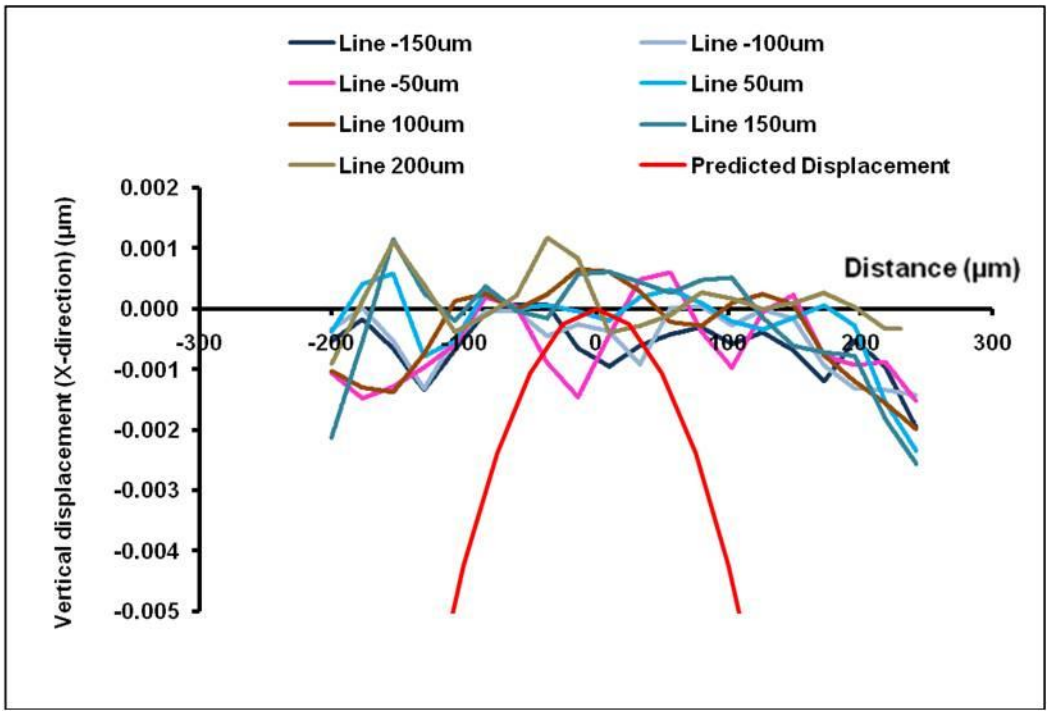

Figure 5-2: Shows the measured vertical displacement in X-direction at different line position within the viewed area. Also shown is the predicted vertical displacement. Both vertical displacements were measured at surface strain (0.000586) for the glass specimen.

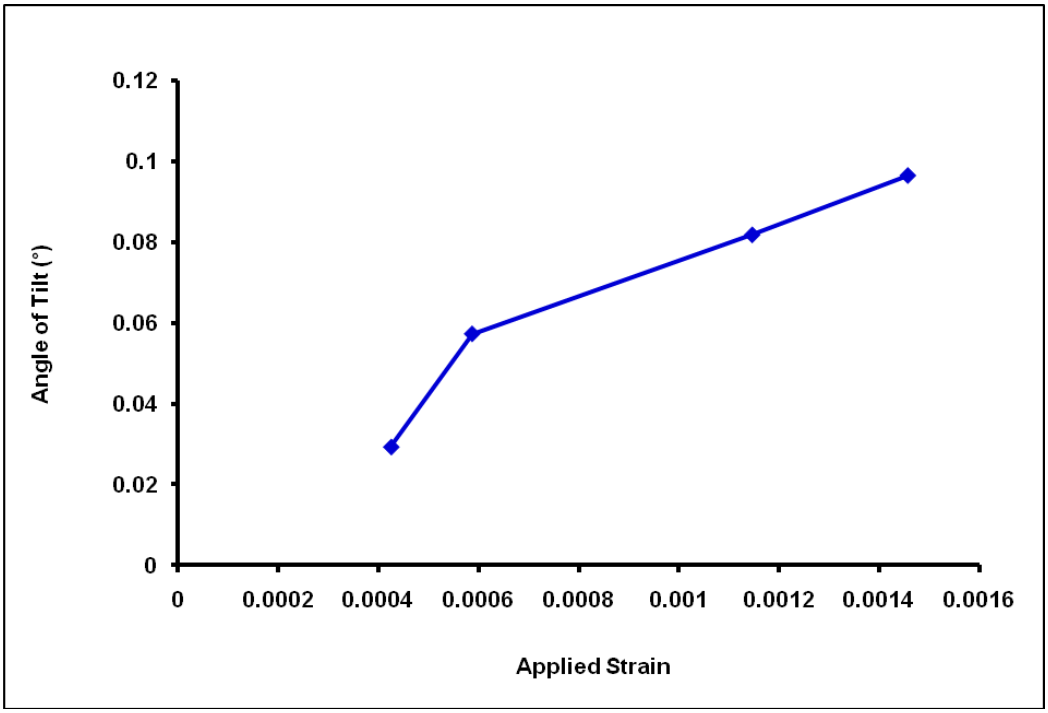

Figure 5-3: Shows the relationship between the tilt angle as a function of the applied strain for the glass specimen.

5.2 Quantitative Measurement of strains for polycrystalline alumina specimen (P-II and Cr-II) using DIC

Figure 4-32a, and Figure 4-35a show the measured strain in the X-direction for the alumina samples and it increased with increasing applied strain. The strain varies with the position due to the combined effects of elastic strains and vertical displacement toward the lens. Figure 4-32b and Figure 4-35b show the measured strain in the Y-direction and it was less than the measured strain in the X-direction with applied strain. The predicted vertical displacement was calculated from the elastic radius of curvature (calculated using simple beam theory) and the position within the viewed area. Figure 4-33, and Figure 4-40 show the effects of the background strain in both X- and Y-directions because the tilting and curvature of the sample. The variation of strain is small and the elastic strains are large compared to any effects of curvature and tilting.

Figure 5-4 a and b for P-II and Cr-II specimens respectively, show that the expected curvature and measured curvatures are comparable. The measured vertical displacement is less than the expected vertical displacement for the alumina specimens as mentioned early in section (5.1). However, it should be noted that the expected strains for alumina are smaller than those for glass, due to the lower elastic modulus of glass, and this agreement may be fortuitous. The apparent tilt causing vertical displacements is shown in Figure 5-5.

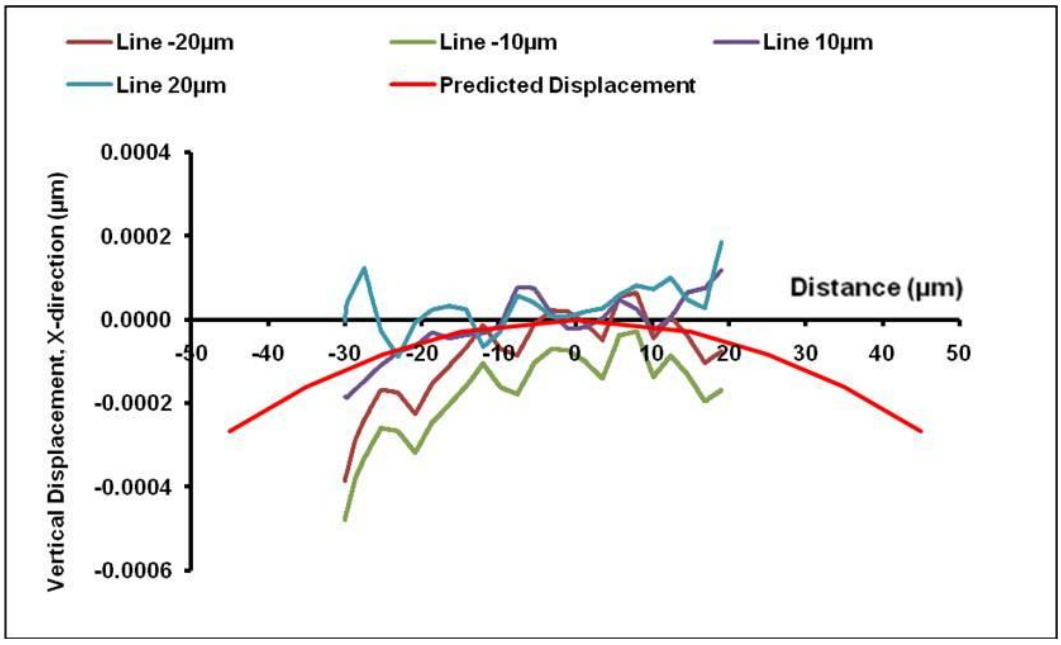

a) P-II Specimen

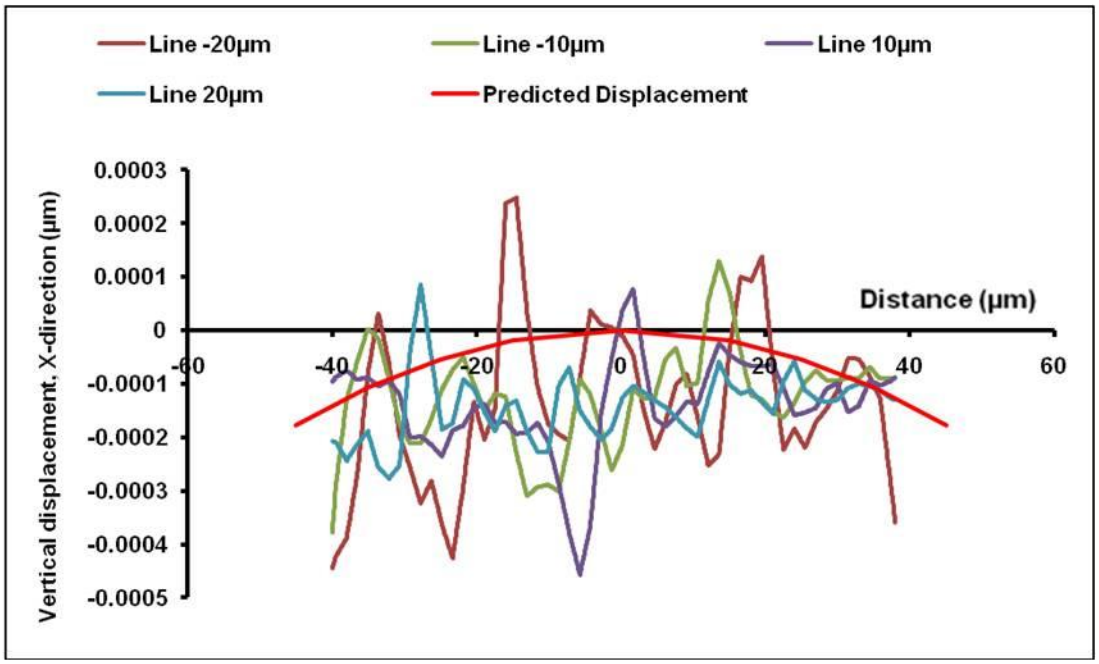

b) Cr-II Specimen

Figure 5-4: Shows the measured vertical displacement in X-direction at different line position within the viewed area and also shows the predicted vertical displacement for a) P-II specimen (surface strain for both displacement is 0.00027) and b) Cr-II specimen (surface strain for both displacement is 0.00018).

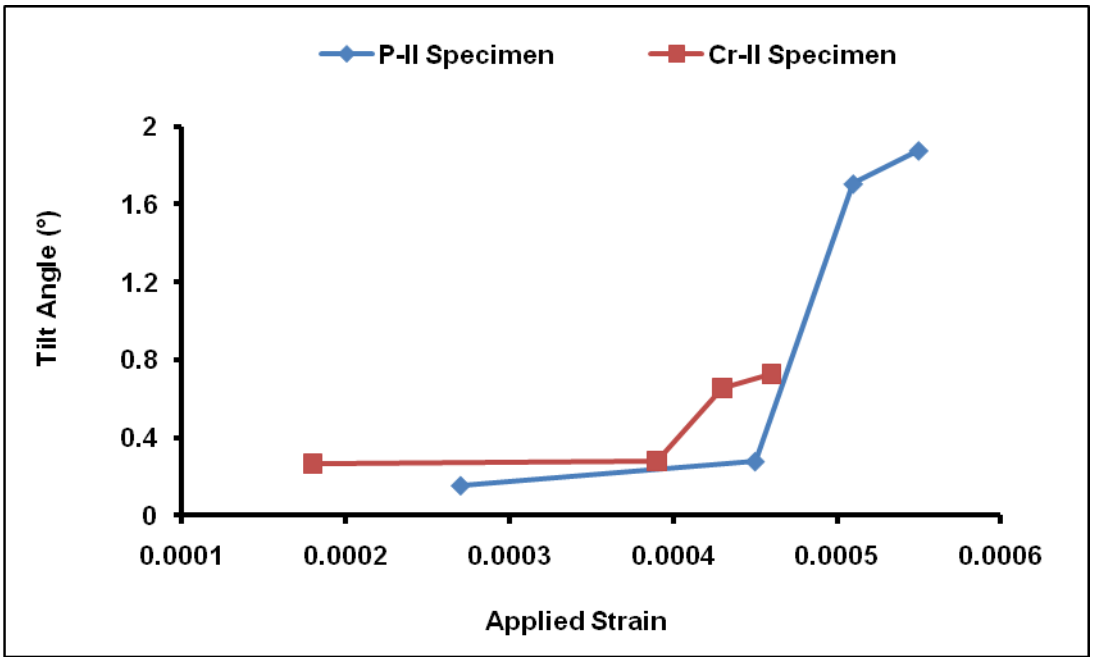

Figure 5-5: Shows the relationship between the tilt angle as a function of the applied strain for the P-II and Cr-II specimens.

Figure 4-30 and Figure 4-37 show the digital image correlation strain (local strain) is less than the applied strain (strain gauge outputs). The digital image correlation does not accurately measure the displacement due to effect the window size on the surface crack opening dispalcement (see Figure 4-46 and Figure 4-47) (i.e. the experimental data was affected by overlapping of window size with the slot). The displacement and displacement difference across slots was measured at different applied strains and was represented as an apparent strain arising from the displacement gradient DIC may therefore be used to observe the slots/cracks, but not to measure their compliance.

5.3 The Surface Crack Opening Displacement for Glass Specimen

Equation 45 was used to calculate the maximum surface crack opening displacement (SCOD) at the free surface. The slot geometry and applied load were important for measuring the surface crack opening displacement [106]. The geometries and mechanical properties were used in Equation 45 (where (υ) is Poisson's ratio is (0.25) [81], (σ) is applied tensile stress, (a) is the slot depth, (c) is a half slot surface length and (E) Young's modulus is (70GPa) [81]). The Equation 45 was used to calculate the SCOD and it depends on the slot depth, (a) but the SCOD is not strong depend the (c). The expected gradient of surface crack opening displacement with applied stain was predicted using Equation 45 and the expected SCOD results are shown in the Table 5-1.

$$SCOD = 4\sqrt{2}(1-\nu^2)(\sigma\frac{a}{E})(1+0.12(1-\frac{a}{c})(\sqrt{1-0.619\frac{a}{c}})) \quad (45)$$

After the image correlation experiment, a trench was made for measuring the depth of focused ion beam (FIB) processed slot. The sections across slot A and slot B were made using focused ion beam are shown in Figure 5-6 at tilt angle 52°. The measured surface crack opening displacement results for slot A and slot B are shown in Figure 4-53.

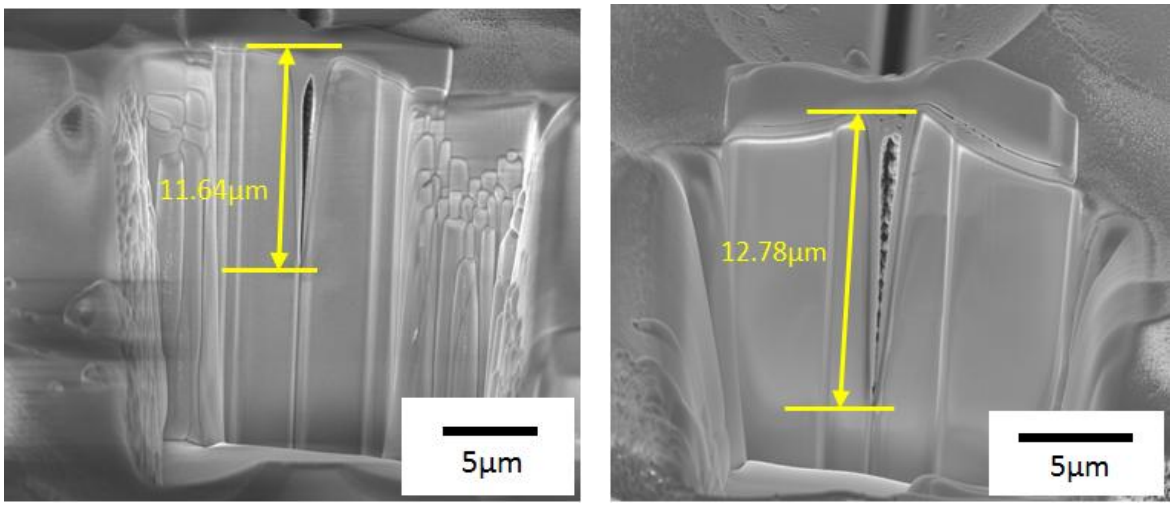

a) b)

Figure 5-6: Shows the slots depth using focused ion beam, FIB at tilt angle 52° and voltage 30 kV and a current of 280 nA for a) Slot A and b) Slot B.

Table 5-1: shows the dimensions and expected gradient of surface crack opening displacement for slot A and slot B

Slots	Length (µm)	Measured depth (µm)	Expected Gradient of SCOD (SCOD (µm)/Applied Strain)
Slot A	40	11.64	66.45
Slot B	20	12.78	54.98

Figure 5-7 shows the surface crack opening displacement for the same defect size using different models. This also shows difference between the analytical model data, obtained from Equation 45 and finite element model data (direct value of SCOD). This difference is due to the stress state and geometry of the slot (i.e. SCOD depends on the crack geometry and loading. For example the relationship for the equation was a semi-elliptical crack under tensile loading [107]). The analytical model prediction and finite element model (direct value of SCOD) were compared with the finite element model (simulation of digital image correlation analysis) that obtained of the effect of window size on the surface crack opening displacement data (see Figure 4-47). The surface crack opening displacement data for the finite element model (simulation of DIC analysis with 128×128 pixels window size, 1 pixel=0.23 µm) was less than the data for the analytical model prediction and finite

element model (direct value of SCOD) due to the effects of window size on the data and overlapping window size with the slot. The analytical model prediction, finite element model (direct value of SCOD), and finite element model (simulation of DIC analysis) are compared with the experimental data at the same defect size. The experimental data is the least sensitive, followed by the FE model (simulation DIC analysis). After these comes the FE model (direct value of SCOD) and finally the analytical model. The DIC data are least sensitive because it does not accurately measure the displacement, also the window sizes have an effect, as does windows overlapping with the slot see Figure 4-46. So, the combined effect is likely to be that the displacements are under-measured and the displacements of the polycrystalline alumina are also going to be under-measured. The comparison between the surface crack opening trend lines and gradients for these data is shown in Figure 5-7 and Table 5-2 respectively.

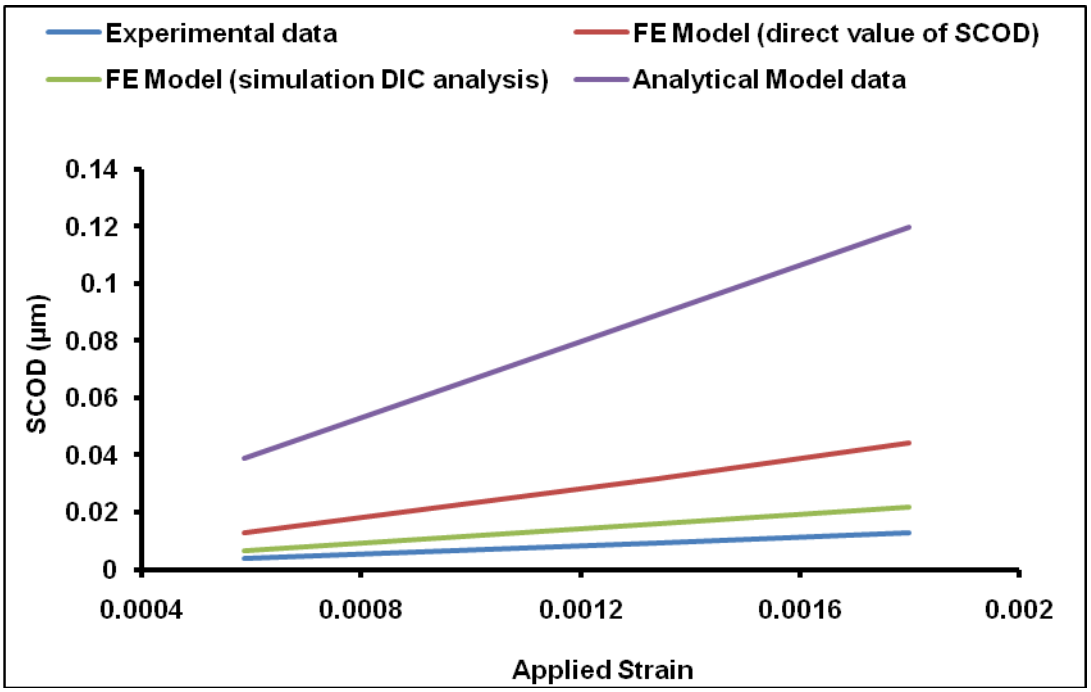

Figure 5-7: Comparison between the experimental data, FEM data, predicted data, and analytical model data for SCOD against the applied strain for the glass slide (slot A).

Table 5-2: The surface crack opening displacement gradient data using different procedures for the slot A in glass specimen.

Procedures	SCOD Gradient
Analytical Model Data	66.45
FE Model (Direct value of SCOD)	24.79
FE Model (Simulation of DIC analysis)	12.04
Experimental Data	7.31

Summary

The background strain in the X and Y-directions was obtained from the curvature and tilting in the specimen. The focus calibration shows there is an apparent strain due to the curvature and tilting of the sample; this could therefore cause a variation of the measured strain.

The background strains measured by DIC are less than those predicted, which suggests that DIC is not sufficiently sensitive to small displacements in these experimental conditions. The trends in the data are consistent with expectations, but the magnitudes are approximately 50% of these expected. This suggests that under the conditions of these experiments, DIC significantly under measures the small displacements, and may not be relied on to accurately measure relative displacements of features.

The displacement and displacement difference across slots was compared between the FEM data and experimental data at different applied strains and was represented as an apparent strain arising from the displacement gradient. Both finite element model data and experimental data show an increase in the local strain with applied strain, but the effect of the window size in the FEM (simulation of DIC data) is smaller than in the experimental data. This suggests that digital image correlation is used to observe the slots/cracks, but not to measure their compliance.

Chapter 6

6 Results II

6.1 Image correlation to study crack nuclei in polycrystalline alumina

6.1.1 Observation of Strain features for P-II Specimen

The image correlation data were used to identify strain features for the P-II specimens. Strains are a result of the displacements of material on either side of a feature. The magnitude of the strain depends on the differential of this displacement and is therefore a nominal strain. Examples of high strain features that are expected to be cracks, due to the crack opening under load are shown in Figure 6-1a. This figure shows the strain features above a threshold of about 0.2%. Figure 6-1b shows the strain map in which a high threshold of about 1% has been applied to hide the noise. There are probably other features below the noise threshold. They disappear at the higher threshold. There are three significant features (Feature A, Feature B, and Feature C) observed above this threshold in the P-II sample. Note that the shape of these features is not significantly affected by the threshold.

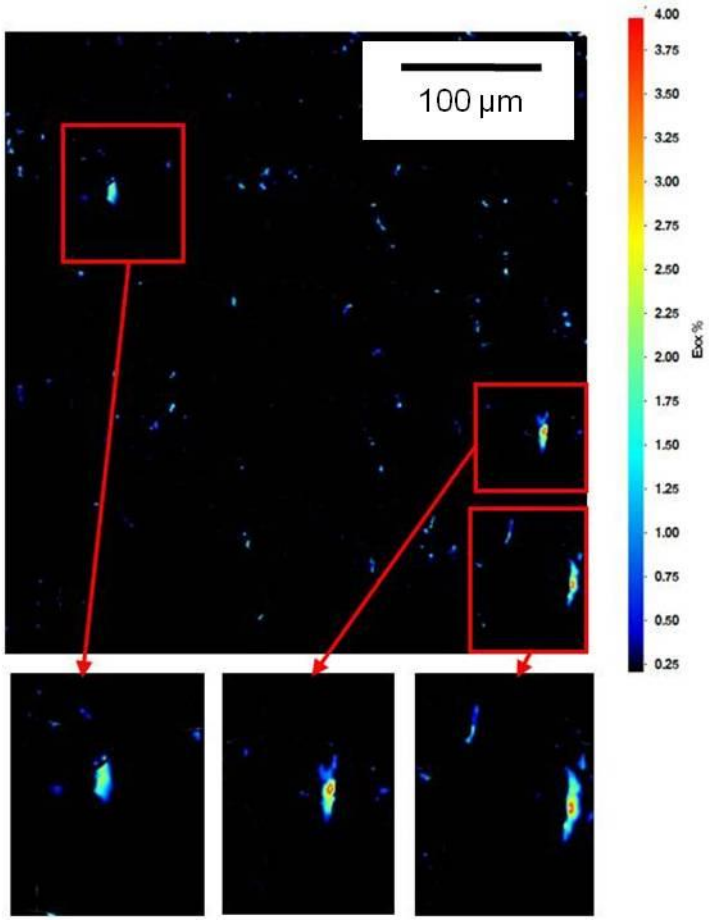

Feature A Feature B Feature C

a) Low Threshold (0.2% strain)

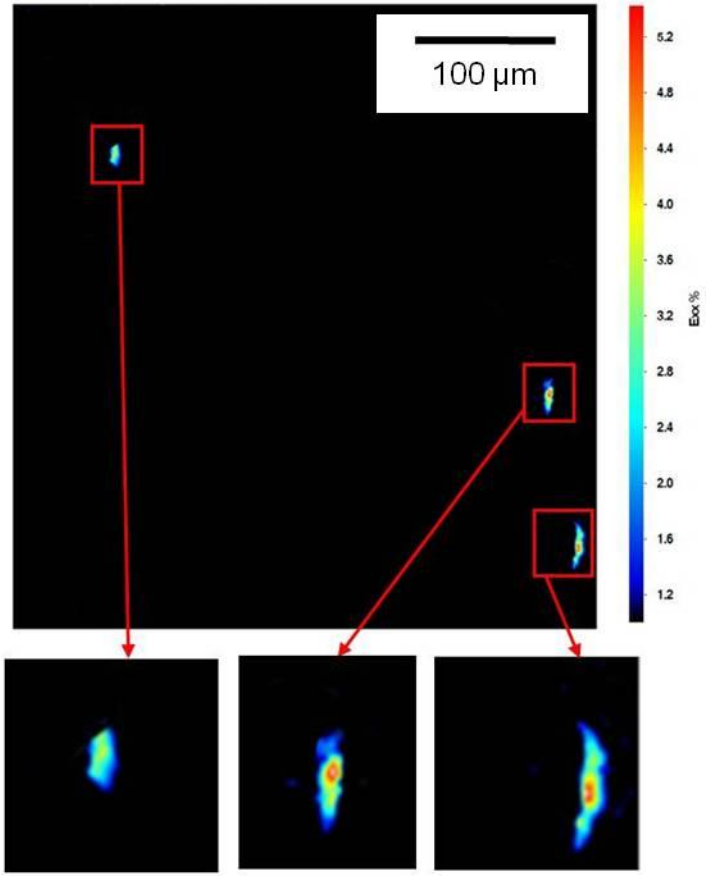

Feature A Feature B Feature C

b) High Threshold (1% strain)

Figure 6-1: Identification of strain features (strain feature A, strain feature B, and strain feature C) by in-situ observation for P-II specimen, a) Low threshold (0.2%), b) High threshold (1%). Both thresholds are at an applied strain 0.00027.

6.1.2 Effect of Applied Strain on the Strain Feature for P-II Specimen

Image correlation of observations at different levels of applied strain reveals cracks, as differentiation of their opening displacements gives features of high localised apparent strain. Analysis by digital image correlation reveals localised regions of high strain normal to the X-direction. These significant features were observed at each increment and were quite clear on the strain map. Therefore these high strain regions were designated as cracks. This data shows the opening of the crack and its length. Figure 6-2 is an example of one strain feature A showing the nominal strain in the X-direction at different strain levels (applied strain also in the X-direction). Figure 6-3 shows the nominal strain in the

Y-direction for the same strain feature A region. Strain feature A is clear that the X-direction strain is affected by applied strain, and not the Y-direction strain.

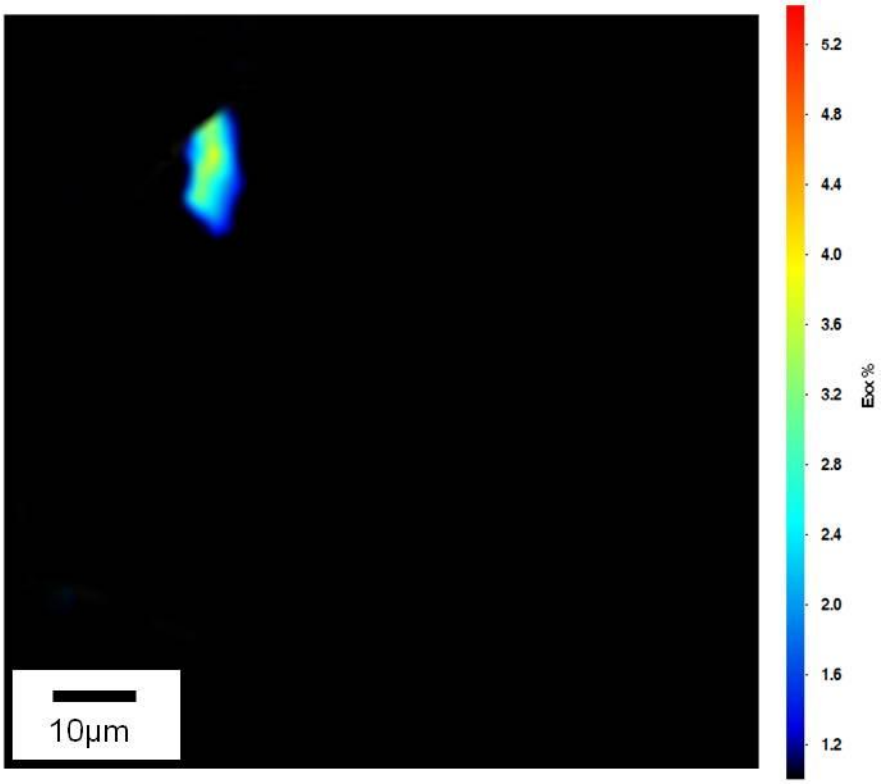

a) Applied strain (0.00027)

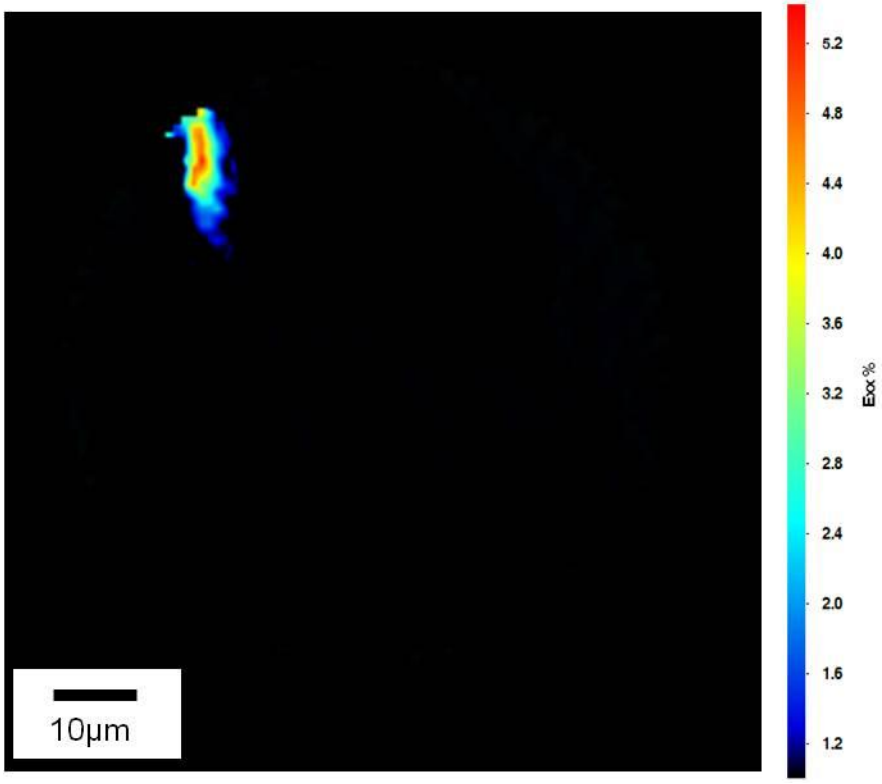

b) Applied strain (0.00045)

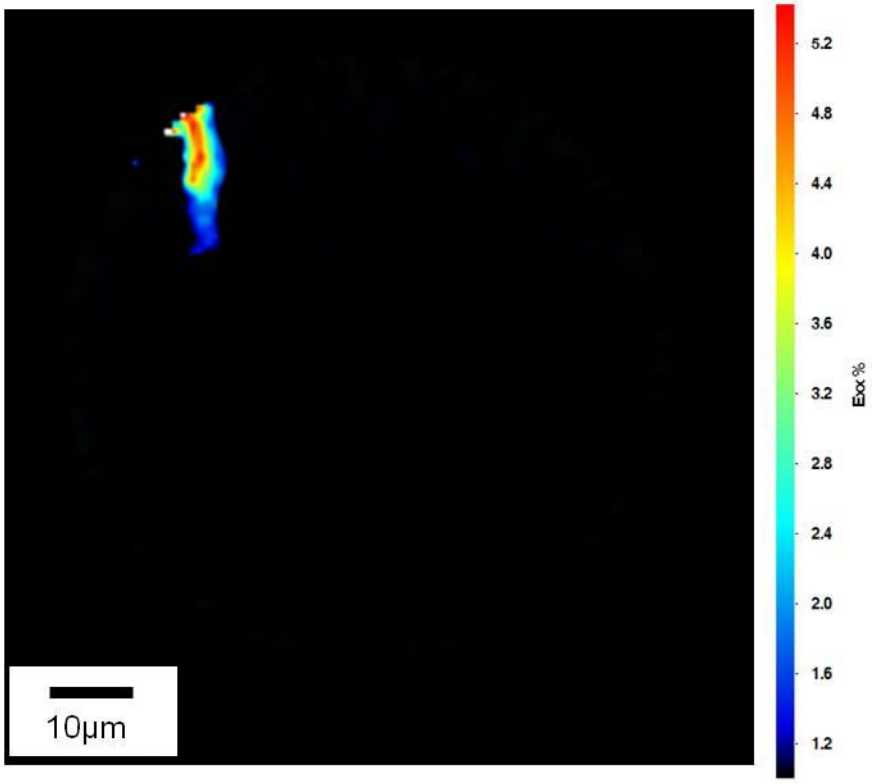

c) Applied strain (0.00051)

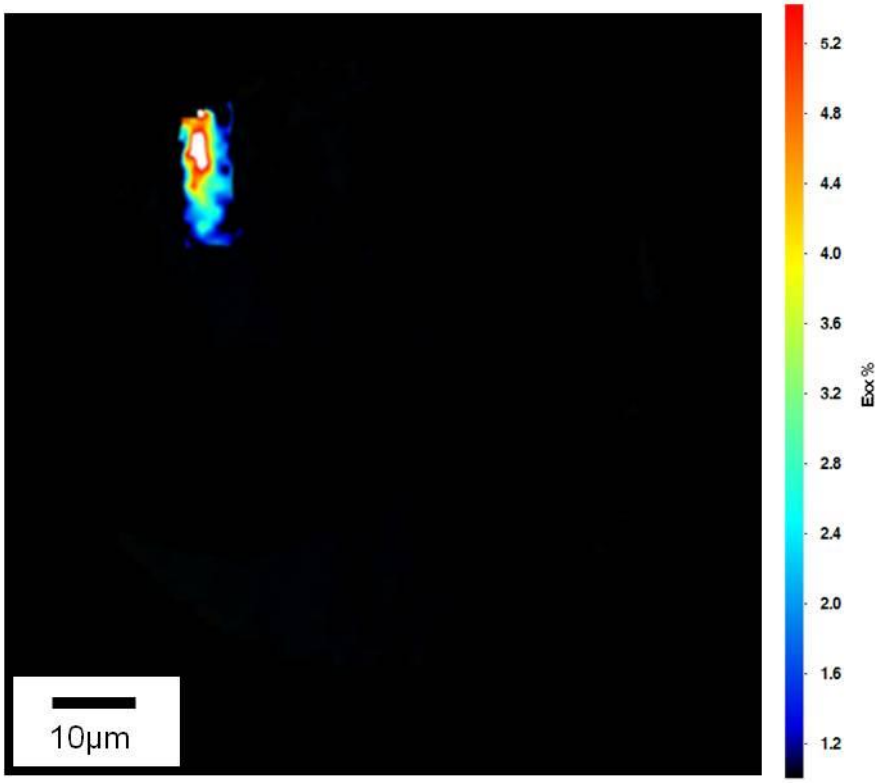

d) Applied strain (0.00055)

Figure 6-2: Illustration of the nominal strain at different applied strain and strain distribution observed by digital image correlation under increasing load in the X-direction for strain feature A in P-II specimen.

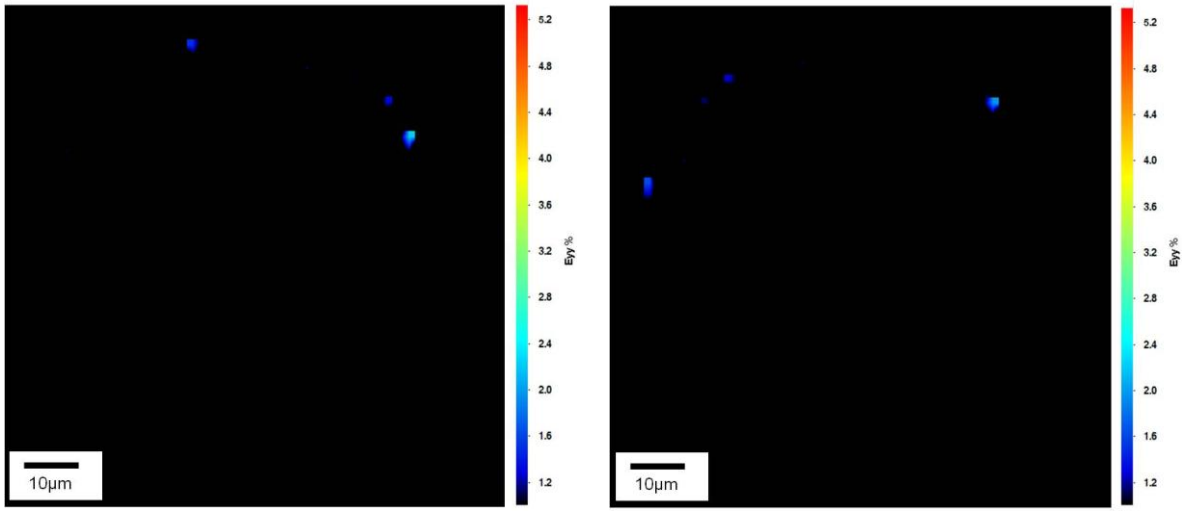

a) Applied strain (0.00027) b) Applied strain (0.00045)

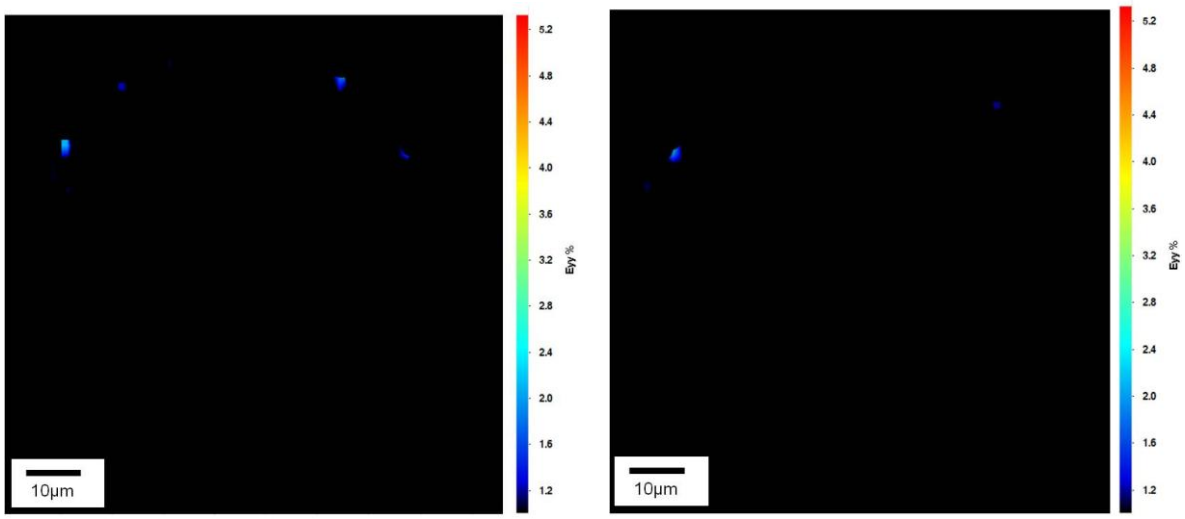

b) Applied strain (0.00051) b) Applied strain (0.00055)

Figure 6-3: Illustration of the nominal strain for the region around strain feature A at different applied strains and strain distributions observed by digital image correlation under increasing load in the Y-direction for P-II specimen.

6.1.3 Observation of strain features for Cr-II Specimen

Figure 6-4 shows a strain feature in the Cr-II specimen. A high threshold of 1% has been applied to hide noise. This shows one strain feature in this sample above the threshold 1% as mentioned early in section (6.1.2).

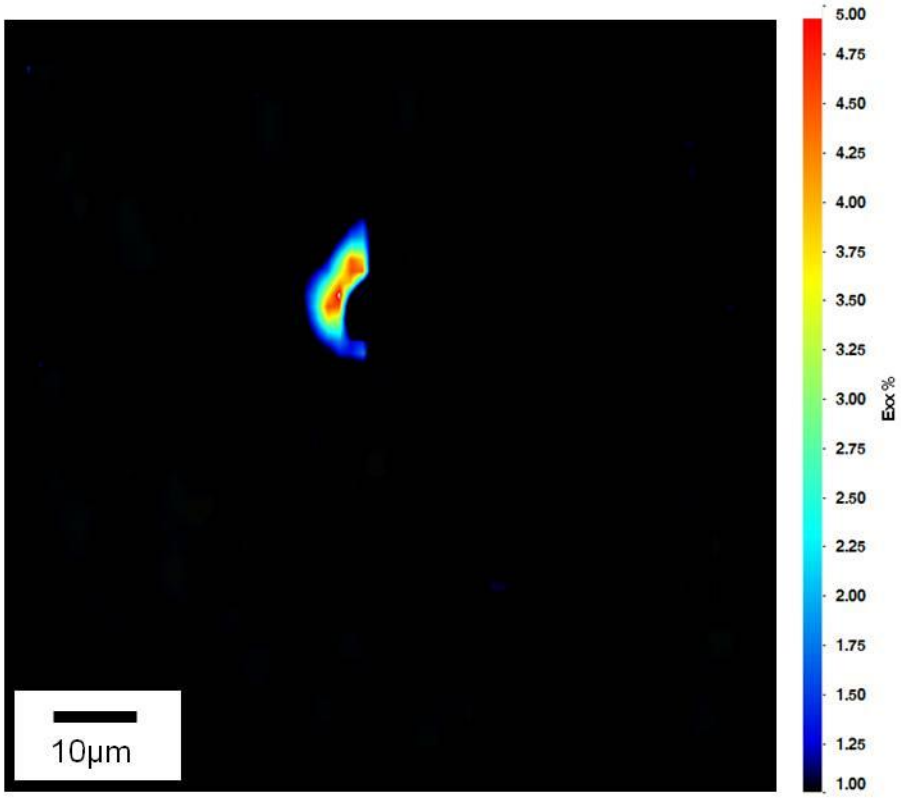

Figure 6-4: Identification of strain feature by in- situ observation for Cr-II specimen at applied strain 0.00046.

6.1.4 Effect of Applied Strain on the Strain Feature for Cr-II Specimen

Figure 6-5 shows the strain feature for the Cr-II specimen and the effect of applied strain on the X-direction nominal strain. The strain feature region does not show any pattern in the Y-direction as shown in Figure 6-6. As mentioned early in the P-II specimen in section (6.1.2) the opening and length of the feature increases slightly as the applied strain are increased. The magnitude of the nominal strain in X-direction increases significantly with applied strain.

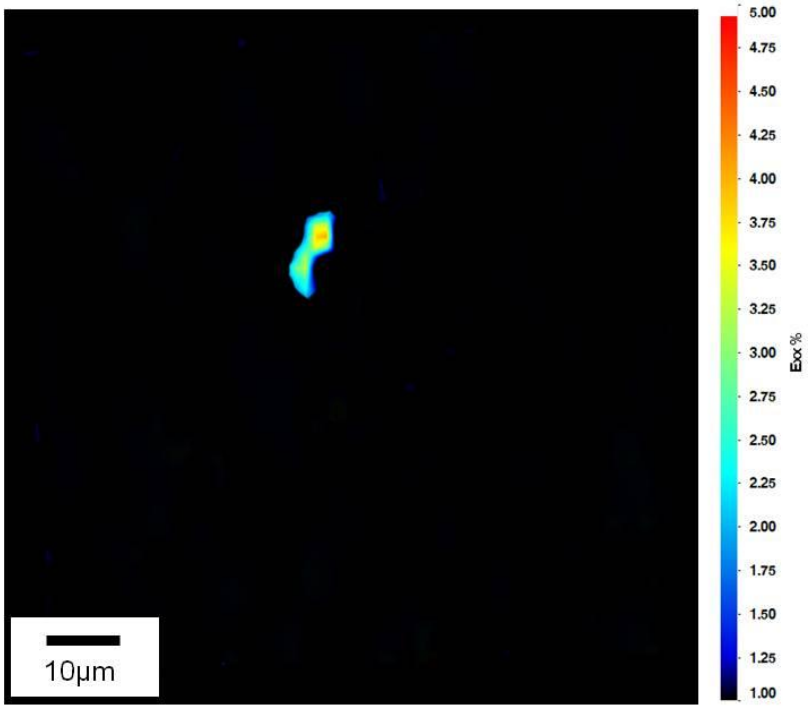

a) Applied strain (0.00018)

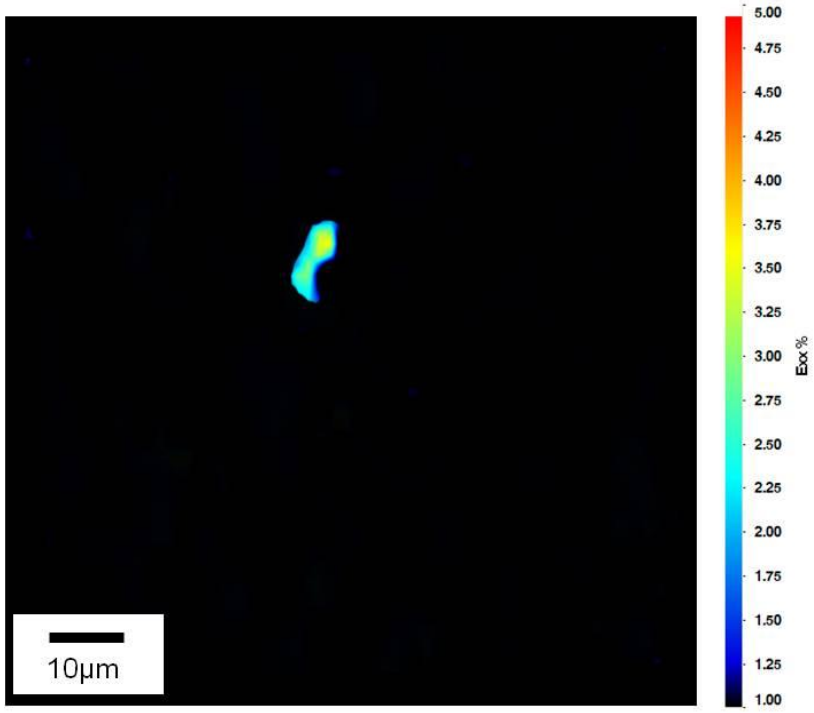

b) Applied strain (0.00039)

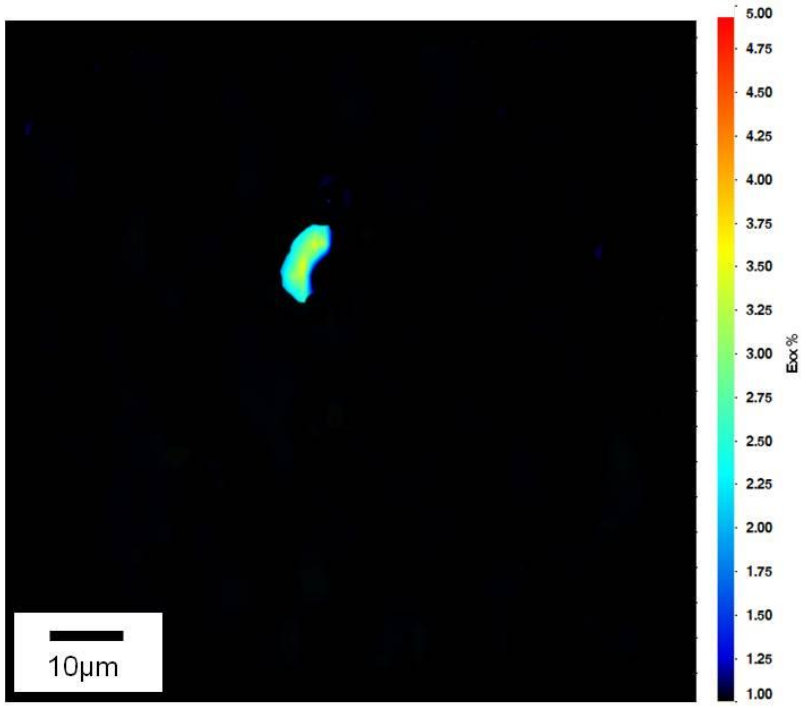

c) Applied strain (0.00043)

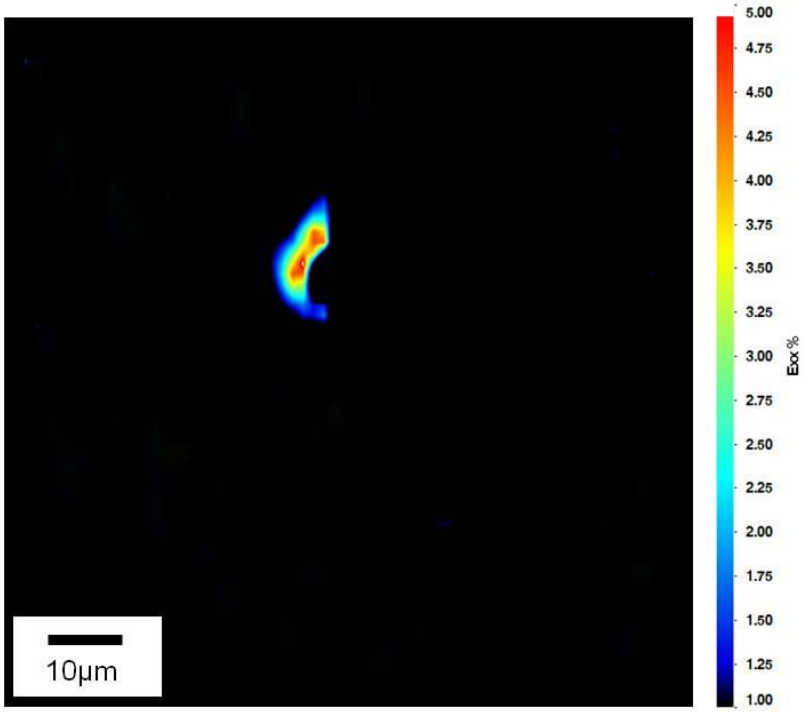

d) Applied strain (0.00046)

Figure 6-5: Illustration of the nominal strain at different applied strain and strain distribution observed by digital image correlation under increasing applied load in the X-direction for Cr-II specimen.

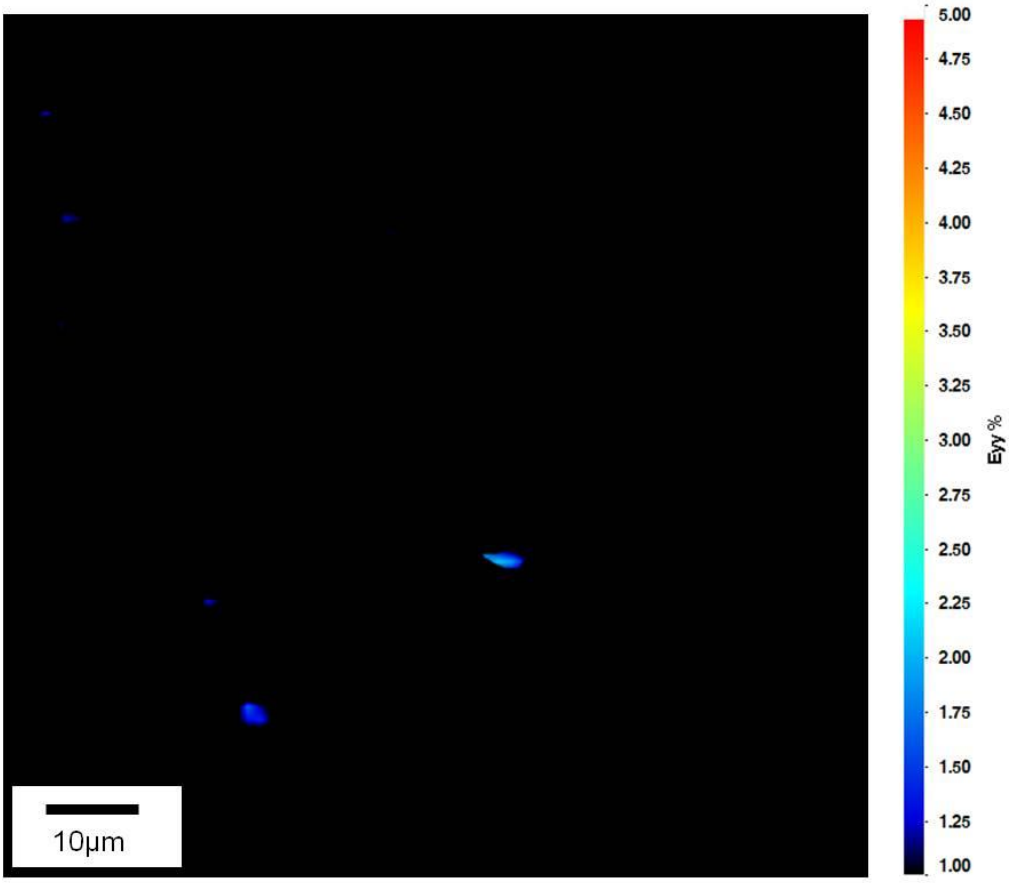

Figure 6-6: Illustration of the region around strain feature at applied strain 0.00046 and strain distribution observed by digital image correlation under increasing applied load in the Y-direction for Cr-II specimen.

6.1.5 Comparing the Peak strain with Background Strain

The peak strain (largest strain for each feature) was measured using a Matlab routine that was written earlier by Haiyan Li ("crack track") [68]. The strain features in the P-II and Cr-II samples are assessed through strain map that are observed above the base threshold. The adjacent of the high strain region are studied and analysed as an single feature. Statistics are then obtained for each feature, such as its length and maximum strain. The localised feature strains are shown in Figure 6-7 for the P-II and Cr-II samples, with a comparison against the background strains (i.e. the average background strains are negligible compared to the strain features). The locations of high strain are assessed to be the result of the surface displacement from regions of low compliance. Examples of these features can be seen in

Figure 6-1a. There is a general trend for increasing feature strain with increasing applied strain, although the data are noisy (i.e. the magnitude of the localised feature strains vary with applied strain).

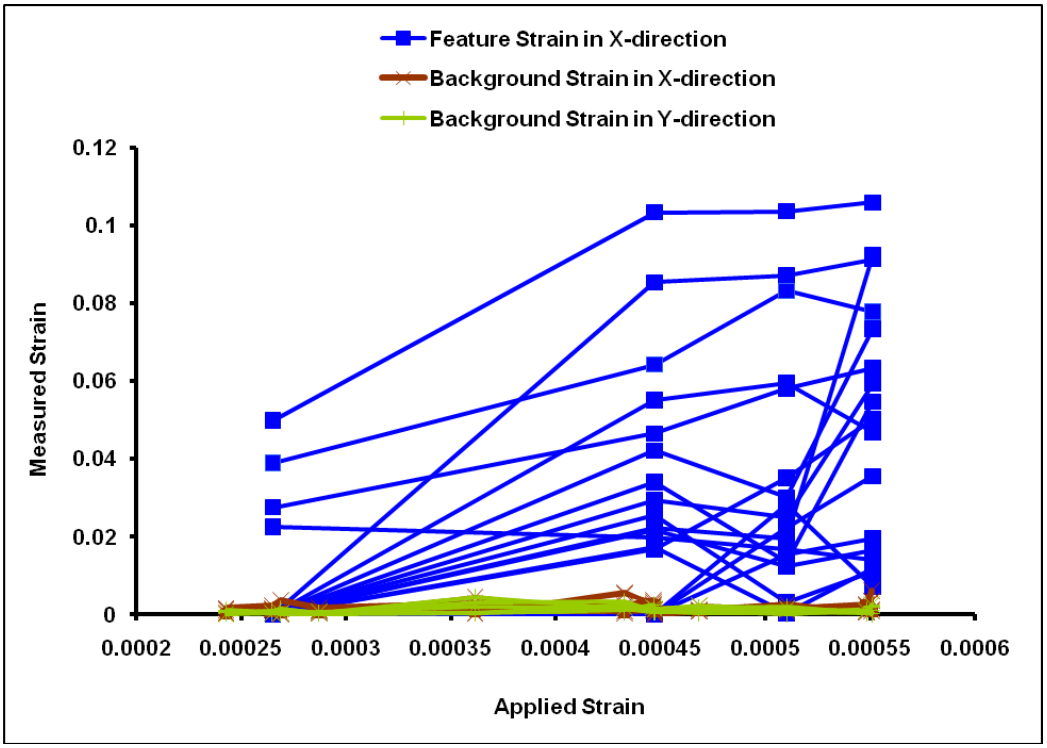

a)

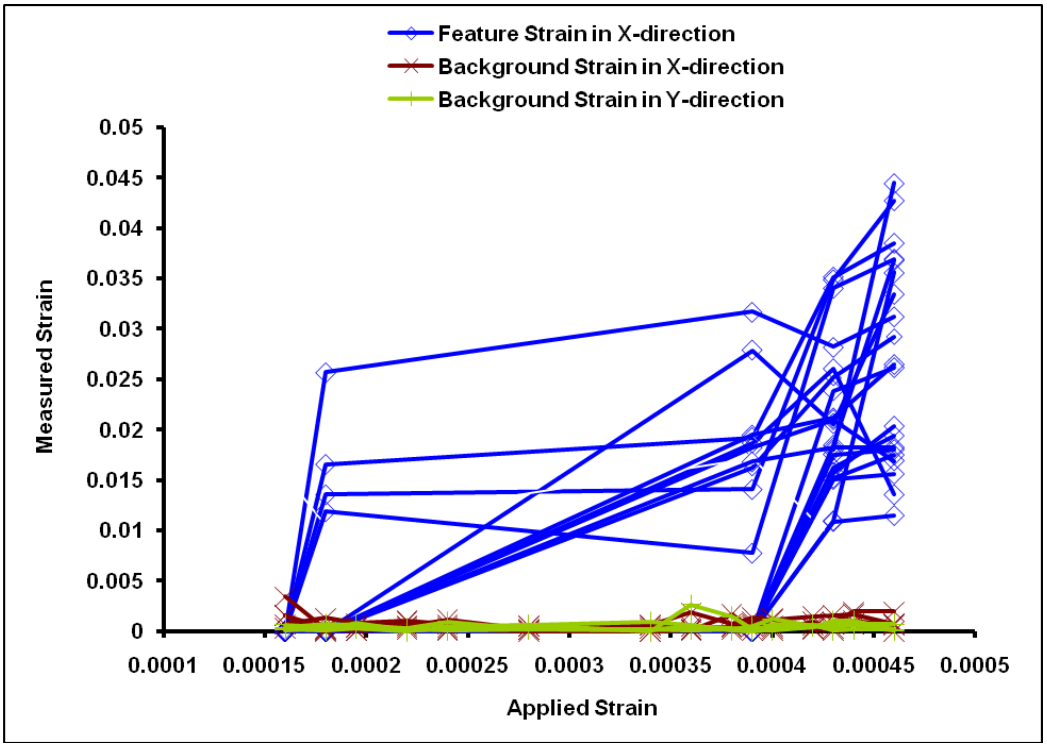

b)

Figure 6-7: Development of the peak feature strain for all the significant strain features which they observed using digital image correlation and background strain versus applied strain for the a) P-II specimen and b) Cr-II specimen. Background strain in X-direction is parallel to the applied bending stress; background strain in Y-direction is perpendicular to the applied bending stress. The background strain is measured in areas with no applied localised strains.

6.1.6 Effect of Threshold on Feature Detection

There are noise induced strain features observed in the strain map as shown in Figure 6-1a, and these features were removed using a high threshold as shown in Figure 6-1b. It was necessary to determine how the choice of threshold affected the population of detected features.

Segmentation and thresholding were used to identify and label these features and the sensitivity to the threshold was investigated (i.e. a threshold can be used to segment the strain map, relative to the background noise, to identify and label these strain features. This allows the development of their maximum strain with applied strain to be tracked). At each increment the detected features were ranked in order of size and then the cumulative probability was calculated for each feature. The number of detected features depends on the

strain increment. The statistical distribution of feature length for the experiment on P-II and Cr-II specimens (i.e. the effect of the strain threshold value on the measured distribution of the strain feature lengths) are shown in Figure 6-8. This shows that above a threshold of 0.002, the population is relatively stable, particularly for the larger features. This indicates that these strain features are being well detected for the lower threshold value. The higher threshold (0.01) loses part of the population at low applied strain, as shown in Figure 6-1b. At the lowest threshold (0.002) there are many more features observed using strain map as shown in Figure 6-1a. The uncertainty in length arises from the window size and overlap used for the DIC analysis.

The observed increase in feature length with applied strain may be due to a real increase in surface length (indicating stable crack growth) or it may be an artifact of the measurement strain being relatively close to the segmentation threshold. The threshold has some effect on the strain feature size are shown Figure 6-9a, and b. These show that same trend of increasing feature length with increasing applied strain, with higher values for the lower threshold.

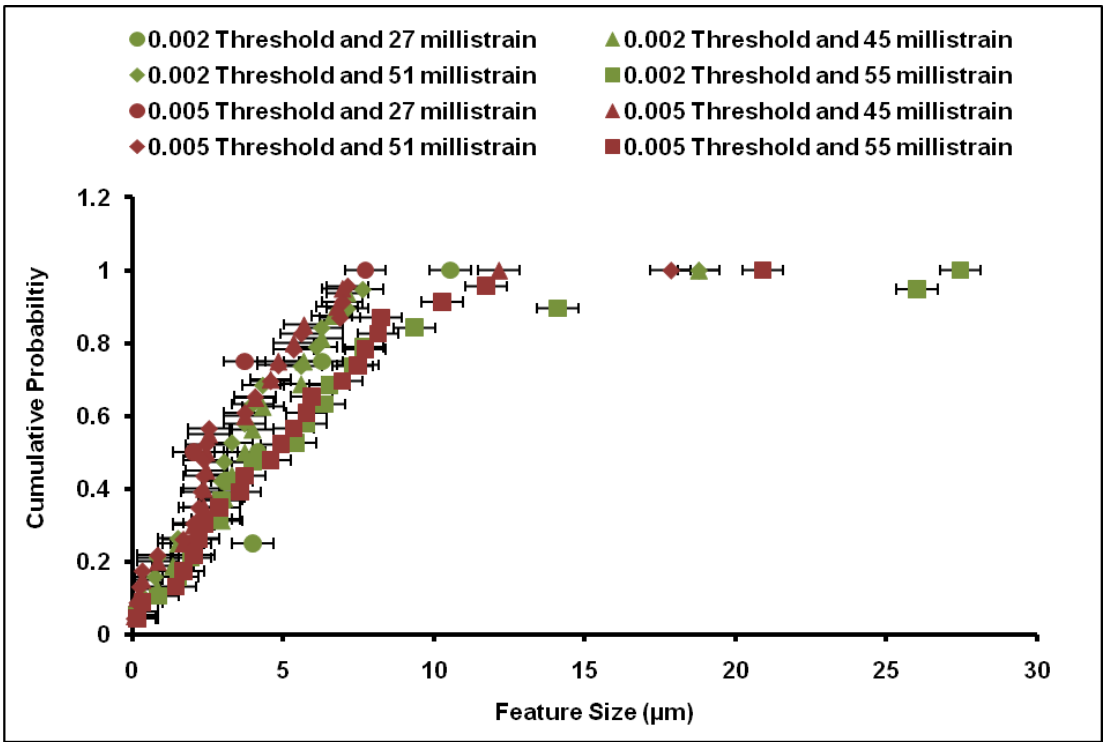

a)

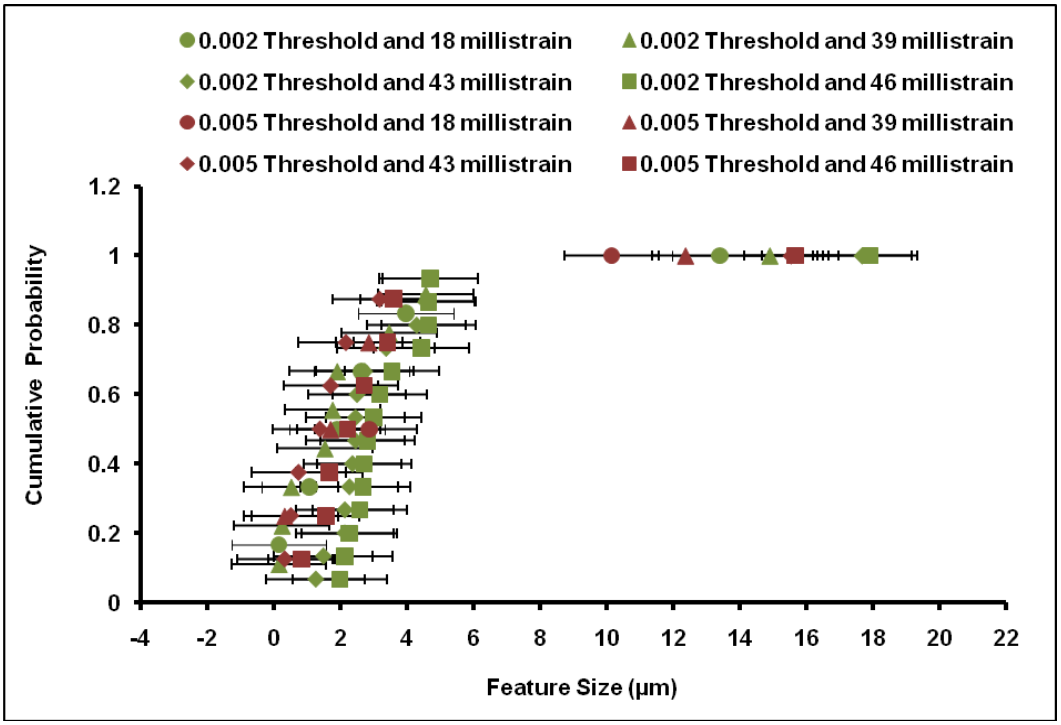

b)

Figure 6-8: Shows the relationship between the strain features size against cumulative probability of the observation of the particular feature size in the dataset at threshold (0.002) and threshold (0.005) at different applied strain for a) P-II specimen and b) Cr-II specimen. (i.e. feature size represents surface strains feature length). Legend describes the applied strain at which the features were measured.

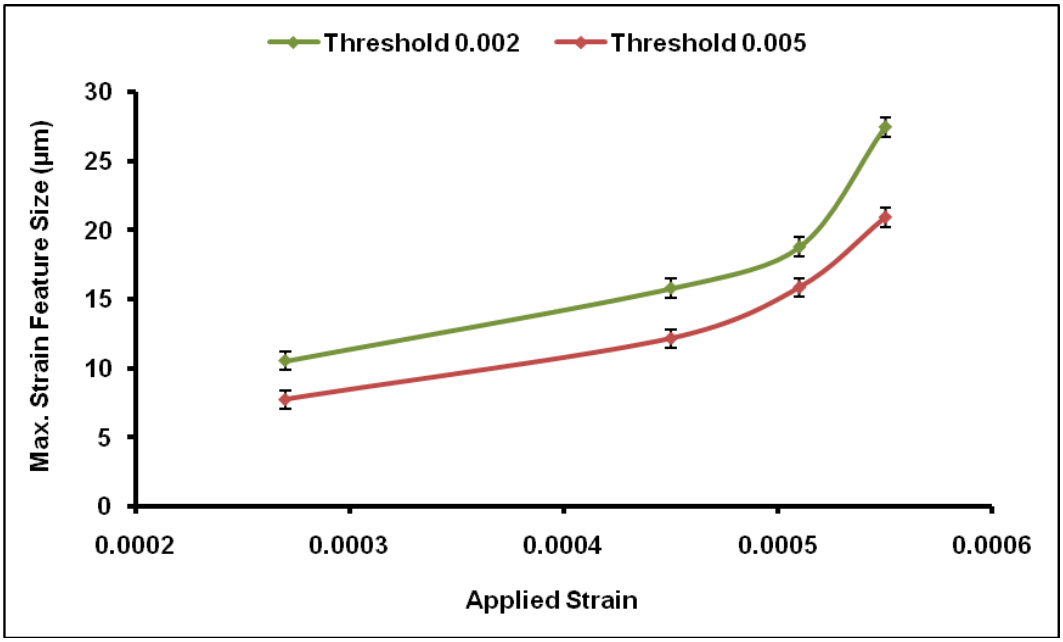

a)

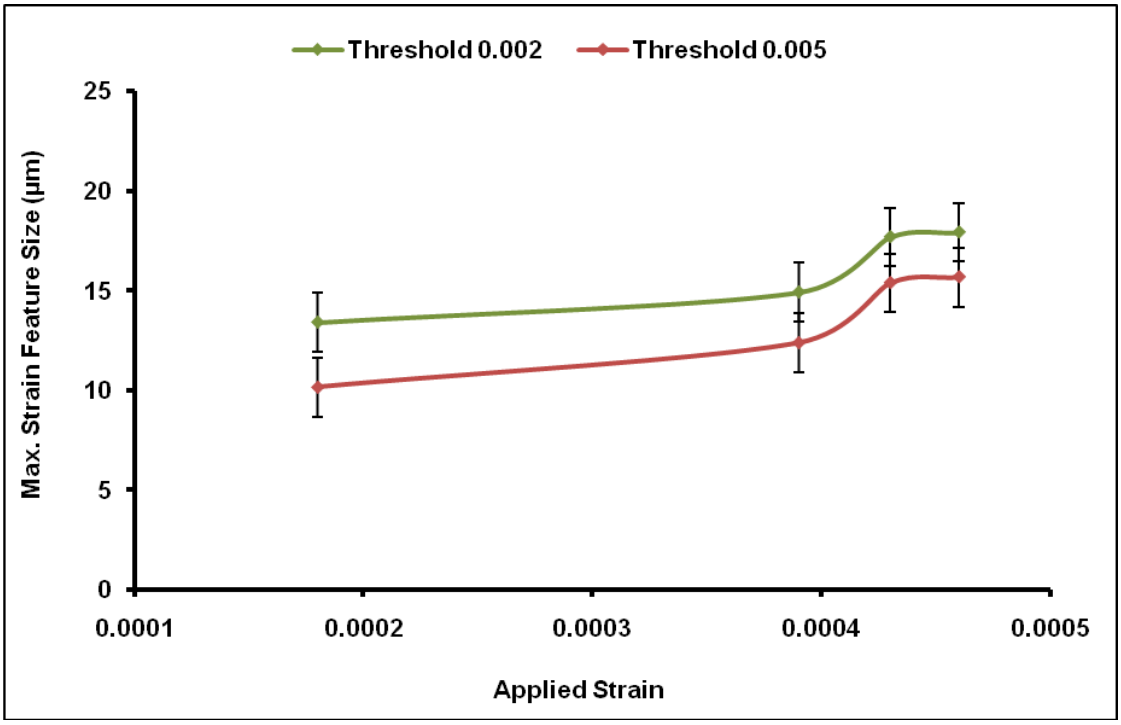

b)

Figure 6-9: Effect of segmentation threshold at different values (0.2% and 0.5%) on the maximum strain feature size using Matlab routine (i.e. crack track) against of the applied strain for the a) P-II Specimen b) Cr-II Specimen.

6.1.7 The strain feature locations for P-II Specimen

The crack nuclei were not observable in the raw images of the microstructure. The digital image correlation data from 25 different locations were stitched together to study a larger area of approximately (500×500 µm) as shown in Figure 6-10a, and the strain features were observed in the region marked using red squares. The microcrack locations for the P-II specimen are shown in Figure 6-10. The locations of the strain features are marked by yellow arrows. These locations are examined in more detail below.

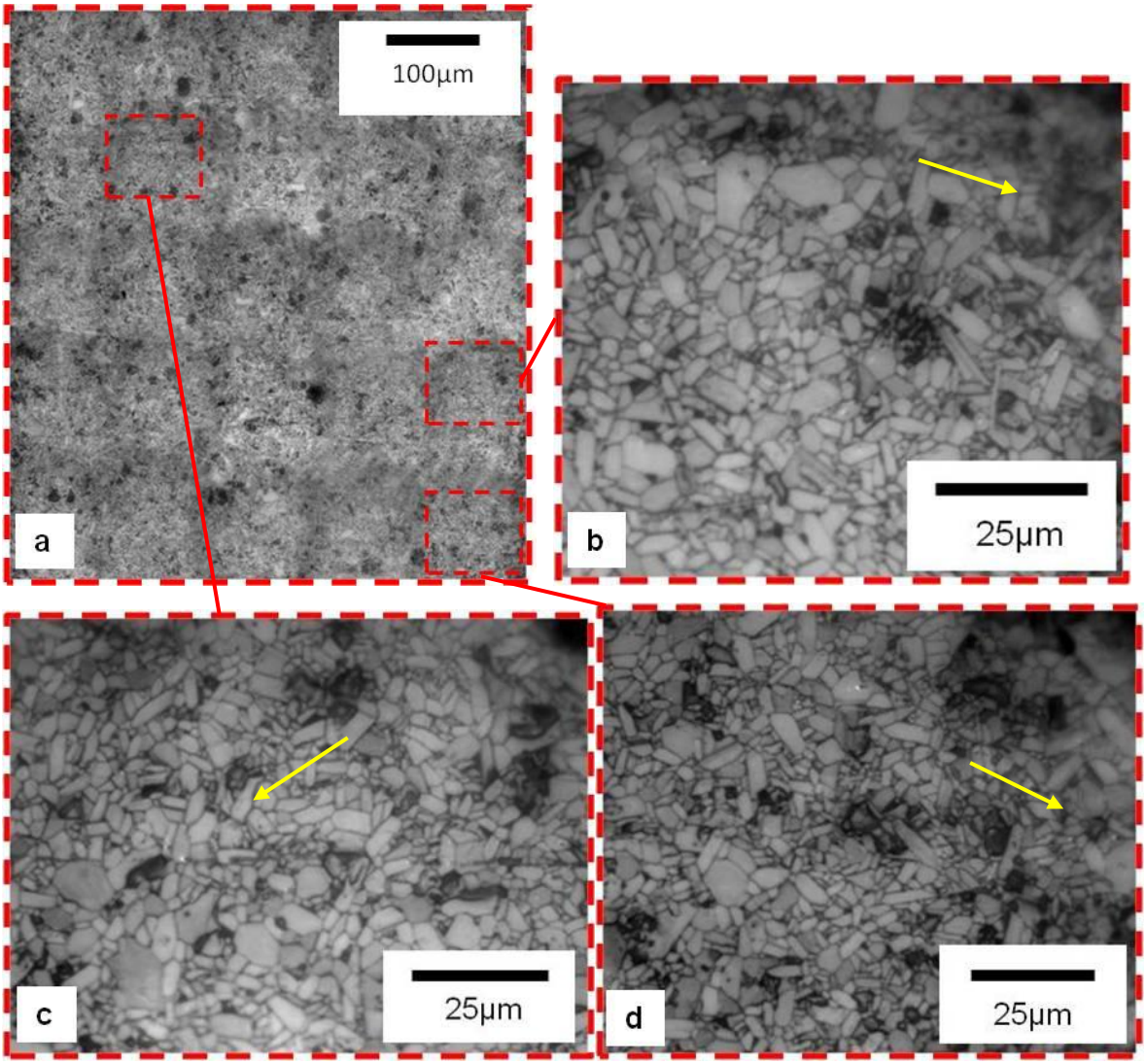

Figure 6-10: Shows the strain features location that observed using digital image correlation at different location and these microcracks non-visible on the raw images a) The data analysed at 25 different locations were stitched together for studying a larger area of approximately (500×500 µm), b) Magnification the location for feature B as shown in Figure 6-10a c) Magnification the location for feature A as shown in Figure 6-10a, and d) Magnification the location for feature C as shown in Figure 6-10a.

Comparison of the locations of these strain features with the microstructure image from which they are derived (see Figure 6-11) shows them to be coincident with grain boundaries, indicating that they are intergranular cracks. The strain features were not associated with porosity, and appear along boundaries that tend to be perpendicular to the applied stress. DIC was achieved on the series images; using window size and overlaps as mentioned in Section (3.3.4.1) to provide a high density displacement vector. An image of

the X-direction strain features overlaid on the optical images and scanning electron microscope images is shown in Figure 6-11 at an applied strain of 0.00027. The X-direction is perpendicular to the cracks (strain features) and parallel to the applied tensile load.

The image correlation data were used to identify strain features and the strain features are shown in Figure 6-11. The optical micrograph and the scanning electron microscope, SEM image shows the strains can be associated with grain boundaries.

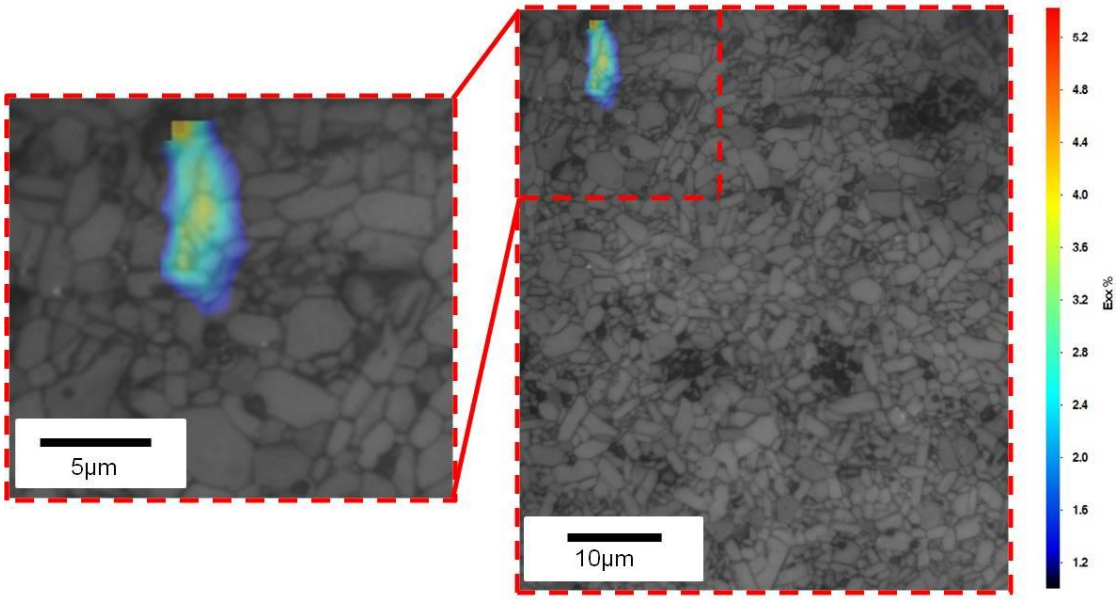

i) Optical Image

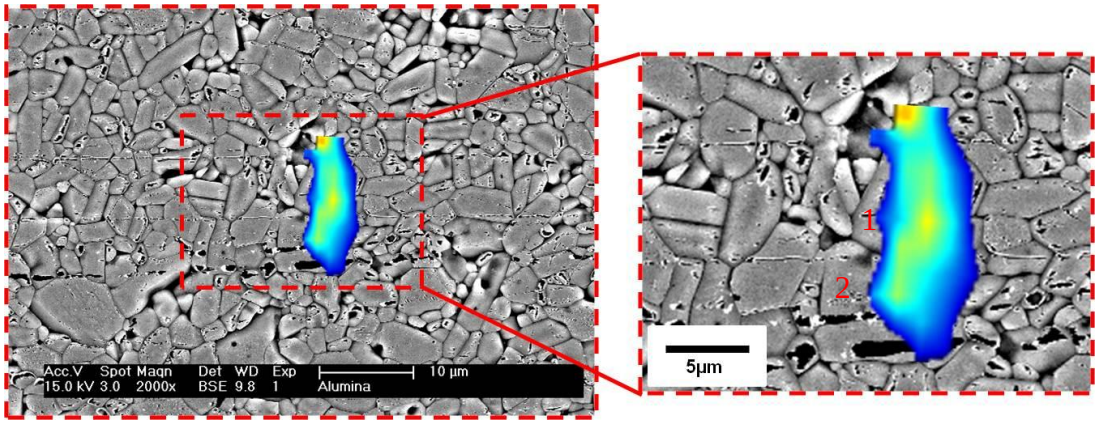

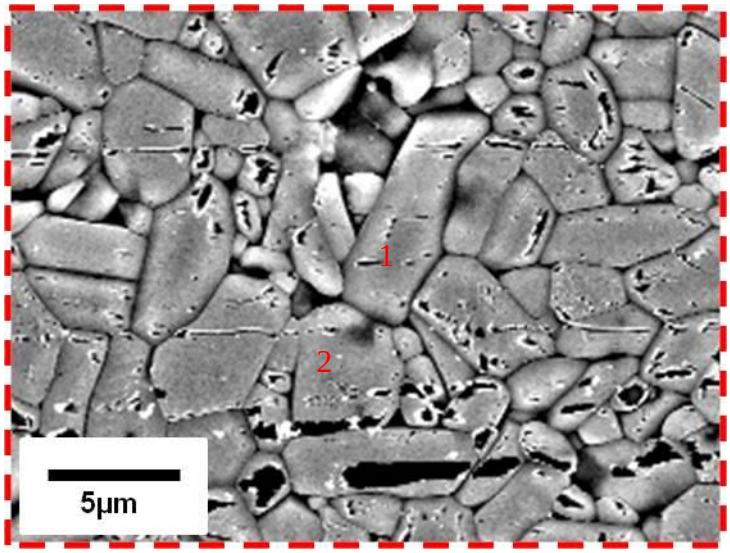

ii) SEM Image

a) Strain Feature A

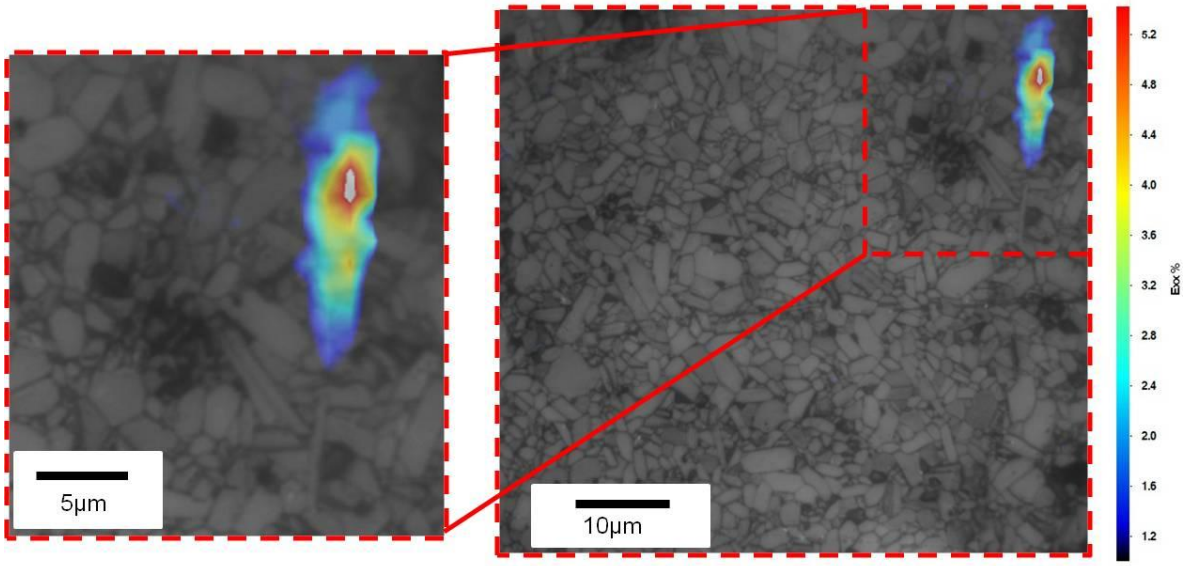

i) Optical Image

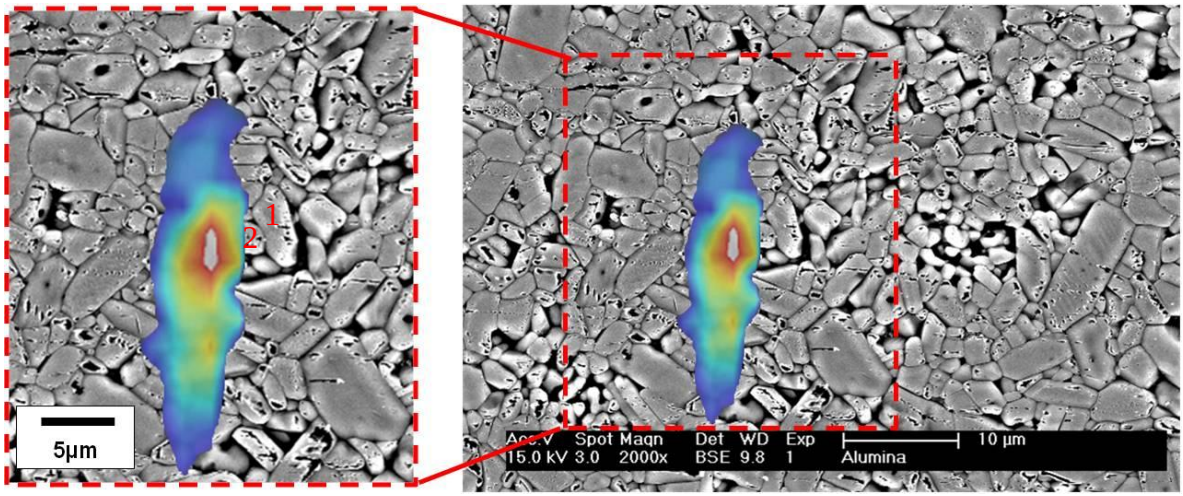

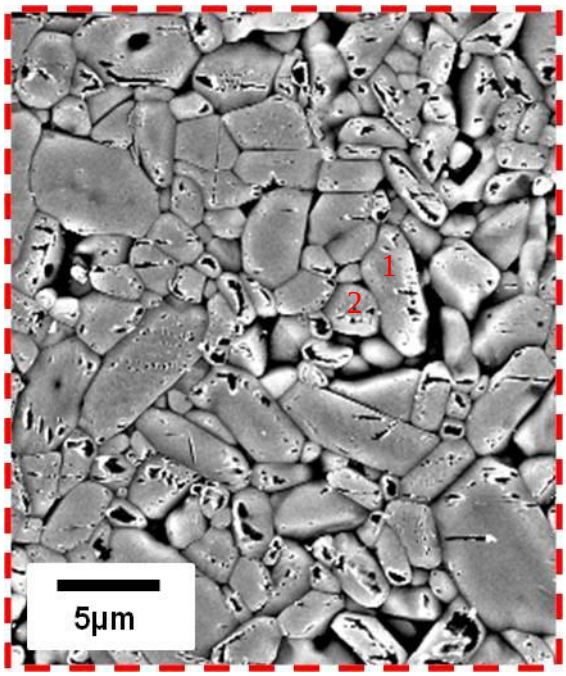

ii) SEM Image

b) Strain Feature B

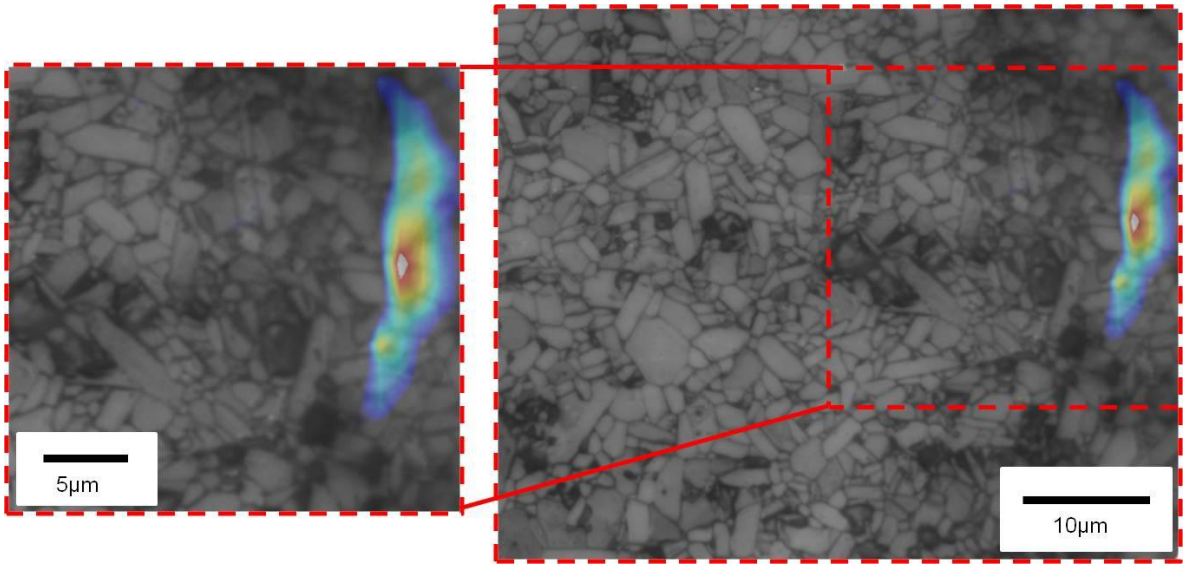

i) Optical Image

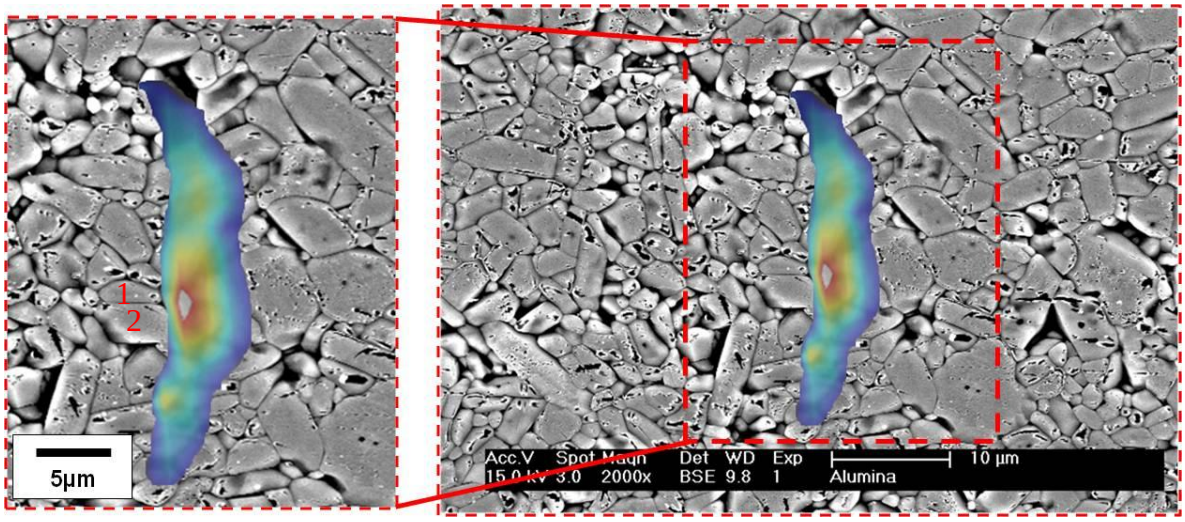

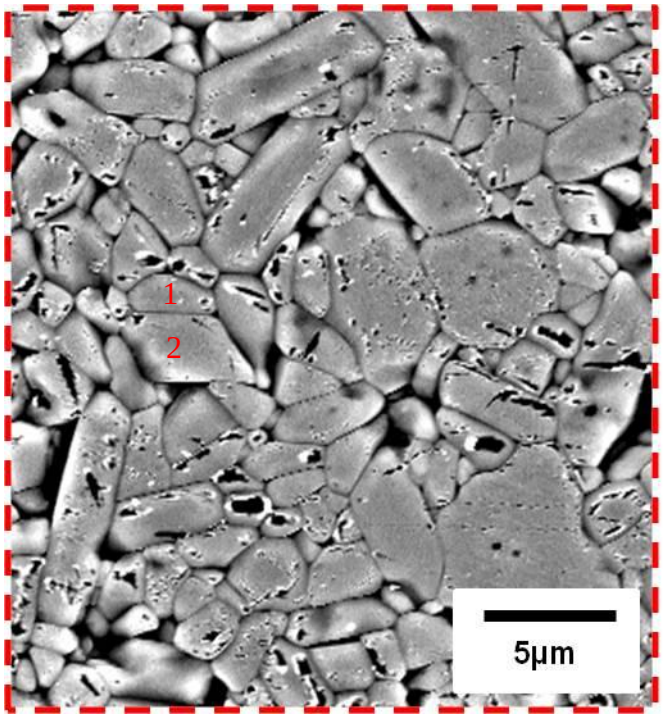

ii) SEM Image

c) Strain Feature C

Figure 6-11: Overlaid the strain features from strain map using digital image correlation on the optical images and scanning electron microscope images at applied strain 0.00027 for P-II specimen for different strain features a) Strain feature A, b) Strain feature B, and c) Strain feature C. The numbers on the SEM images show the closest grains from these strain features.

6.1.8 The strain feature locations for Cr-II specimen

The crack nuclei were not observable in the raw optical images as mentioned early in section (6.1.7) for the P-II sample. The results are shown in Figure 6-12 and Figure 6-13.

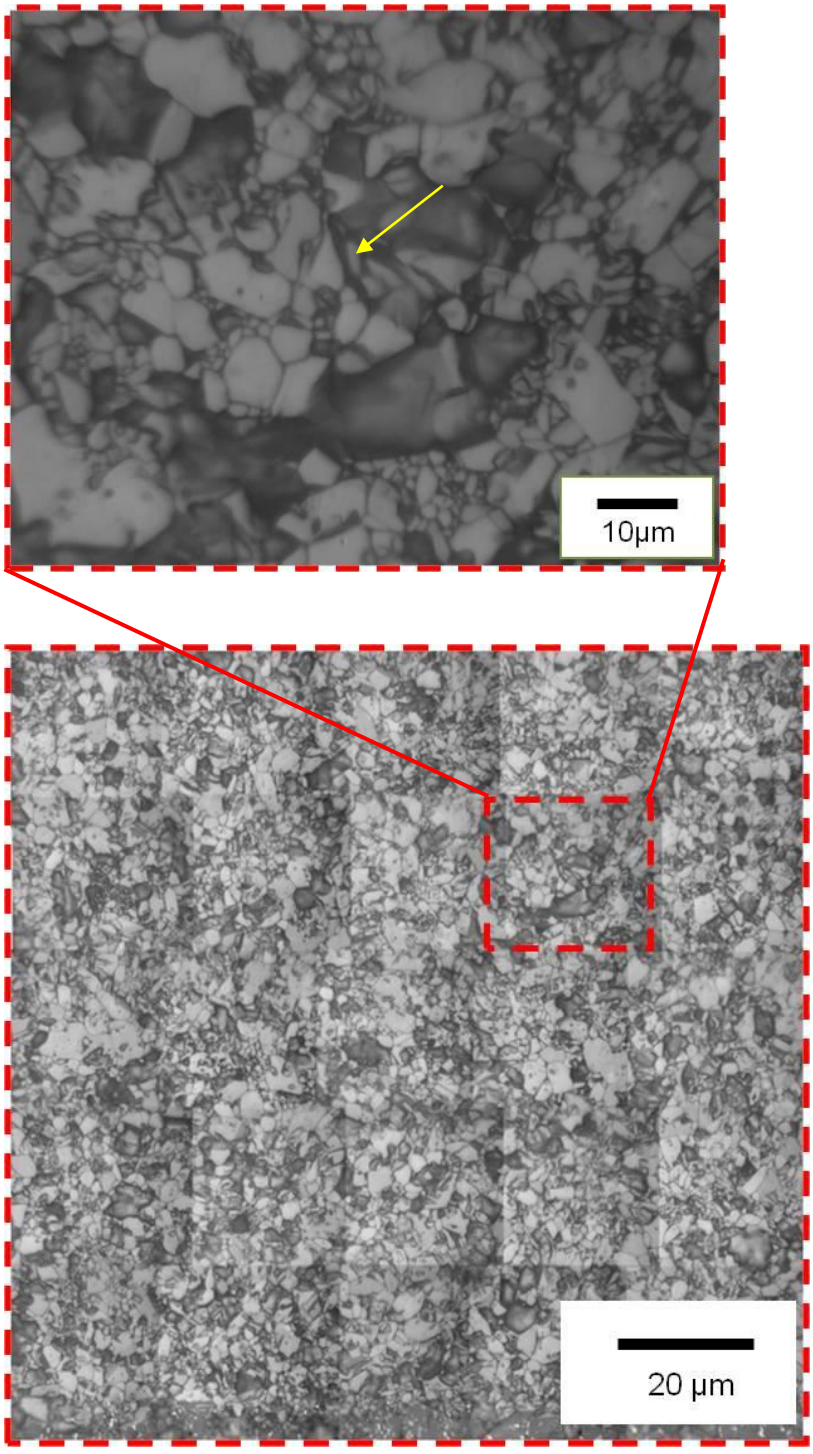

a)

b)

Figure 6-12: Shows the strain feature location that observed using digital image correlation at a certain location and these microcracks are invisible on the raw images a) Magnified the red square (see Figure 6-12b) which was represented the strain feature location as marker by the yellow arrow, b) The analyses area from 25 different locations were stitched together to study larger area of approximately (500×500µm).

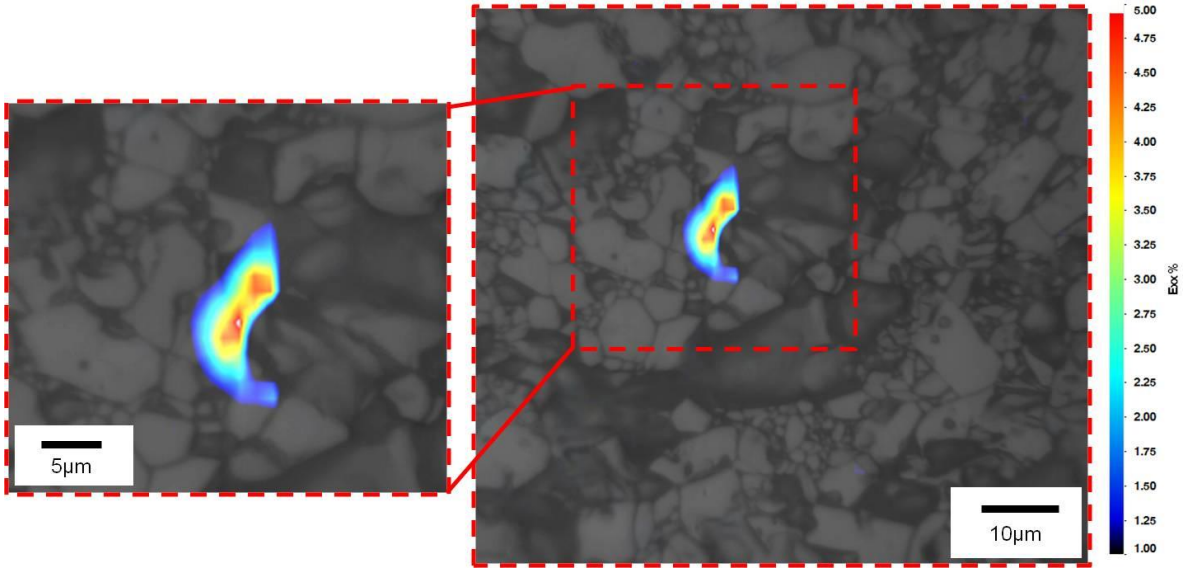

a) Optical Image

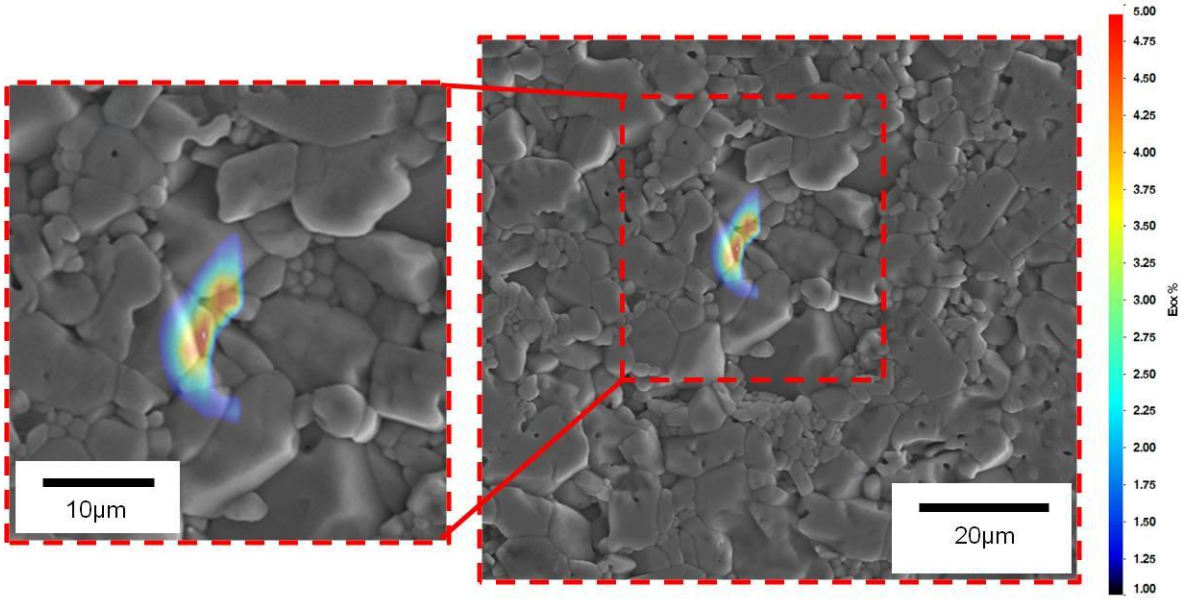

b) SEM Image

Figure 6-13: Overlaid the strain feature on the strain map using DIC on the a) Optical image and b) Scanning electron microscope image for the Cr-II sample at applied strain (0.00046). The dotted red square shows the area of interest for these strain features.

6.1.9 Behaviour of the Strain Features using Line Profile for P-II specimen

Surface displacements due to the tensile load using four point bending test were measured for strain features A, B, and C by digital image correlation analysis. An X-direction

displacement map is overlaid on the optical image to show the strain features at different location as shown in Figure 6-14 at applied strain is 0.00055.

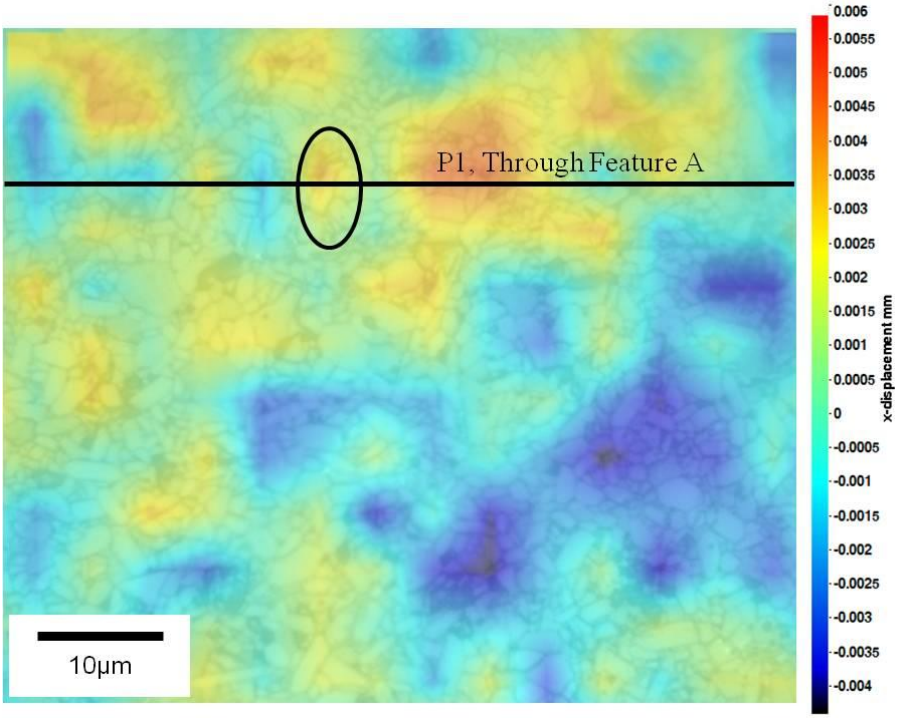

a) Strain Feature A

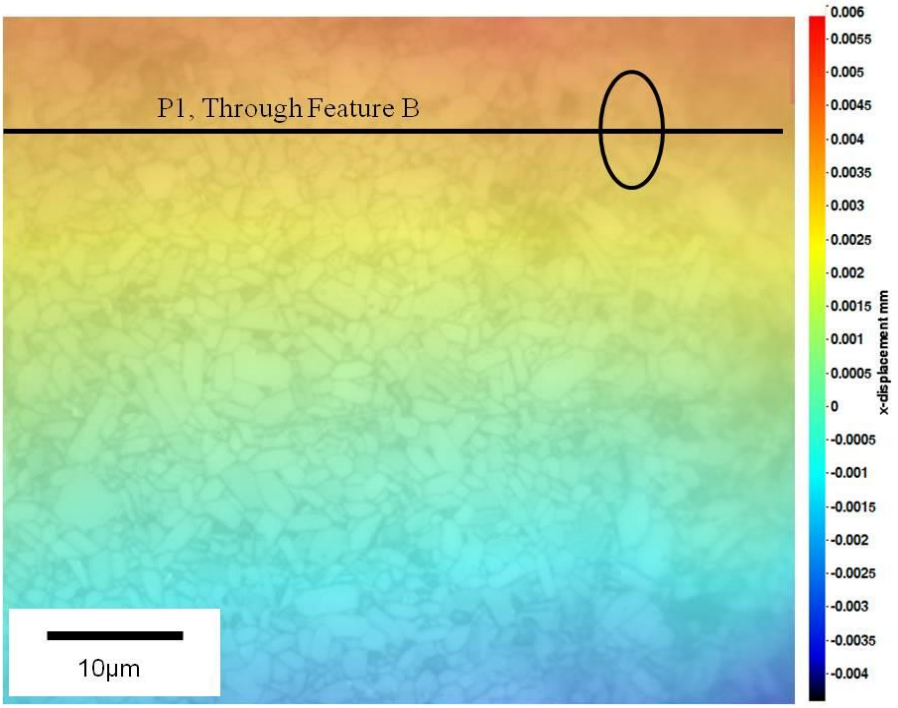

b) Strain Feature B

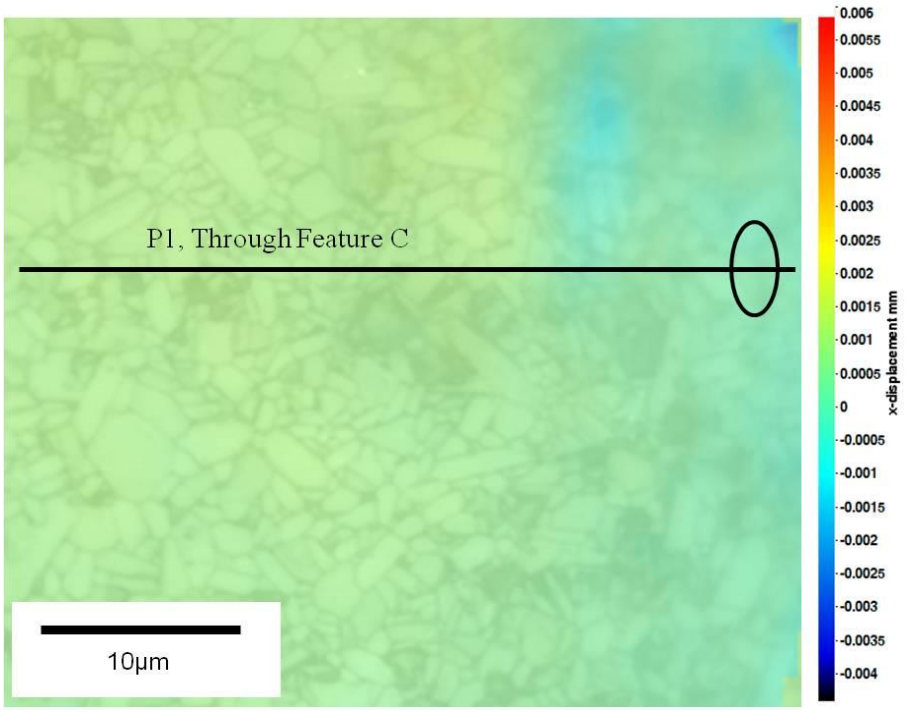

c) Strain Feature C

Figure 6-14: The displacement map in x-direction using DIC overlaid on the optical image using window size 64×64 pixels and overlap 50%, applied strain is (0.00055). The strain feature location was positioned using black ellipse marker. The black line shows the line profile through the strain feature in P-II specimen using DIC for a) Strain feature A, b) Strain feature B, and c) Strain feature C.

The analysis followed the method used for the FE model in section (4.2.7.1), in which the displacement profiles along the line (P1) through the feature and the background trend (P13) were compared. The displacement plots in X-direction were measured using LAVision Davis (line profile method) at the location through the strain features (A, B, and C) (i.e. P1) and also the displacement through these strain features was normalised using a best fit line (i.e.P13) using function SLOPE and INTERCEPT and this method gives a line of best fit for a set of data points as shown in Figure 6-15. The displacement results were taken at window size and overlap as mentioned before in Section (3.3.4.1). The effect of applied strain (evaluated using the strain gauge) is shown in Figure 6-15. The locations of the observed strain features are shown Figure 6-14.

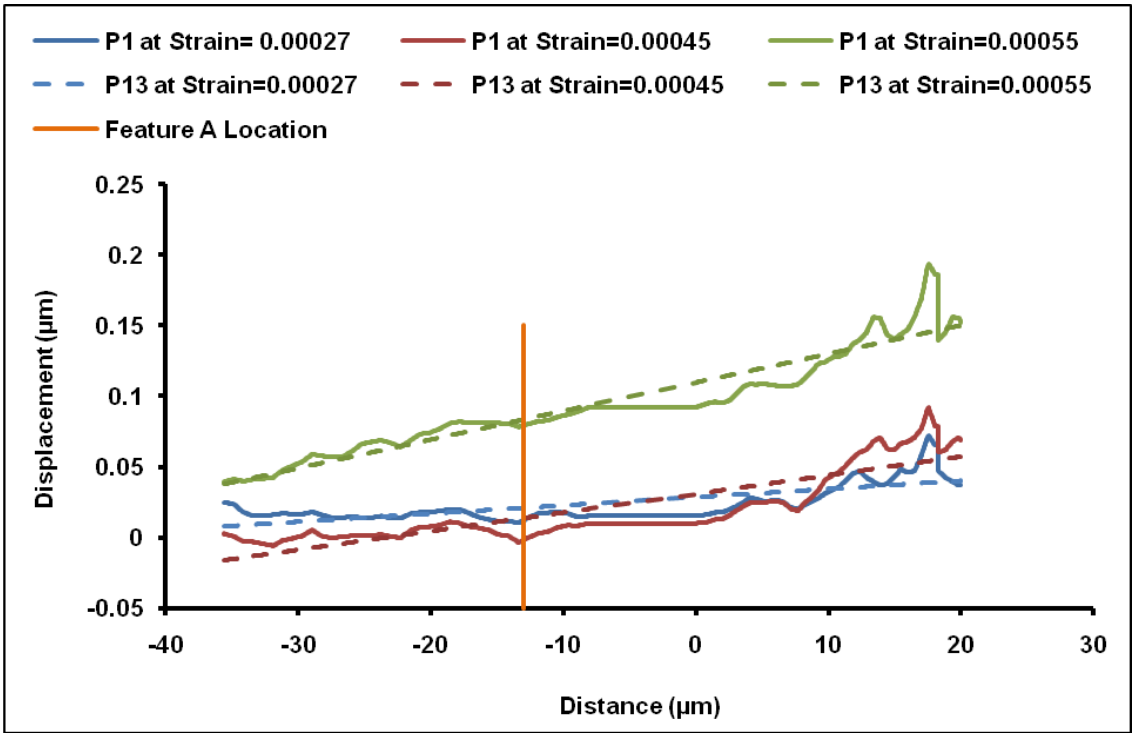

i) Strain Feature A with entire a data set (i.e. distance from -35 µm to 19 µm)

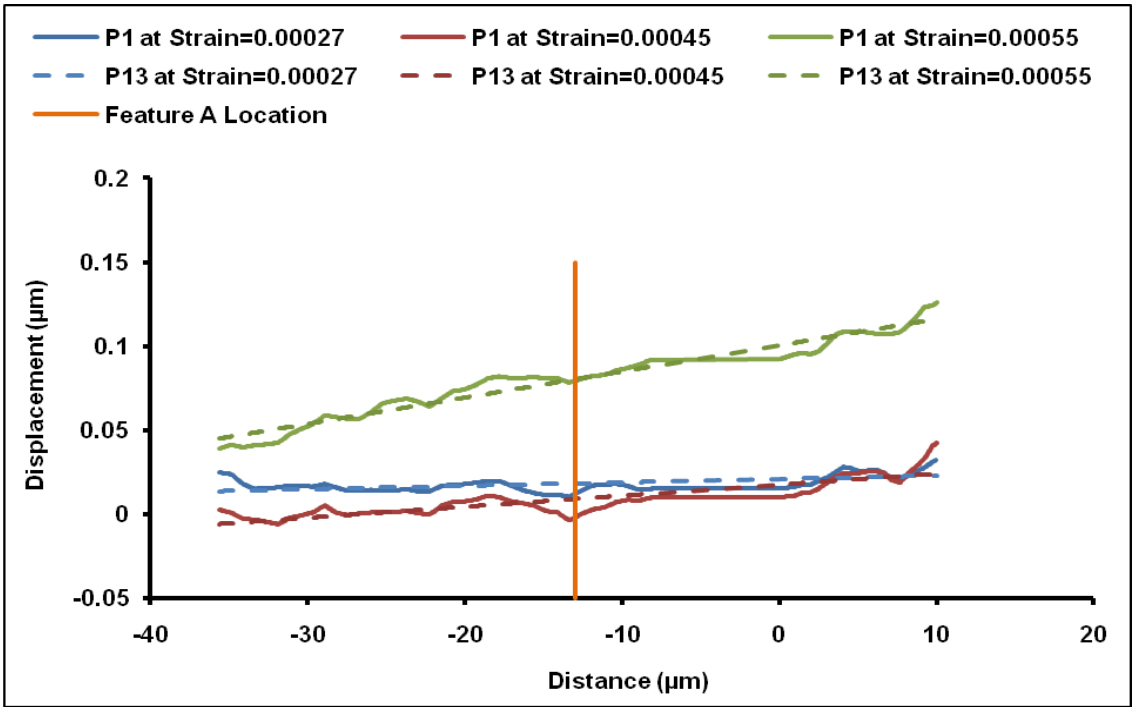

ii) Strain Feature A after cutting off the noise from the data set (i.e. distance from -35 µm to 10 µm)

a) Strain feature A

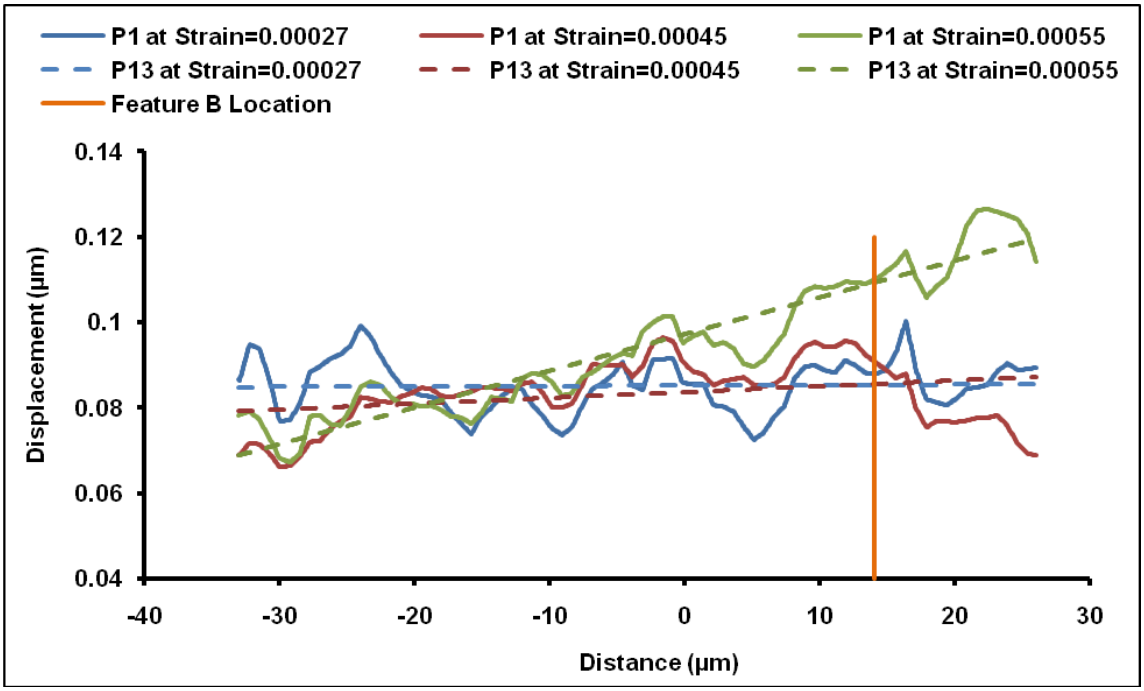

b) Strain feature B

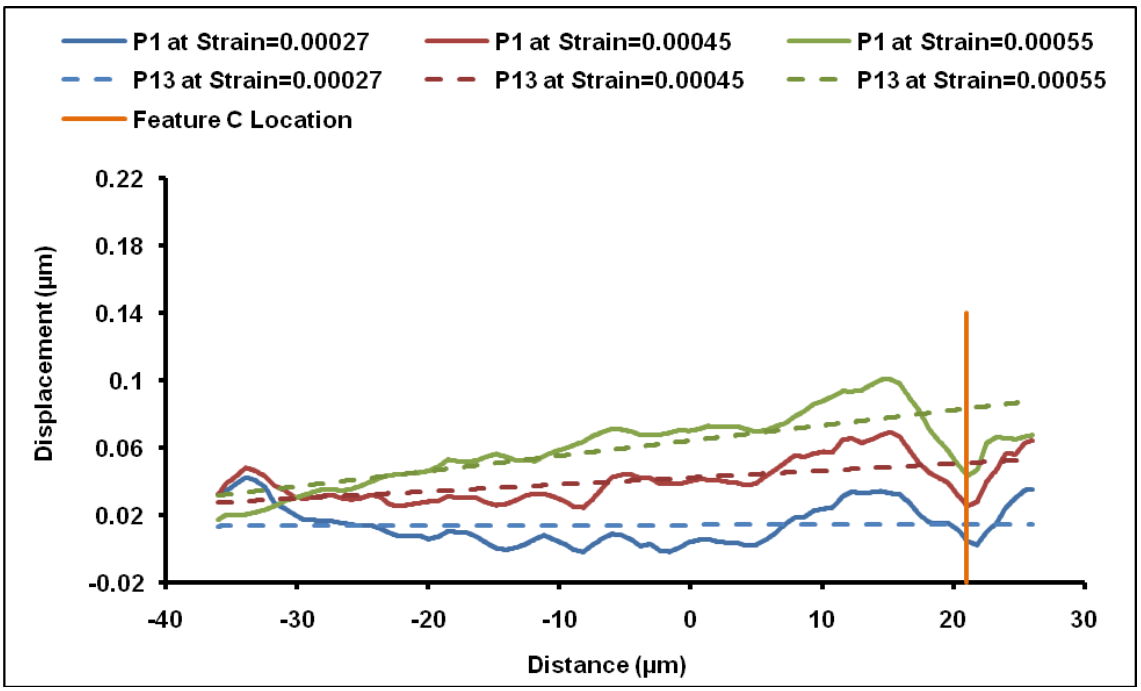

c) Strain feature C

Figure 6-15: Shows the vector displacement against the distance from the left of the viewed area in X-axis for different strain features and also, showing the best fit for the displacement through the strain features for a) Strain feature A, b) Strain feature B and c) Strain feature C. Interrogation window size and overlap as mentioned before in the Section (3.3.4.1) at different applied strains.

The displacement difference was measured between the displacement through the strain feature in line P1 and the displacement in line P13 (i.e. P13 represents the displacement for the best fit line of the displacement across the strain feature). The difference between the displacements in path through the strain feature and best fit for the displacement through the strain feature and also, the location of the observed strain features are shown in Figure 6-16, as a function of applied strain.

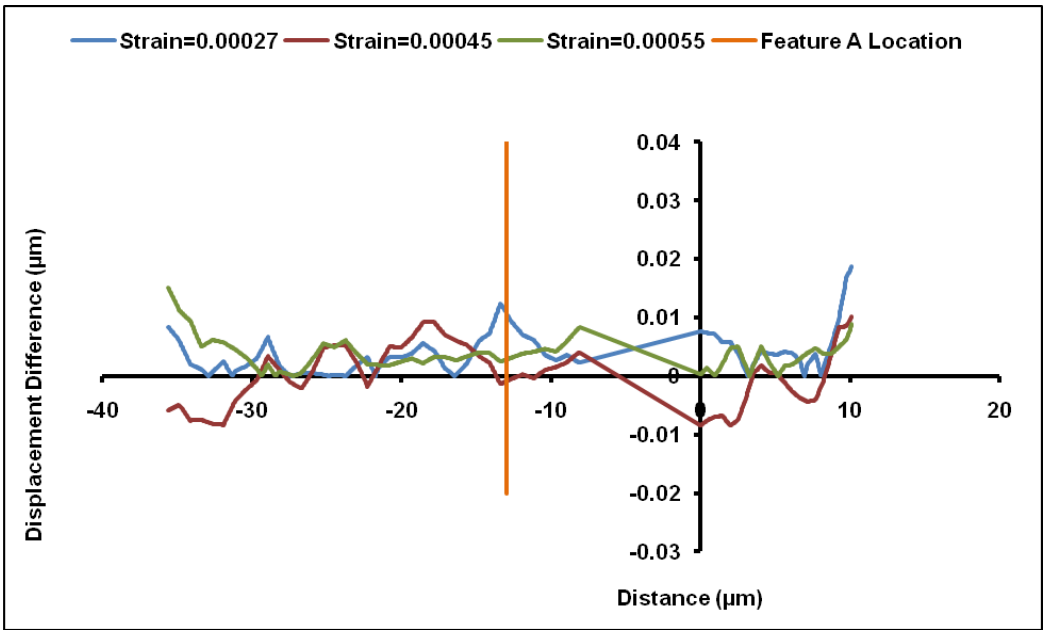

a) Strain Feature A

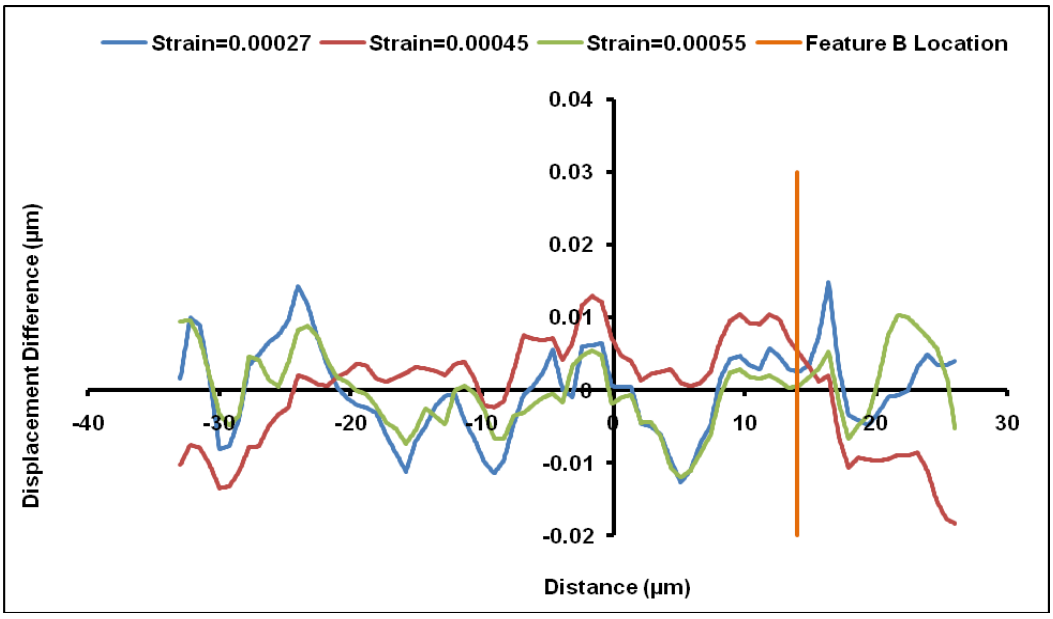

b) Strain Feature B

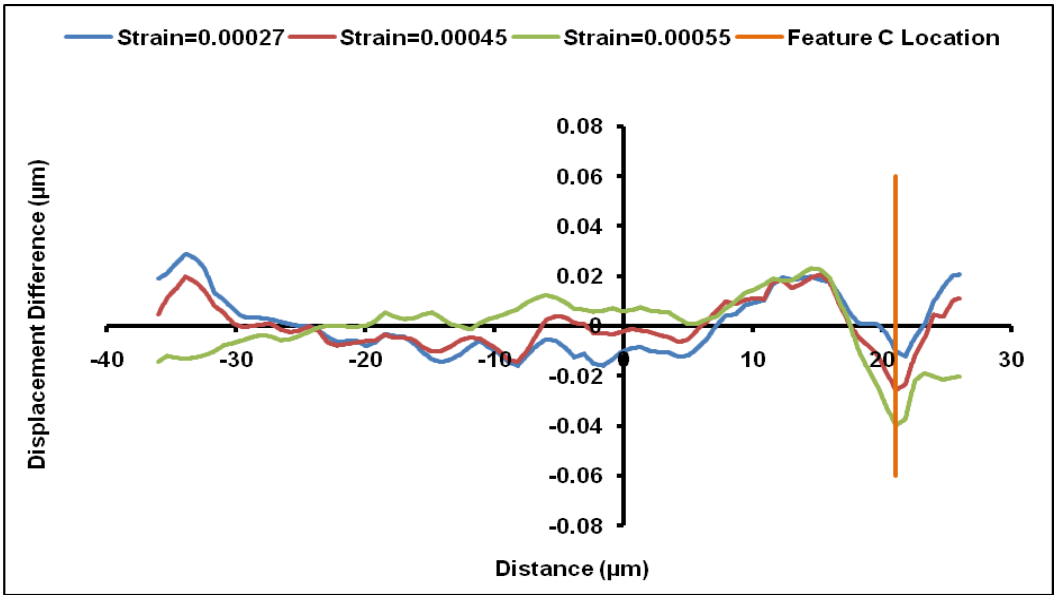

c) Strain Feature C

Figure 6-16: The difference between the displacement through (across) the strain feature and the best fit for the displacement through the strain feature as a function of the distance on each side of the strain feature at window size and overlaps as mention before in section (3.3.4.1) and also, at different applied strain for a) Strain feature A, b) Strain feature B, and c) Strain feature C.

6.1.10 Behaviour of the Strain Feature using Line Profile for Cr-II specimen

Surface displacements due to the applied load using a four point bending test were measured for strain feature by digital image correlation analysis. An X-direction displacement map is overlaid on the optical image to show the strain feature at the specific location, where applied strain is (0.00046) as shown in Figure 6-17 and the method mentioned before for P-II sample in section (6.1.9). The window size and overlap were mentioned in section (3.3.4.1).

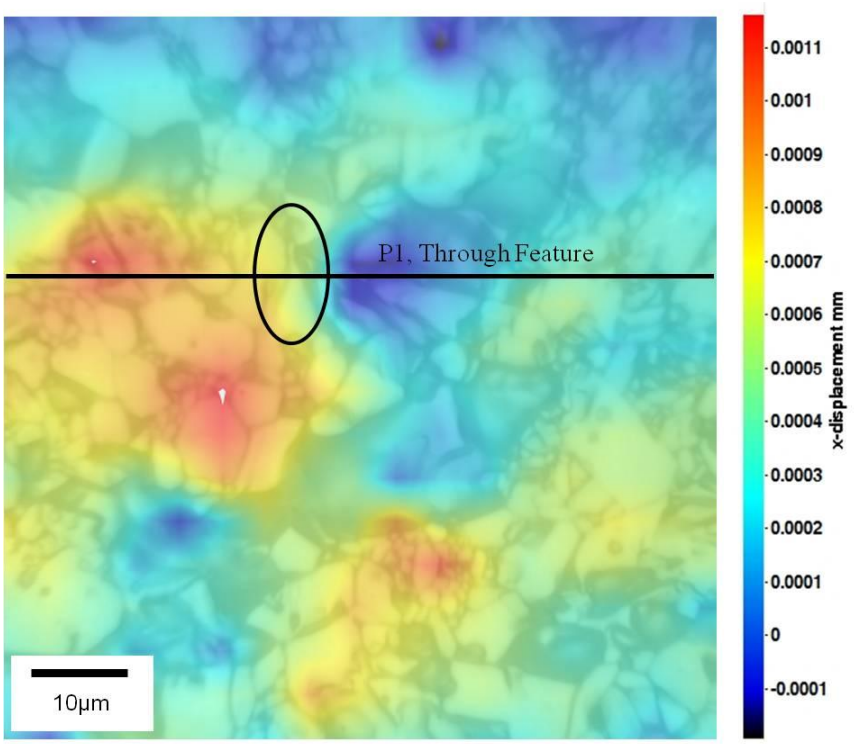

Figure 6-17: The displacement map overlaid on the optical image using window size and overlap as mentioned in section (3.3.4.1) at applied strain of (0.00046). The strain feature location was positioned using a black ellipse marker and also, the black line shows the line profile using DIC through the strain feature for Cr-II specimen.

The displacement plots in X-direction were measured using digital image correlation as shown in Figure 6-17 as mention before for P-II sample. The displacement results were taken using window size and overlap as mentioned previously in Section (3.3.4.1). The effect of applied strain (evaluated using the strain gauge) on the displacement is shown in Figure 6-18.

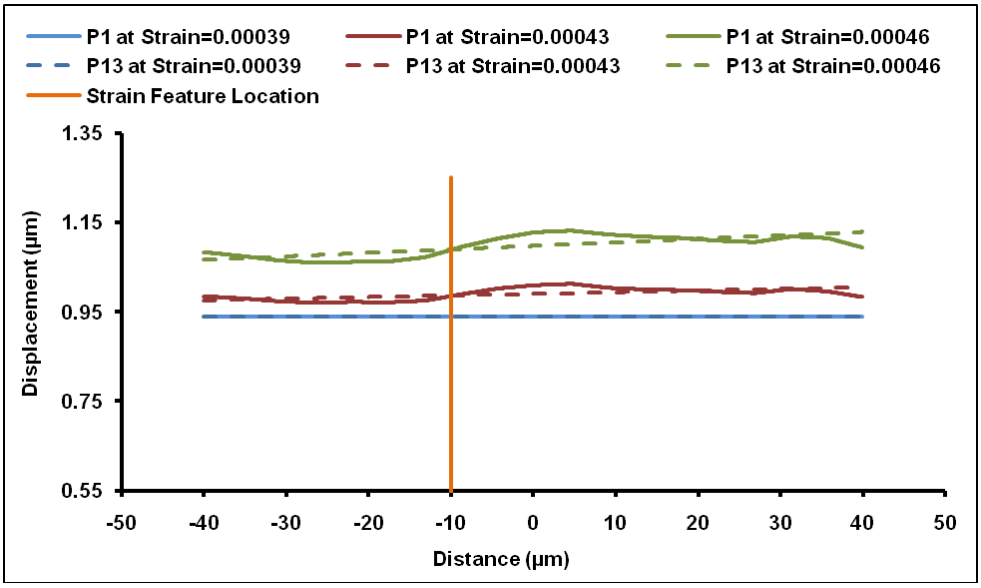

Figure 6-18: Shows the vector displacement against the distance from the left of the viewed area in x-direction for the displacement through the strain feature. Also shown is the best fit for the displacement through the strain feature at different applied strains. Interrogation window size and overlap as mentioned previously in section (3.3.4.1).

Figure 6-19 is used to measure the displacement difference between displacements on two lines as mentioned previously for P-II sample in section (6.1.9) as a function of applied Strain is shown in Figure 6-19.

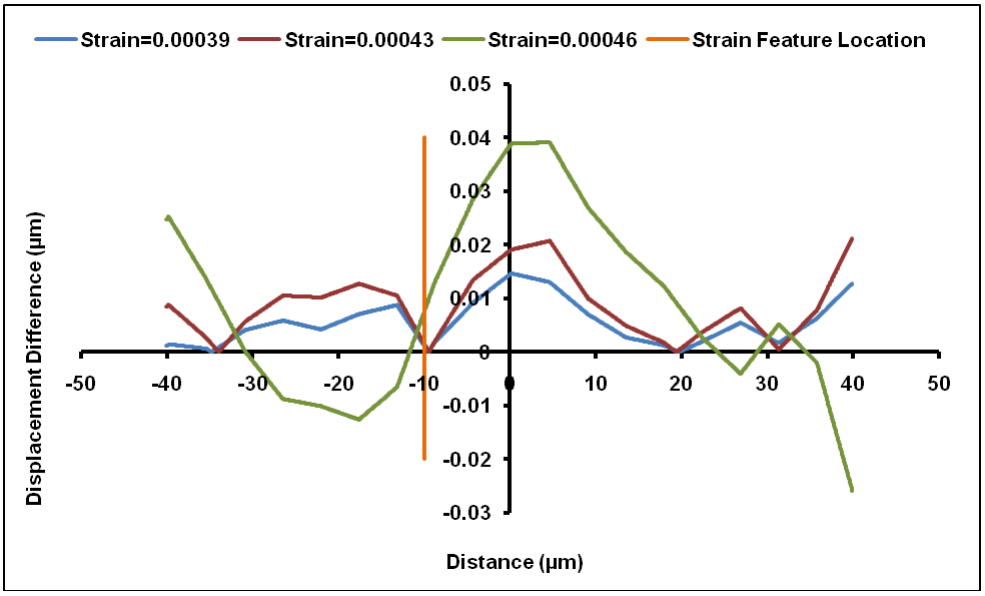

Figure 6-19: The displacement difference between the displacement through (across) the strain feature and the best fit line for the displacement through the strain feature as a function of the distance on each side of the strain feature at window size and overlaps as mention early in section (3.3.4.1) at different applied strains for the Cr-II sample.

6.2 Grain Boundary Plane Analysis

6.2.1 Preparation of the surface for electron backscatter diffraction, EBSD

The P-II specimens were prepared for electron backscatter diffraction using different methods as mentioned in the experimental chapter in Section (3.4). The CAMSCAN microscope was used to assess the surface by check the indexing (Kikuchi Patterns). The mechanical polishing procedure was used to prepare the sample surface of interest for EBSD and the surface was assessed using a CAMSCAN microscope and the indexing (Kikuchi Patterns) was about 60% and the step size was (0.5µm). The results show the surface preparation for electron back scatter diffraction are shown in Figure 6-20.

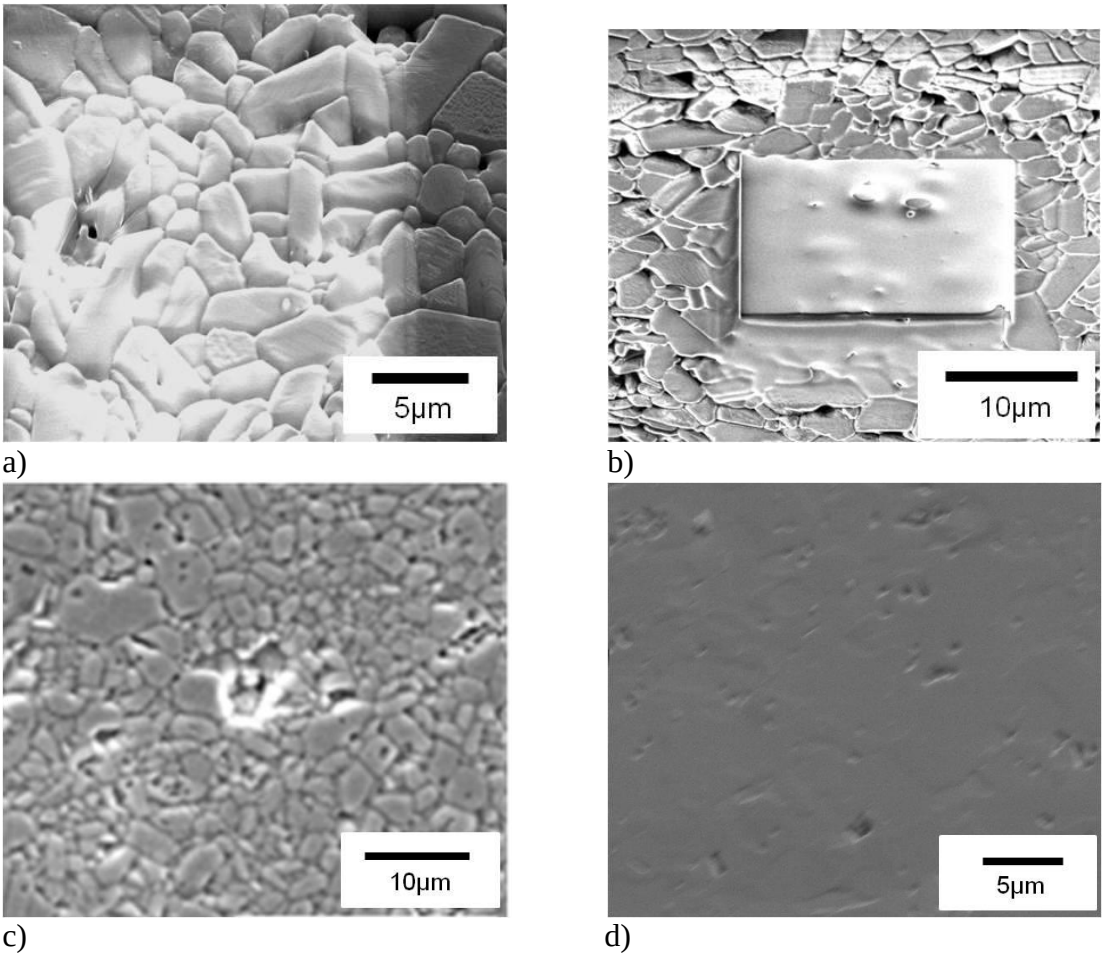

Figure 6-20: Shows the surface preparation for electron backscatter diffraction using different techniques for P-II specimen a) Using FIB to remove gold coating, b) Using FIB to remove gold coating and thin layer of the etched layer, c) Using Gatan machine to remove gold coating and thin layer of the etched layer, and d) Using mechanical polishing to prepare the surface for EBSD. These techniques are described in detail in chapter in Section (3.4).

The focused ion beam (FIB) was used to find out the region of interest for P-II specimen and Cr-II specimen using slots as reference markers, as shown in Figure 6-21, and then work out the position of the feature relative to these markers. The region of interest was polished using mechanical polishing to achieve the EBSD map. The sample was tested to check the indexing (Kikuchi Patterns) using a scanning electron microscope (CAMSCAN). Typically the indexing was about (50%-60%) with a step size of (0.5 μm).

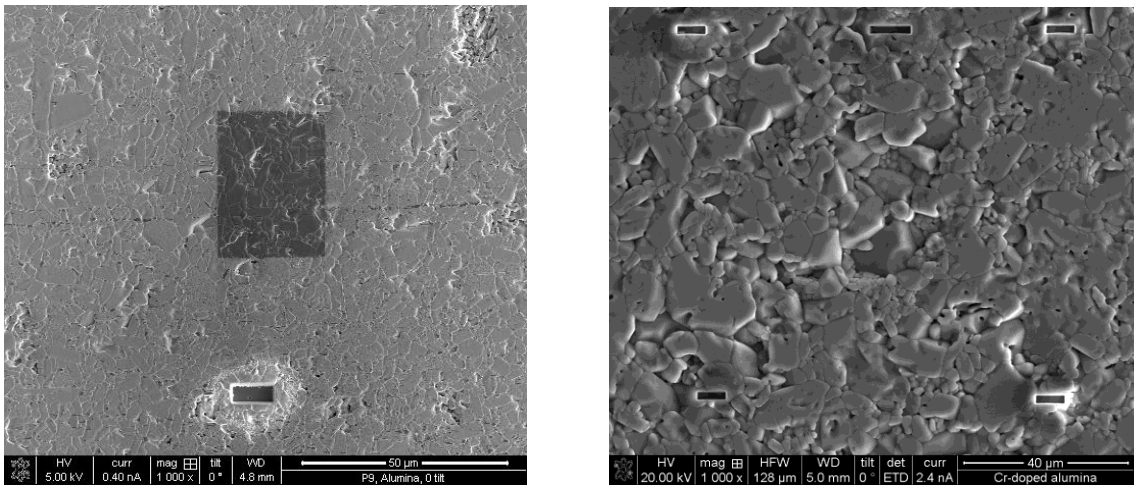

a) b)

Figure 6-21: The regions of interesting for the a) strain feature A in P-II specimen and b) strain feature in Cr-II specimens. The cracks observed on these regions using digital image correlation.

6.2.2 Grain Boundary Plane Procedure

The grain boundaries of interest was analysed using focused ion beam samples allows grain boundary planes to be calculated as shown this method in [100, 108] for the P-II specimen and Cr-II specimen. The true angles α and β showing the three dimensional orientations of the grain boundary of interest are determined from FIB specimen.

Two FIB cross sections were made to study grain boundary planes in the P-II and Cr-II samples. The FIB cross section had a depth of between 5 and 10 μm and was cut out perpendicular to the interesting grain boundaries. The grain boundary plane was then calculated using the method explained in reference [100, 108]. The trench was cut out perpendicular to the grain boundary of interest for measuring the projected and true grain boundary angles with different tilting angles for the P-II and Cr-II samples.

6.2.2.1 Focused Ion Beam for P-II and Cr-II Samples

6.2.2.1.1 Strain Feature A for P-II Specimen

The aim of the electron backscatter diffraction (EBSD) is to determine the grains orientations adjacent to the crack (boundaries of interest). Figure 6-22 shows the scanning electron microscope image and the electron backscatter diffraction map for the grain boundary of interest (cracked boundary). Yellow arrows show the grain boundary of interest as shown in Figure 6-22.

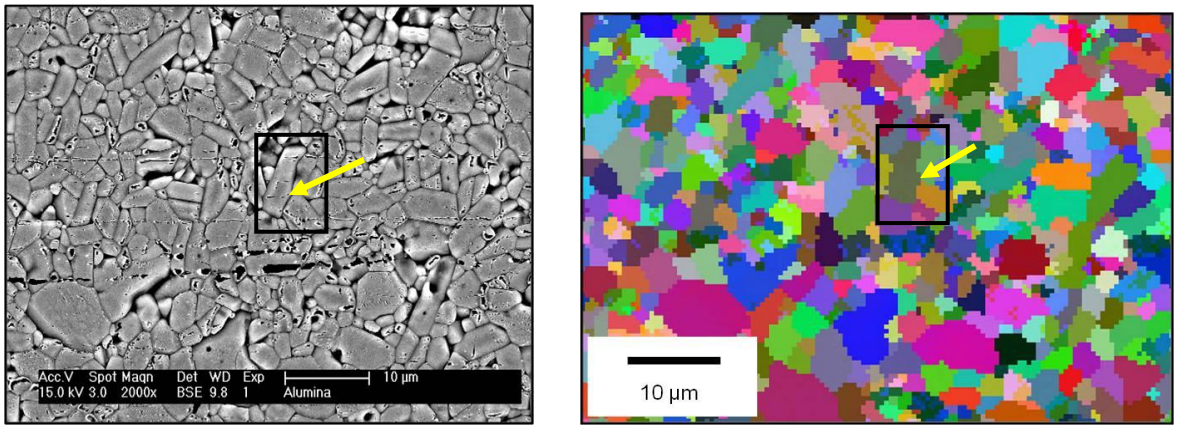

a) b)

Figure 6-22: a) Shows the SEM image for the grain boundary of interest and b) Shows the electron backscatter diffraction for the orientation of the grain boundary of interest. Both images for strain feature A in P-II specimen and yellow arrows show the grain boundary of interest on the SEM image and EBSD map.

Figure 6-23 shows the focused ion beam (FIB) region, labelled using yellow marker across the grain boundary of interest (cracked boundary) for the strain feature A in the P-II sample.

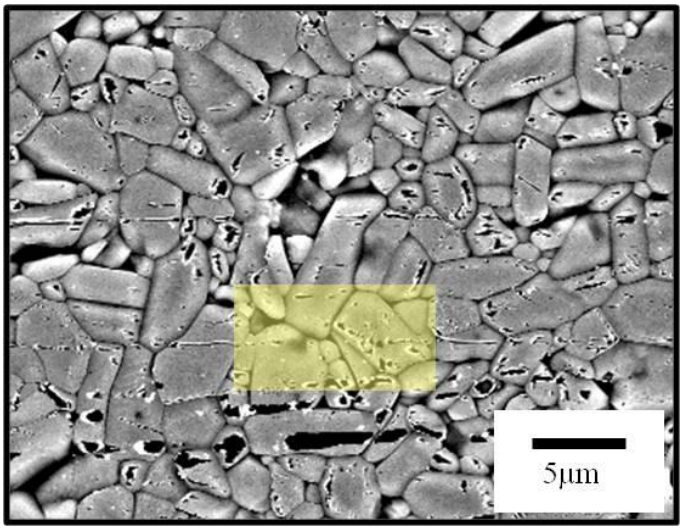

Figure 6-23: The focused ion beam region marked by the yellow rectangle across the cracked boundary observed by digital image correlation for strain feature A in P-II sample.

The focused ion beam was used to make a trench across the strain feature A in the P-II specimen as shown in Figure 6-24. The strain feature was studied using grain boundary plane as shown in Figure 6-25.

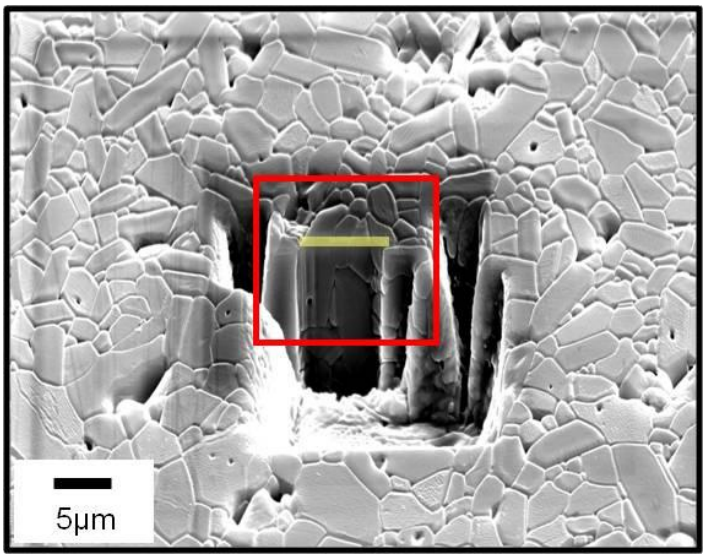

Figure 6-24: Traces of grain boundaries on the P-II specimen surfaces tilted through (52°) using a scanning electron microscope (SEM).

The region indicated by the red square in Figure 6-24, and the crystal orientations for the grains of interest, are shown in Figure 6-25.

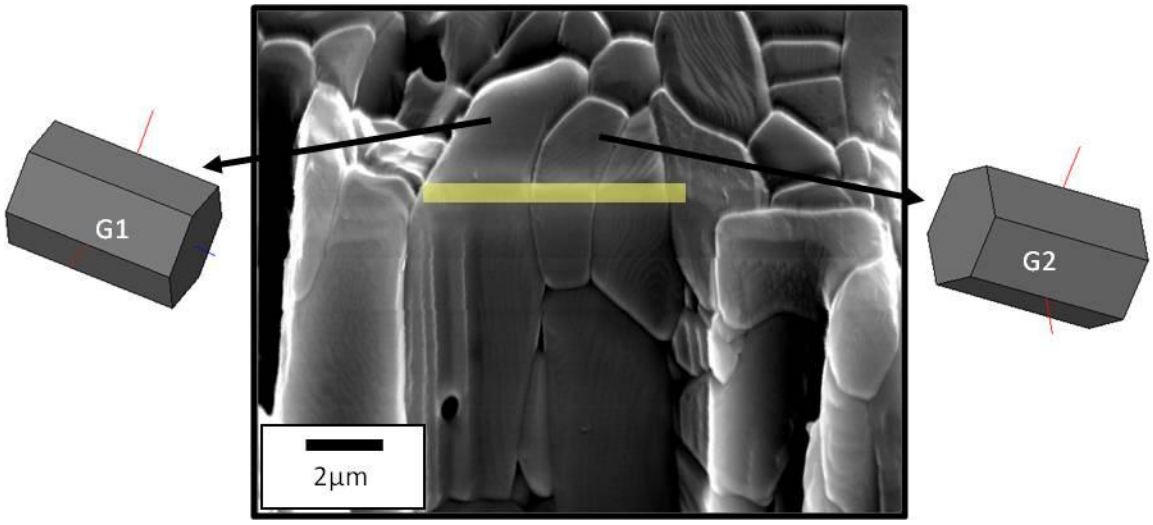

b)

Figure 6-25: Crystal orientation for the grains of interest using channel 5 (Tango software) for the grains on the RHS and LHS of the cracked boundaries.

Figure 6-26 shows the traces of a grain boundary on two adjoining specimen surfaces (upper and lower face). The projected beta angle ($\bar{\beta}$) was measured on the lower face as shown in Figure 6-26.

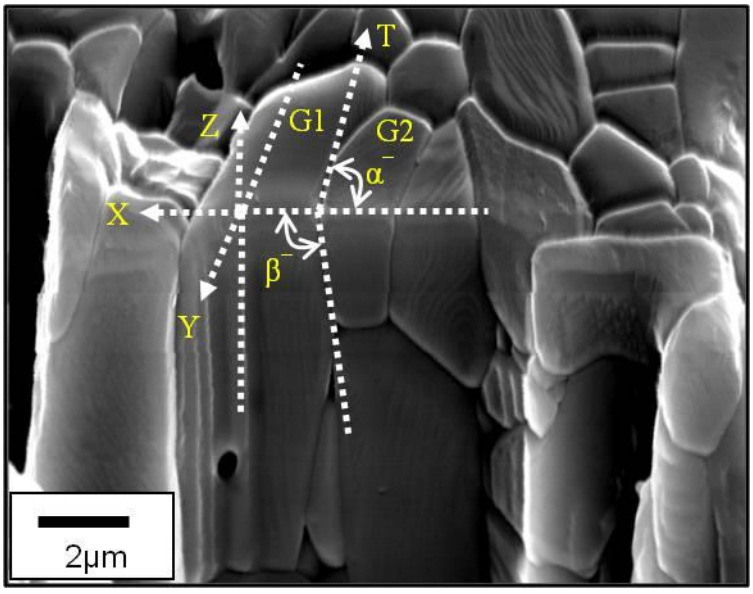

Figure 6-26: Schematic diagram showing the traces of a grain boundary on two adjoining specimen surfaces, orthogonal surfaces (upper and lower face) after FIB trench cutting.

Figure 6-27 shows the overlaid scanning electron microscope image on the electron backscatter diffraction map. In this case a rotation of the EBSD map of about 6° was required to get good match between the SEM image and EBSD map as they were recorded on different occasions. Figure 6-27 shows the true alpha angle (α) on the upper face.

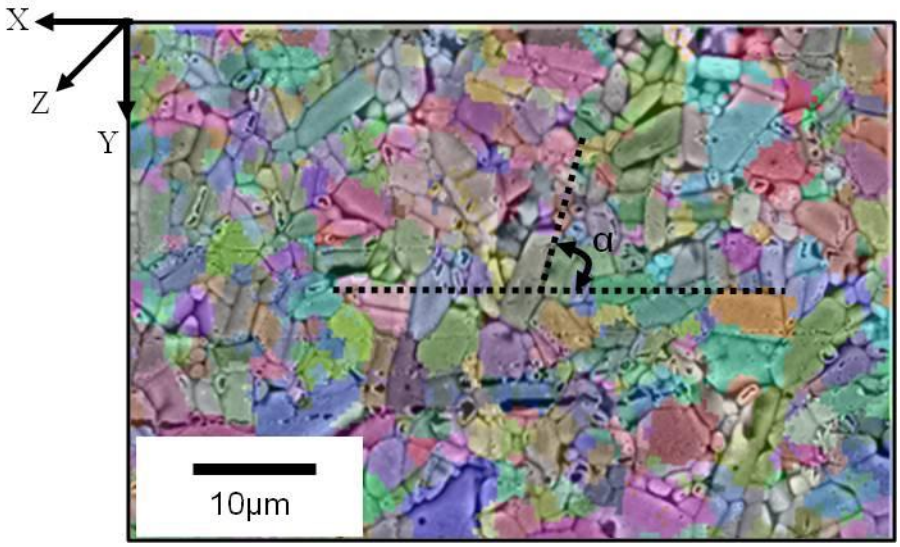

Figure 6-27: Shows the EBSD map overlaid on the SEM image. The EBSD map is rotated by about (6^o) to match the SEM image to get true angle (α) on the upper face for the strain feature A in P-II sample to show the selected boundary and trench location.

The angles were measured using Adobe Photoshop software and the projected alpha angle ($\bar{\alpha}$) and the projected beta angle ($\bar{\beta}$) was shown in Figure 6-26 and (θ) is the tilting angle. Tilting angle was 52° for measuring projected beta and alpha as shown in Figure 6-26. The true angle alpha (α) was measured on the EBSD map as shown in Figure 6-27 and this map is already corrected for tilt and this angle was compared with the true alpha angle which was measured from the upper face in the Figure 6-26 using Equation 46. The true beta angle (β) was measured from lower face in the Figure 6-26 using Equation 47 [100]. The relationship between the true and projected angles for alpha and beta as a function of a tilt angles as described in section (6.2.2.1.4).

$$\alpha = \tan^{-1}[(\tan\alpha^{-})/\cos\theta] \quad (46)$$

$$\beta = \tan^{-1}[(\tan\beta^{-})/\cos(90-\theta)] \quad (47)$$

6.2.2.1.2 Strain Feature B for P-II Sample

Figure 6-28 shows the scanning electron microscope image and the electron backscatter diffraction map for the grain boundary of interest (cracked boundary) as labelled by the black square marker and the yellow arrows. This shows the grain boundary of interest for the feature B in sample P-II is shown in Figure 6-28 as mentioned before for strain feature A in section (6.2.2.1.1).

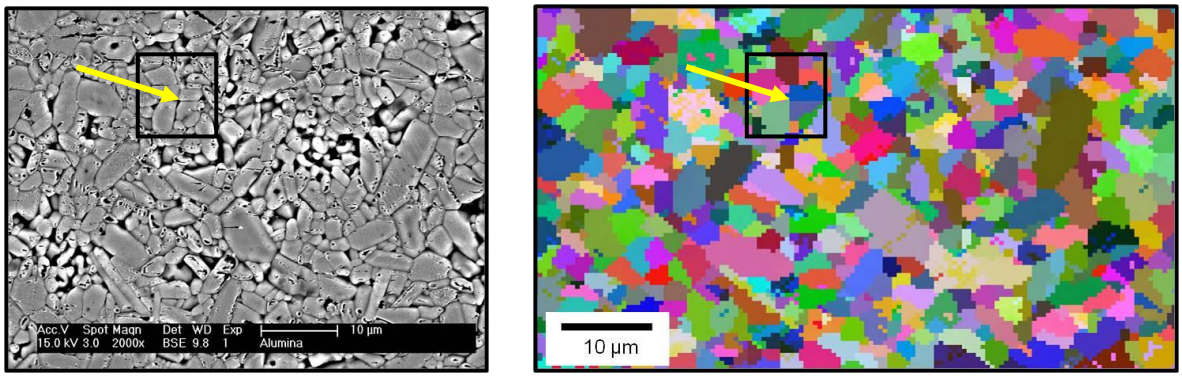

a) b)

Figure 6-28: a) Shows the SEM image for the grain boundary of interest as labelled by black square and b) Shows the EBSD for the orientation of the grain boundary of interest for strain feature B in P-II specimen and the grain boundary of interest as labelled by arrows on the SEM image and EBSD map.

Figure 6-29 shows the focused ion beam region, labelled using a yellow marker across the cracked grain boundary for the strain feature B in P-II sample.

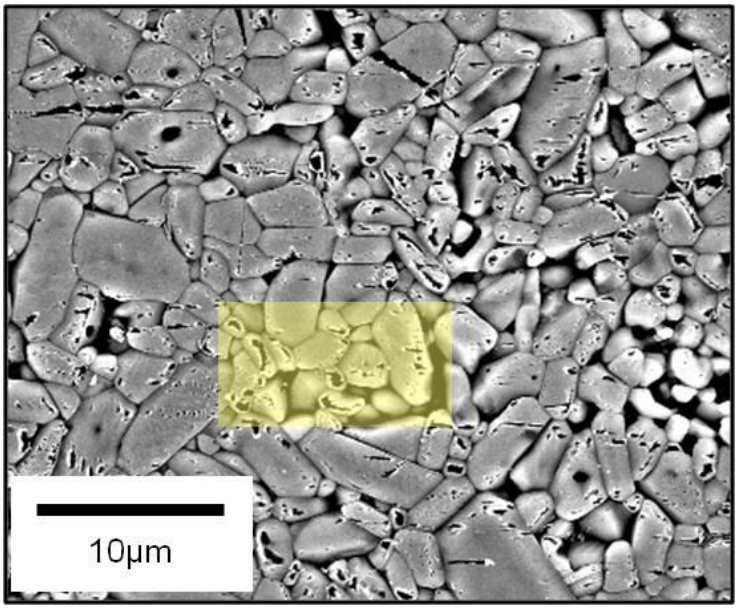

Figure 6-29: focused ion beam region marked with a yellow rectangle across the cracked boundary which was observed using digital image correlation.

Focused ion beam was used to make trench across the strain feature B in the P-II specimen as shown in Figure 6-30. The strain feature was studied using grain boundary plane as shown in Figure 6-31.

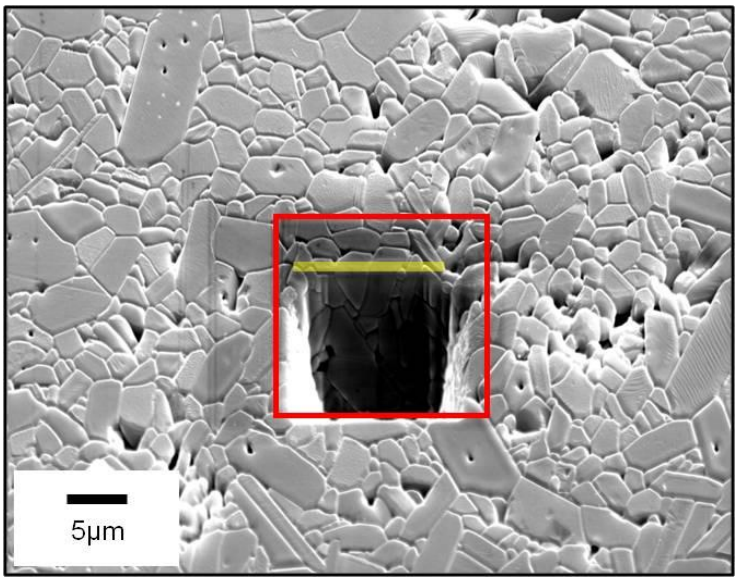

Figure 6-30: Traces of grain boundaries on the P-II specimen surfaces tilted through (52°) for strain feature B.

Figure 6-31 shows a magnification of the red region marker as shown in Figure 6-30 and crystal orientations for the grains of interest (i.e. grains near to the boundary of interest) are shown in Figure 6-31.

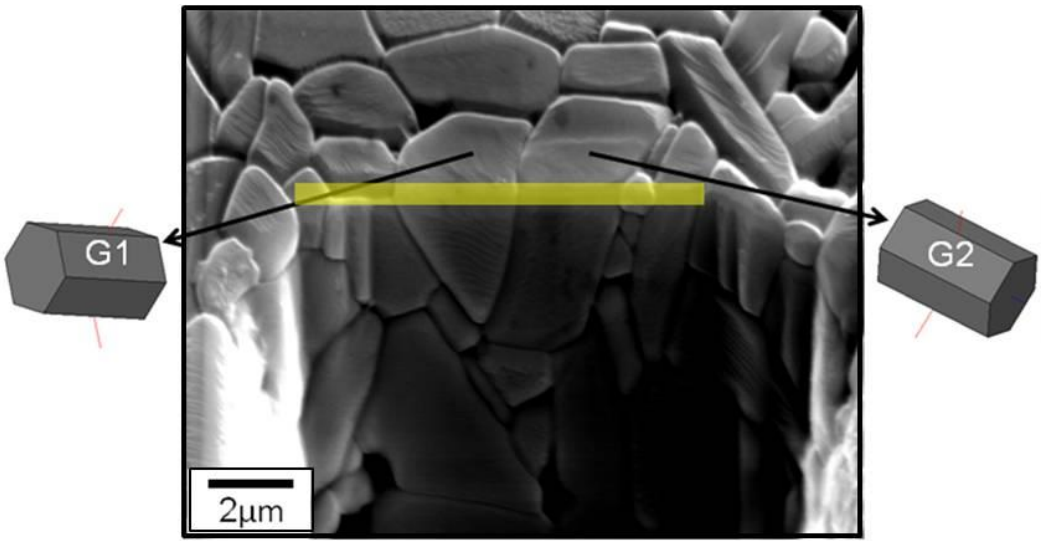

Figure 6-31: The crystal orientation using channel 5 for the grains on the either side of the cracked boundaries of feature B in sample P-II.

Figure 6-32 is a schematic diagram showing the traces of a grain boundary on two adjoining specimen surfaces (upper and lower face). The projected beta angle ($\bar{\beta}$) was measured for the lower face as shown in Figure 6-32.

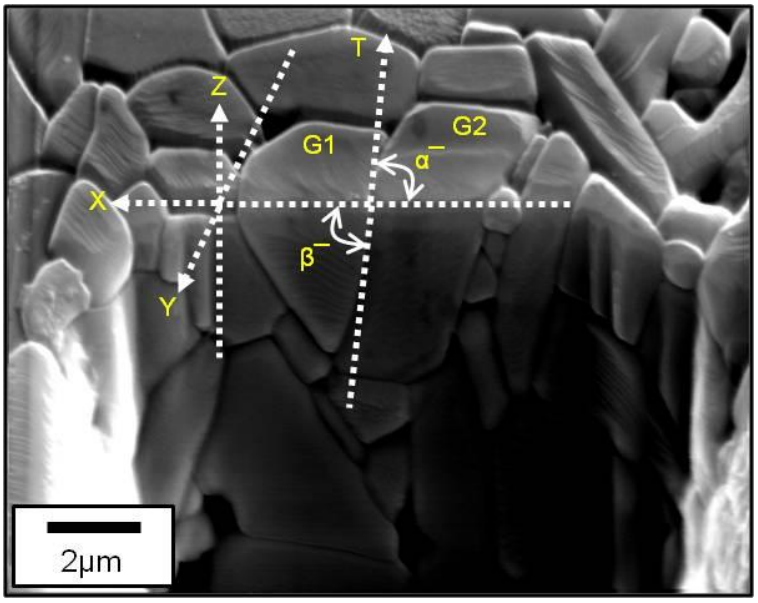

Figure 6-32: Schematic diagram showing the traces of a grain boundary on two adjoining specimen surfaces, orthogonal surfaces (upper and lower face) after FIB trench cutting.

Figure 6-33 shows the overlaid scanning electron microscope image on the electron backscatter diffraction map for strain feature B and also, shows the true angle (α) on the upper face for the feature B in the P-II sample.

The true angles alpha (α) and beta (β) were calculated using Equations (46) and (47) [100] as mention earlier for strain feature A in section (6.2.2.1.1). The plots for projected and true angles for alpha and beta at different tilt angles as described in section (6.2.2.1.4).

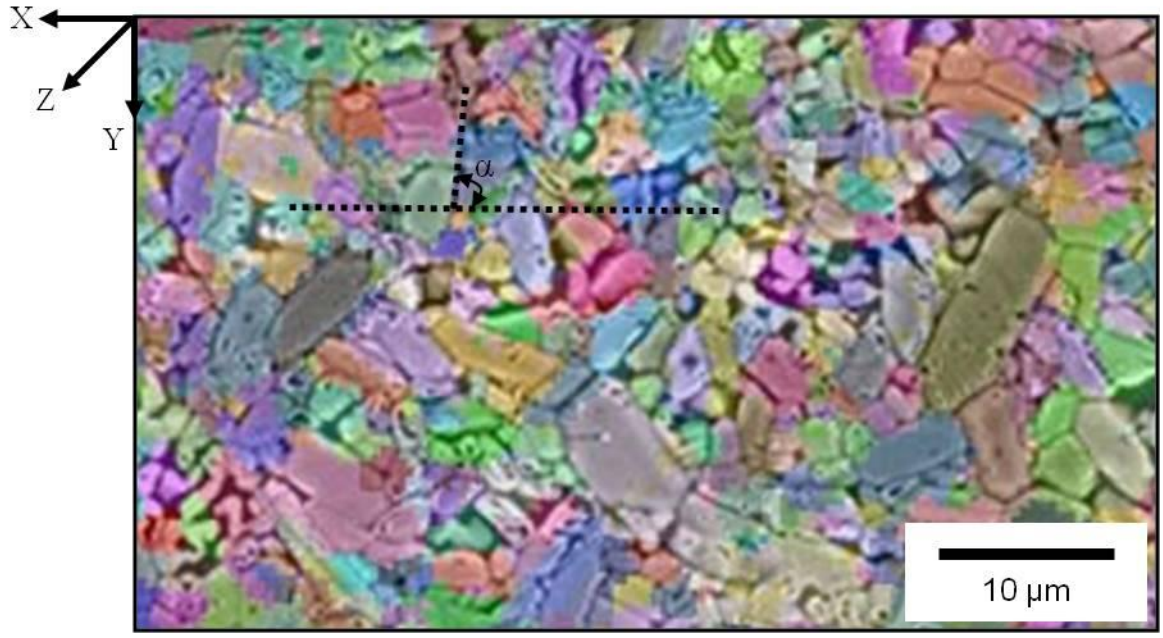

Figure 6-33: Shows the EBSD map overlaid on the SEM image after rotation EBSD map is about (6^{o}) to properly match with the SEM image to get true angle (α) on the upper face for the strain feature B in P-II sample. Also shown is the selected boundary and trench location.

6.2.2.1.3 Strain Feature for Cr-II Sample

Figure 6-34 shows the scanning electron microscope image and the electron backscatter diffraction map for the grain boundary of interest (cracked boundary), labelled with a black rectangle marker and red arrow for the cracked boundary in Cr-II sample. This follows the same procedure for strain feature A in P-II sample in section (6.2.2.1.1).

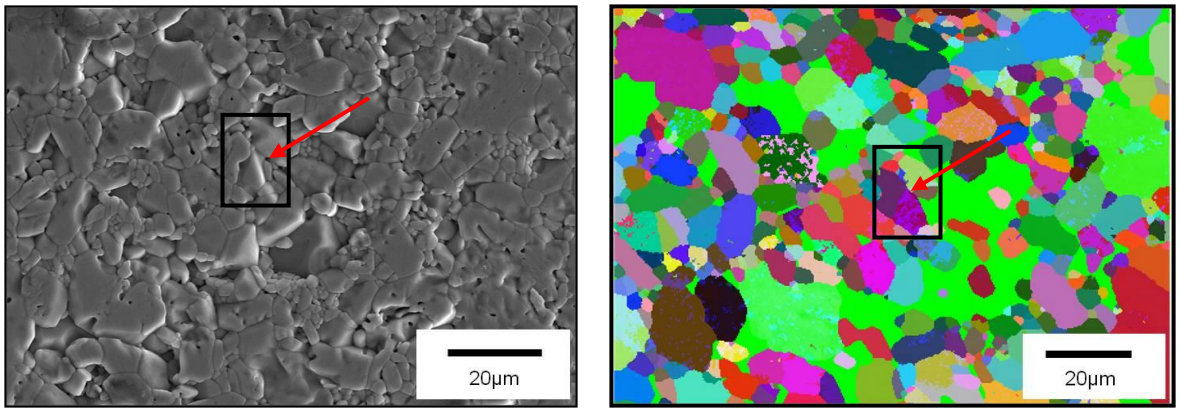

a) b)

Figure 6-34: a) Shows the SEM image for the grain boundary of interest and b) Shows the EBSD (i.e. the green regions on the EBSD map shows the non-indexed regions) for the orientation of the grain boundary of interest as labelled by red arrow for the boundaries of interest for strain feature in Cr-II specimen.

Figure 6-35 shows the focused ion beam region, labelled by a yellow marker across the grain boundary of interest (cracked boundary) as mention earlier for strain feature A in the P-II sample in section (6.2.2.1.1).

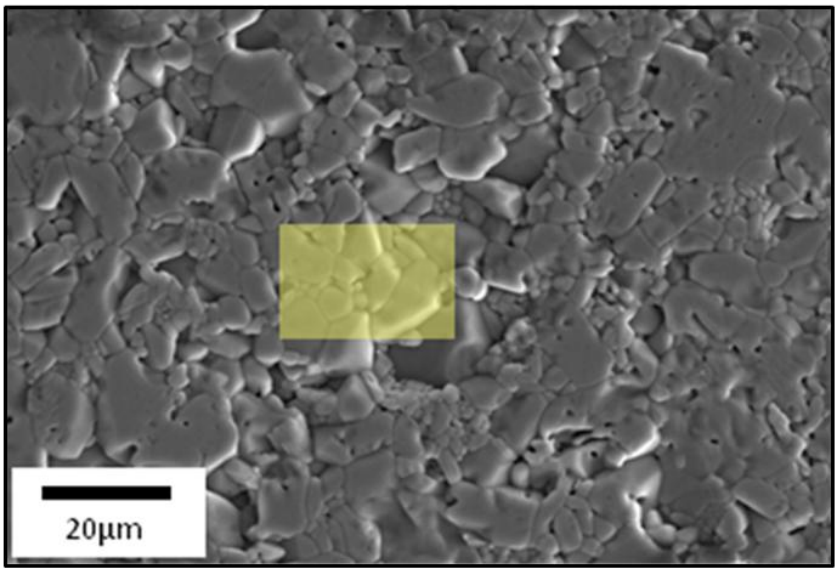

Figure 6-35: Shows the focused ion beam region labelled by a yellow rectangle across the cracked boundary which was observed by digital image correlation for the strain feature in Cr-II sample.

The focused ion beam was used to make a trench across the strain feature for the Cr-II specimen as shown in Figure 6-36. The feature was studied using grain boundary plane as

shown in Figure 6-37 as mentioned before for strain feature A in the P-II sample in section (6.2.2.1.1).

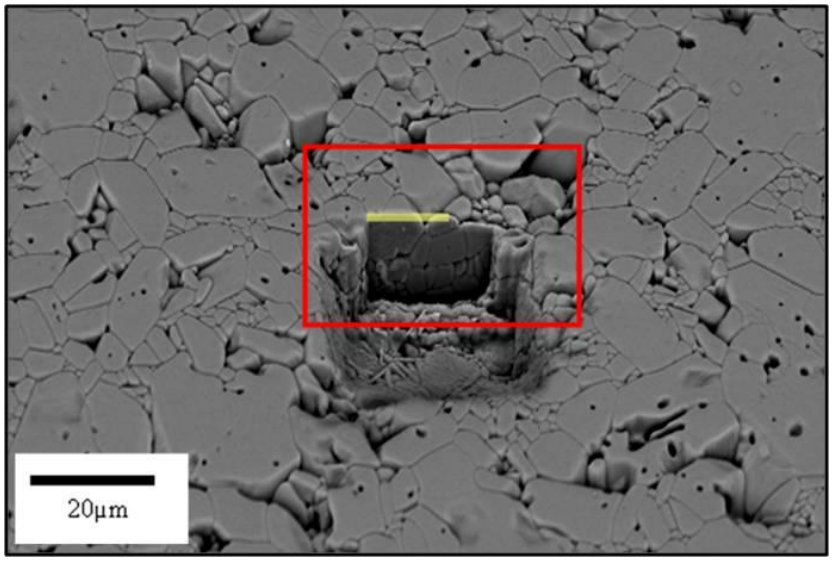

Figure 6-36: Traces of grain boundaries on the Cr-II specimen surfaces tilted through (52°) using SEM.

A magnification of the red region in the Figure 6-36 showing the crystal orientations for the grains of interest is shown in Figure 6-37.

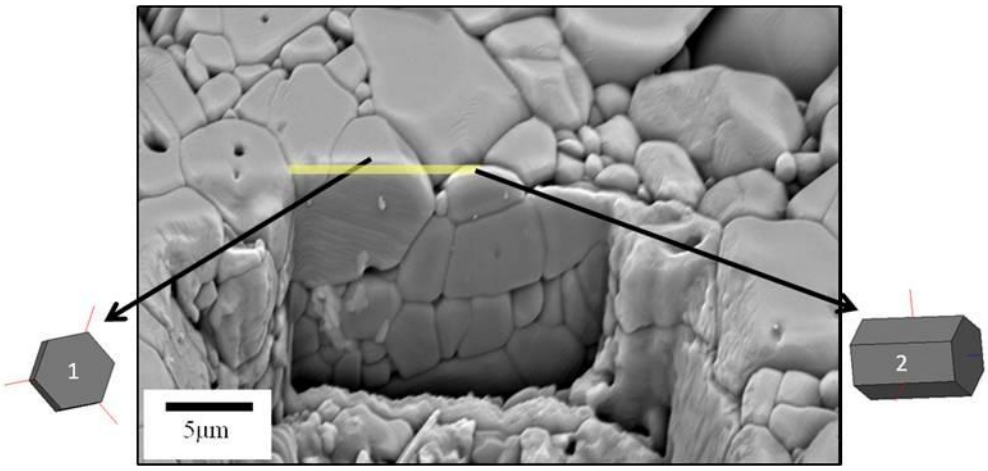

Figure 6-37: Shows the crystal orientation using channel 5 (Tango Software) for the grains on the RHS and LHS of the cracked boundaries in Cr-II specimen.

Figure 6-38 schematic diagram showing the traces of a grain boundary on two adjoining specimen surfaces (upper and lower faces) as shown in Figure 6-38 and the projected beta angle ($\bar{\beta}$) was measured of the lower face as shown in Figure 6-38.

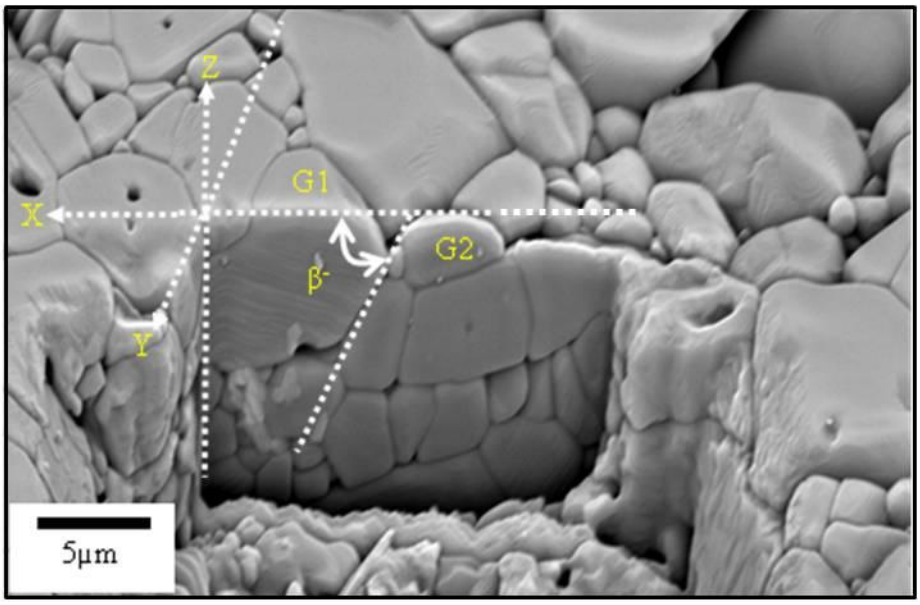

Figure 6-38: Schematic diagram showing the traces of a grain boundary on two adjoining specimen surfaces, orthogonal surfaces (upper and lower face) after FIB trench cutting. Also shown is the projected beta angle.

Figure 6-39 shows the overlaid scanning electron microscope image on the electron backscatter diffraction map. In this case the required rotation of the EBSD map is about 10° to get good correlation between SEM image and EBSD map for the grain boundary of interest and the data were recorded on separate cases. The true angle (α) was measured on the upper face for strain feature in Cr-II sample as shown in Figure 6-39 as mentioned before in strain feature A in P-II sample in section (6.2.2.1.1).

The true angle alpha (α) was measured on the EBSD map as shown in Figure 6-39. The beta (β) were calculated using the equations 47 [100] as mentioned earlier in strain features in P-II sample in section (6.2.2.1.1). The plots for projected and true angles for alpha and beta as a function of the tilt angles as described in section (6.2.2.1.4).

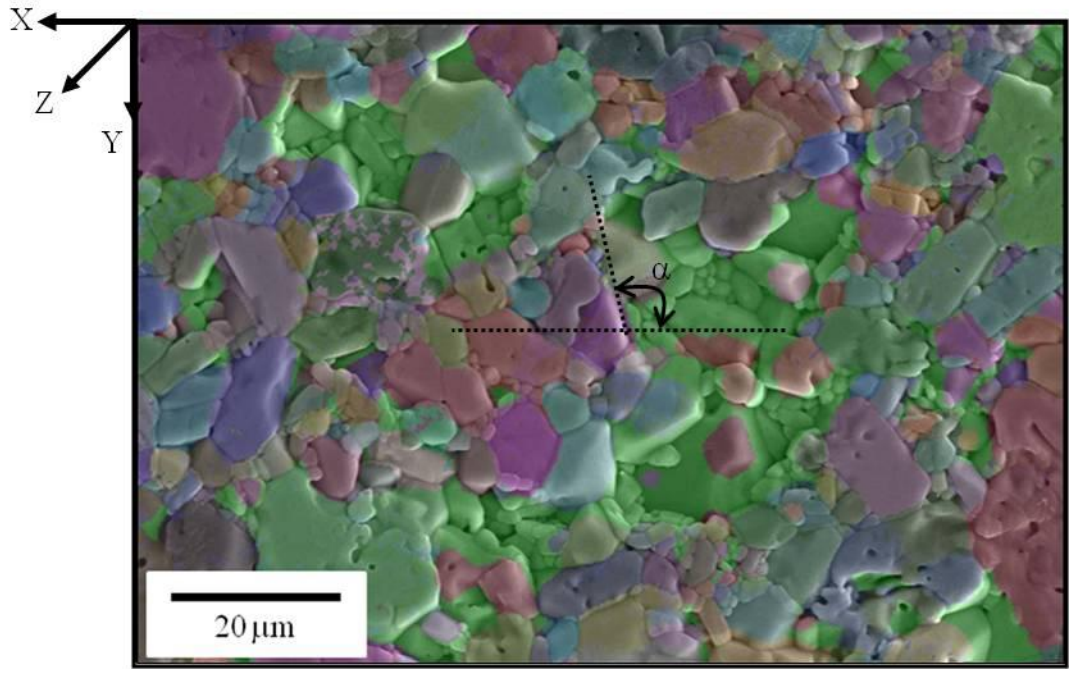

Figure 6-39: Shows the EBSD map overlaid on the SEM image. The EBSD map is rotated by (10^o) to the SEM image to get the true angle (α) for the upper face for the strain feature in Cr-II sample to show the selected boundary and trench location.

6.2.2.1.4 Projected and True angles for Alpha and Beta in P-II and Cr-II Specimens

Trench images were recorded at different tilting angles (40^o, 52^o, and 60^o) using SEM as in Figure 6-40 for specimens P-II and Cr-II. The projected angles of the grain boundary plane were measured and the true angles were then calculated using Equations 46 and 47 as mentioned early for the strain feature A in the P-II sample in section (6.2.2.1.1). The true alpha angle for the Cr-II was measured just from overlaid EBSD map on the SEM image due to the FIB trench being at a triple point on the upper face as shown Figure 6-40iii. The results showing the relationship between the tilting angles versus projected and true angles are shown in Figure 6-41 and Figure 6-42 for P-II and Cr-II samples respectively. Figure 6-41a, shows the measured (projected) alpha and corrected (true) alpha for each tilt angle and compare that with the true alpha from overlaid EBSD map on the SEM image. The aim of these plots is to get confidence that the angles alpha and beta were calculated correctly from the images.

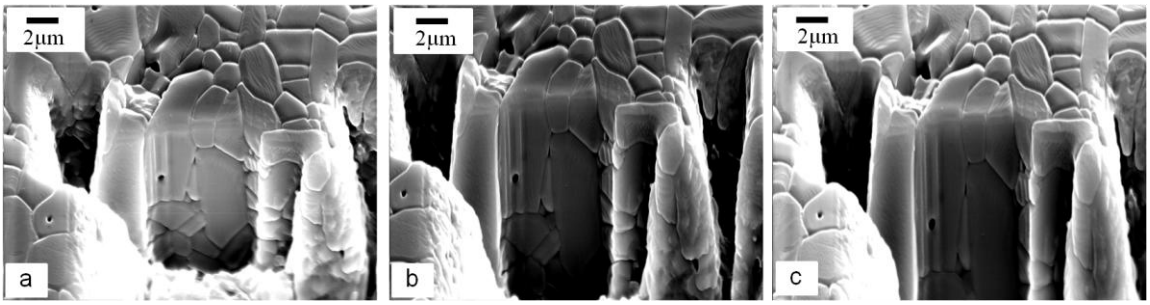

i) Strain Feature A in P-II Sample

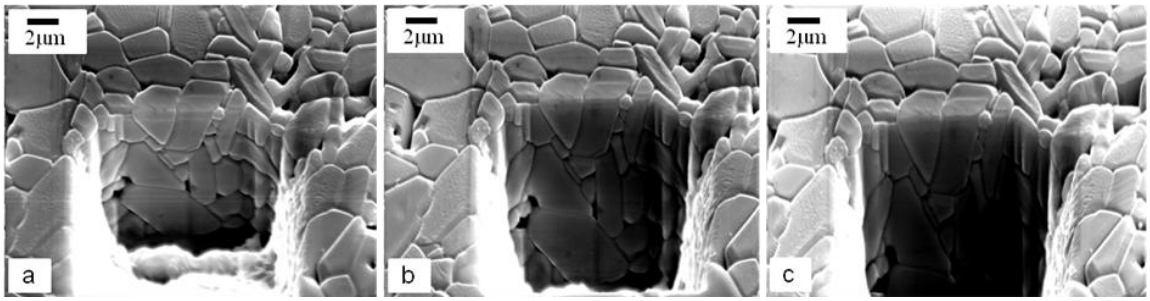

ii) Strain Feature B in P-II Sample

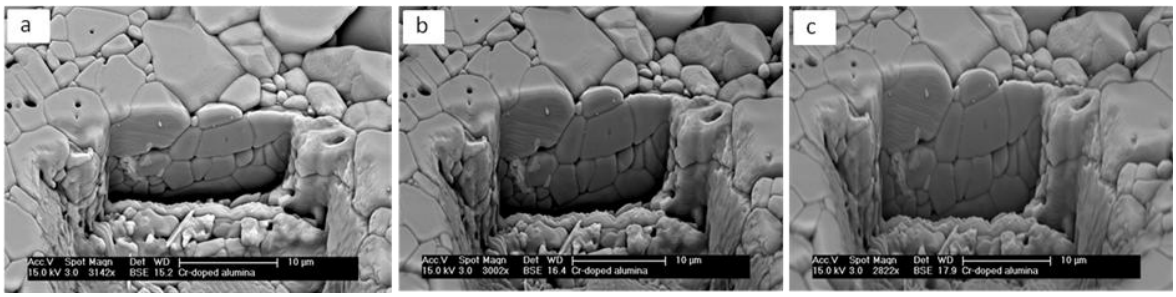

iii) Strain Feature in Cr-II Sample

Figure 6-40: Traces of grain boundary on two surfaces (upper and lower surfaces) for i) Strain Feature A in P-II Specimen, ii) Strain Feature B in P-II Sspecimen, and iii) Strain Feature in Cr-II Specimen at different tilt angles a) 40^{o},b) 52^{o}, and c) 60^{o}. These tilt angles have been done using the scanning electron microscope.

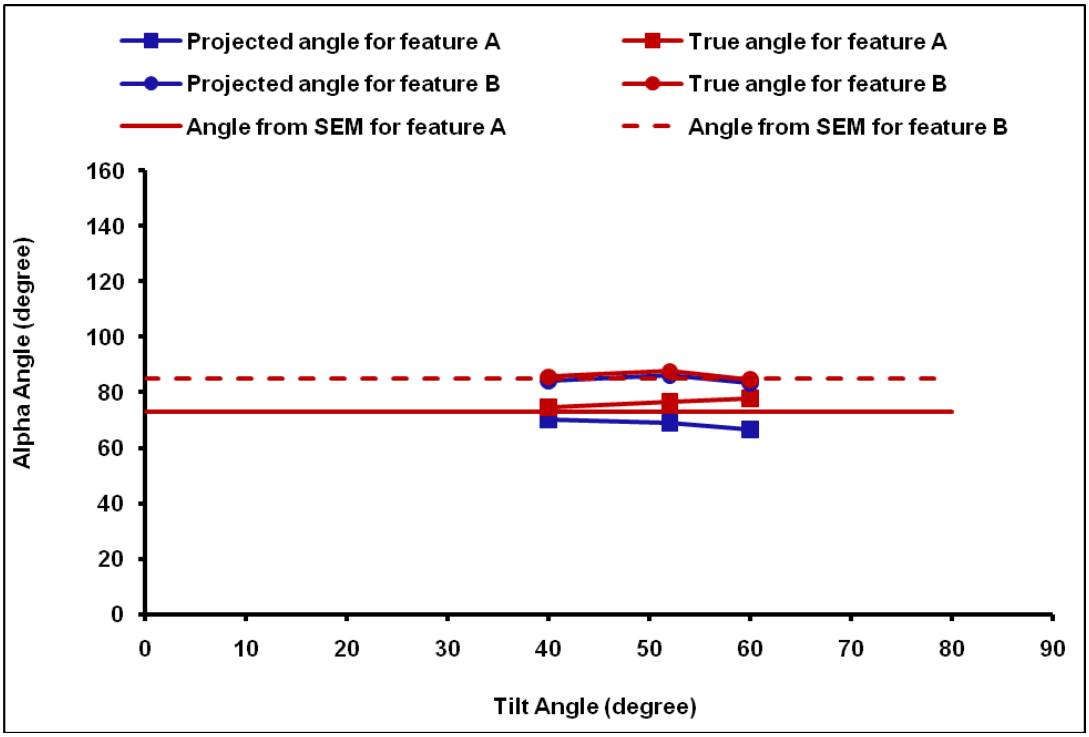

a)

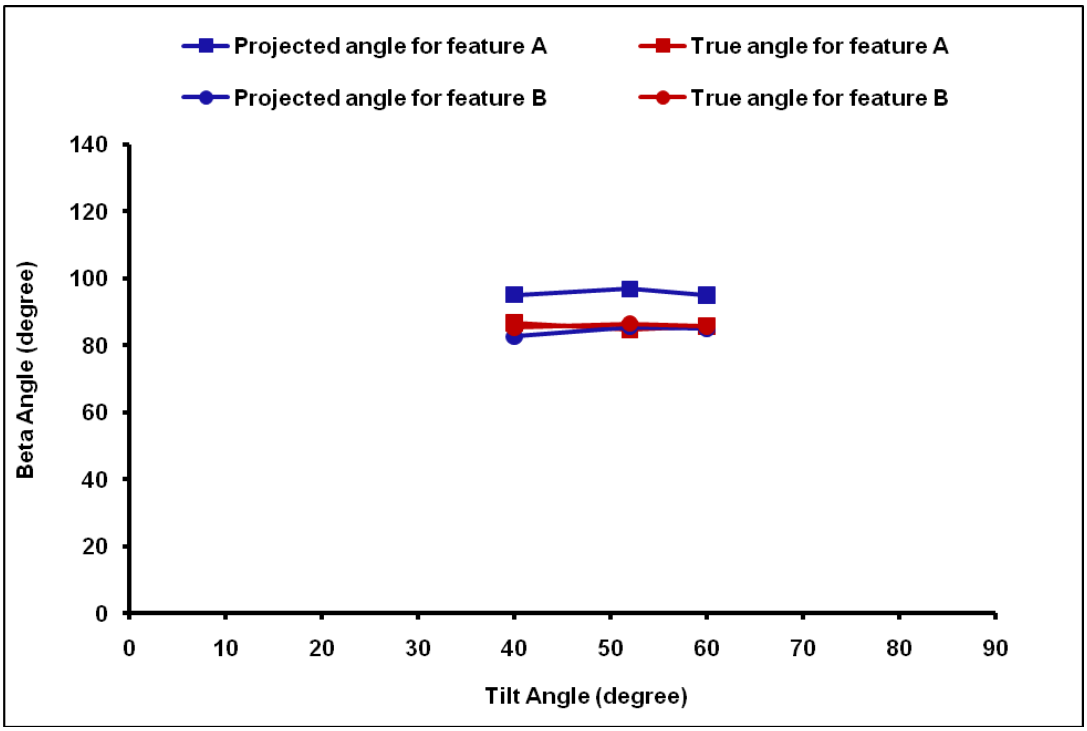

b)

Figure 6-41: The relationship between the true and projected angles as a function of the tilting angles for a) Alpha angle (α) b) Beta angle (β) in P-II specimen.

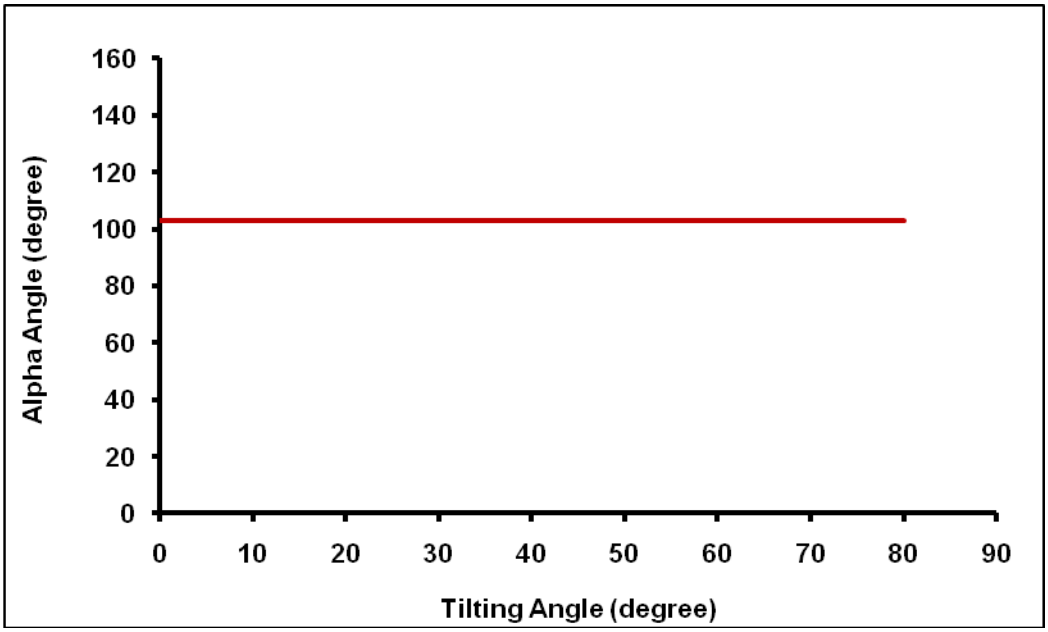

a)

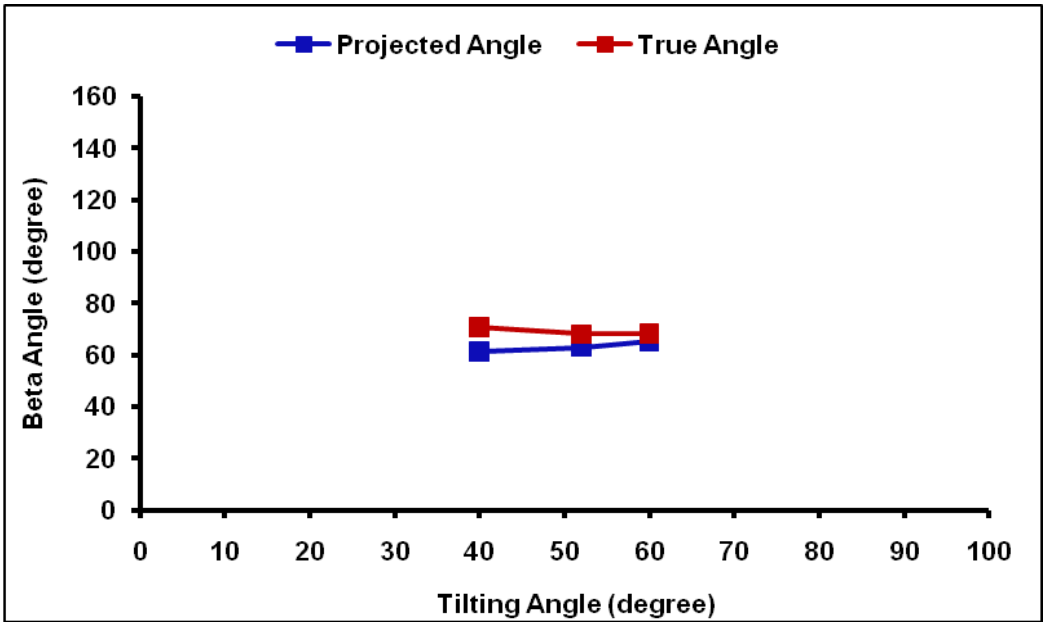

b)

Figure 6-42: The relationship between the true and projected angles as a function of the tilting angles for a) True alpha angle was measured from Figure 6-39 (α) from overlaid EBSD map on the SEM image and b) Beta angle (β) for Cr-II samples.

6.2.2.2 Grain boundary plane Pole for P-II and Cr-II Specimens

The grain boundary plane poles for the P-II specimen and Cr-II specimen are plotted on pole figures. For reference these were then compared with the basal plane (0001). The true angles alpha and beta were measured in the planes xy and xz respectively and both angles were relative to the X-axis. The uncertainty of the pole orientations was shown using a dotted red circle. The grain boundary plane was plotted depends on the average true angles. The uncertainty for the true alpha angle was measured from overlaying and rotating the EBSD map and the SEM image to get a good matching between them. Uncertainty in the true beta angle was measured from the range of three values that were measured at different tilt angles are shown in Table 6-1. The results for the grain boundary plane pole and the basal plane pole are shown in Figure 6-43.

Table 6-1: Shows the average true angles (α and β) for strain features A and B in P-II sample and also for strain feature in Cr-II sample.

Materials	Features	Average True Angles with uncertainty, (°)	
		Alpha, α	Beta, β
P-II Specimen	Strain Feature A	73±3	84±2
	Strain Feature B	85±2	87±2
Cr-II Specimen	Strain Feature	103±4	68±3

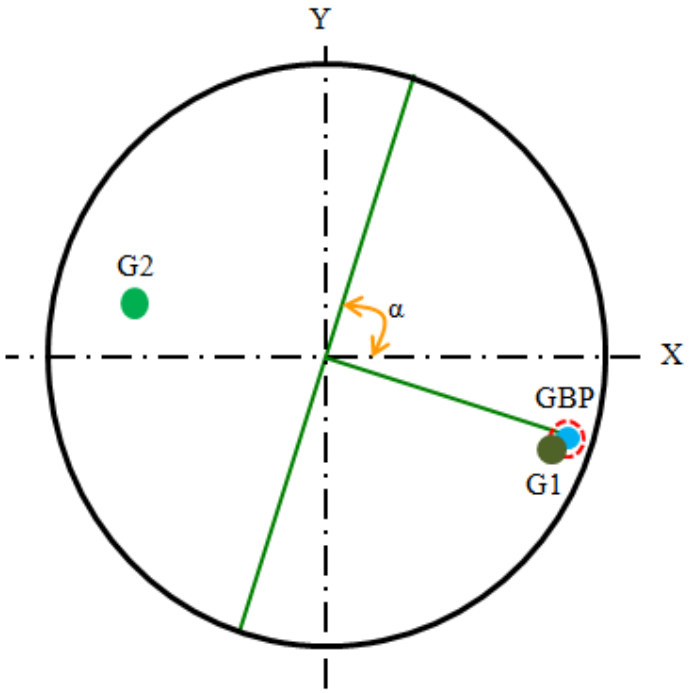

a) Strain Feature A in P-II Specimen

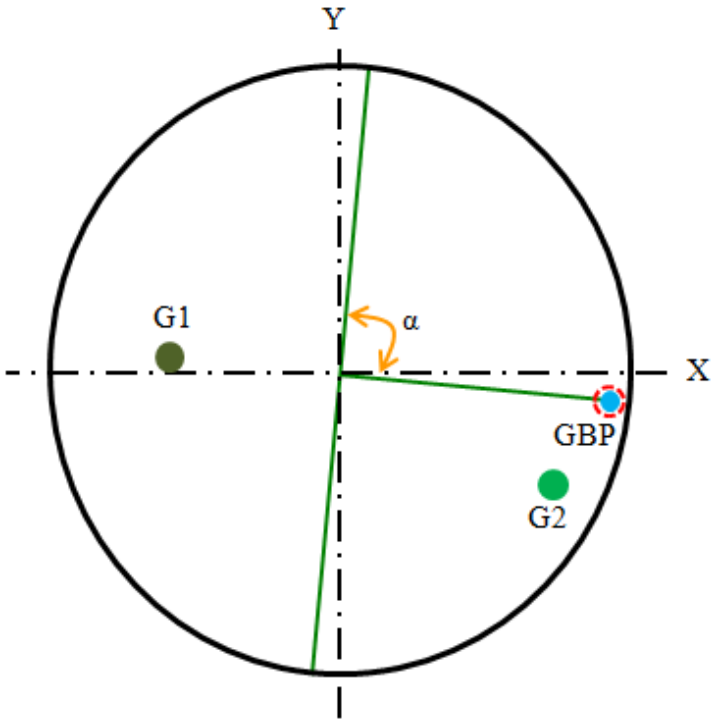

b) Strain Feature B in P-II Specimen

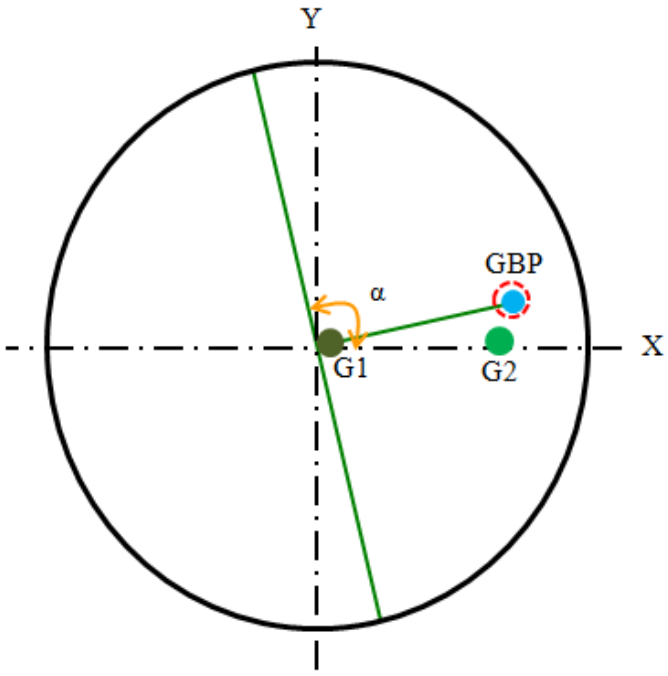

c) Strain Feature in Cr-II Specimen

Figure 6-43: Pole figures for the grain boundary plane G12, of the basal facet plane (0001) in alumina in grains G1 (dark) and G2 (light). The boundary plane is close to the (0001) facet plane in a) G1 for strain feature A in P-II specimen, b) G2 for strain feature B in P-II specimen and c) G2 for strain feature in Cr-II specimen.

Summary

The strain features were identified for the P-II and Cr-II sample using DIC at low threshold (0.2%) and at high threshold (1%). The strain features were increased with increasing applied strain in the X-direction but there is not significant feature were observed in the Y-direction. The peak strain (highest strain) for these features were compared with the background strain in both direction X and Y and there is a general trend for increasing feature strain with increasing applied strain and also the results shows effect threshold on the strain feature detection. The cracks nuclei were not observable in the raw images of the microstructure and comparison the locations of these strain features with the microstructure image. The overlaid strain map on the microstructure image shows them to be coincident with the grain boundaries. The surface displacement for these strain features was measured at different applied strain in the X-direction and the SCOD was measured of the difference between the displacements across the strain feature from the best fit for the displacement through the strain feature. The grain boundaries of interest were prepared for the EBSD using different methods and FIB was used to create trench across the grain boundaries of interest. The grain boundary plane poles for the P-II and Cr-II samples are plotted on the pole figures.

6.3 Hertzian Indentation Analysis

6.3.1 Hertzian Ring cracks

The Hertzian test was used to produce the ring cracks on the smooth and coarse polished polycrystalline alumina specimen which were difficult to measure without preparation of the alumina sample surface as mentioned earlier in the experimental chapter in Section (3.5.3). Hertzian ring cracks formed on P-II and Cr-II specimens are shown in Figure 6-44.

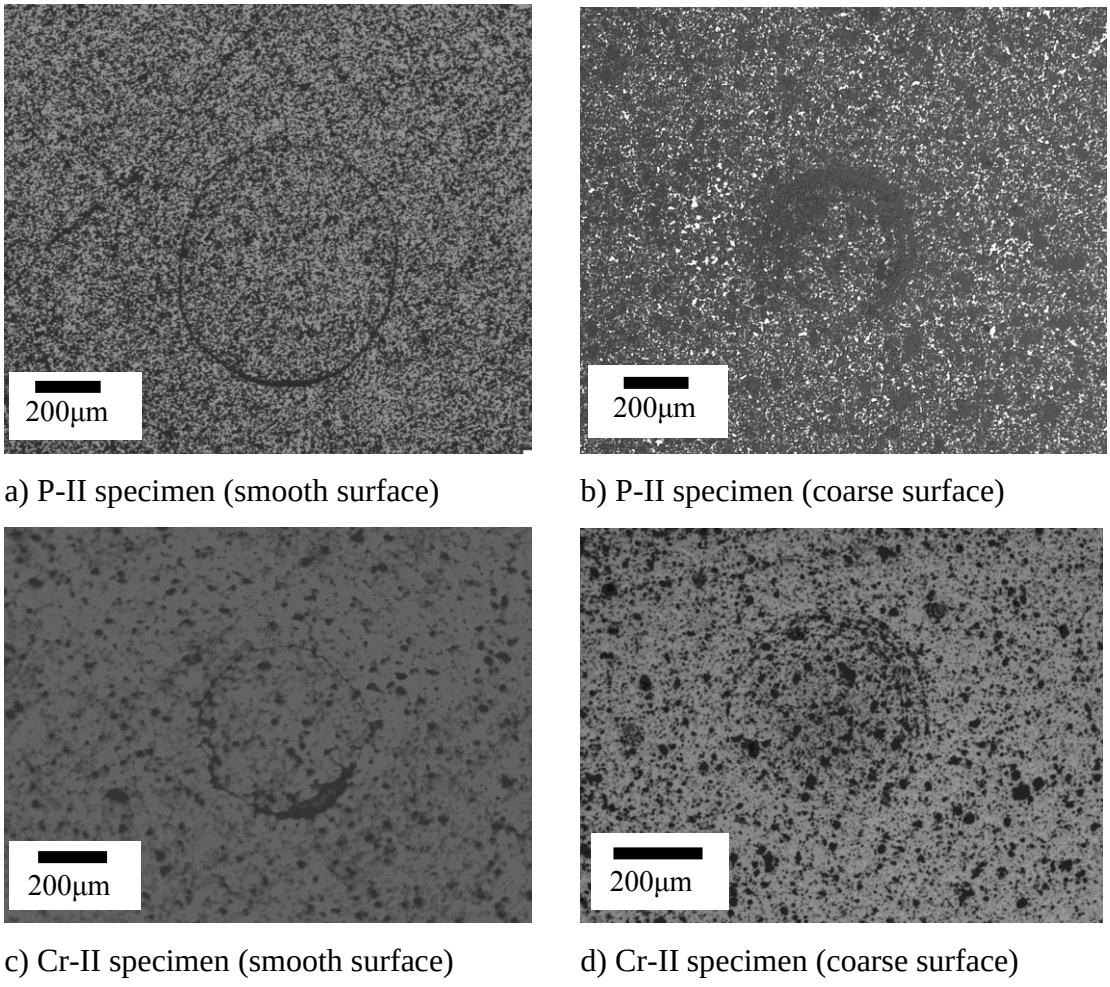

a) P-II specimen (smooth surface) b) P-II specimen (coarse surface)

c) Cr-II specimen (smooth surface) d) Cr-II specimen (coarse surface)

Figure 6-44: Shows ring cracks produced on the P-II and Cr-II specimens. The sphere indenter radius was R=2.5 μm. The ring cracks are visible after the sample was etched using KOH a, c) Smooth polished for the P-II and Cr-II specimens and b, d) Coarse polished for P-II and Cr-II specimens respectively.

6.3.2 The cumulative probability of fracture

Equation 48 was used to calculate the cumulative probability of fracture for the P-II and Cr-II samples [101].

$$P_n = \frac{n}{N+1} \qquad (48)$$

Where: (P_n) represents the cumulative probability of failure, (n) represents the order number of the readings (the data arrangement from the minimum to the maximum of the failure load) and (N) represents the total number of experiment data.

The (P_n) for the P-II and Cr-II specimens are shown in Figure 6-45 for the smooth surface (i.e. well polished) and coarse surface. The minimum failure load was provided from these plots and the coarse sample has higher population to find the defects.

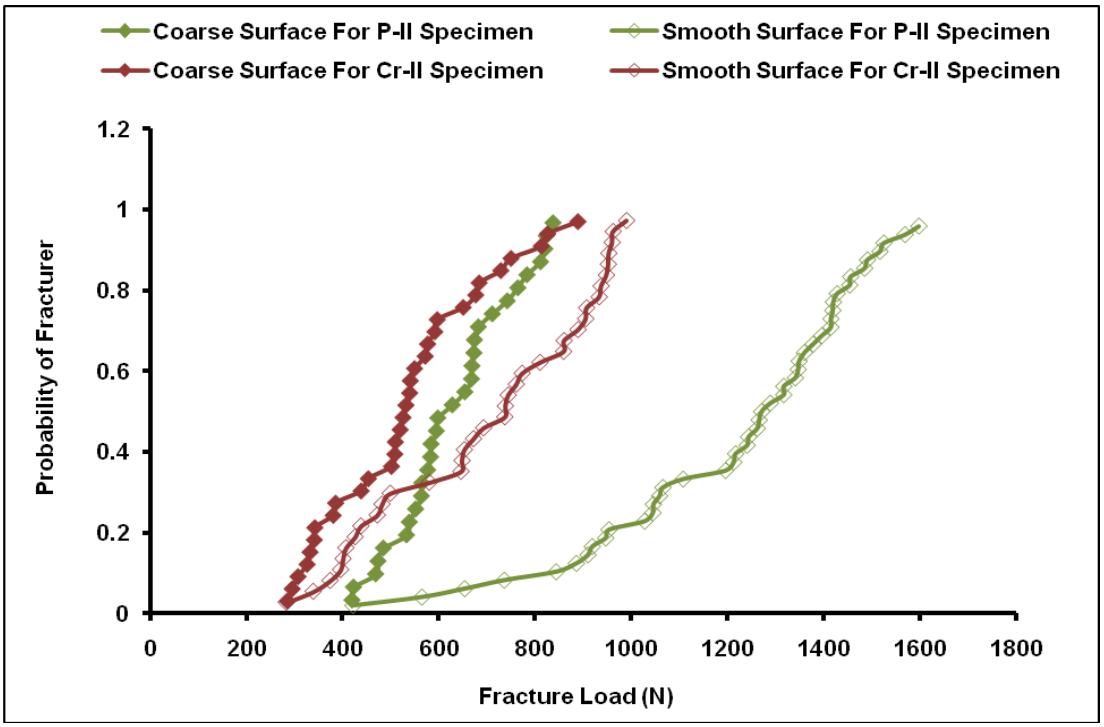

Figure 6-45: Cumulative probability of failure against the failure load in the P-II specimen and Cr-II specimen for the coarse and smooth surface.

Figure 6-46 shows the data for the ring crack radius as a function of the fracture load and the ring crack radius for P-II and Cr-II specimens increased with fracture load. The uncertainty in the ring crack radius was measured in the individual measurement, for each

point there are three measurements and the uncertainty was 1.48 μm and 1.34 μm for P-II and Cr-II sample respectively.

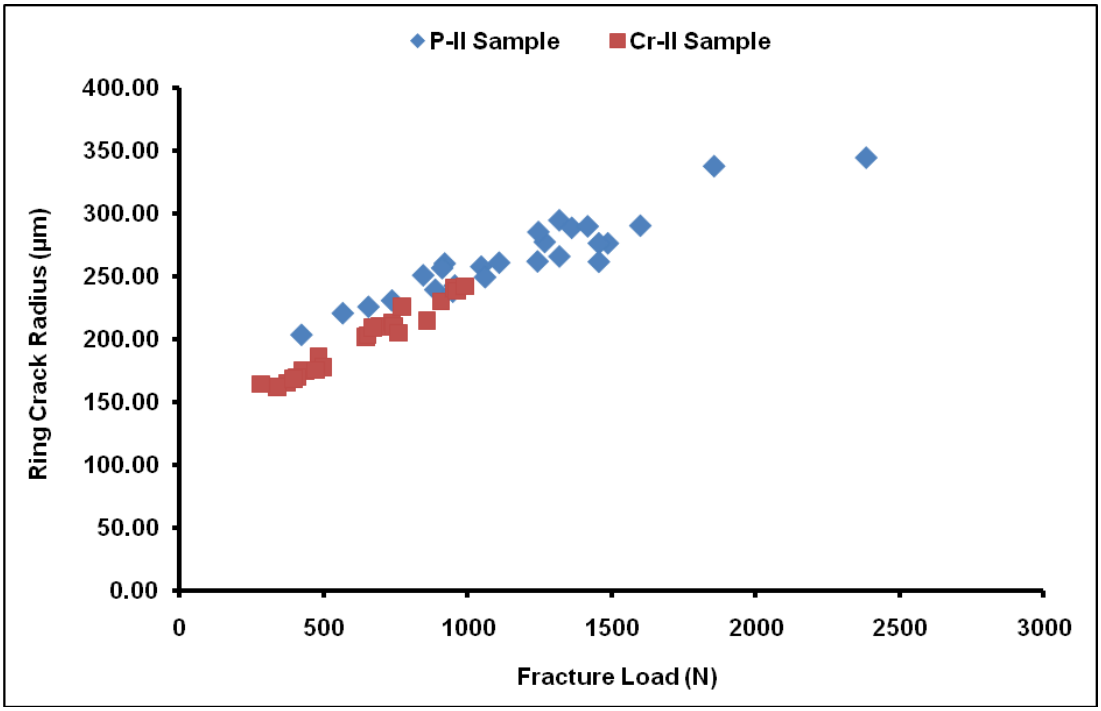

Figure 6-46: Shows the ring crack radius for smooth polished surface as a function of the fracture load for P-II and Cr-II specimen using alumina indenter. The uncertainty in the ring crack radius is 1.48 μm and 1.34 μm for P-II and Cr-II samples respectively.

6.3.3 Fracture Toughness calculation

The fracture toughness was measured at the minimum load and also for the coarse surface due to the probability to find the small cracks is higher than the smooth surface. The radial tensile caused to produce the cracks around the contact area (see Equation 49) [80, 101]:

$$a = \left(\frac{3RP}{4E^*}\right)^{1/3} \tag{49}$$

$$E^* = \frac{E}{2\left(1-\nu^2\right)} \tag{50}$$

Where:

(E), (ν) represent the Young modulus and Poisson's ratio respectively for the indenter and the specimen (i.e. the sample and indenter was made from the alumina).

The Hertzian test was provided the fracture toughness, (K_{1C}) for the P-II and Cr-II samples were calculated by Equation 51 [101]:

$$K_{1C} = \sqrt{\frac{E^* \times P_{\min}}{C \times R}} \quad (51)$$

Where:

P_{min} represents the minimum load to initiate the cracks on the sample surface, (C) represents the constant of materials and there is relationship between the materials constant and the Poisson's ratio, for example (ν = 0.24 and C=2790 for alumina) [101], (R) represents the sphere indenter radius is (2.5 mm). The results for the fracture toughness at smooth and coarse surfaces for the P-II and Cr-II specimens are shown in Table 6-2.

Table 6-2: Shows the minimum load and the fracture toughness for P-II and Cr-II specimens at different surface finishes.

Specimen	Minimum Fracture Load P_{min}, (N)		Fracture Toughness K_{1C}, (MPa.m$^{1/2}$)	
	Smooth Surface	Coarse Surface	Smooth Surface	Coarse Surface
P-II Specimen	422±67.4	420±39.4	3.54±0.57	3.52±0.16
Cr-II Specimen	283±76.2	286±73.8	2.89±0.25	2.91±0.39

6.3.4 Defect Size Population

The aim of this test was to achieve the population of defect sizes. For example, Figure 6-47 shows the distributions of crack sizes for P-II specimen. The details for the procedure and all the equations used for measuring the defect size are mentioned early in section (3.5.4).

The crack sizes were determined from the measurements of the ring crack radius and the failure load at different values at the stress intensity factor is equal to the fracture toughness. There is relationship between the equations which were used for the Hertzian indentation analysis and the initial value of crack size (c) then Goal Seek was used to get a high or lower solution of crack size as there is a peak in the curve. Figure 6-47 shows two sets of

distributions for crack size for P-II specimen and it is important to decide which solution is real small or large defect size [80].

Figure 6-47 shows the relationship between the stress intensity factor against the defect size and both normalised by the radius of the contact area at (ν = 0.24). The small crack at the contact area development to the ring crack radius due to the stress at this region is radial tensile stress. The stress intensity factor for the large cracks were negative due to these cracks was not in the tensile region. Figure 6-47 shows the (K_I) increase with increasing the applied load and the ring crack radius. Here the dash blue curve and grey curve were plotted at fracture load 1317 N and 422 N and ring crack radii 266 µm and 204 µm respectively and all the curves at fracture toughness 3.5MPa.m$^{1/2}$.

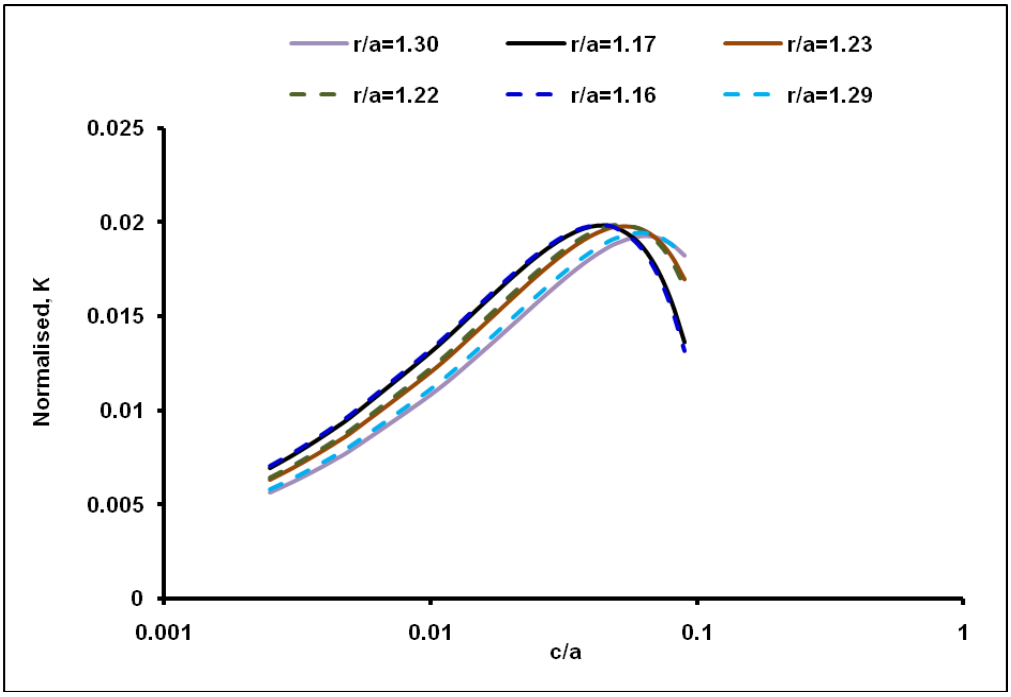

Figure 6-47: Shows the stress intensity factor against the defect size after normalized by the radius of the contact region at (ν=0.24) for P-II specimen.

6.3.5 Gumbel distribution for Defect Size

The distribution of the defect size and population of the defects were described using a Gumbel distribution as description in experimental chapter in section (3.5.5). Using the

Gumbel extreme value distribution, this extreme value analysis allows comparison of crack size (crack depth) distribution for P-II and Cr-II values.

Figure 6-48 shows that the P-II specimen has a population of defects that are larger than those in the Cr-II specimen, using fracture toughness 3.5 MPa.m$^{1/2}$ and 2.9 MPa.m$^{1/2}$ for P-II and Cr-II samples respectively (see Table 6-2). Normalising by average grain size (the Cr-II samples have larger grain size) shows that the defects are larger than the grain size, and the defect in the P-II sample have lengths that are larger, in terms of the average numbers of grain per crack, than the Cr-II sample.

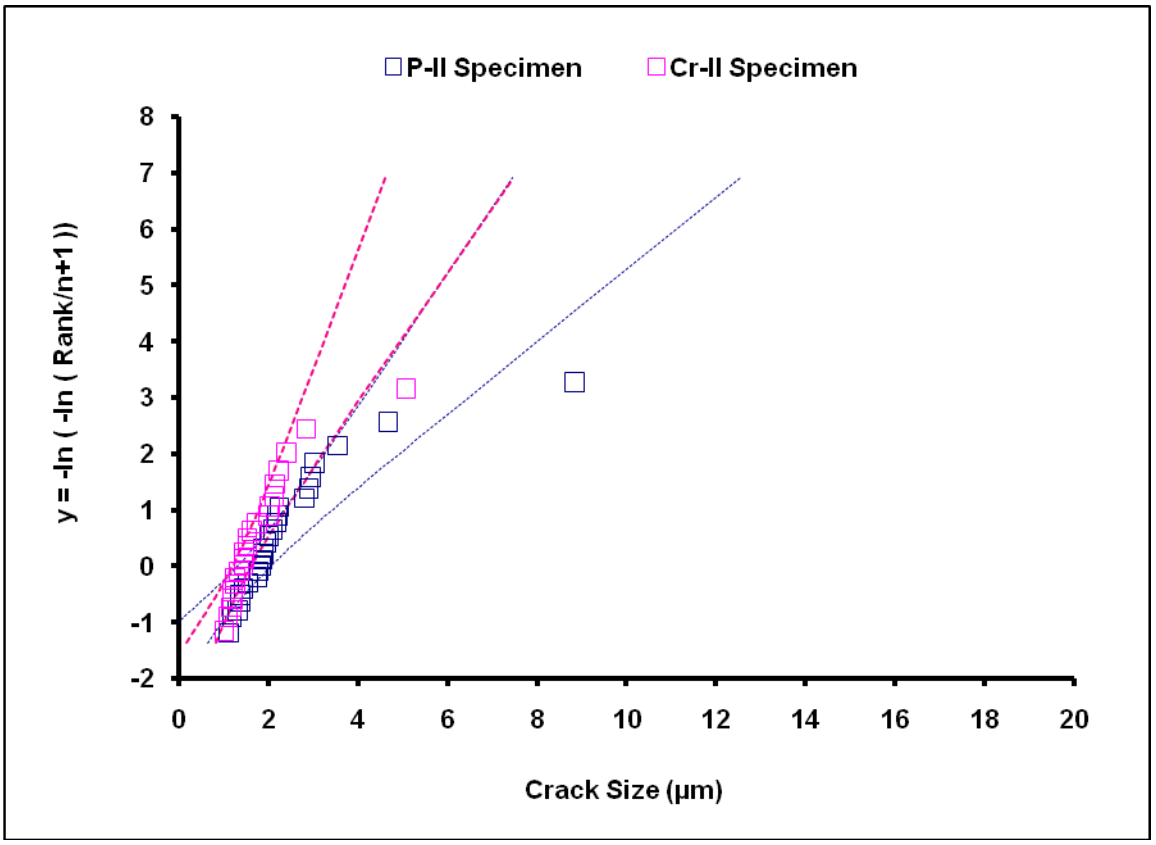

a)

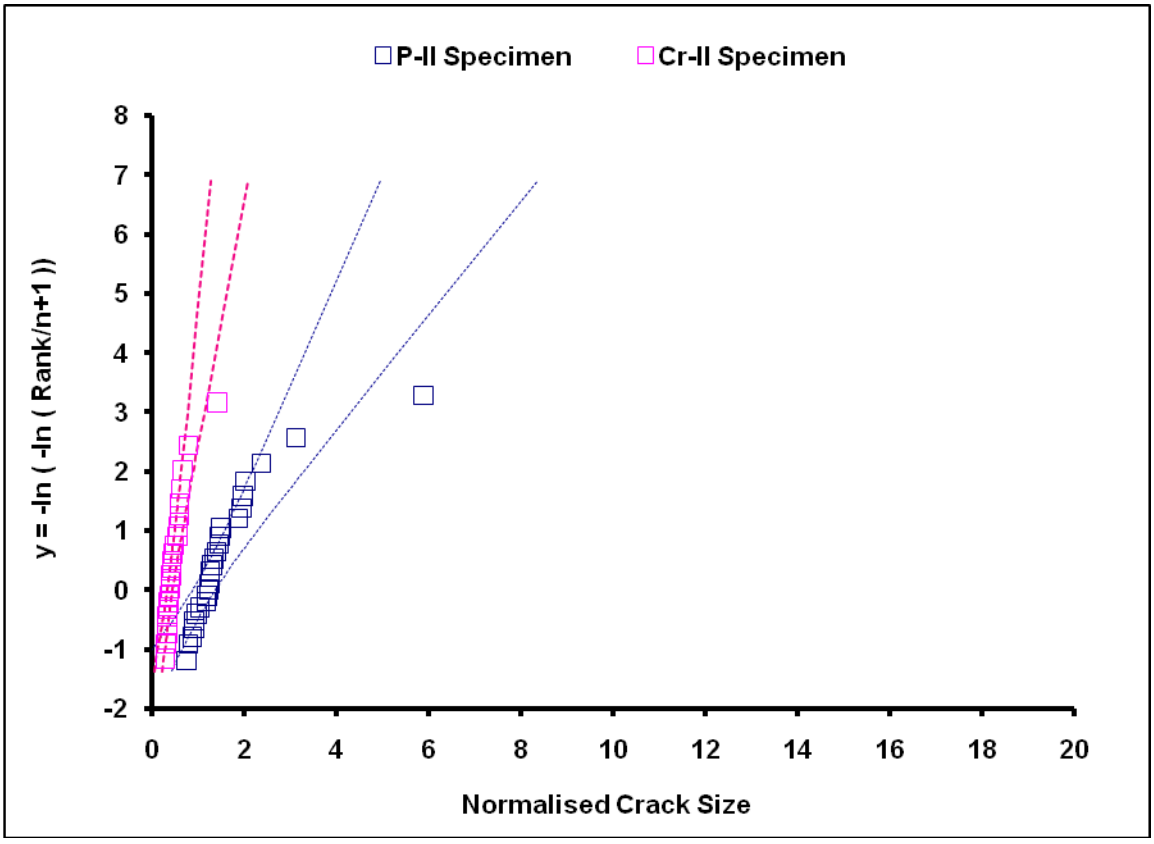

b)

Figure 6-48: The distribution for the small defect size was used using Gumbel distribution against the crack length for a) Normal crack size and b) Normalised crack size.

6.3.6 Determination of surface crack densities

The cracks population in terms of the searched area was estimated using Hertzian indentation test and the flaw densities developed of the stressed area neighbouring to the indentation site [79]. Appendix shows the relationship between the maximum and minimum radii against the applied load for Warren's data [79]. The purpose of that analysis was to show the equations of Warren's method were applied correctly by comparing the calculated values with values read from the plots in [79] (see Appendix C). Good agreement was obtained, so the data obtained in this project have been analysed.

In both samples P-II and Cr-II specimens, the sample and indenter parameters were elastic properties (ν = 0.24), (E = 390 GPa), indenter radius (R = 2.5 mm), Fracture toughness (K_{1C} = 3.5MPa.m$^{1/2}$, 2.9MPa.m$^{1/2}$) and defect size was obtained from the ring crack radius,

the failure load and the fracture toughness as mentioned early in section (6.3.3) (for example, c = 2.24 µm, and 2.23 µm) for P-II and Cr-II specimens respectively. The searched area was calculated by subtracting the area at maximum crack radius from area at the minimum crack radius. The full method is described in section (3.5.6).

Figure 6-49 is an example to show the effect of the cracks on the values of maximum ring crack radius (r_{max}) and minimum ring crack radius (r_{min}) against the applied load for cases where stress intensity factor is equal to the fracture toughness.

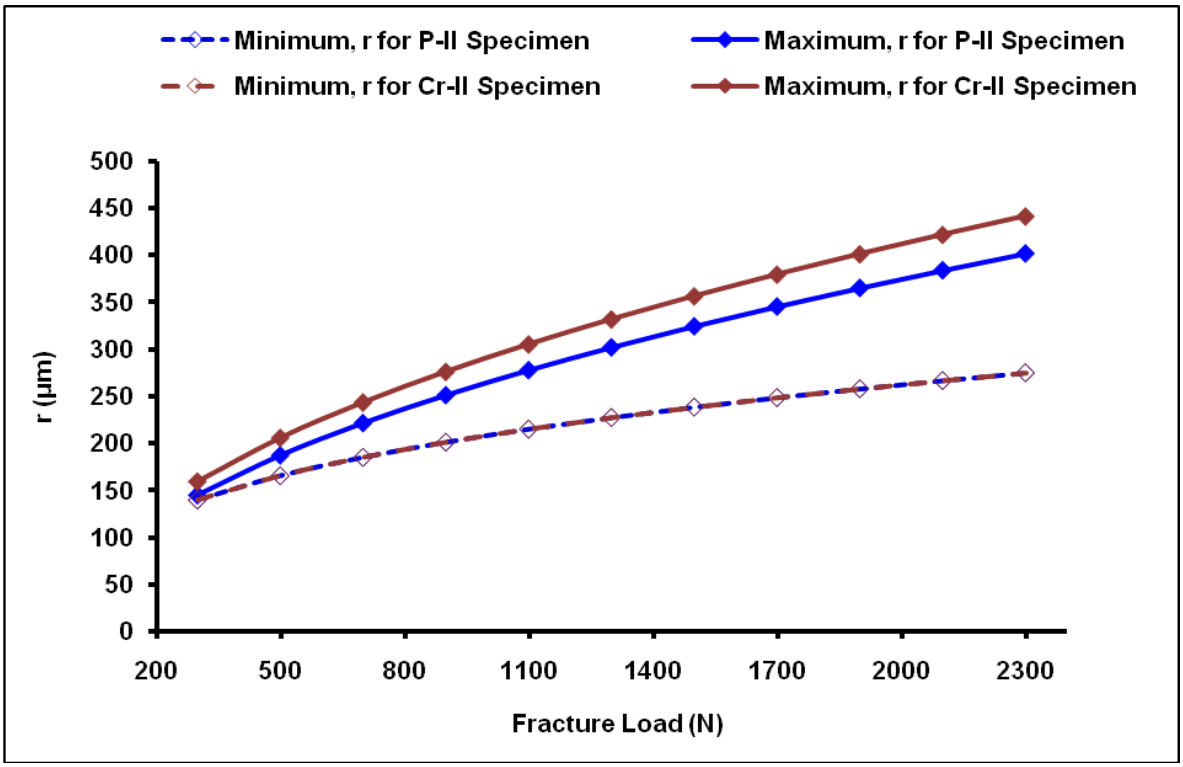

Figure 6-49: Shows the maximum (r_{max}) minimum (r_{min}) and radii at which $K_I=K_{IC}$ versus applied load. The crack depth is 2.24 µm and 2.23 µm, the sphere radius is 2.5 mm. Poisson's ratio is (0.24), Young modulus 390 GPa and the fracture toughness of the substrate is 3.5 MPa.m$^{1/2}$ and 2.9 MPa.m$^{1/2}$ for P-II and Cr-II specimen respectively.

Table 6-3 and Table 6-4 shows the data points for P-II and Cr-II specimens and also the number of defects for each defect size. The density of defects can be calculated by dividing the number of defects of a particular size of defect in the searched area. The defect sizes are shown in Table 6-3 and Table 6-4 shows for P-II and Cr-II specimen respectively. Figure 6-50 shows flaw density determined from the searched area as described in section

(3.5.6) at sphere radius (2.5 mm) for the P-II and Cr-II specimens. The normalised flaw density distribution was almost the same for the P-II and Cr-II specimen. The flaw density was normalised (i.e. the flaw density divided by number of grains per unit area) and defect size was normalised (i.e. the defect size divided by grain size 1.5 μm and 3.6 μm for P-II and Cr-II specimen respectively) and the distribution for flaw density are shown in Figure 6-50b.

A log-normal distribution (using the Excel LOGNORMDIST function) was fitted to the flaw density distribution and the purpose of the fitting was to show that the data could fit a log-normal distribution. The log-normal distribution function depends on the crack or defect size and the Arithmetic mean of distribution (i.e. adjust to fit distribution; it is not very sensitive to this) and standard deviation of the distribution (i.e. adjust to fit distribution; it is quite sensitive to this) for getting the probability mass. The Arithmetic mean of distribution, and standard deviation of the distribution values for P-II and Cr-II samples are shown in Table 6-5 and the results for the flaw distribution plots are shown in Figure 6-50.

Table 6-3: Shows the defect sizes, number of defects, searched area, and flaw density for the P-II specimen (i.e. Defect size represents crack depth).

Defect Size, c $\times 10^{-6}$ (m)	**Number of Defects, n(c)**	**Searched Area A(c) $\times 10^{-7}$($m^{2)}$**	**Flaw Density, n(c)/A(c) $\times 10^{6}$ (m^{-2})**
1-2	14	1.48	93.98
2-3	8	2.27	35.11
3-4	2	2.87	6.95
6-7	1	3.61	2.76
8-9	1	5.17	1.93

Table 6-4: Shows the defect sizes, number of defects, searched area, and flaw density for the Cr-II specimen.

Defect Size, c $\times 10^{-6}$ (m)	Number of Defects, n(c)	Searched Area A(c) $\times 10^{-6}$(m^{2})	Flaw Density, n(c)/A(c) $\times 10^{6}$ (m^{-2})
1-2	15	1.55	9.66
2-3	7	1.34	6.15
3-5	1	0.334	2.99
5-7	1	0.456	2.19

Table 6-5: Shows the Arithmetic mean and standard deviation of the distribution for the P-II and Cr-II samples.

Samples	Arithmetic mean	standard deviation
P-II	0.005	0.33
Cr-II	0.005	0.5

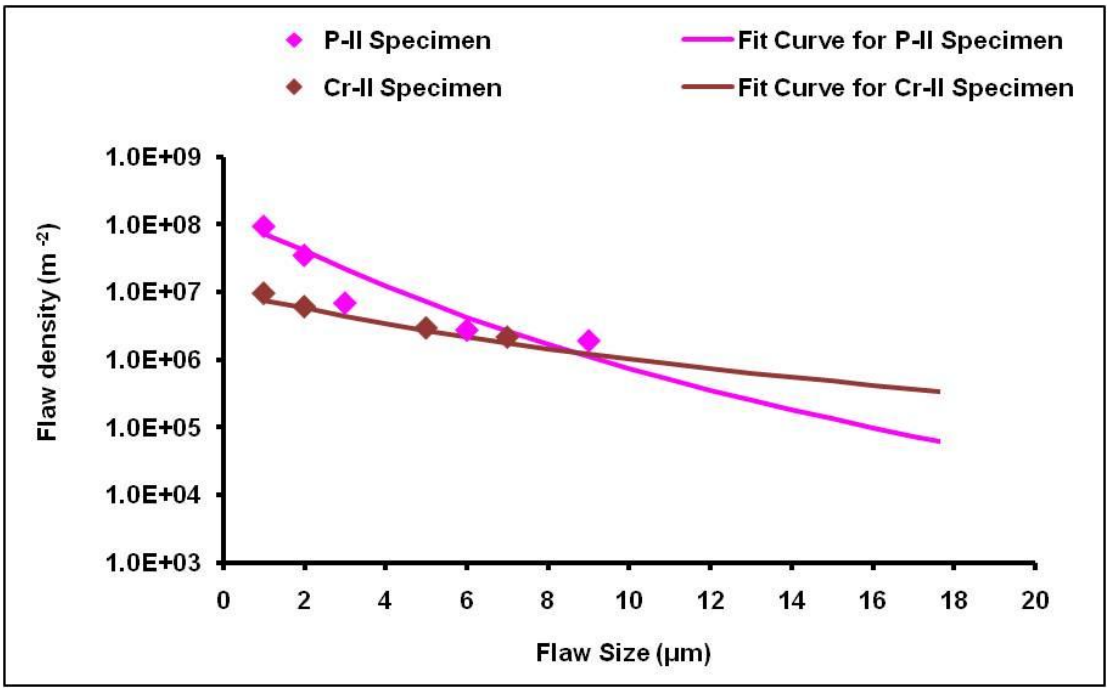

a)

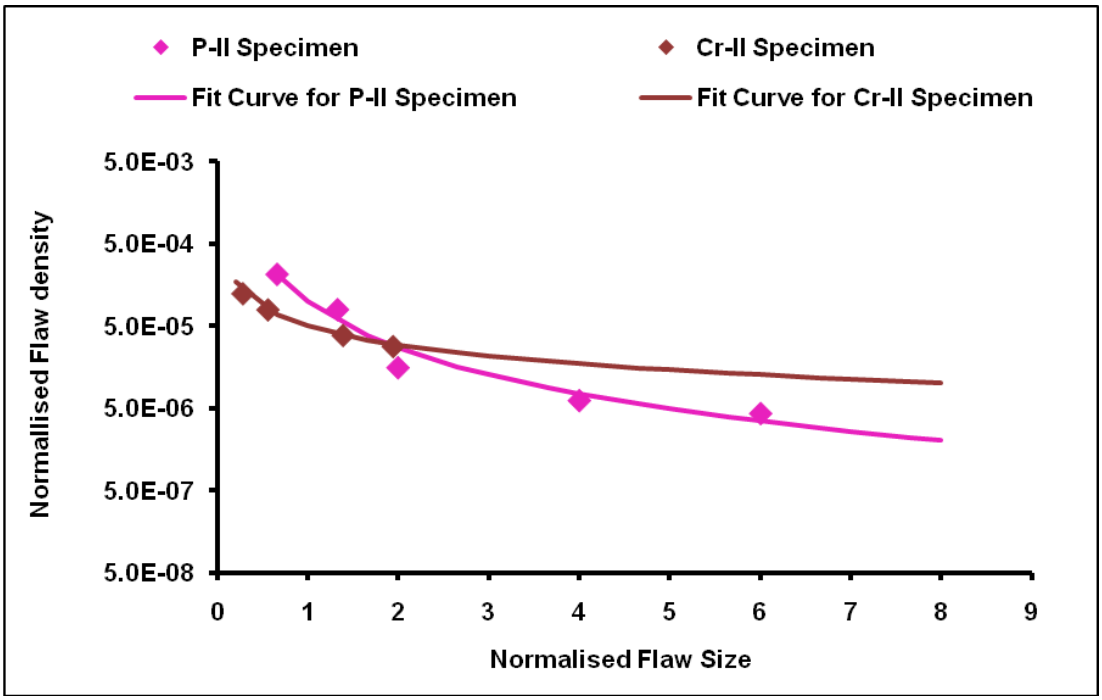

b)

Figure 6-50: Shows flaw density determined from the searched area for the sphere radii of (2.5 mm) for the P-II and Cr-II specimens for a) Normal flaw density distribution and b) Normalised flaw density distribution (i.e. flaw size normalised by the grain size and flaw density normalised by the number of grains per unit area). The flaw density axes use a logarithmic scale. (Flaw size represents crack depth).

Figure 6-51 shows the comparison between Warren's data for the well polished surface [109] at different sphere radii (r = 2.5, 5, 10, and r=20 mm) with the experimental data at sphere radius (r = 2.5 mm) and the flaw density distributions are similar of the small crack size for the Warren's data and experimental data as shown in Figure 6-51.

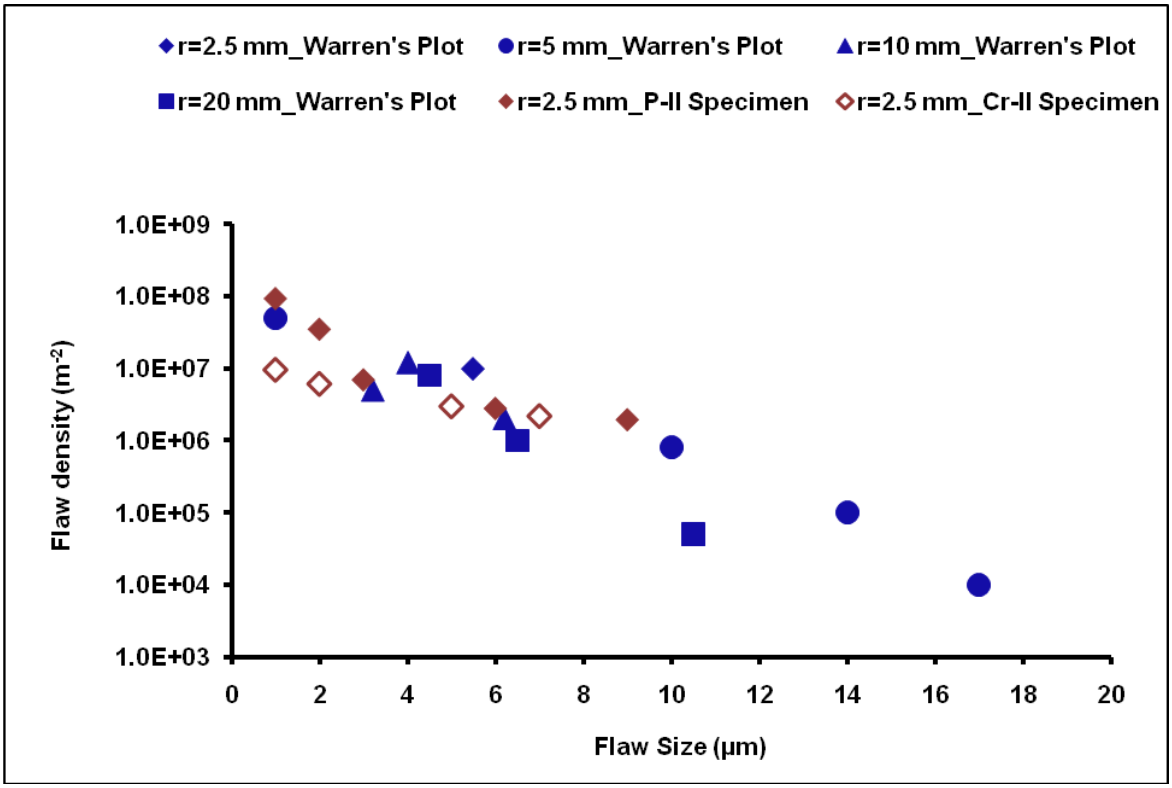

Figure 6-51: Comparison flaw density plots between the Warren's data at different sphere radii (r = 2.5, 5, 10, and 20mm) [79] and the experimental data at sphere radius (r = 2.5 mm).

Summary

The ring crack radius was observed for the P-II and Cr-II sample using optical microscope. The failure cumulative probability was measured for the smooth and coarse surface preparation in the P-II and Cr-II sample. The minimum load was used to measure the (K_{1C}) and the cracks initiated on the sample surface and then will grow into ring crack. The defect size and defect population were assessed using searched area in the Hertzian test.

Chapter 7

7 Discussion II

7.1 Microstructural Analysis

The microstructural analysis (see Figure 4-1 and Figure 4-2) shows the microstructure consists of non-equiaxed grains and pores. The grain growth is not uniform for the alumina microstructure [33]. The alumina microstructure has a porosity is about 0.5% due to the recent sintering method is used to process the alumina samples [22].

7.2 2D Observation of Intergranular Cracking

7.2.1 Digital Image Correlation

The digital image correlation is used to calculate the vector displacement accuracy and the noise level depends on the surface preparation and interrogation window size. The sample surface has a high contrast variation and spots as shown in Figure 4-5, and Figure 4-8, for the glass and polycrystalline alumina samples respectively. The levels of noise were 0.0160 μm, 0.0018 μm, and 0.0042 μm for the glass, P-II, and Cr-II samples respectively at different magnification, window size and overlap as detailed in sections (3.3.3.1 and 3.3.4.1). The noise level was different between the P-II and Cr-II samples due to the smaller grain size for P-II compared to the Cr-II sample (i.e. the number of the features for the P-II sample is higher than the Cr-II sample). The noise level was different between the glass and polycrystalline alumina samples because the feature size for the glass sample is higher than the feature size for the polycrystalline alumina samples (P-II and Cr-II) and also, the magnification used for the glass specimen was lower than used for polycrystalline alumina samples (i.e. the magnification was X100 and X20 for the polycrystalline alumina (P-II and Cr-II specimens) and glass sample respectively) (see Figure 4-13).

7.2.2 Detection of Intergranular Cracks by Digital Image Correlation

7.2.2.1 The characteristics of Strain features

The image correlation data is used to obtain a strain map from the measured relative displacements. The magnitude of the strain depends on the gradient of this displacement (i.e. the displacement magnitude and the gauge length). This strain features that increase in their strain magnitude as the applied strain is increased (i.e. the strain features were orthogonal to the applied load in the X-direction) (see Figure 6-2 and Figure 6-5), but showed no significant variation in the orthogonal Y-direction (see Figure 6-3 and Figure 6-6).

The strain features values depend on the chosen threshold. Figure 6-7 a, and b shows there is a general trend of increasing strain feature magnitude with applied strain but the background strains (parallel, ε_{xx} and perpendicular, ε_{yy} to the applied strain) do not change significantly. The dimensions of the strain features depend on the chosen threshold. Figure 6-8 a, b and Figure 6-8 a, b show that the surface length tends to increase with applied strain. For example see Figure 7-1 which shows the effect of the threshold on the population of cracks detected. If the threshold were sufficiently low then the distribution would be expected to become stable (i.e. nearly constant) for the longest features with increasing load. If the threshold were too high, then fewer strain features would be observed, but the microstructure of large defects should be stable in length once they emerge from the noise as the applied strain increased. The behaviour observed indicates that the chosen threshold of 1% is sufficiently low to capture the approximate dimensions of the larger features, but as their dimensions depend on the threshold, it is clear that the measured dimension is only approximate. A simple sketch of the effect of threshold on the length of a strain feature at different applied load is shown in Figure 7-1.

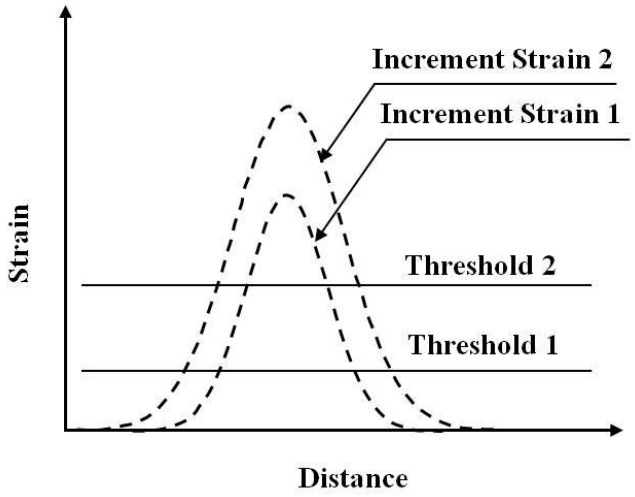

Figure 7-1: Show a simple sketch of the effect of threshold on the length of a strain feature at different increment applied strain.

The overlay of the strain maps on the microstructure (Figure 6-11 and Figure 6-13) shows that the strain features are associated with the grain boundaries.

7.2.2.2 Measured Displacement Difference

The most accurate method for measuring the displacement is to compare the displacements in a line across the feature with those along a path that is adjacent to it. Such measurements (Figure 6-15 and Figure 6-18) show that the displacement increases with applied strain. The digital image correlation displacement measurements should be regarded as qualitative, as the heterogeneity of contrast in the images was insufficient for accurate measurement of displacement at this magnification.

Figure 6-16 and Figure 6-19 show the surface crack opening displacement were not well measured. The finite element model data was represented as an apparent strain arising from the displacement gradient. The simulation method from finite element model data shows the surface crack opening displacement was not well measured due to effects from window size and overlapping the window size with the slot as mentioned in section (5.3). This suggest that the DIC is used to observe the cracks but not to measure their compliance (i.e. the displacement difference was not well measured by digital image correlation as it does not accurately measure the displacement and also, effect the window size on the surface crack opeing dispalcemen).

7.2.3 Destructive analysis of Grain Boundary Planes

The focused ion beam, (FIB) and electron backscatter diffraction (EBSD) analysis and trace analysis of grain boundaries was used to obtain the orientation the grain boundary planes (see Figure 7-2). The forms of the facetted planes in the polycrystalline alumina [51, 110, 111] and the facet planes for the grain boundaries compare to the poles of low energy facet planes in alumina in the adjacent grains. The facet pole planes in the alumina [112] are (0001), $\{01\bar{1}2\}$, $\{11\bar{2}3\}$, $\{01\bar{1}1\}$ and $\{01\bar{1}0\}$ [51].

The analysis was done for seven boundaries for the P-II specimen and four boundaries for the Cr-II specimen, of which three were associated with strain features and hence considered to be cracked. The grain boundary pole was plotted on the pole figures generated by Tango Software from electron backscatter diffraction, EBSD data, since all the measurements are relative to the microscope system, not the crystal system. The uncertainty of the grain boundary plane pole orientations was shown using a dotted red circle. An example is shown in Figure 7-2 in which the pole of grain boundary G12 or strain feature A (the cracked boundary) is near the basal plane of grain G1 in the P-II sample and the grain boundary plane G12 or strain feature B and Cr- strain feature are close to the basal plane of grain G2 in the P-II and Cr-II sample respectively for the upper hemisphere. There is a tendency for the cracked grain boundaries to have a plane that has at least one normal that is close to the basal plane normal (i.e. two cracked boundaries and one cracked boundary were observed in P-II and Cr-II samples respectively). The Table 7-1 shows that although some boundaries were observed to be close (i.e. within 4°) to particular facet planes this was not frequent for the upper or lower hemisphere. The smallest angles were measured between the pole of grain boundary and the basal plane of grain for the upper or lower hemisphere is shown in Table 7-1 and Table 7-2. This is consistent between this model and three-dimensional observations of grain boundary plane orientations in a coarse grain size alumina by diffraction contrast tomography and it shows different orientation for many boundaries [54]. Figure 7-3 shows grain boundary plane poles for the non-cracked boundaries.

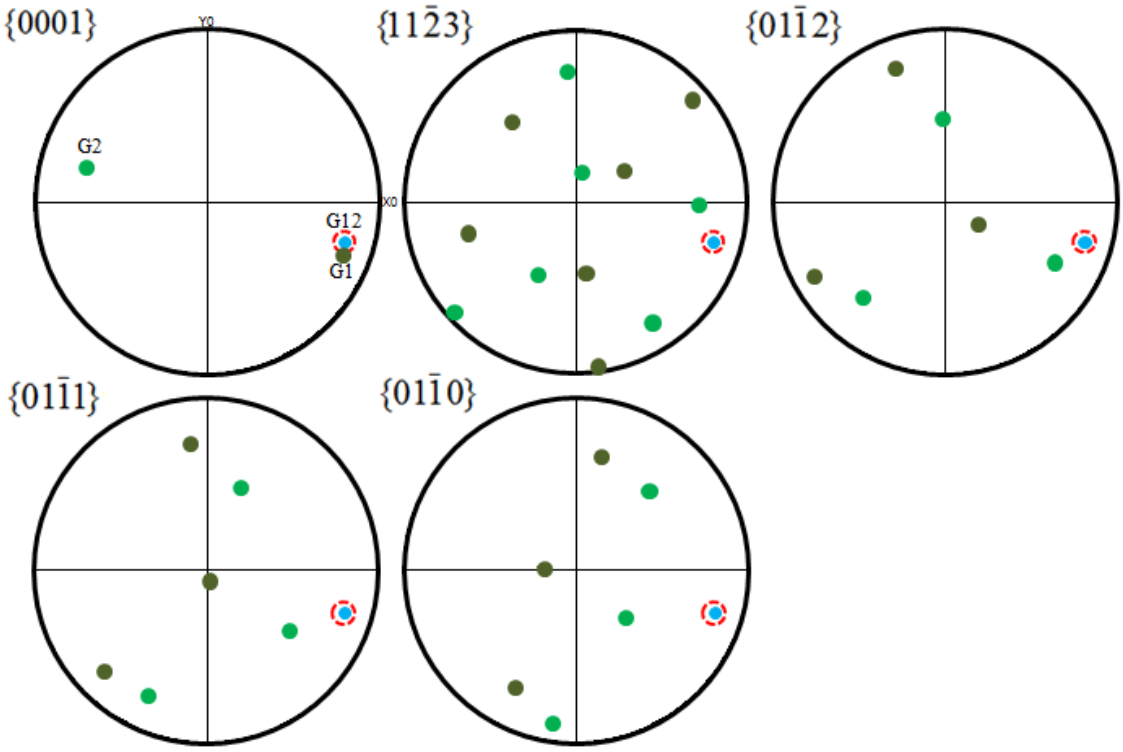

a) Strain feature A in P-II Sample

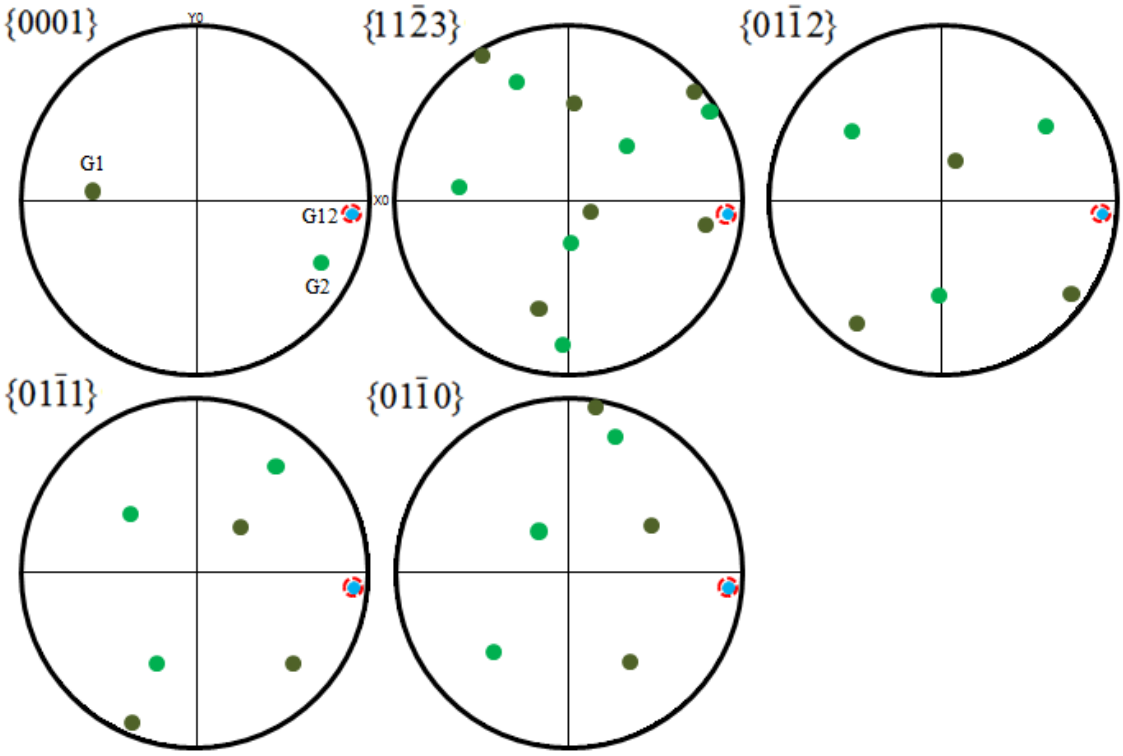

b) Strain feature B in P-II Sample

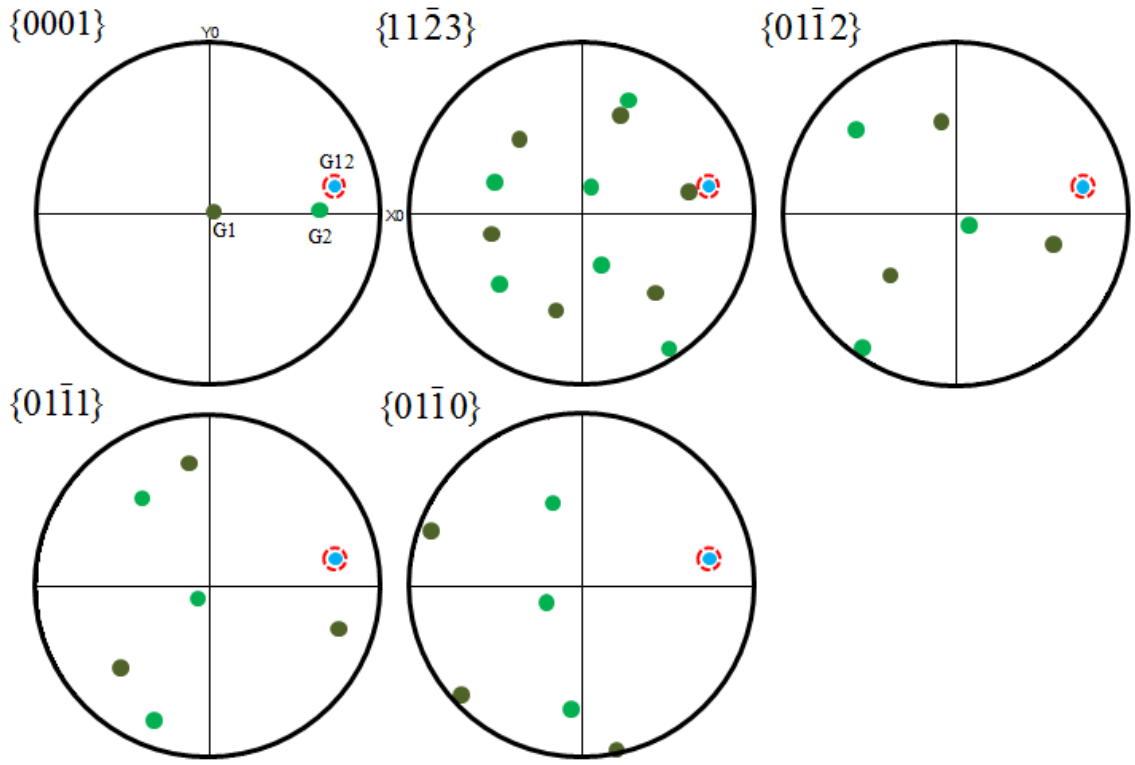

c) Strain feature in Cr-II Sample

Figure 7-2: Pole figures for the grain boundary plane, G12 of the common facet plane in the polycrystalline alumina (P-II and Cr-II samples) in grains G1 (dark) and G2 (light) for the upper hemisphere. The boundary plane is near the basal facet plane (0001) in the G1 for strain feature A in P-II sample and the G2 in strain feature B in sample P-II and the strain feature in Cr-II sample. a) Strain feature A in the P-II sample, b) Strain feature B in the P-II sample, and c) Strain feature in the Cr-II sample.

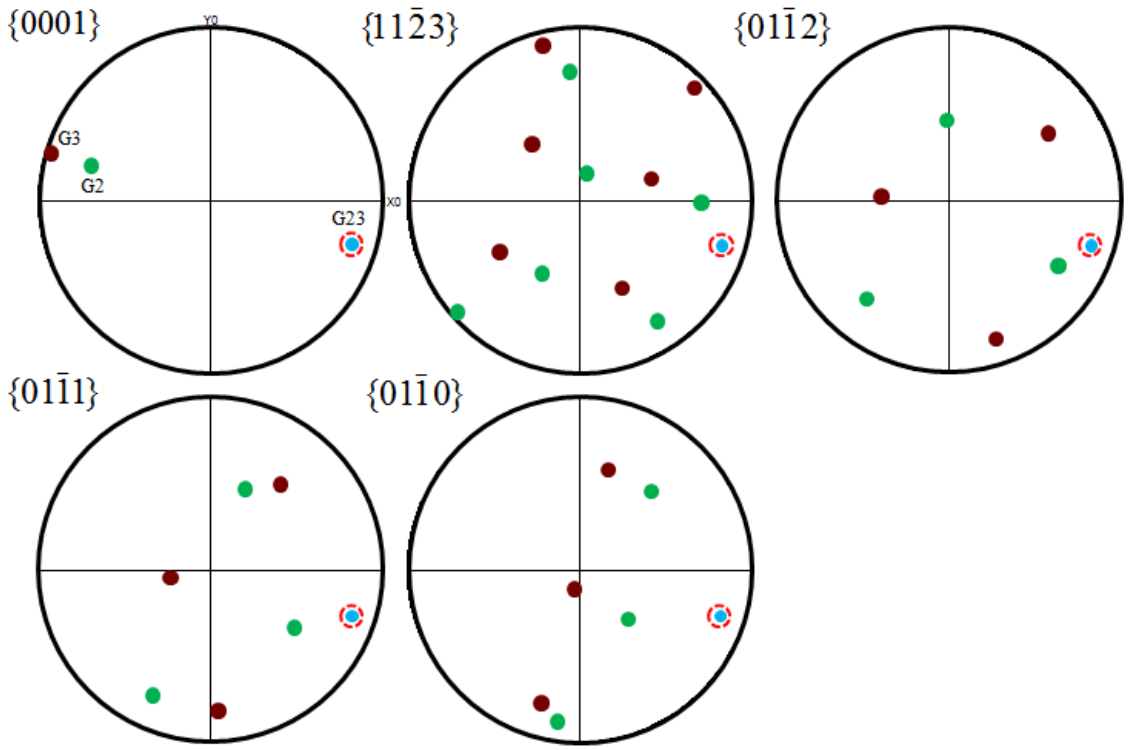

a) Non-cracked boundary in the strain feature A region in P-II Sample

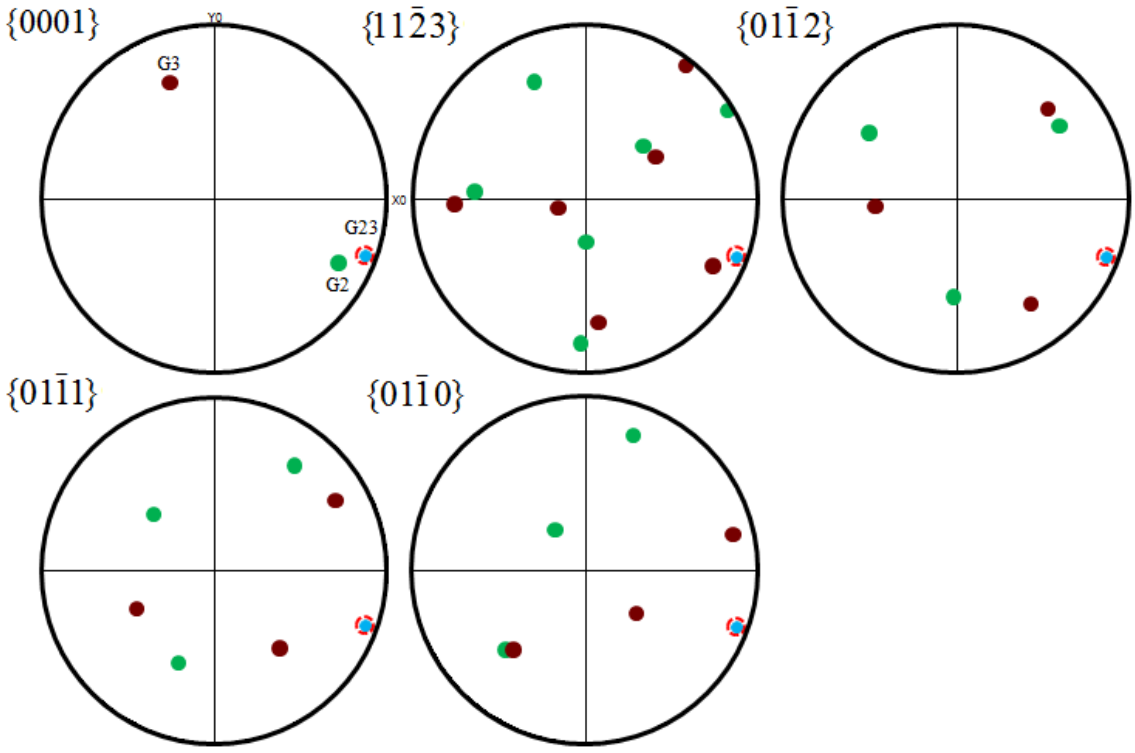

b) Non-cracked boundary in the strain feature B region in P-II Sample

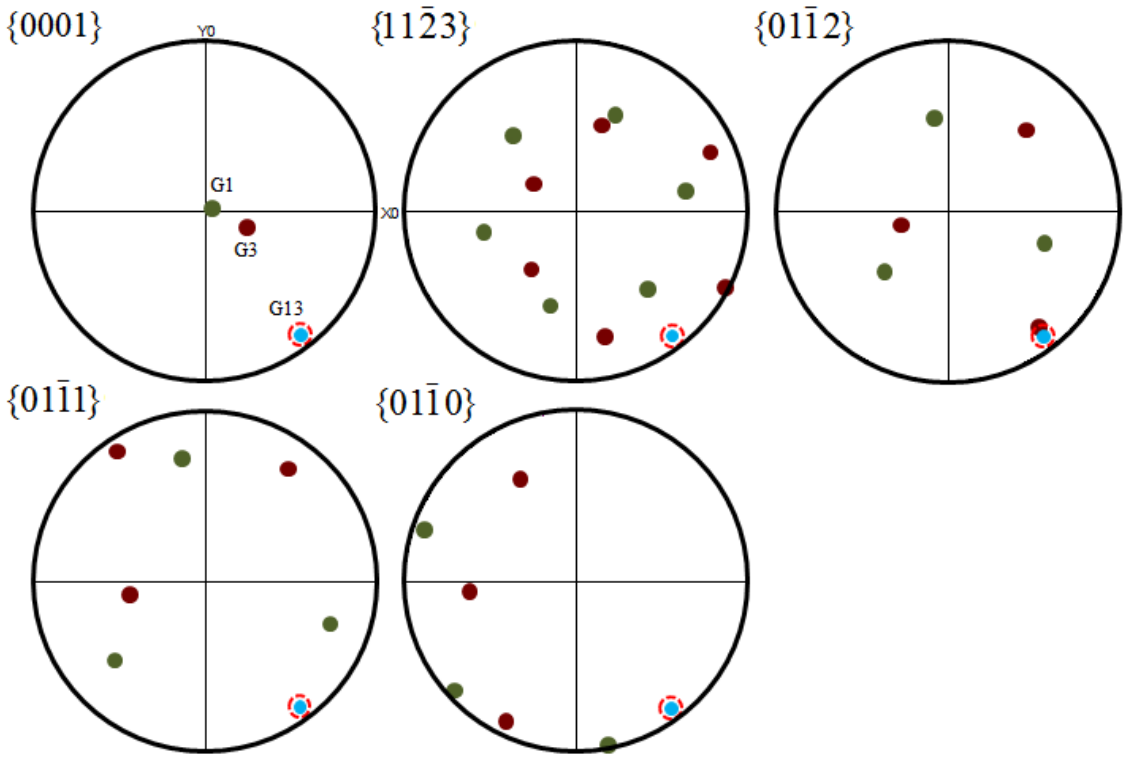

c) Non-cracked boundary in the strain feature region in Cr-II Sample

Figure 7-3: Pole figures for the grain boundaries plane, G23 and G13 of the common facet plane in the P-II and Cr-II samples respectively. The boundary plane is not near the basal facet plane (0001) in the G1, G2 nor G3 for a) Non cracked boundary close to the strain feature A in the P-II sample, b) Non cracked boundary close to the strain feature B in the P-II sample, and c) Non cracked boundary close to the strain feature in the Cr-II sample.

7.3 Modelling of Intergranular Strains

An anisotropy thermal expansion caused the intergranular cracking along the grain boundaries [45]. There is different thermal expansion between a-axis and c-axis stresses at grain boundaries in the hexagonal single phase polycrystals for alumina and the different thermal expansion developed as the cooling from the processing temperature. Such boundaries are predicted to develop higher tensile stress.

7.3.1 A simple model for intergranular strains

The residual stresses caused the cracking and these stresses are introduced due to the anisotropy coefficient thermal expansion during cooling from the sintering temperature to the room temperature in the polycrystalline samples [113-115]. The anisotropy in the

crystallographic directions and misorientation between the adjacent grains caused the different stresses at the boundaries which produced the intergranular cracking [41].

The relative stresses that develop at these grain boundaries were estimated by considering the requirement to accommodate the net displacement between grains that arises during cooling from the firing temperature (typically 1680°C). To estimate this, the coefficient of the thermal expansion normal to the grain boundary plane was calculated for each grain, assuming an elliptical variation with orientation between the maximal and minimal values (i.e. perpendicular and parallel to the (0001)) of 9.38×10^{-6} and 8.62×10^{-6} K^{-1} respectively [33]. A neighbourhood of many grains of varying orientation surrounds each grain; hence the relative displacement between the centres of adjacent grains is determined by the bulk thermal expansion coefficient, which was taken to be an average crystal thermal expansion coefficient (9.00×10^{-6} K^{-1}). The net intergranular displacement was calculated by subtracting the bulk dimensional change (average thermal expansion coefficient × temperature change × sum of grain dimensions) from the sum of the dimensional changes of adjacent grains (thermal expansion coefficient perpendicular to boundary × temperature change × grain dimension). This net displacement is dominated by the coefficient of the thermal expansion normal to the boundary for individual grains. Higher tensile stresses are therefore expected at the grain boundary if one of the grains has its (0001) pole aligned closer to the grain boundary pole.

The total component of the displacement perpendicular to the grain boundary was calculated with a simple model using grain and grain boundary orientations and the grain size. The movement of the centres of the grains as the temperature changes is governed by the average thermal expansion coefficient, CTE of the material. However, the strain at the grain boundary develops if the two grains contract relative to each other.

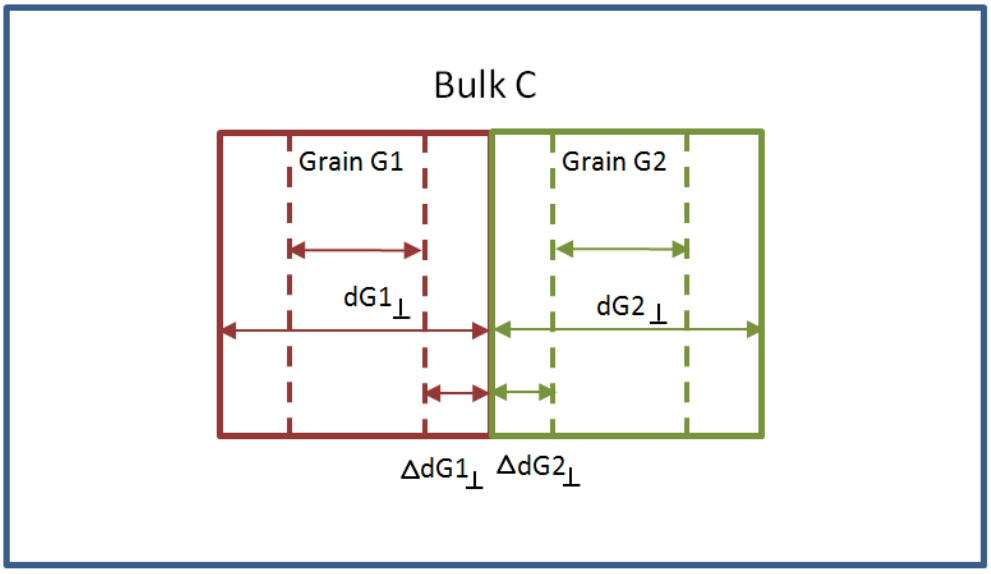

Figure 7-4: Schematic image of the grain G1 and grain G2 in bulk C to show the grain size, dG and displacement, ΔdG for G1 and G2 perpendicular to the grain boundary. This also, shows the shrinkage for the grains G1 and G2.

The change in dimension of each grain perpendicular to the grain boundary depends on the size of the grains and the grains orientation and the change in dimension of the orientation around the pair of grains (perpendicular to the grain boundary). This depends on the total size of the two grains and the average of CTE of the microstructure. Figure 7-4 shows grain G1 and grain G2 from the same material where shrinkage for the grain G1 is not the same for the grain G2 due to the anisotropy of thermal expansion coefficient.

The effect of the orientation on the thermal expansion coefficient, CTE was estimated using the formula for the radius of an ellipse [116], which has axes for the maximum and minimum CTE value of the crystal is shown in Figure 7-5. The CTE perpendicular to the grain boundary was calculated using Equation (52), (see Figure 7-6). The dimensions of each grain were measured perpendicular to the grain boundary on the imaged surface. The cracked boundaries tend to be those with higher values of net thermal expansion coefficient (CTE) (i.e. the sum of the thermal expansion coefficients normal to the grain) (see Figure 7-7).

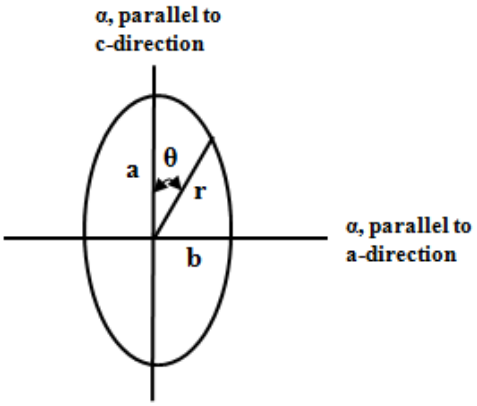

Figure 7-5: Shows the maximum thermal expansion (a) and minimum thermal expansion (b) in the hexagonal structure.

$$r(\theta)=\frac{ab}{\sqrt{(b\cos\theta)^2+(a\sin\theta)^2}} \tag{52}$$

Where:

Thermal expansion coefficient (CTE), α is anisotropic.

a, represents the CTE in c-direction of the hexagonal structure (i.e. parallel to (0001)) is 9.38×10^{-6} K^{-1} [33].

b, represents the CTE in a-direction of the hexagonal structure (i.e. perpendicular to (0001)) is 8.62×10^{-6} K^{-1} [33].

r (θ), represents the CTE perpendicular to boundary is 8.62×10^{-6} K^{-1} and the average CTE is 9×10^{-6} K^{-1}.

θ, represents the angle between {0001} pole and boundary plane (°).

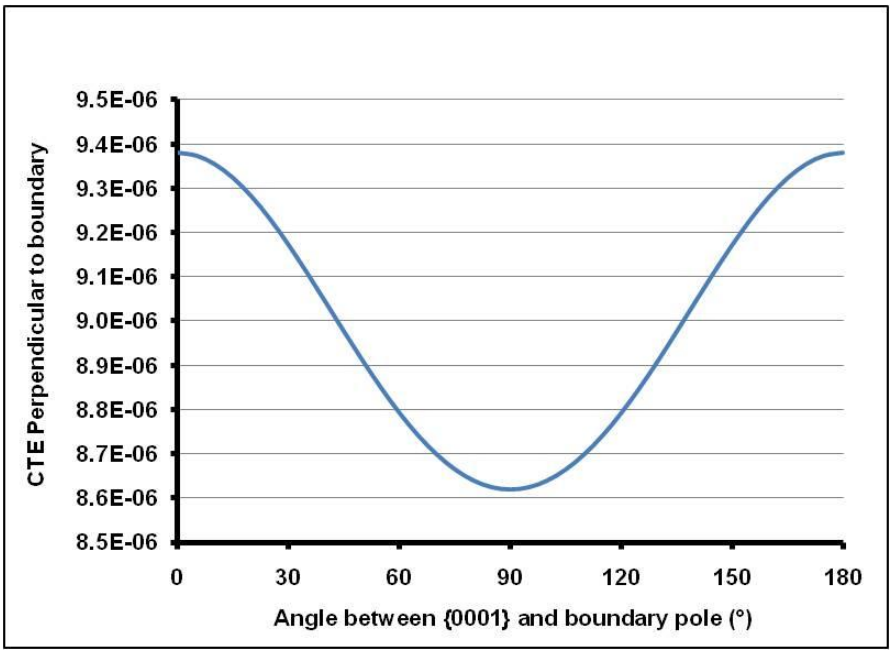

Figure 7-6: Shows the coefficient of the thermal expansion perpendicular to boundary as a function to the angles between the (0001) and boundary pole.

Where: (dG1) and (dG2) represents the grain size perpendicular to the grain boundary for (G1) and (G2) respectively. The displacement perpendicular to the grain boundary ($\Delta dG_{\perp}$) was calculated using equations (53) and (54) and the total displacement (ΔdG_{total}) using equation (55).

$$\Delta dG1_{\perp} = \alpha_{\perp} \times dG1_{\perp} \times \Delta T \quad (53)$$

$$\Delta dG2_{\perp} = \alpha_{\perp} \times dG2_{\perp} \times \Delta T \quad (54)$$

$$\Delta dG_{total} = \Delta dG1_{\perp} + \Delta dG2_{\perp} \quad (55)$$

The bulk and net displacement were calculated using equations (56) and (57).

$$Bulk\ \ displacement = \alpha_{average} \times \Delta T \times \left(dG1_{\perp} + dG2_{\perp}\right) \quad (56)$$

$$Net\ \ displacement = Total\ \ displacement - Bulk\ \ displacement \quad (57)$$

The nominal stress was calculated for the nominal strain and it is measured by assuming this displacement is accommodated by stretching the two grains (this is not strictly correct, since it neglects how the displacement is accommodated due to the mechanical constraints

of the surrounding grains). The effective stress was calculated, assuming that the displacement is accommodated over a distance that is a proportional to grain size (i.e. the width of strained region and this may be something that changes, depending of the geometry of grains and it were assumed to be 5% of average grain size). The displacement at the grain boundary depends on the grain size and the angle between {0001} and grain boundary plane. The nominal strain, stress and effective stress were calculated using equations 58, 59 and 61.

$$\varepsilon_{Nominal} = Net\ \ displacement / \left(dG1_{\perp} + dG2_{\perp}\right) \tag{58}$$

$$\sigma_{Nominal} = E_{C-direction} \times \varepsilon_{Nominal} \tag{59}$$

$$dG_{Average} = \left[\left(dG1_{\perp} + dG2_{\perp}\right)/2\right] \tag{60}$$

$$\sigma_{effective} = (Net\ \ displacement / Width\ of\ \ Strained\ \ \mathrm{Re}gion) \times E_{C-direction} \tag{61}$$

Seven boundaries examined using focused ion beam (FIB) and electron backscatter diffraction (EBSD) for two strain features (A and B) in P-II sample and four boundaries examined for the strain feature in Cr-II sample. The grain boundaries G12 referred to the boundary between the grain G1 and the G2 in P-II and Cr-II samples for the boundaries of interest (cracked boundaries). Two strain features were observed to be cracks in P-II sample and one strain feature was observed to be a crack in Cr-II by using digital image correlation studied. It should be noted that no cracks were visible in these boundaries of interest using scanning electron microscope and optical microscope.

The sum of the coefficient of the thermal expansion (CTE sum) (sum of the coefficient of the thermal expansion perpendicular to the grain boundary for the grains on the RHS and LHS to the boundary of interest), the net displacement, and the effective stress were calculated (see Figure 7-7, Figure 7-8, and Figure 7-9).

The uncertainty was obtained from the mean and then the range (maximum and minimum) from the uncertainty in angles. The maximum uncertainty in the net displacement, CTE sum, and effective stress were calculated by subtracting the maximum value of the CTE from the average value of the CTE and the minimum uncertainty was calculated by subtracting the average value of the CTE from the minimum value of the CTE as shown in Figure 7-7.

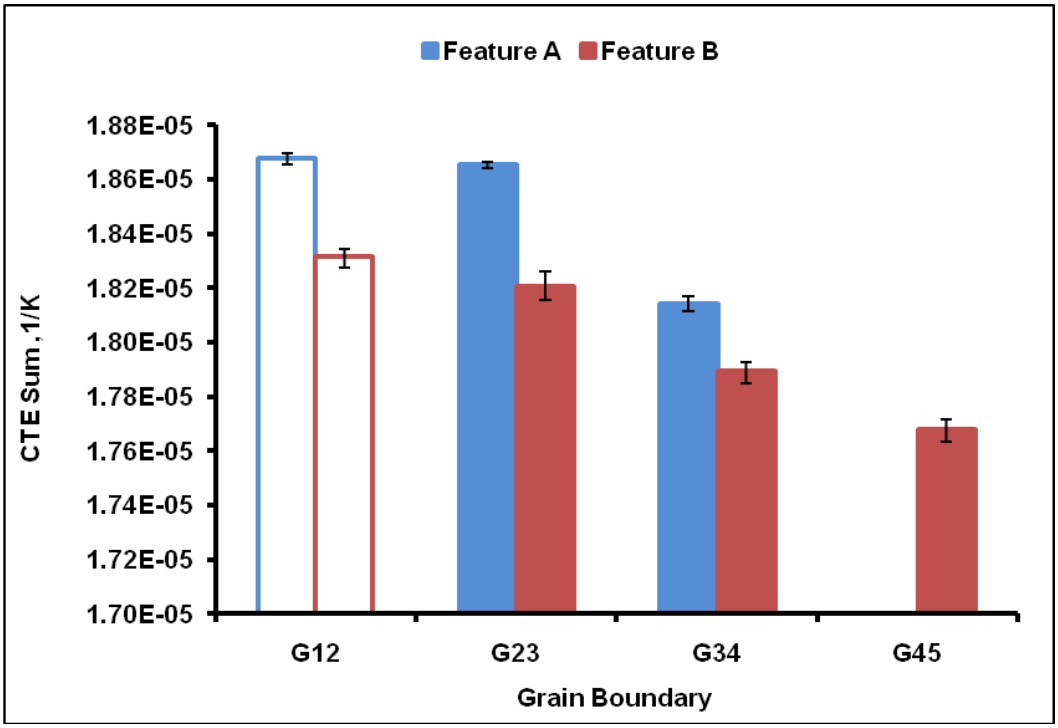

a)

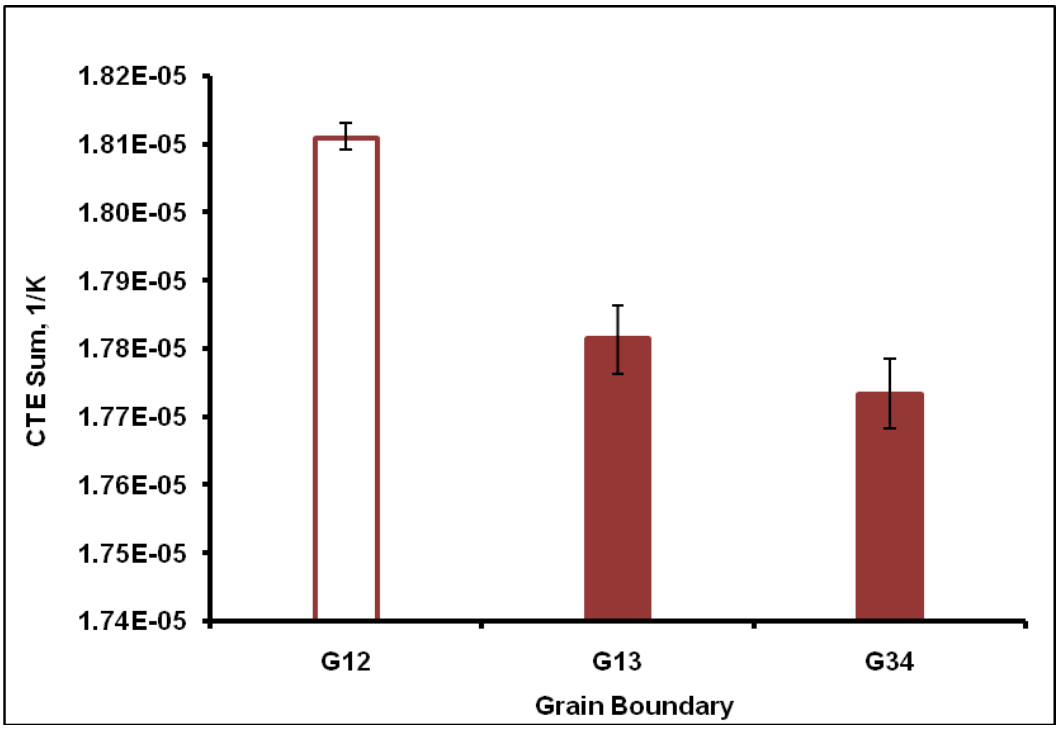

b)

Figure 7-7: The maximum thermal expansion coefficient against the grain boundary for a) P-II sample and b) Cr-II sample. (Hollow bars show the cracked boundaries).

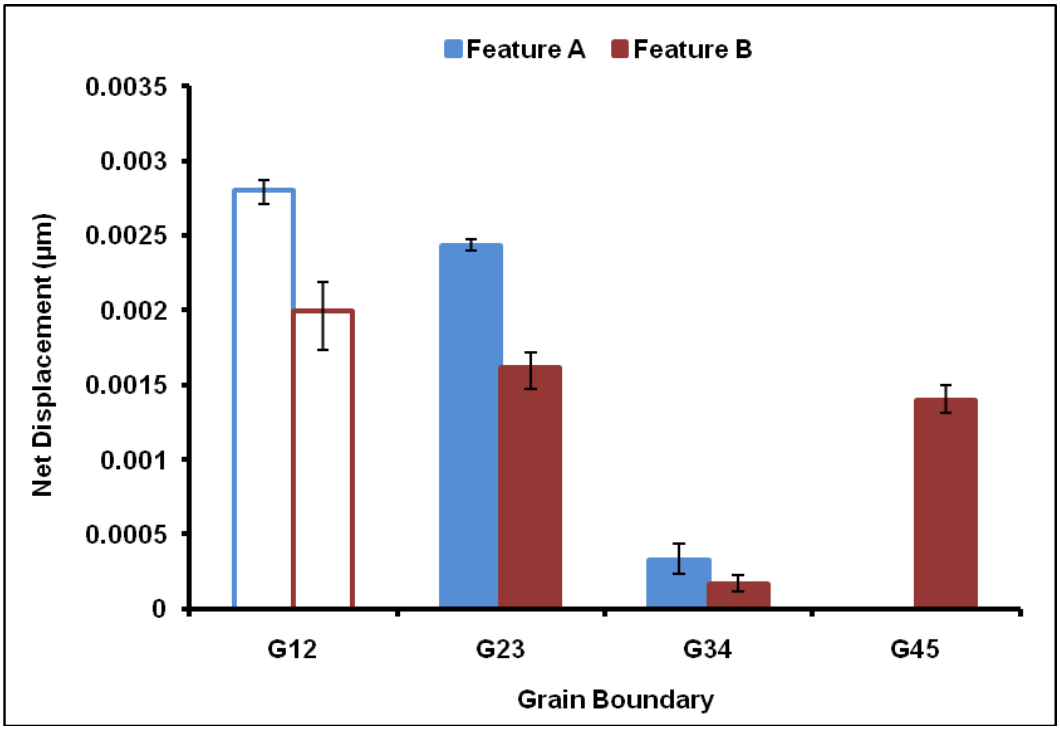

a)

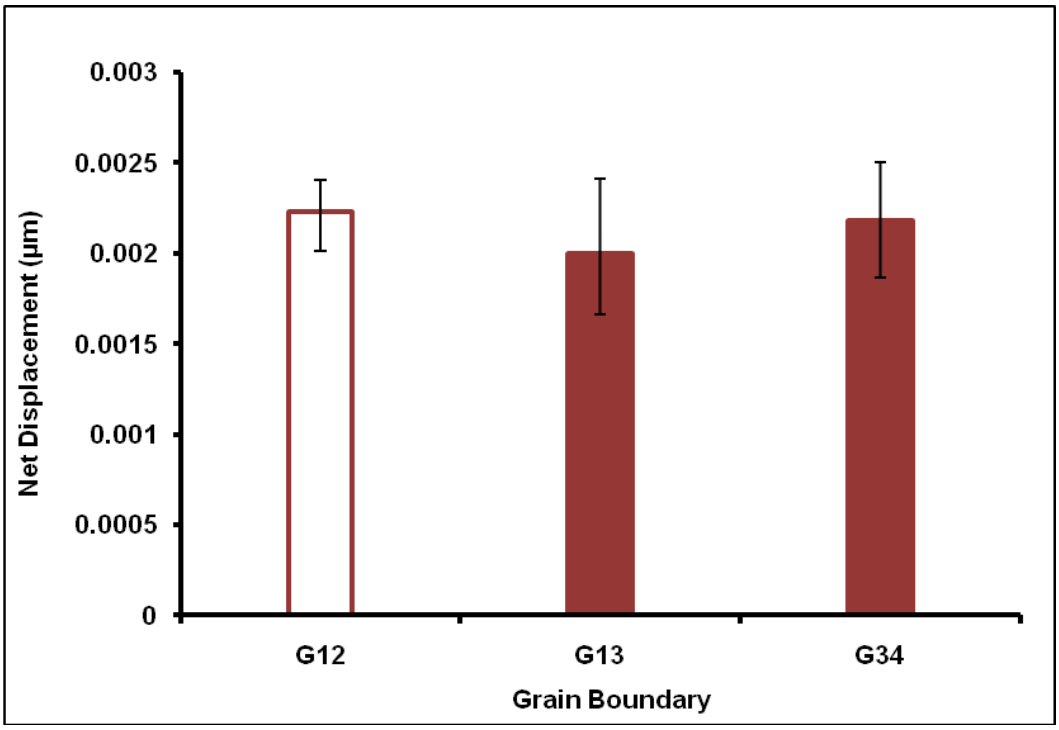

b)

Figure 7-8: The net thermal displacement perpendicular to the boundary against the grain boundary for a) P-II sample and b) Cr-II sample. (Hollow bars show the cracked boundaries).

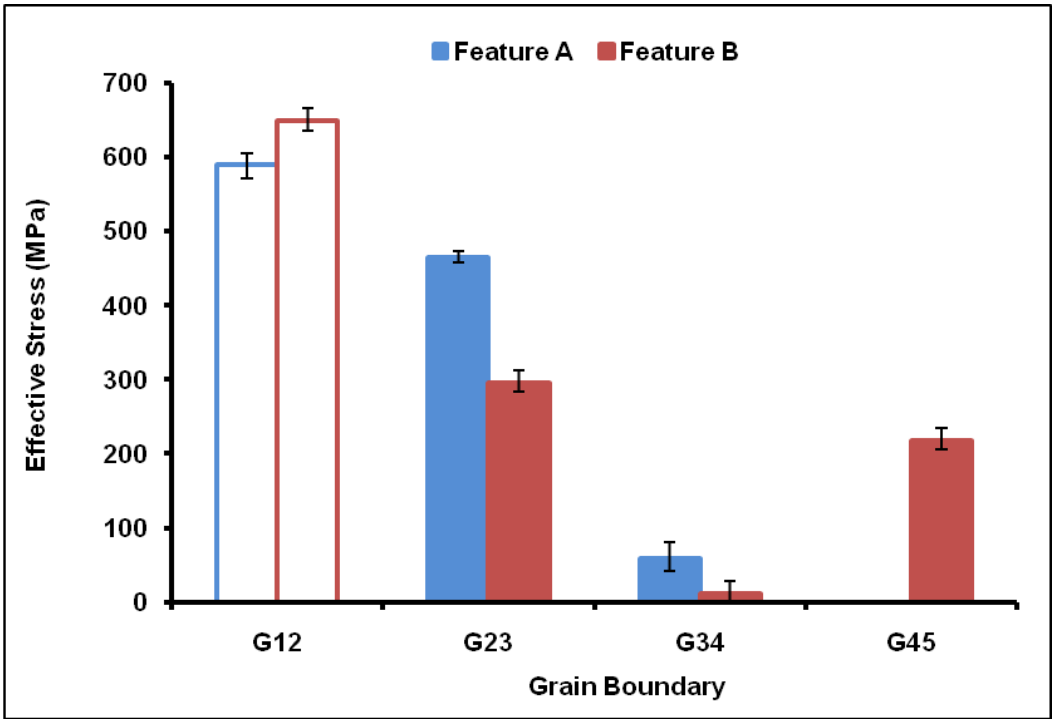

a)

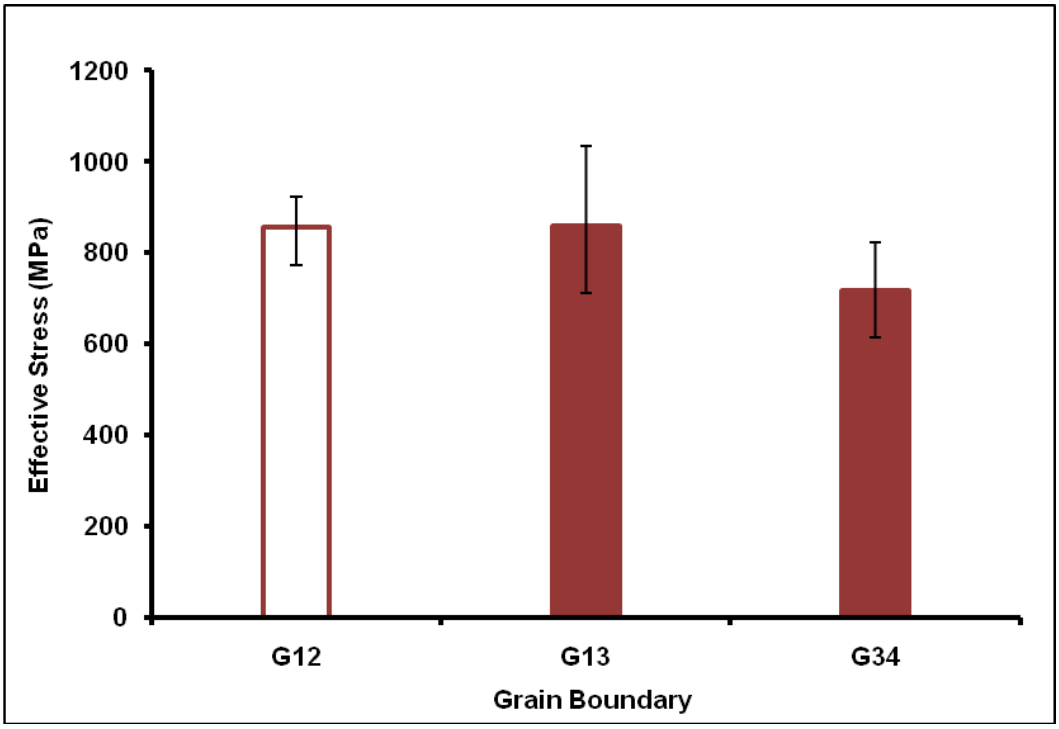

b)

Figure 7-9: Prediction of thermal stresses with uncertainties using a simple model, for the thermal stress at boundary (effective stress) versus the grain boundary for the a) P-II sample and b) Cr-II sample. (Hollow bars show the cracked boundaries).

Data for the angles between the grain boundary poles and the pole for the facet planes and the misorientation between the basal poles of adjacent grains are given. The results have been explained in Table 7-1 and Table 7-2 show the average angle between the grain boundary plane pole and the nearest crystallographic pole. There is no correlation with cracking and the relative crystal misorientation between the grains as shown in Appendix B. Appendix B shows the range for the angles between the grain boundary pole and the crystallographic pole (0001).

Table 7-1: Relationships between grain orientations and observations of cracking: Data for the angles between the grain boundary poles and the pole for the facet planes and the misorientation between the basal poles of adjacent grains are given for the P-II sample.

Location	Grain Boundary & Grains		Grain Size (μm)	Angle between (0001) poles	Angle between the grain boundary pole and the nearest crystallographic pole					Observation
					(0001)	$\{1\bar{1}23\}$	$\{01\bar{1}2\}$	$\{01\bar{1}1\}$	$\{01\bar{1}0\}$	
Feature A	G12	G1	2.34	137.5°	**4.0°**	40.0°	49.0°	62.5°	65.5°	**Cracked**
		G2	1.89		18.0°	25.5°	19.0°	33.5°	51.0°	
	G23	G2	1.89	28.0°	19.5°	25.5°	21.0°	36.5°	53.0°	Not cracked
		G3	1.95		8.0°	52.5°	51.5°	63.5°	80.5°	
	G34	G3	1.67	59.5°	12.0°	52.0°	47.0°	61.0°	79.0°	Not cracked
		G4	2.00		61.0°	22.0°	**3.5°**	8.0°	24.5°	
Feature B	G12	G1	3.25	116.0°	26.0°	18.0°	32.0°	41.0°	55.5°	**Cracked**
		G2	3.29		35.5°	31.0°	43.5°	55.0°	77.5°	
	G23	G2	2.98	117.0°	16.5°	34.0°	34.0°	47.0°	66.5°	Not cracked
		G3	0.69		51.5°	17.0°	39.5°	46.5°	55.0°	
	G34	G3	0.79	76.5°	52.0°	32.5°	40.5°	46.5°	37.0°	Not cracked
		G4	0.69		43.0°	18.0°	19.5°	33.5°	48.0°	
	G45	G4	0.96	99.0°	41.0°	15.0°	19.0°	34.0°	46.5°	Not cracked
		G5	2.18		77.0°	17.5°	29.0°	21.5°	19.0°	

Table 7-2: Relationships between grain orientations and observations of cracking: Data for the angles between the grain boundary poles and the pole for the facet planes and the misorientation between the basal poles of adjacent grains are given for the Cr-II sample.

Grain Boundary & Grains		Grain Size (μm)	Angle between (0001) poles	Angle between the grain boundary pole and the nearest crystallographic pole					Observation
				(0001)	$\{11\bar{2}3\}$	$\{01\bar{1}2\}$	$\{01\bar{1}1\}$	$\{01\bar{1}0\}$	
G12	G1	6.5	60°	64°	**6°**	31°	24°	31°	**Cracked**
	G2	1.2		**10°**	23.5°	61°	59.5°	43°	
G13	G1	6.5	24°	55°	26.5°	41°	32°	28°	Not cracked
	G3	2.1		46°	23°	**8°**	5.5°	22°	
G34	G3	2.1	66°	45°	**13°**	32.5°	36°	27°	Not cracked
	G4	4.5		63°	**8°**	18°	**2.5°**	15°	

7.3.2 Image-based Finite Element Modelling

A finite element model has been written by David Gonzales, to predict intergranular strains by image-based finite element modelling [55]. It is briefly summarized in the literature review chapter in section (2.2). The thermal stress along boundaries and within the grains shows there is a significant variation in the stress values (for example, the average thermal stress is about 300 MPa for pair of grains). The distribution was uniform for the misorientation between the neighbouring grains but the intergranular stress does not depend on the grain misorientation and the grain facet as shown in Figure 7-10 a, and b. The trend was clear to show the intergranular stress increase at the grain boundary when the one or more grains has facet close to facet basal plane (0001) pole are shown in Figure 7-10. This is consistent with the simple model developed in this thesis.

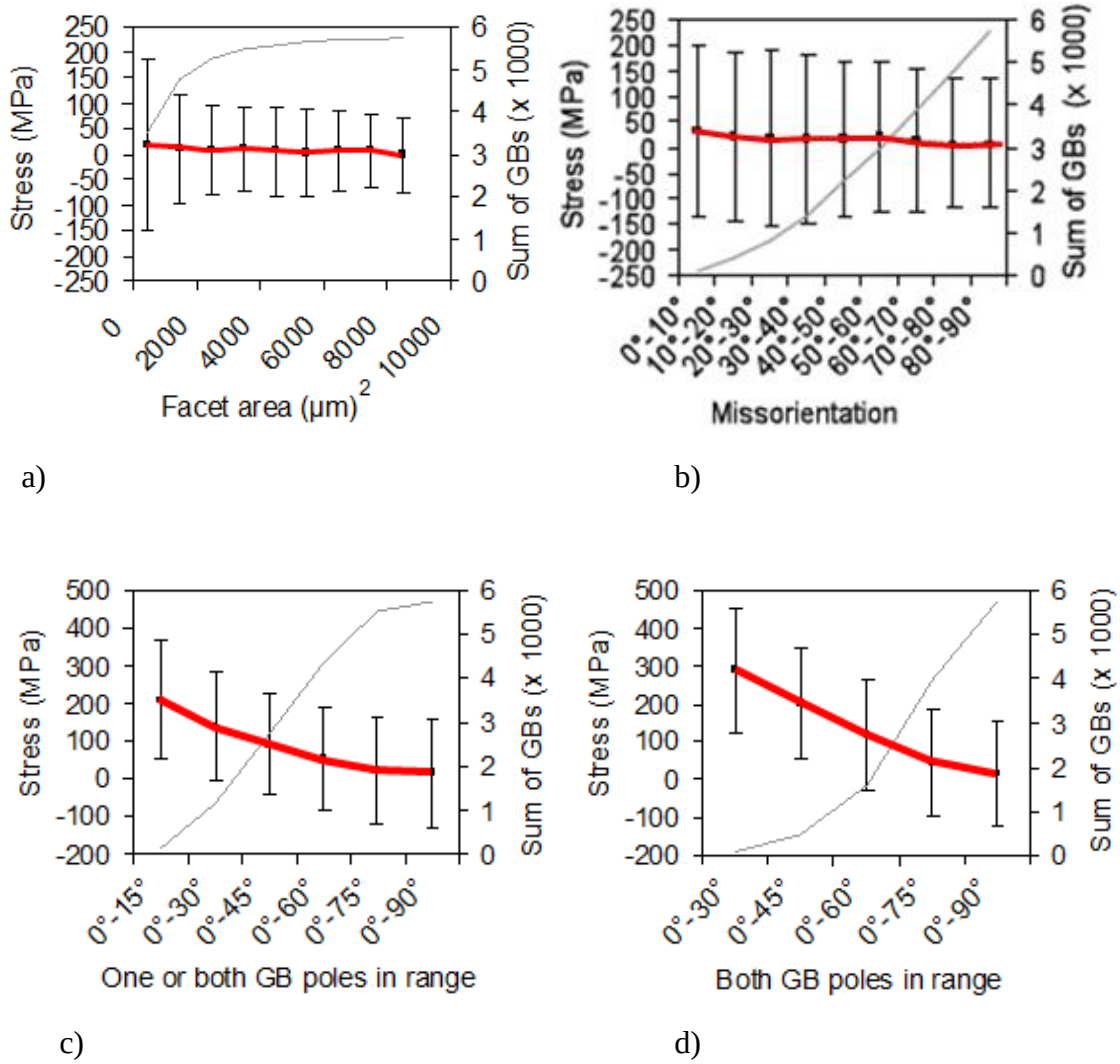

Figure 7-10: The finite element model to measure the stress across the boundaries a) The thermal stress versus the grain boundary plane area, b) The intergranular stress against the (0001) pole misorientation for the grains neighbouring, c) The stress as a function of the basal plane pole misorientation for one grain or both grain adjacent, and d) The stress against the (0001) pole misorientation and the boundary pole for the neighbouring grains. The thin grey line shows the cumulative number of the grain boundaries which was covered the large number of grain and the number of grain boundary more than (5000 boundaries) [55].

The simple model presented in section (7.3.1) predicts that a larger thermal expansion coefficient and grain dimension perpendicular to the grain boundary encourage high tensile stresses, i.e. larger grains with facets close to the basal plane. This appears to be generally supported by the observations of cracking detected by digital image correlation, but is clearly insufficient to explain the detected incidences of cracking. The intergranular stress

in 3D model depends on the facet plane pole misorientation for the grain boundaries in one grain or the both neighbouring grains [55]. This agrees with the simple model presented here. The same model did not show any sensitivity of the average grain boundary stress to the relative grain misorientations. The observations presented from simple model presented in section (7.3.1), and also the outputs of the 3D model, suggest that grain boundary facets close to the basal plane will encourage crack nucleation along the boundaries in polycrystalline alumina.

Summary

- DIC can be used to detect the intergranular cracks in a fine grain size alumina.
- Focused ion beam milling and electron backscatter diffraction (i.e. destructive analysis of grain boundary planes) can be used to study grain boundary planes and grain boundary orientation.
- High thermal stresses (to accommodate larger thermal displacements) are predicted for the cracked boundaries and highest tensile stresses when the basal plane (0001) is close to the grain boundary plane.
- Grain facets close to (0001) tend to develop high tensile residual stress and these boundaries can act as crack nuclei.

7.4 Indirect Observation of Defect Density and Size

Indirect observation of defect density and size were done using Hertzian indentation testing. The smooth and coarse surface in P-II and Cr-II samples were prepared using different methods as mentioned in the experimental chapter. The fracture toughness was measured for the coarse surface due to the probability to find the small defects sizes in this surface was higher than the smooth surface [117]. From Table 6-2 as mentioned in Section (6.3.3) the values obtained for fracture toughness by Hertzian indentation are different for each surface finish. The probability to detect the defects affected by the sample surface preparation and these defects caused the fracture at the minimum load but the fracture toughness did not affect by the surface finish. There are more flaws were observed on the coarse finished surface and there is one crack propagated to the ring crack radius [118]. The fracture toughness value was of P-II sample with grain size 1.5 μm was 3.52 $MPa.m^{1/2}$ for the coarse finished surface and this value was close to the fracture toughness 3.58 $MPa.m^{1/2}$ for an equivalent microstructure with grain size 1.2 μm in reference [101] for the alumina sample and also for the coarse finished surface.

The measured flaw density for the P-II sample obtained by Hertzian test is higher than flaw density for the Cr-II sample (see Figure 6-50 a). This may simply be due to the difference in grain size (i.e. the grain size for P-II sample, 1.5 μm is less than grain size for Cr-II sample, 3.6 μm), and hence the number of grains in the imaged area. The grain size affects the size and number of defects, but as discussed in section (7.3.1) it may also affect the intergranular stresses and hence may affect the likelihood of cracking. Figure 6-50 b shows that after normalising the flaw density (i.e. the flaw density normalised by the number of grains per unit area), the frequency is almost the same for both materials (P-II and Cr-II samples). This suggests that any effect of grain size on the tendency for crack nucleation is too small to measure, or non-existent.

The defect density was also calculated using Hertzian indentation. The smooth samples had the same surface finish as the DIC experiments, and it is of interest to compare the defect densities. The total area examined by digital image correlation experiments (see Figure 7-11 a) were smaller than the total stressed area in the Hertzian indentation testing (see Figure 7-11 b for one ring crack radius), the difference between the total areas

for DIC and Hertzian test of approximately (20.6). However, as each Hertzian experiment involved over 26 tests, the total inspected areas are 5.4×10^{-6} m^2 and 0.25×10^{-6} m^2 for Hertzian test and DIC experiment respectively. The each Hertzian test gave one ring crack radius, r at the crack size, c and fracture load P_F, in the viewed area. The crack densities were estimated from these data and it was as a function of the crack size. The same crack size does not find for each test because the Hertzian indentation has a stress intensity factor value is larger than the fracture toughness for any crack of this size and also due to the test location was not close to the other sizes [7].

The digital image correlation analysis detects a part of the population (see Figure 7-12) at low threshold of about (0.002) (see Figure 6-1a). For example, in the strain map a high threshold of about (0.01) has been applied to eliminate background noise (see Figure 6-1b). The magnitude of the crack opening displacement is predicted to decrease with defect size, so there will be other shallower features below the noise threshold (0.002) that are not counted in the defect density.

Figure 7-13 a shows the flaw density calculated using the digital image correlation data (i.e. crack length was measured using Matlab routine as mention in section (6.1.6)), the summed defect density observed by Hertzian indentation (flaw density determined from the searched area) and also by integration of the log-normal fit to the Hertzian indentation data (between limits of 18 μm and 1 μm). Figure 7-13 b shows the same data, normalised by the grain size (i.e. normalised distribution, flaw size normalised by the grain size and flaw density normalised by the number of grain per unit area for DIC experiment, Hertzian test, and also, for the integration of the log-normal fit to the Hertzian data). The normalised distribution has been done to observe the effect of the grain size on the flaw size and density, and hence the number of grains in viewed area. The uncertainty was measured from effect of one more or one fewer cracks observed in the digital image correlation experiment and Hertzian test. The maximum uncertainty was measured from subtract the maximum flaw density from the total flaw density and the total flaw density subtracted from the minimum flaw density for calculating the minimum uncertainty in flaw density for the Hertzian test and DIC experiment.

The DIC experiments only use a stress in one direction as mention in (results chapter I) in section (4.2.5).The small defects are propagated to the ring crack due to the stress around

the contact area is the radial stress. In both tests (digital image correlation and Hertzian) only use the stress in one direction (tensile stress). The small crack size was used to determine the flaw density in Hertzian indentation test when the stress intensity factor is equal to the fracture toughness. The acoustic emission was used to detect all the cracks which were propagated into the ring crack radius [79].

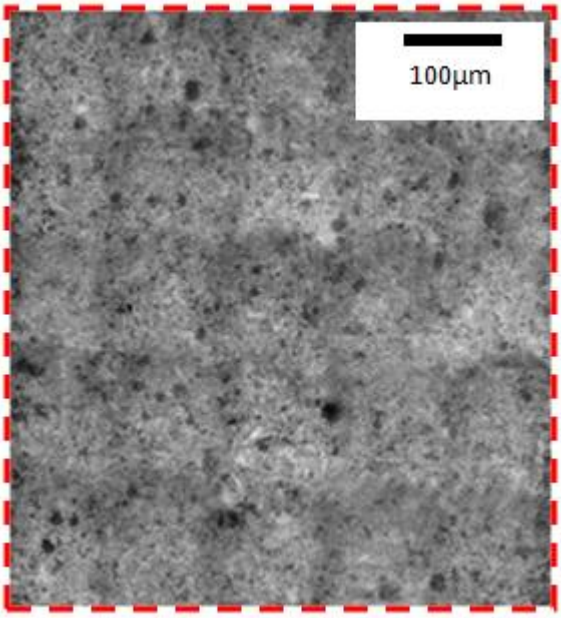

a) Total stressed area in digital image correlation experiment.

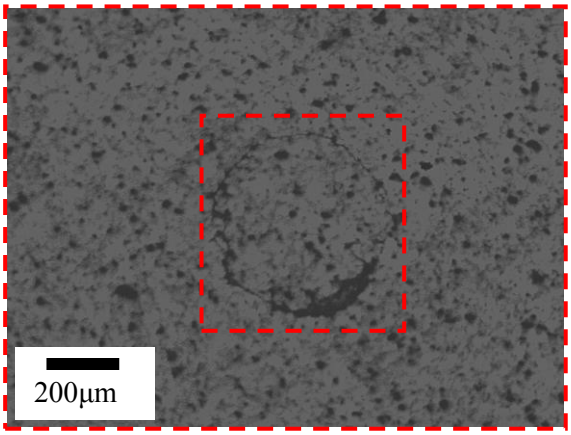

b) Stressed area for an individual ring crack radius in Hertzian test.

Figure 7-11: Shows the stressed area in a) Digital image correlation experiments and b) Hertzian test for an individual ring crack radius.

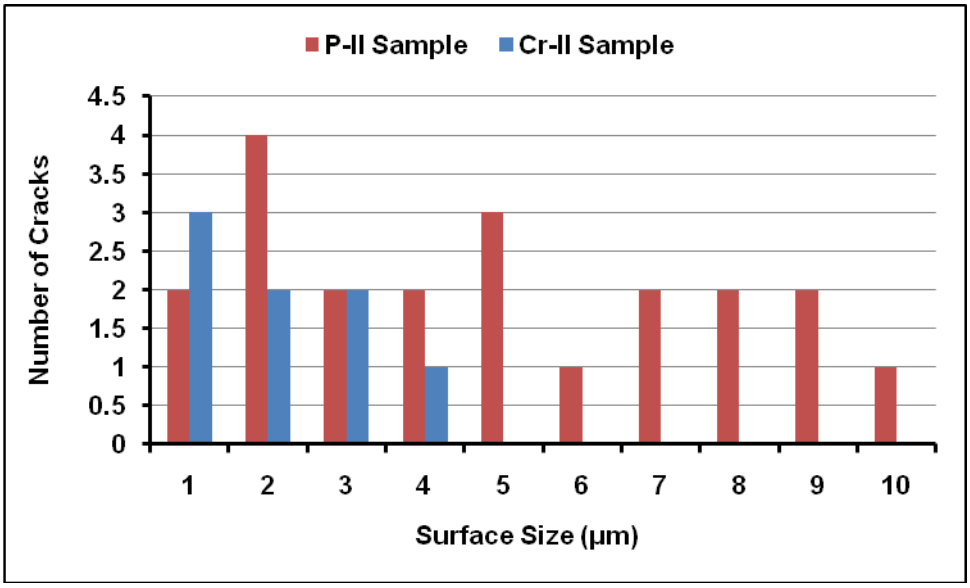

Figure 7-12: Shows the flaws population for the P-II and Cr-II samples using DIC experiments.

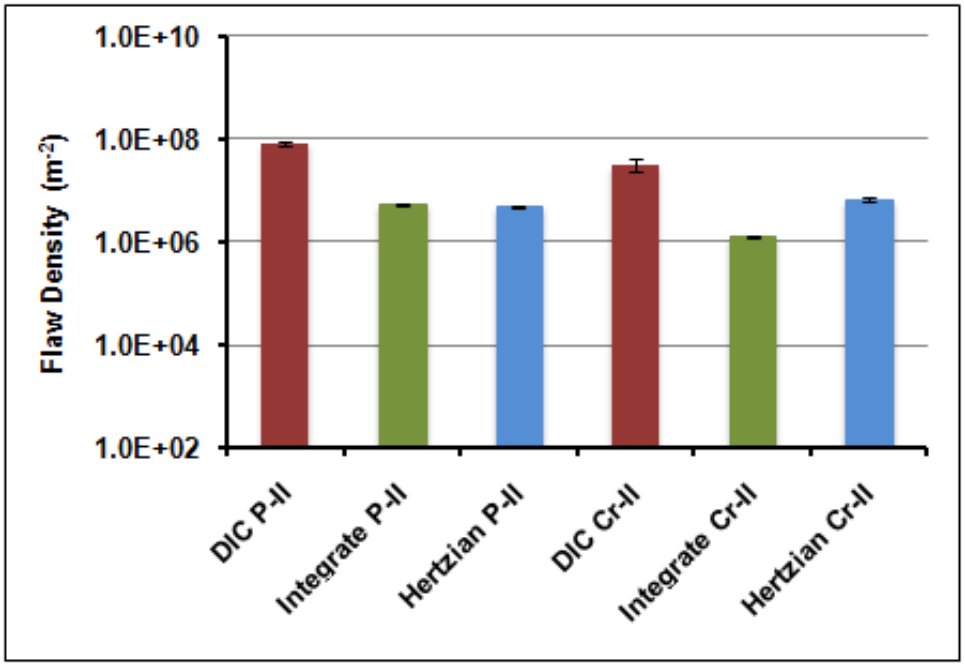

a)

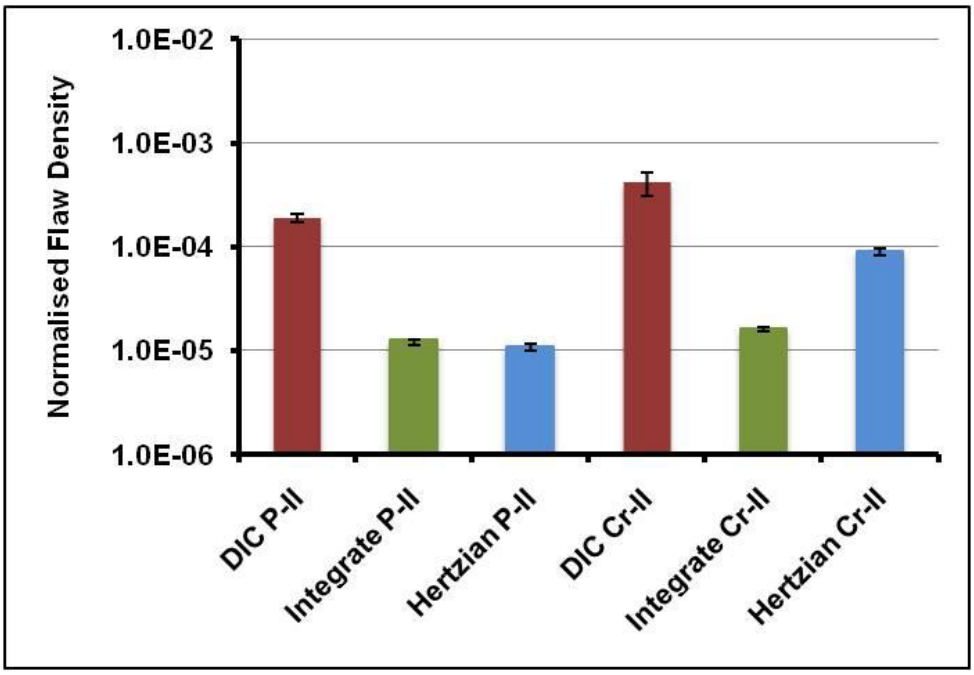

b)

Figure 7-13: a) Shows the flaw density distribution and b) Shows normalised flaw density distribution for the Hertzian indentation and digital image correlation in the P-II and Cr-II samples.

Summary

Indirect observation of defect density and size was done using Hertzian testing. The fracture toughness values were measured at minimum fracture load by Hertzian indentation which it is different for each surface finish. The probability to identify the cracks affected by the sample surface preparation and these cracks caused the fracture at the minimum load but the fracture toughness did not affect by the surface finish. The measured flaw density for the P-II sample obtained by Hertzian test and digital image correlation is higher than flaw density for the Cr-II sample; this may simply be due to the difference in grain size. The total area examined by digital image correlation experiments was smaller than the total stressed area in the Hertzian indentation testing. The defect density for the Hertzian testing was calculated from the small flaw size at fracture toughness is equal to the stress intensity factor. The acoustic emission was used to detect the small flaw sizes which were propagated into a ring crack system.

Chapter 8

8 Conclusions and Future Work

8.1 Conclusions

A summary of the main findings from this work follows:

8.1.1 Microstructure

The microstructures of the studied polycrystalline aluminas were untextured with non-equiaxed grains and pores. The average grain size of the pure alumina (P-II) was 1.5 μm and that of the Cr-doped alumina (Cr-II) was 3.6 μm.

8.1.2 Digital Image Correlation

I. The cracks nucleated (i.e. strain feature A and strain feature B in P-II sample and the strain feature in Cr-II sample) are always normal to the applied stress.

II. The average surface strains measured by DIC are less than those predicted. The data from DIC test is similar to the expectation data, but the magnitudes are approximately 50% of these expected. This suggests that under the conditions of these experiments, DIC significantly under measures the small displacements, and may not be relied on to accurately measure relative displacements of features.

III. The displacement and displacement difference across slots was compared between the finite element model, FEM data and experimental data (i.e. DIC data) at different applied strain and was represented as an apparent strain arising from the displacement gradient. Both finite element model data and experimental data show an increase the local strains with applied strain, but the effect is smaller than in the experimental data. This suggests that DIC is used to observe the slots/cracks, but not to measure their compliance, from which depth might have been inferred.

IV. Digital image correlation was sufficiently sensitive to observe the crack nuclei and development of cracks in fine polycrystalline alumina specimen, which would otherwise be invisible. The cracks are observed by their opening strain from the strain map which can be used to measure the strain feature surface length. The strain

feature depth may not be estimated, however, due to the unreliability of their compliance measurements.

8.1.3 Grain Boundary Plane

I. Grain boundary plane measurements have been done using focused ion beam, FIB milling and electron backscatter diffraction, EBSD (destructive analysis).

II. The locations of the crack nuclei are consistent with grain boundaries at which high tensile stresses are predicted using a simple model for intergranular thermal strains. The highest tensile stresses are predicted at the boundaries of larger grains with close to the basal plane facets (0001).

III. Comparison of the ranking of predicted stresses at boundaries that were observed to crack, or did not crack, is broadly consistent with model predictions.

8.1.4 Hertzian Indentation

I. The fracture toughness K_{IC} value was of the finer grain size pure alumina (P-II sample) with grain size 1.5 μm was 3.52 MPa.m$^{1/2}$. The fracture toughness of the coarser grain size Cr-doped alumina (Cr-II sample) with grain size 3.6 μm was 2.91 MPa.m$^{1/2}$.

II. The flaw density for the pure alumina (P-II sample) is higher than flaw density for the Cr-doped alumina (Cr-II sample). This may be due to the difference in grain size, which it is affected by role of grain size on stress at grain boundaries. The normalising of the flaw density (i.e. the flaw density normalised by the number of grains per unit area), the frequency is almost the same for both materials (P-II and Cr-II samples). This suggests that any effect of grain size on the tendency for crack nucleation is too small to measure.

III. A comparison was made between the populations obtained by digital image correlation data, the summed defect density observed by Hertzian indentation and also by integration of the log-normal fit to the Hertzian indentation data. Different results were obtained when comparing the population of different materials using the same method for P-II and Cr-II samples. The same data was got when normalised the flaw density by the number of the grain size for the different

materials using the same method for P-II and Cr-II samples. The defect density for the P-II sample obtained by DIC and Hertzian test is higher than the defect density for the Cr-II sample.

8.2 Future Work

A number of suggested areas for further examination are detailed below:

8.2.1 Modification to Microstructure

The aim of this further work is to determine whether modification to microstructure may influence defect density and strength. During the processing, the silica is added to the alumina and then firing the alumina at temperature 1400 °C and this technique will produce the facet planes [119]. There are some materials that are added to the alumina during the sintering to obtain good mechanical properties and the population of the facet grain boundary is controlled during the firing [120]. The failure stress is increased with the small grain size due to the materials with small grain size having many defects and the failure will occur from these defects [47].

The flaw densities in the fine grained alumina were measured by DIC experiment and Hertzian test. The microstructure is modified by etching conditions to get the microstructure with coarse grained materials and then DIC experiments and Hertzian tests are used to calculate the defects population.

8.2.2 Surface Preparation and Measuring the Residual Stress Using FIB and DIC

The purpose of this experiment is to monitor the distribution of residual stress across the grain boundary for polycrystalline alumina. The focused ion beam (FIB) instruments and DIC techniques are applied in the last decade because the technological advances. In this experiment the slot is achieved across the grain boundary and it is milled in the alumina samples using a high beam current using FIB. The digital image correlation is used to measure the displacement across the slot and there is relationship between the surface crack opening displacement and the residual stress.

The focused ion beam [121] is used to prepare the alumina surface for digital image correlation and the purpose from that to improve the vector displacement accuracy. The metallic features are deposited on the sample surface using focused electron beam [122].

There are many techniques are used to deposit nano-features on the sample surface for DIC [123]. These small features and the optical non-contact method [124, 125] are good to provide higher vector displacement accuracy using digital image correlation. Many applications needs a high magnification using scanning electron microscope and digital image correlation is used to measure the vector the displacement at this magnification [126, 127]. The purpose from this experiment is to apply SEM to improve the magnification and image quality for the P-II and Cr-II sample in the DIC test.

8.2.3 DIC to Study the Crack Nuclei at the Edge in Finer Grained Alumina

The objective for this experiment is to observe crack nuclei in polycrystalline alumina microstructures in the region close to the edge of the sample as shown in Figure 8-1. Four point bend fracture tests are conducted under displacement control; with samples of nominal dimensions of 48×10.6×2.05 mm as shown in Figure 8-1. The edges of the samples are polished to remove cutting damage, which would reduce sample strength. The outer and inner spans are 48.0 mm and 5.0 mm respectively. Steel rolling pins are used to minimize contact friction, and self-aligned to the sample using a ball bearing.

The upper surface of the sample has a strain gauge adjacent to the viewed region to measure the applied strain as shown in Figure 8-1. The displacement is incremented by intervals of 0.02 mm (equal to a strain increment of approximately 0.1 milli-strains) at 60 minute intervals. A 12-bit Image Pro X CCD digital camera (2048×2048 pixels) is used to record 20 images at each of 25 locations at each increment, covering a total area of approximately (500×500 μm). A lens with X100 magnification is used, with a working distance of 0.25 mm. The analysed field of view of each image is 100×100 μm. Improvements in the optical path during the project gave resolutions 0.046 μm/pixel for polycrystalline alumina sample.

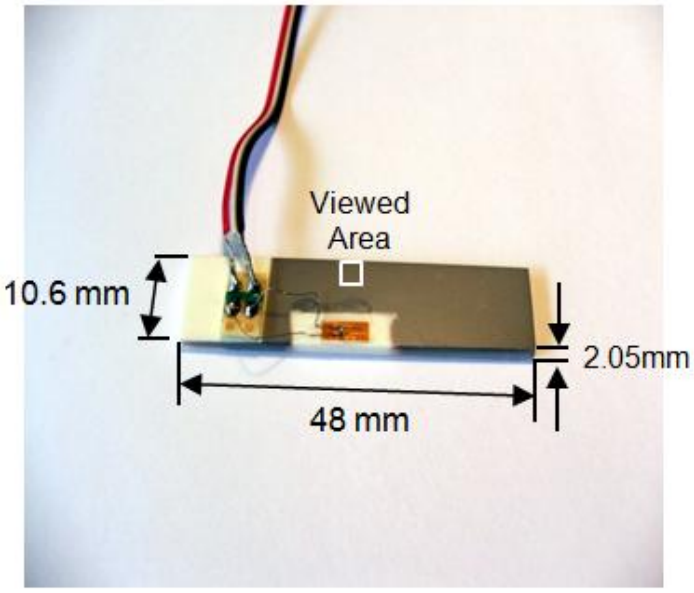

Figure 8-1: Shows the viewed area location on the polycrystalline alumina sample surface near to the edge of the sample.

8.2.4 DIC to Study of the Crack Nuclei in Coarser Grained Alumina

Using digital image correlation to observe the crack nucleation in the coarse polycrystalline alumina where average grain size is 99 μm as shown in Figure 8-2.

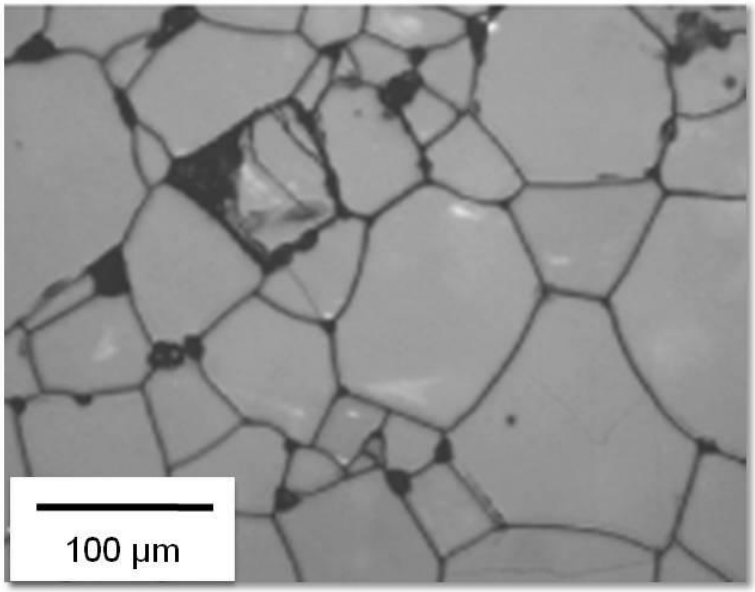

Figure 8-2: Shows the coarse alumina with equiaxed grain and average grain size is about 99 μm [33].

The details for this experiment are shown below:

1) The polycrystalline alumina is etched at the low temperature when the compound $CuO - TiO_2 - Nb_2O_5$ is added to sintering alumina at firing temperature 1000 °C or lower [128]. The purpose of this experiment is surface preparation for the digital image correlation of the coarse polycrystalline alumina sample using thermal etching at lower temperature approximately (150-200 °C) below the sintering or firing temperature.
2) Using four point bend test to apply load using a micrometer to supply small displacements and it is incremented in intervals of 0.02 mm.
3) A 12-bit Image Pro X CCD digital camera (2048×2048 pixels) is used to record 20 images at each of 25 locations at each increment, covering a total area of approximately (500×500 μm).
4) A lens with X100 magnification is used, with a working distance of 0.25 mm and the analysed field of view of each image is 100×100 μm.
5) Digital Image Correlation is then carried out on a networked Dual Processor PC (2×2.8 GHz Processor, 2 GB RAM) with Davis Strain Master 2D software for acquisition visualisation (LA Vision, Germany). The interrogation window size is used 128×128 pixels and overlap 50%.
6) Destructive analysis was performed using electron backscatter diffraction, EBSD to observe the grains orientation and focused ion beam, FIB to provide the trench across the area of interest. The purpose of the destructive analysis is to obtain the crystal orientation for the grains and grain boundaries of interest and also measure the thermal displacement and effective stress across the boundary of interest (cracked boundaries).

References

1. R. G. Munro, Evaluated material properties for a sintered alpha-alumina. Journal of The American Ceramic Society, 1997. Vol 80 (8), p. 1919-1928.
2. J. Seidel, N. Claussen, J. Rodel, Reliability of Alumina Ceramics - Effect of Grain-Size. Journal of The European Ceramic Society, 1995. Vol 15(5), p. 395-404.
3. A. G. Evans, Dimensional Analysis of The Grain-Size Dependence of Strength. Journal of The American Ceramic Society, 1980. Vol 63, p. 115-116.
4. R. W. Rice, R. C. Pohanka, Grain-Size Dependence of Spontaneous Cracking in Ceramics. Journal of The American Ceramic Society, 1979. Vol 62, p. 559-563.
5. J. R. Matthews, F. A. McClintock, and W. J. Shack, Statistical Determination of Surface Flaw Density In Brittle Materials. Journal of The American Ceramic Society, 1976. Vol 59: p. 304-308.
6. J. D. Poloniec and T. R. Wilshaw, Determination of Surface Crack Size Densities in Glass. Nature-Physical Science, 1971. Vol 229 (8), p. 226-227.
7. T. R. Wilshaw, Hertzian Fracture Test. Journal of Physics D-Applied Physics, 1971. Vol 4(10), p. 1567-1581
8. A. S. Argon, Distribution of Cracks on Glass Surfaces. Proc. R. Soc. Lond. A 1959. Vol 250, p. 482-492.
9. I. Levin, D. Brandon, Metastable Alumina Polymorphs: Crystal Structures and Transition Sequences. J. Am. Ceram. Soc., 1998. Vol 81 (8), p. 1995–2012.
10. E. Dorre, H. Hubner,, Alumina-Processing Properties and Applications. Berlin: Springer-Verlag. 1984, p. 1-267.
11. Z. R. Ismagilov, R. A. Shkraabina, N. A. Koryabkina, New technology for production of spherical alumina supports for fluidized bed combustion. Catalysis Today, 1999. Vol 47, p. 51-71.
12. W. H. Gitzen, Alumina as a ceramic material, Columbus: The American Ceramic Society. 1970.
13. R. S. Zhou, R. L. Snyder, Structures and Transformation Mechanisms of the yitta gamma and theta Transition Aluminas. Acta Cryst. 1991. Vol 47, p. 617-630.

14. R. Franchy, G. Schmitz, P. Gassmann, and F. Bartolucci, Growth of thin, crystalline oxide, nitride, and oxynitride films on NiAl and CoGa surfaces. Appl. Phys., 1997. Vol 65, p. 551–566.
15. S. Vasefi, M. Parvari, Alkaline earth metal oxides on γ-Al2O3 supported Co catalyst and their application to mercaptan oxidation. Korean Journal of Chemical Engineering, 2010, Vol. 27 (2), p. 422-430.
16. J. M. McHale, A. Auronx, A. J. Perrotta, A. Navrotsky, Surface Energies and Thermodynamic Phase Stability in Nanocrystalline Aluminas. Science, 1997. Vol. 277 (8), p. 277-788.
17. K. Jiang, D. Music, K. Sarakinos, J. Schneider, Ab initio study of effects of substitutional additives on the phase stability of γ -alumina. Journal of Physics: Condensed Matter, 2010. Vol 22, 505502 (8pp).
18. W. E. Lee, P. D. Lagerlof, Structural and Electron Diffraction Data for Sapphire (α-Al_2O_3), Journal of Electron Microscopy Technique, 1985, Volume 2 (3), P.247-258.
19. A. Zimmermann, W. C. Carter, E. R. Fuller, Damage evolution during microcracking of brittle solids. January of Acta Materialia, 2001, Vol 49 (1): p 127-137.
20. R. L. Coble, Transparent Alumina and Method of Preparation, 1962, Vol (20).
21. R. Morrell, Handbook of Properties of Technical & Engineering Ceramics. Part 2. Data Reviews, Section I. High-alumina ceramic. 1987:p 255.
22. http://www.almath.co.uk/, Almath Crucibles ltd.
23. http://www.matweb.com/search/PropertySearch.aspx, Material Property Data.
24. Handbook of Industrial Material. Vol. 803 p. 1992. Oxford: Elsevier Advanced Technology.
25. W. D. Kingery, Introduction to Ceramics. 1960: John Wily & Sons, Inc., New York. London.
26. D. J. Green, An introduction to the mechanical properties of ceramics,. 1998, United Kingdom.

27. W. D. Kingery, M. Berg, Study Of The Initial Stages of Sintering Solids by Viscous Flow, Evaporation-Condensation, And Self-Diffusion. Journal of Applied Physics, 1955. Vol 26 (10), p. 1205-1212.
28. S. I. Bae, S. G. Baik, Sintering And Grain-Growth Of Ultrapure Alumina. Journal of Materials Science, 1993. Vol 28 (15), p. 4197-4204.
29. X. L. Tian, A. B. Yu, Change of residual stress after grinding Al_2O_3 ceramics, in Advances in Grinding and Abrasive Processes. 2004, Trans Tech Publications Ltd: Zurich-Uetikon. p. 481-484.
30. Z. Z. Jinchuan, Advanced Cutting and Grinding Technologies of Brittle Materials. 1996, U.S. Oxford Science Press.
31. Y. Fang, T. Fossier, K. W. White, Crack path simulation and identification in polycrystalline alumina. Scripta Materialia, 2004. Vol 50 (1), p. 127-130.
32. Y. Fang, K. Ravi-Chandar, K. W. White, Influence of surface residual stress state on crack path evolution in polycrystalline alumina. Journal of The American Ceramic Society, 2002. Vol 85 (7), p. 1783-1787.
33. S. G. Yousef, J. Rodel, E. R. Fuller, A. Zimmermann, B. S. El-Dasher, Microcrack evolution in alumina ceramics: Experiment and simulation. Journal of The American Ceramic Society, 2005. Vol 88 (10), p. 2809-2816.
34. R. I. Todd, B. Derby, Thermal stress induced microcracking in alumina–20% SiC_p composites. Acta Materialia, 2004. Vol 52 (6): p. 1621-1629.
35. R.I. Todd, M. A. M. Bourke, C. E. Borsa, R. J. Brook., Neutron diffraction measurements of residual stresses in alumina/SiC nanocomposites. Acta Materialia, 1997. Vol 45(4): p. 1791-1800.
36. T. Mura, Micromechanics of defects in solids. Vol. 2^{nd} Edition, Martinus Nijhoff 1987: Publishers, Dordrecht, The Netherlands.
37. P. J. Withers, H . K. D. H. Bhadeshia, Residual stress part 1 - Measurement techniques. Materials Science and Technology, 2001. Vol 17 (4), p. 355-365.
38. V. Hauk, Structural and residual stress analysis by non-destructive methods,. Elsevier, Amsterdam 1997.
39. P. J. Withers, H. K. D. H. Bhadeshia, Residual stress part 2 - Nature and origins. Materials Science and Technology, 2001. Vol 17 (4), p. 366-375.

40. M. T. Hutchings, P.J. Withers, T.M. Holden, T. Lorentzen, Introduction to the characterisation of residual stress by neutron diffraction. 2005: Boca Raton, Taylor & Francis Group, London, UK.
41. V. R. Vedula, S. J. Glass, D. M. Saylor, G. S. Rohrer, W. C. Carter, S. A. Langer, E. R. Fuller, Residual-stress predictions in polycrystalline alumina. Journal of The American Ceramic Society, 2001. Vol 84 (12), p. 2947-2954.
42. Q. Ma, D. R. Clarke, Piezospectroscopic Determination of Residual-Stresses in Polycrystalline Alumina. Journal of The American Ceramic Society, 1994. Vol 77 (2), p. 298-302.
43. A. Zimmermann, E. R. Fuller, J. Rodel, Residual stress distributions in ceramics. Journal of The American Ceramic Society, 1999. Vol 82 (11), p. 3155-3160.
44. R. W. Davidge, T. J. Green, The Strength of Two-Phase Ceramic/Glass Materials. Journal of Materials Science 1968. Vol 3, p. 629-634.
45. R. W. Davidge, Cracking at grain boundaries in polycrystalline brittle materials Acta Metallurgica, 1981. Vol 29 (10), p. 1695 10 1702.
46. A. G. Evans, Microfracture From Thermal Expansion Anisotropy -I. Single Phase Systems. Acta Metallurgia, 1978. Vol 26, p. 1845-1853.
47. Y. FU, A. G. Evans, Some Effects of Microcracks on the Mechanical Properties of Brittle Solids-I. Stress, Strain Relations. Acta metall, 1985. Vol. 33(8.): p. 1515-1523.
48. R. W. Davidge, Cracking at grain boundaries in polycrystalline brittle materials Acta Metallurgica, 1981. Vol. 29, p. 1695 - 1702.
49. A.G. Evans and Y. Fu, The mechanical behaviour of alumina: a model anisotropic brittle solid,. In: A.G. Evans, Editor, Fracture in Ceramic Materials, Noyes Publications, NJ, 1984. 10: p. pp. 56–88.
50. D. W. Susnitzky, C. B. Carter, Structure of Alumina Grain Boundaries Prepared with and without a Thin Amorphous Intergranular Film. J. Am. Ceram. Soc. 1990. 73, (8), p. 2485-2493.
51. T. J. Marrow, A. King, P. Reisching, S. Rolland du Roscoat, and W. Ludwig, Diffraction Contrast Tomography of Polycrystalline Alumina, In Acers Sosman Award Symposium: Three - Dimensional structural of Interfacial Network, 2009.

52. M. L. Kronberg, Plastic deformation of single crystals of sapphire: Basal slip and twinning Acta Metallurgica, September 1957. Vol 5 (9),: p. 507-524.

53. V. Randle, G. Owen, Mechanisms of grain boundary engineering. Journal of Acta Materialia, 2006. Vol 54, p. 1777–1783.

54. T. J. Marrow, A. King, P. Reischig, S. Rolland du Roscoat, W Ludwig, Three-dimensional Tomography of Alumina. Sosman Memorial Award symposium, MS&T 2009, Pittsburgh, PA.

55. T. J. Marrow, M. A. Aswad, J. Q. Fonseca, and P. J. Withers, In-situ observation and modelling of intergranular cracking in polycrystalline alumina. Journal of Key Engineering Materials, 2011, Vol (465), P. 560-563.

56. C. J. Tay, C. Quan, Y. H. Huang, Y. Fu, Digital image correlation for whole field out-of-plane displacement measurement using a single camera. Optics Communications, 2005. Vol 251, p. 23–36.

57. H. A. Bruck, S. R. McNeill, M. A. Sutton and W. H. Peters,, Digital image correlation using Newton–Raphson method of partial differential correction. Experimental Mechanics 1989. Vol 29,(3): p. 261–267.

58. G. Vendroux, W. G. Knauss, Submicron deformation field measurements, part II, improved digital image correlation, Exp. Mech., 1998. Vol 38(2), p. 86-92.

59. J. Q. Da Fonseca, P. M. Mummery, P. J. Withers, Full-field strain mapping by optical correlation of micrographs acquired during deformation. Journal of Microscopy-Oxford, 2005. Vol 218, p. 9-21.

60. B. K. Bay, T. S. Smith, D. P. Fyhrie, M. Saad, Digital Volume Correlation: Three-Dimensional Strain Mapping Using X-Ray Tomography. Experimental Mechanics, , 1999. Vol. 39 (3), p.217-226.

61. A. M. Fincham, G. R. Spedding, Low cost, high resolution dpiv for measurements of turbulent fluid flow. Experiments in Fluids, 1997. Vol. 23, p.449-462.

62. W. F. Clocksin, K. F. Chives, P. H. S. Torr, J. Q. Da Fonseca, P. J. Withers, Inspection of surface strain in materials using dense displacement fields. In: R. Pyez, *et al*. (Eds.).Proceedings of the 4th International Conference on New Challenges in Mesomechanics. Aalborg University, 2002. Vol.2, p.467-474.

63. W. F. Clocksin, J. Q. Da Fonseca, P. J. Withers, P. H. S. Torr, Image processing issues in digital strain mapping. Proceedings of the SPIE, 2002, Vol (4790), p.384-395.

64. M. R. Joyce, T. J. Marrow, P. Mummery, B. J. Marsden, Observation of microstructure deformation and damage in nuclear graphite. Engineering Fracture Mechanics, 2008. Vol 75, p. 3633–3645.

65. Michael A. Sutton, J.-J.O.H.W.Schreier, Image Correlation for Shape, Motion and Deformation Measurements. Springer Science Business Media, LLC 2009.

66. P. Zhou, K. E. Goodson, Subpixel displacement and deformation gradient measurement using digital image/speckle correlation (DISC). Optical Engineering, 2001. Vol 40 (8), p. 1613-1620.

67. LaVision, DaVis Strain MasterMaster Softerware Manual 7.1. 2006, LaVision GmbH, Gottingen.

68. L. Haiyan, J. A. Duff, T. J. Marrow, In-Situ Observation of Crack Nucleation in Nuclear Graphite by Digital Image Correlation. 008 ASME Pressure Vessels and Piping Division Conference, Chicago, Illinois, USA, July 27-31, 2008.

69. M. Mostafavi, J. A. Duff, T. J. Marrow, In-Situ Observation of Damage Nucleation in Graphite Under Biaxial Flexural Loading. 18th European Conference on Fracture, ECF 18, in Dresden, Germany, August 30- September 03, 2010.

70. J. A. Duff, T. J. Marrow, In-Situ Observations of Intergranular Stress Corrosion Cracking. Proceedings of the 2008 ASME Pressure Vessels and Piping Conference PVP, 2008.

71. S. Rahimi, D. L. Engelberg, J. A. Duff, T. J. Marrow, In situ observation of intergranular crack nucleation in a grain boundary controlled austenitic stainless steel. Journal ofMicroscopy, 2009. Vol. 233 (3): p. 423–431.

72. A. A. Khan, T. J. Marrow, In-situ Observation of Damage Mechanisms by Digital Image Correlation during Tension and Low Cycle Fatigue of Magnesium alloys. 12th International Conference on Fracture in Canada, ICF 2009.

73. V. Srinivasan, S. Radhakrishnan, X. Zhang, G. Subbarayan, T. Baughn, and L. Nguyen, High Resolution Characterization of Materials Used in Packages Through Digital Image Correlation. Proceedings of IPACK ASME InterPACK 5, 2005.

74. S. Roux, F. Hild, Stress intensity factor measurements from digital image correlation: post-processing and integrated approaches. International Journal of Fracture 2006. Vol 140(4), p. 140–157.

75. B. R. Lawn, Fracture of Brittle Solids -Second Edition. Cambridge University Press, 1993. Cambridge, UK.

76. B. R. Lawn, R. Wilshaw, Review Indentation fracture: principles and applications. Journal of Materials Science 1975. 10 (6): p. 1049-1081.

77. A. S. Argon, Surface Cracks on Glass. Proceedings of The Royal Society of London Series A-Mathematical And Physical Sciences, 1959. Vol 250 (1263): p. 472-481.

78. A. S. Argon, Distribution of Cracks on Glass Surfaces. Proceedings of The Royal Society of London Series A-Mathematical And Physical Sciences, 1959. Vol 250 (1263): p. 482-492.

79. P. D. Warren, D. A. Hills, S. G. Roberts, Influence of Surface Cracks on Hertzian Fracture. J. Hard Mater. 1994. Vol 5, p. 213-227.

80. P. D. Warren, D.A. Hills, S.G. Roberts, Surface Flaw Distributions in Brittle Materials and Hertzian Fracture. Journal of Materials Research, 1994. Vol 9(12): p. 3194-3202.

81. P. D. Warren, Determining The Fracture-Toughness of Brittle Materials By Hertzian Indentation. Journal Of The European Ceramic Society, 1995. Vol 15, p. 201-207.

82. P. Ostojic, R. McPherson, A review of indentation fracture theory: its development, principles and limitations. April 1987, Vol 33,(4,), p. 297-312.

83. F. C. Frank, B. R. Lawn, On the Theory of Hertzian Fracture. Proc. R. Soc. Lond. A 1967, Vol. 299, p. 291-306.

84. M. T. Laugier, Toughness determination of some ceramic tool materials using the method of Hertzian indentation fracture. Journal of Mater. Sci., 1985. Vol. 4(12), p. 1542-1544.

85. S. G. Roberts, Hertzian testing of ceramics. British Ceramic Transactions, 2000. Vol. 99(1), p. 31-38.

86. A. Franco Jr., S. G. Roberts, Surface mechanical analyses by Hertzian indentation. Cerâmica, 2004, Vol. 50, p. 94-108.

87. R. Warren, Measurement of The Fracture Properties of Brittle Solids By Hertzian Indentation. Journal of Acta metall, 1978. Vol 26,p. 1759-1769.

88. R. Mouginot, D. Maugis, Fracture indentation beneath flat and spherical punches journal of Mater. Sci., 1985. Vol. 20,(12), p. 4354-4376.

89. Pace Technologies Educational, http://www.metallographic.com/Basics.htm.

90. P. J. Goodhew, F. J. Humphreys, R. Beanland, Electron Microscopy and Analysis. 2000, 3rd Edition, London: Taylor Francis.

91. F. J. Humphreys, Review - Grain and subgrain characterisation by electron backscatter diffraction. Journal of Materials Science 2001. Vol 36, p. 3833 – 3854.

92. ASTEM. Standard Test Methods for Determining Average Grain Size. Designation: E112-96.

93. J. C. Wurst, J. A. Nelson, Lineal Intercept Technique for Measuring Grain Size in Two-Phase Polycrystalline Ceramics,. Journal of the American Ceramic Society, 1972.

94. T. C. Chu, W. F. Ranson, M. A. Sutton, W. H. Peters, Applications Of Digital-Image-Correlation Techniques To Experimental Mechanics. Experimental Mechanics, 1985. Vol 25(3), p. 232-244.

95. H. A. Bruck, S. R. McNeill, M. A. Sutton, W. H. Peters, Digital Image Correlation Using Newton-Raphson Method of Partial-Differential Correction. Experimental Mechanics, 1989. Vol 29(3), p. 261-267.

96. P. P. Benham, R. J. Crawfod, C. G. Armstrong, Mechanics of Engineering Materials,. 1997, UK, Longman, 2nd edition.

97. C. A. Volker, A. M. Minor, G. Editor., Focused Ion Beam Microscopy and Micromachining. Mrs Bulletin, 2007. Vol. 32.

98. ABAQUS, User's Manual. 2008: ABAQUS Inc., Prvidence, Rhode Island, Version 6.9.

99. Y. M. Wong, P. J. Scully, H. J. Kadim, V. Alexiou, R. J. Bartlett, Automation and dynamic characterization of light intensity with applications to tapered plastic optical fibre. Journal of Optics A-Pure And Applied Optics, 2003. Vol 5(4): p. S51-S58.

100. V. Randle, Crystallographic Characterization of Planes in The Scanning Electron-Microscope. Journal of Materials Characterization, 1995. Vol. 34(1), p. 29-34.

101. A. Franco, S. G. Roberts, and P. D. Warren, Fracture toughness, surface flaw sizes and flaw densities in Al_2O_3. Journal of Acta Materialia, 1997. Vol. 45(3): p. 1009-1015.

102. A. Franco Jr., S. G. Roberts, Surface Mechanical Analysis by Hertzian Indentation. Cerâmica, 2004. Vol. 50, p. 314.

103. Handbook, CK 10, One Tonne Testing Machine', For Microcrack detection , by engineering system (Nottm), Jule 1996.(Issue 2).

104. M. Kowaka, Introduction life prediction planet materials: application of the extreme value statistical method for corrosion analysis, New York: Allerton Press. 1994.

105. P. M. Wood, J. A. Duff, T. J. Marrow, .Imaging Autoclave Development for In-Situ Optical Measurement of High Temperature Aqueous Corrosion Processes. International Conference of Fracture 12. 2009. Ottawa, Canada.

106. J. E. Hack, G. R. Leverant, On The Prediction of the Surface Crack Opening Displacement of a part through Crack,. Int Journ of Fracture, USA 1980.

107. D. Z. Feng, Q. C. Hong, Investigation of Surface Crack Opening Displacement and Its Application In Pressure-Vessels And Piping. International Journal of Pressure Vessels And Piping, 1992. Vol 52 (2), p. 227-239.

108. V. Randle, D. Dingley, Measurement of Boundary Plane Inclination in a Scanning Electron-Microscope. Scripta Metallurgica, 1989. Vol 23 (9), p. 1565-1569.

109. P. Warren, Fracture of brittle materials: effects of test method and threshold stress on the Weibull modulus Journal of The European Ceramic Society, Mar 2001, Vol 21 (3): p. 335-342.

110. M. Iwasa, R. C. Bradt, Fracture Toughness of Single-Crystal Alumina. Structure and Properties of Mgo and Al_2O_3, Journal of American Ceramic Society, 1984. Vol. 10, P767.

111. M. V. Klassen-Neklyudova, K. S Bagdasarov, Ruby and Sapphire: A Coll, Book. Moscow, Nauka ,1974.

112. C. Jung-Hae, K. Doh-Yeon, Equilibrium shape of internal cavities in sapphire. Journal of The American Ceramic Society, 1997. Vol 80 (1), p. 62-68.

113. J. A. Kuszyk, R. C. Bradt, Influence of Grain Size on Effects of Thermal Expansion Anisotropy in MgTi,O,. Journal of the American Ceramic Society, 1973. Vol. 56 (8), p. 420-423.

114. J. J. Cleveland, R. C. Bradt, Grain Size/Microcracking Relations for Pseudobrookite Oxides. The American Ceramic Society, 1978. Vol. 61 (11-12), p. 478-481.

115. R. W. Rice, R. C. Pohanka, Grain-Size Dependence of Spontaneous Cracking in Ceramics. The American Ceramic Society, Seattle. Washington, 1979. Vol. 62 (11-12), p.559-563.

116. H. Eves, A Survey of Geometry, rev. ed., Allyn & Bacon, Boston MA, 1965.

117. N. Sridhar, W. Yanh, D. J. Srolovitz, Microstructural Mechanics Model of Anisotropic-Thermal-Expansion-Induced Microcracking. Journal of American Ceramic Society, 1994. Vol 77 (5), p. 1123-38.

118. S. G. Roberts, C. W. Lawrence, Y. Bisrat, Determination of Surface Residual Stresses in Brittle Materials by Hertzian Indentation: Theory and Experiment. Joul. AM. Ceram. Soc., 1999. Vol 82 (7), p. 1809-1816.

119. M. J. Kim, S. M. Kim, and D. Y. Yoon, “Singular Grain Boundaries in Alumina Doped with Silica,” Journal of the American Ceramic Society, vol.87, no.3, pp. 507-509, 2004.

120 S. J. Dillon, H. Miller, M. P. Harmer, and G. S. Rohrer, “Grain boundary plane distributions in aluminas evolving by normal and abnormal grain growth and displaying different complexions,” International Journal of Materials Research, vol.101, no.1, pp. 50-56, 2010.

121 N. Sabate, D. Voget, J. Keller, A. Gollhardt, J. Marcos, I Grícia, C. Cané, B. Michel , FIB-based technique for stress characterisation on thin films for reliability purposes. Microelectronic Engineering, 2007. Vol. 84 (5-8), p. 1783-1787.

122 I. Utke, P. Hoffmann, J. Melngailis, Gas-assisted focused electron beam and ion beam processing and fabrication. Journal of Vacuum Science & Technology, 2008. Vol. B 26(4), p. 1197-1276.

123 B. Bhushan, Springer Handbook of Nanotechnology. Berlin, 2004. Springer-Verlag.

124 P. K. Rastogi, Photomechanics. Berlin, London: Springer, 2000.

125 J. S. Sirkis, T. J. Lim, Displacement and strain-measurement with automated grid methods. Experimetal Mechanics, 1991. Vol 31(4), p. 382-388.

126. H. Jin, L. Wy, J. Korellis, Micro-scale deformation measurement using the digital image correlation technique and scanning electron microscope imaging. Journal of Strain Analysis for Engineering Design, 2008. Vol. 43(8), p. 719-728.

127. M. A. Sutton, N. Li, D. C. Joy, A. P. Reynolds, X. Li, Scanning electron microscopy for quantitative small and large deformation measurements Part I: SEM imaging at magnifications from 200 to 10,000. Experimental Mechanics, 2007. Vol. 47 (6), p. 775-787.

128. K. Shigeno, H. Katsumura, H. Kagata, H. Asano, O. Inoue, Low Temperature Sintering of Alumina by CuO_2-TiO_2-Nb_2O_5 Additives, Journal of Key Engineering Materials, 2006, Vol. 320, P. 181-184.

Appendix A: Microstructure Analysis

Figure A-1 shows images taken by optical microscope after sample preparation for the P-I and Cr-I specimens. Figure A-2 shows images taken by scanning electron microscope for thermally etched and gold coated samples. The microstructure shows pores, labelled with arrows and grains shapes. Figure A-3 shows the examples of a micro-crack due to anisotropy coefficient of the thermal expansion in the P-I sample along its boundary.

The P-I and Cr-I specimens were only available with dimensions smaller than the dimensions necessary for four point bending samples that were used for digital image correlation experiments.

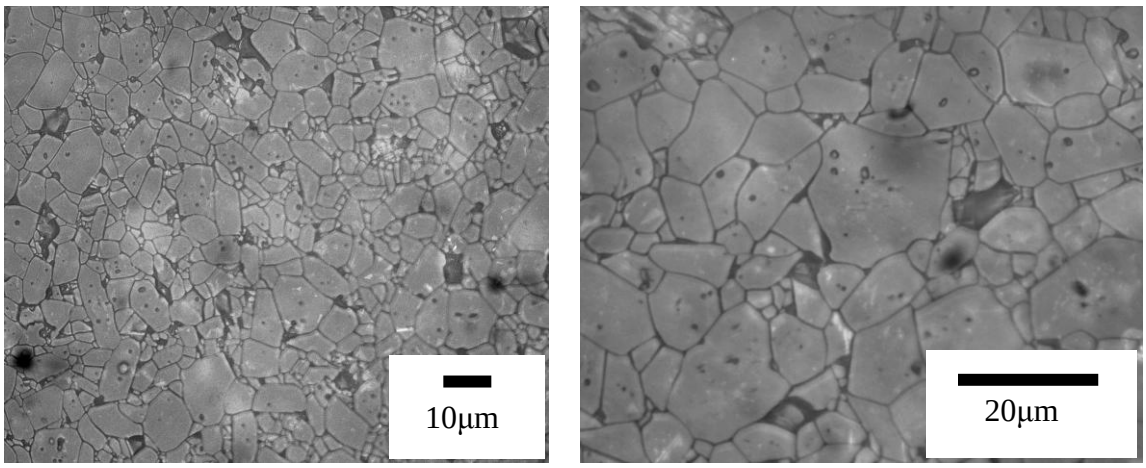

a) **b)**

Figure A-1: Optical images for the polycrystalline alumina samples, a) P-I Specimen, and b) Cr-I Specimen after thermal etching.

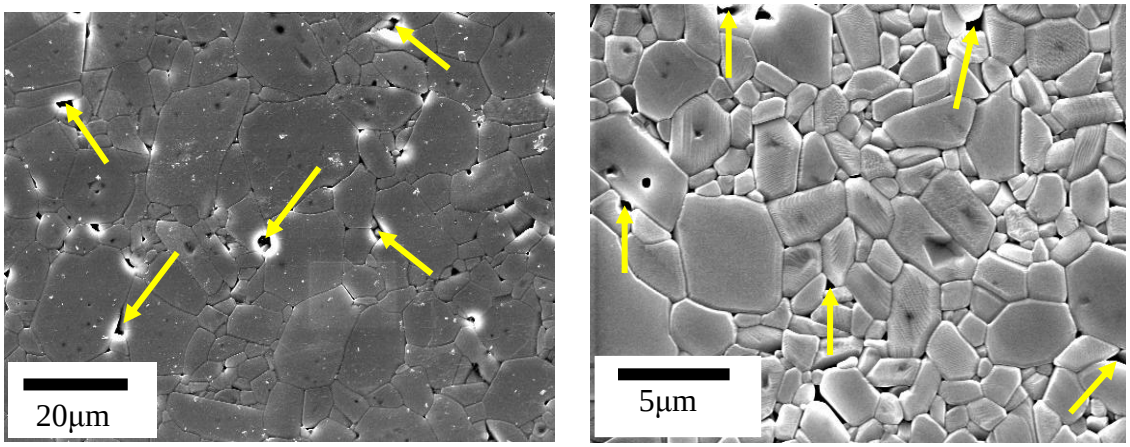

a) **b)**

Figure A-2: Scanning electron microscope images for the polycrystalline samples a) P-I specimen, and b) Cr-I specimen. The samples were prepared by thermal etching and gold coating.

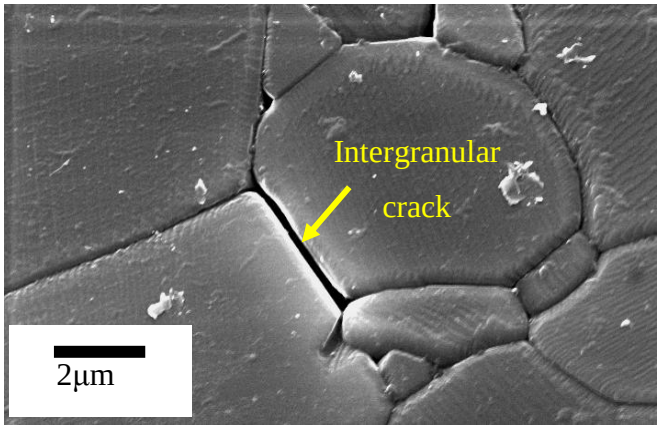

Figure A-3: Scanning electron microscope image showing the microcrack at grain boundary in the P-I sample.

The local orientation map for different samples is shown in Figure A-4. The EBSD maps of the P-I and Cr-I samples.

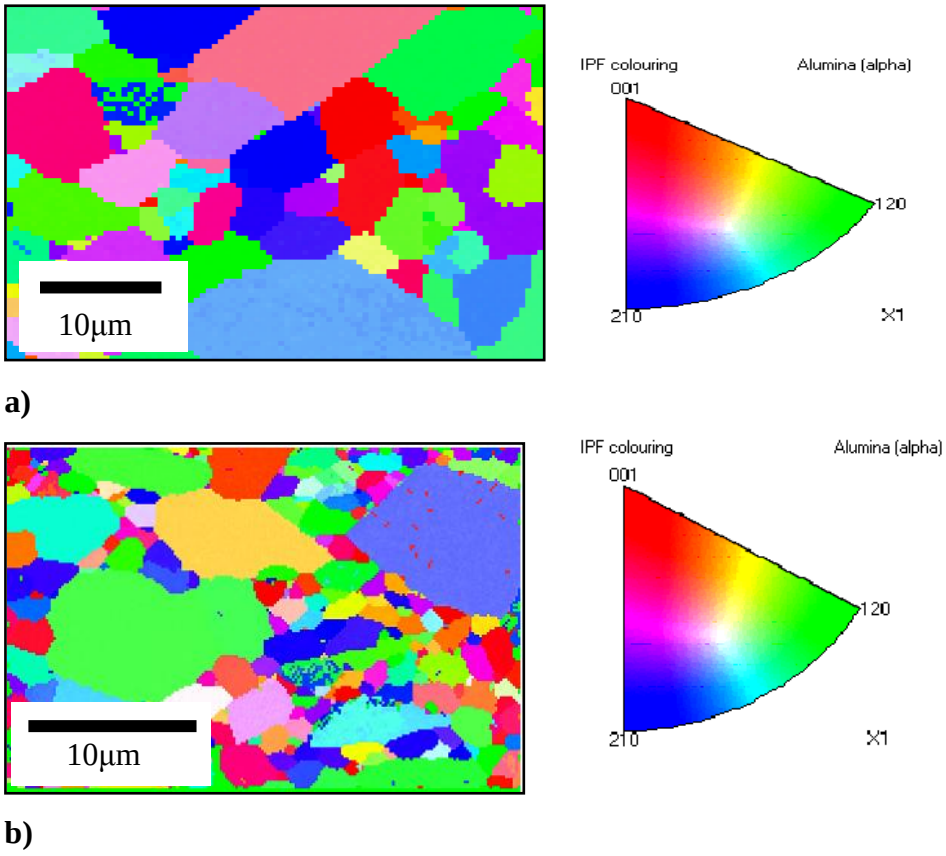

Figure A-4: Electron back scattered diffraction, EBSD maps for the polycrystalline alumina samples a) P-I specimen, and d) Cr-I specimen at step size (0.2 µm) and the level of indexing achieved was about (60% to 70%).

Appendix B: Grain Boundary Plane Analysis

The focused ion beam, FIB and electron backscatter diffraction, EBSD analysis and trace analysis of grain boundaries was used to obtain the orientation the grain boundary planes for the P-II and Cr-II samples are shown in Figure B-1. Pole figures for the grain boundaries plane, G34 and G45 of the common facet plane in the polycrystalline alumina and the grain boundary plane pole is not close to the basal plane (0001) facet plane of the grains G3, G4 or G5 in the P-II and Cr-II sample for the boundaries did not observe crack on these boundaries (non–cracked boundary).

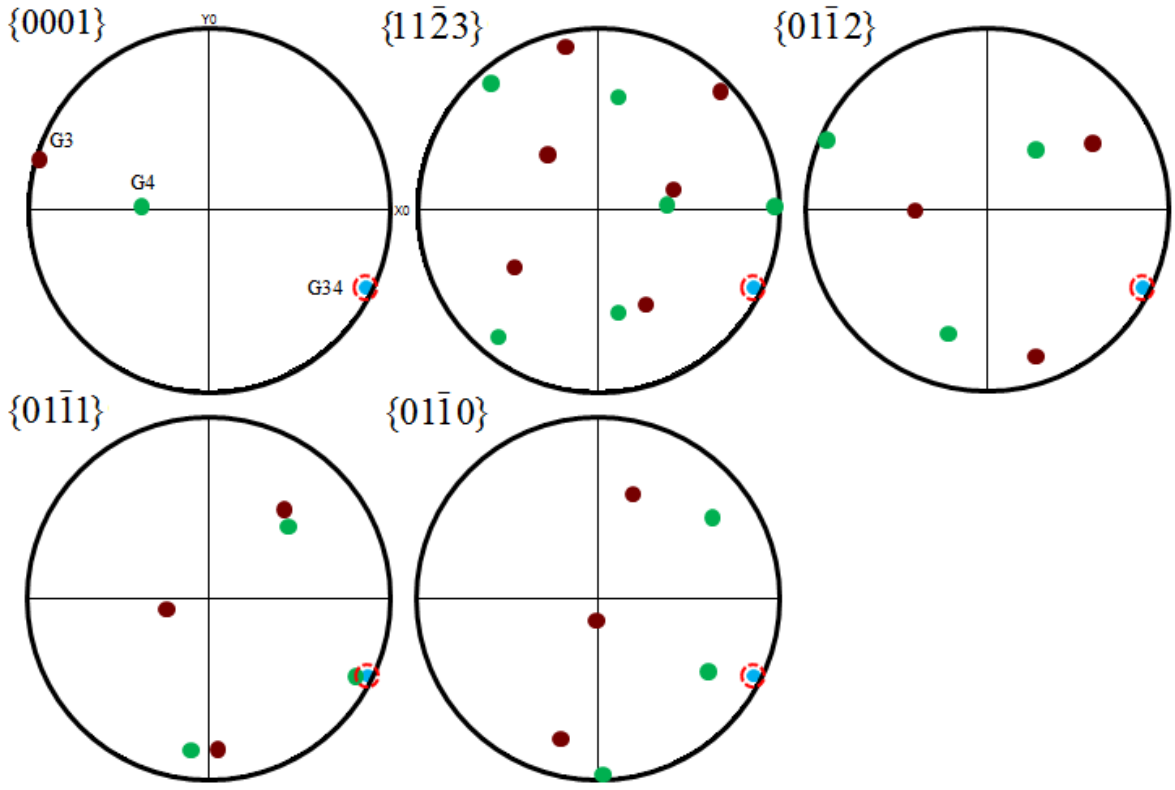

a) Non-cracked boundary in the strain feature A region in P-II Sample

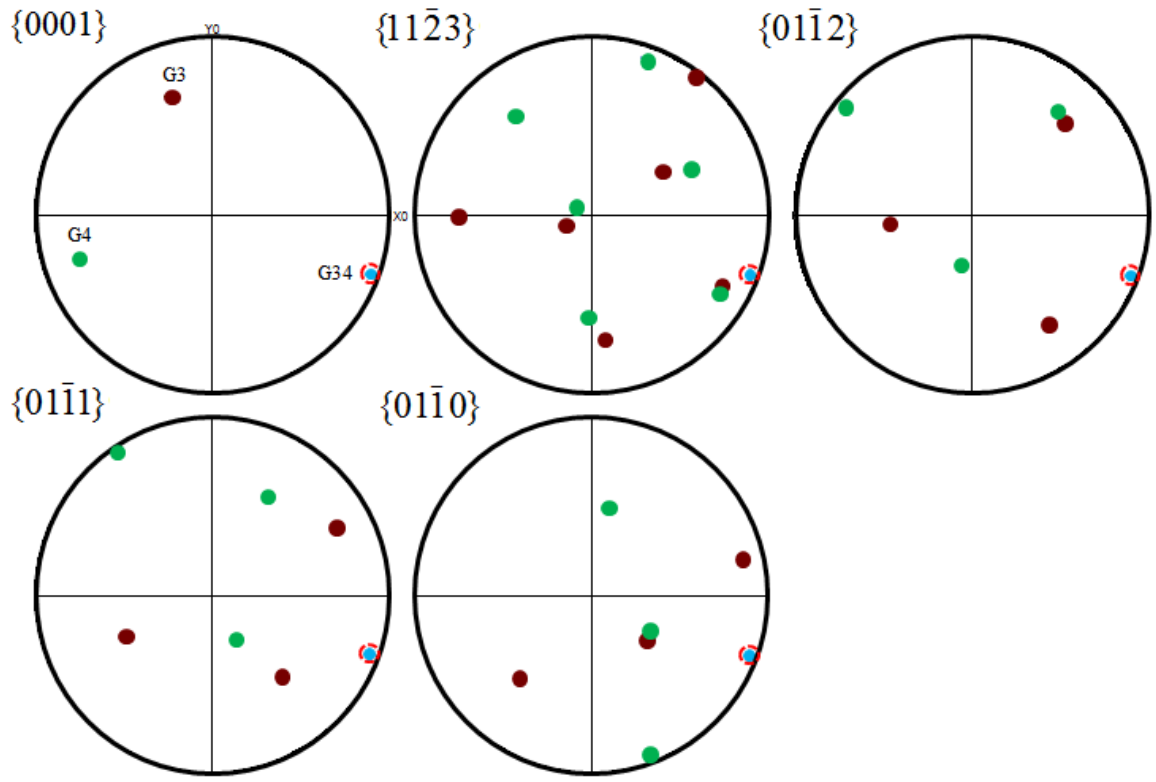

b) Non-cracked boundary in the strain feature B region in P-II Sample

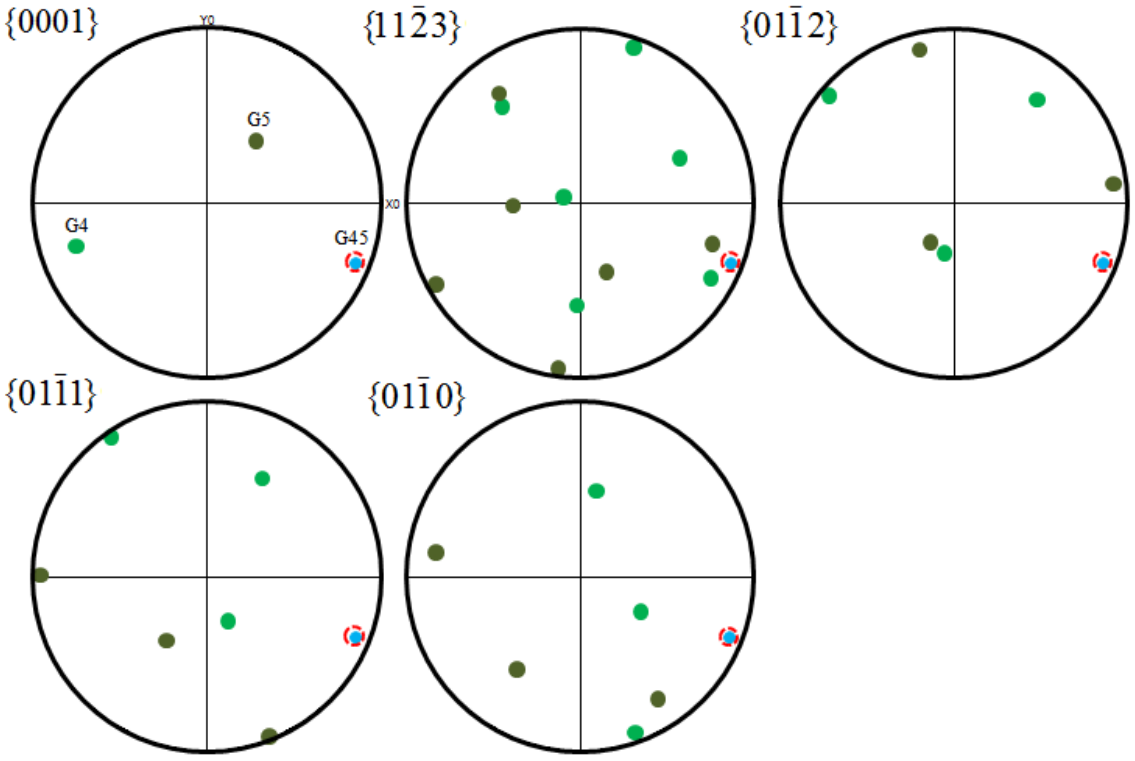

c) Non-cracked boundary in the strain feature B region in P-II Sample

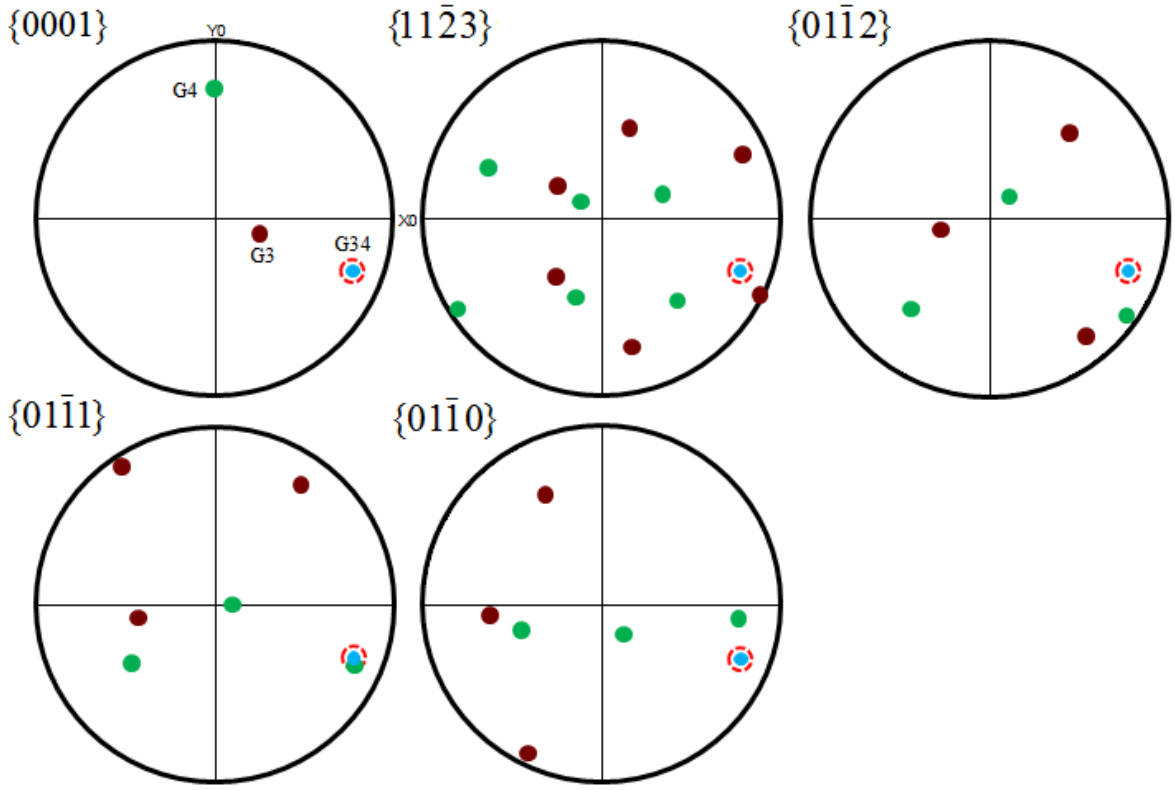

d) Non-cracked boundary in the strain feature region in Cr-II Sample

Figure B-1: Pole figures for the grain boundaries plane, G34 and G45 of the common facet plane in the polycrystalline alumina and the grain boundary plane is not near the (0001) facet plane in the G3, G4 or G5 for a) Non cracked boundary in region of the strain feature A in the P-II sample, b, c) Non cracked boundary in the region of the strain feature B in the P-II sample, and d) Non cracked boundary in the region of the strain feature in the Cr-II sample.

There is no relationship between cracking boundaries and misorientation across the boundary (see Figure B-2).

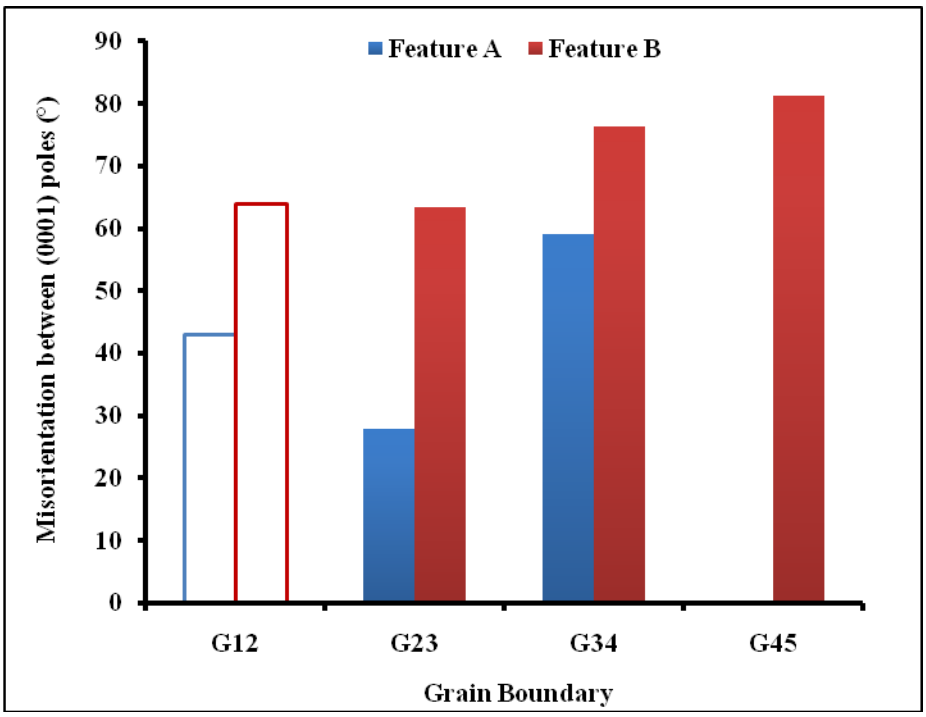

a)

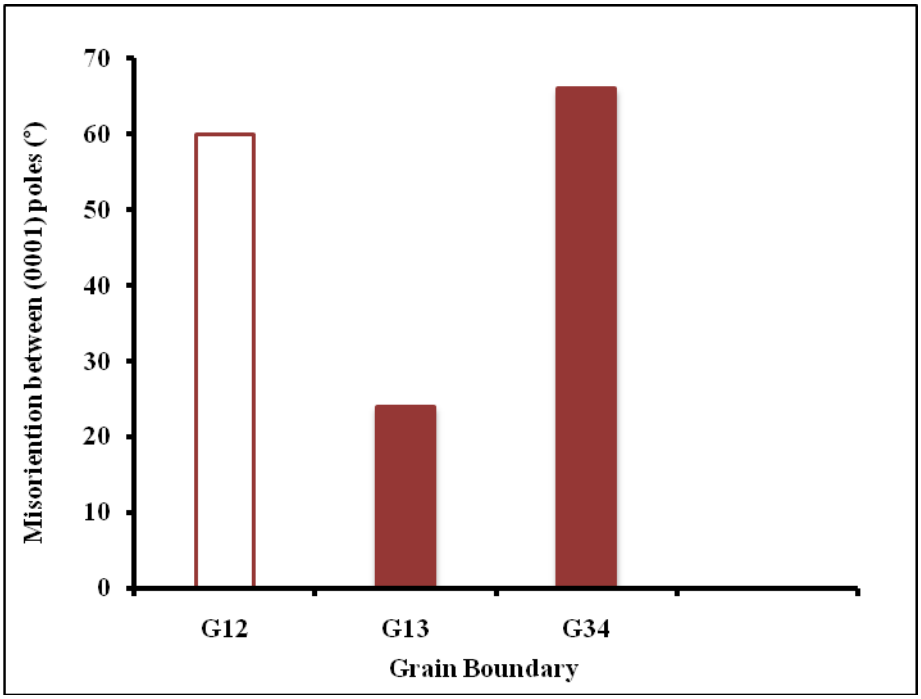

b)

Figure B-2: Shows the misorientation between grains as a function of the grain boundary for a) strain feature A and strain feature B in P-II sample and b) strain feature in Cr-II sample. (Hollow bars show the crack boundaries).

Data for the range for the angles between the grain boundary poles and the pole for the basal facet plane (0001) and the misorientation between the basal poles of adjacent grains are given. The results have been explained in Table B-1 to Table B-8 showing the average angle between the grain boundary plane pole and the neatest crystallographic pole.

Table B-1: Shows the angles between the grain boundary pole and the pole for the facet plane (0001) at alpha angle, α (76°, 87°) and beta angle, β (86°, 89°) for the strain feature A and strain feature B respectively in the P-II sample.

Location	Grain Boundary & Grains		Grain Size (µm)	Angle between (0001) poles	Angle between the grain boundary pole and the crystallographic pole (0001)	Observation
Feature A	G12	G1	2.34	137.5°	**6.0°**	**Cracked**
		G2	1.89		20.0°	
	G23	G2	1.89	28.0°	20.5°	Not cracked
		G3	1.95		6.0°	
	G34	G3	1.67	59.5°	9.0°	Not cracked
		G4	2.00		61.0°	
Feature B	G12	G1	3.25	116.0°	29.0°	**Cracked**
		G2	3.29		37.0°	
	G23	G2	2.98	117.0°	20.0°	Not cracked
		G3	0.69		53.0°	
	G34	G3	0.79	76.5°	56.0°	Not cracked
		G4	0.69		40.5°	
	G45	G4	0.96	99.0°	40.0°	Not cracked
		G5	2.18		75.0°	

Table B-2: Shows the angles between the grain boundary pole and the pole for the facet plane (0001) at alpha angle, α (76°, 87°) and beta angle, β (82°, 85°) for the strain feature A and strain feature B respectively in the P-II sample.

Location	Grain Boundary & Grains		Grain Size (μm)	Angle between (0001) poles	Angle between the grain boundary pole and the crystallographic pole (0001)	Observation
Feature A	G12	G1	2.34	137.5°	**4.5°**	**Cracked**
		G2	1.89		16.0°	
	G23	G2	1.89	28.0°	17.5°	Not cracked
		G3	1.95		9.0°	
	G34	G3	1.67	59.5°	10.0°	Not cracked
		G4	2.00		58.0°	
Feature B	G12	G1	3.25	116.0°	24.5°	**Cracked**
		G2	3.29		36.0°	
	G23	G2	2.98	117.0°	16.0°	Not cracked
		G3	0.69		51.5°	
	G34	G3	0.79	76.5°	52.5°	Not cracked
		G4	0.69		40.0°	
	G45	G4	0.96	99.0°	39.5°	Not cracked
		G5	2.18		75.5°	

Table B-3: Shows the angles between the grain boundary pole and the pole for the facet plane (0001) at alpha angle, α (70°, 83°) and beta angle, β (82°, 85°) for the strain feature A and strain feature B respectively in the P-II sample.

Location	Grain Boundary & Grains		Grain Size (μm)	Angle between (0001) poles	Angle between the grain boundary pole and the crystallographic pole (0001)	Observation
Feature A	G12	G1	2.34	137.5°	**5.5°**	**Cracked**
		G2	1.89		18.0°	
	G23	G2	1.89	28.0°	21.5°	Not cracked
		G3	1.95		4.0°	
	G34	G3	1.67	59.5°	12.0°	Not cracked
		G4	2.00		62.0°	
Feature B	G12	G1	3.25	116.0°	28.0°	**Cracked**
		G2	3.29		36.0°	
	G23	G2	2.98	117.0°	19.0°	Not cracked
		G3	0.69		51.5°	
	G34	G3	0.79	76.5°	54.5°	Not cracked
		G4	0.69		44.0°	
	G45	G4	0.96	99.0°	44.0°	Not cracked
		G5	2.18		78.5°	

Table B-4: Shows the angles between the grain boundary pole and the pole for the facet plane (0001) at alpha angle, α (70°, 83°) and beta angle, β (86°, 89°) for the strain feature A and strain feature B respectively in the P-II sample.

Location	Grain Boundary & Grains		Grain Size (µm)	Angle between (0001) poles	Angle between the grain boundary pole and the crystallographic pole (0001)	Observation
Feature A	G12	G1	2.34	137.5°	**3.0°**	**Cracked**
		G2	1.89		16.0°	
	G23	G2	1.89	28.0°	18.5°	Not cracked
		G3	1.95		8.0°	
	G34	G3	1.67	59.5°	13.5°	Not cracked
		G4	2.00		59.0°	
Feature B	G12	G1	3.25	116.0°	25.0°	**Cracked**
		G2	3.29		34.5°	
	G23	G2	2.98	117.0°	17.0°	Not cracked
		G3	0.69		47.0°	
	G34	G3	0.79	76.5°	50.0°	Not cracked
		G4	0.69		43.0°	
	G45	G4	0.96	99.0°	43.0°	Not cracked
		G5	2.18		77.0°	

Table B-5: Shows the angles between the grain boundary pole and the pole for the facet plane (0001) at alpha angle, α (107°) and beta angle, β (71°) for the strain feature in the Cr-II sample.

Location	Grain Boundary & Grains		Grain Size (µm)	Angle between (0001) poles	Angle between the grain boundary pole and the crystallographic pole (0001)	Observation
Strain Feature	G12	G1	6.5	60°	65.0°	**Cracked**
		G2	1.2		11.0°	
	G13	G1	6.5	24°	56.0°	Not cracked
		G3	2.1		47.0°	
	G34	G3	2.1	66°	46.0°	Not cracked
		G4	4.5		65.0°	

Table B-6: Shows the angles between the grain boundary pole and the pole for the facet plane (0001) at alpha angle, α (107°) and beta angle, β (65°) for the strain feature in the Cr-II sample.

Location	Grain Boundary & Grains		Grain Size (μm)	Angle between (0001) poles	Angle between the grain boundary pole and the crystallographic pole (0001)	Observation
Strain Feature	G12	G1	6.5	60°	63.0°	**Cracked**
		G2	1.2		9.5°	
	G13	G1	6.5	24°	54.0°	Not cracked
		G3	2.1		43.0°	
	G34	G3	2.1	66°	44.0°	Not cracked
		G4	4.5		62.0°	

Table B-7: Shows the angles between the grain boundary pole and the pole for the facet plane (0001) at alpha angle, α (99°) and beta angle, β (65°) for the strain feature in the Cr-II sample.

Location	Grain Boundary & Grains		Grain Size (μm)	Angle between (0001) poles	Angle between the grain boundary pole and the crystallographic pole (0001)	Observation
Strain Feature	G12	G1	6.5	60°	64.5°	**Cracked**
		G2	1.2		10.5°	
	G13	G1	6.5	24°	57.0°	Not cracked
		G3	2.1		48.0°	
	G34	G3	2.1	66°	47.0°	Not cracked
		G4	4.5		66.0°	

Table B-8: Shows the angles between the grain boundary pole and the pole for the facet plane (0001) at alpha angle, α (99°) and beta angle, β (71°) for the strain feature in the Cr-II sample.

Location	Grain Boundary & Grains		Grain Size (μm)	Angle between (0001) poles	Angle between the grain boundary pole and the crystallographic pole (0001)	Observation
Strain Feature	G12	G1	6.5	60°	62.0°	**Cracked**
		G2	1.2		9.0°	
	G13	G1	6.5	24°	53.0°	Not cracked
		G3	2.1		45.0°	
	G34	G3	2.1	66°	43.0°	Not cracked
		G4	4.5		61.0°	

Appendix C: Hertzian Indentation Analysis

Figure C-1a shows the relationship between the maximum and minimum ring crack radius against the applied load for Warren's data. The Figure C-1a shows the equations were applied correctly by comparing the calculated values with values read from the plots in the Warren's paper [109]. Figure C-1b shows the good agreement between the plots was measured using Warren's data with the plot was plotted by read from the plots in [109].

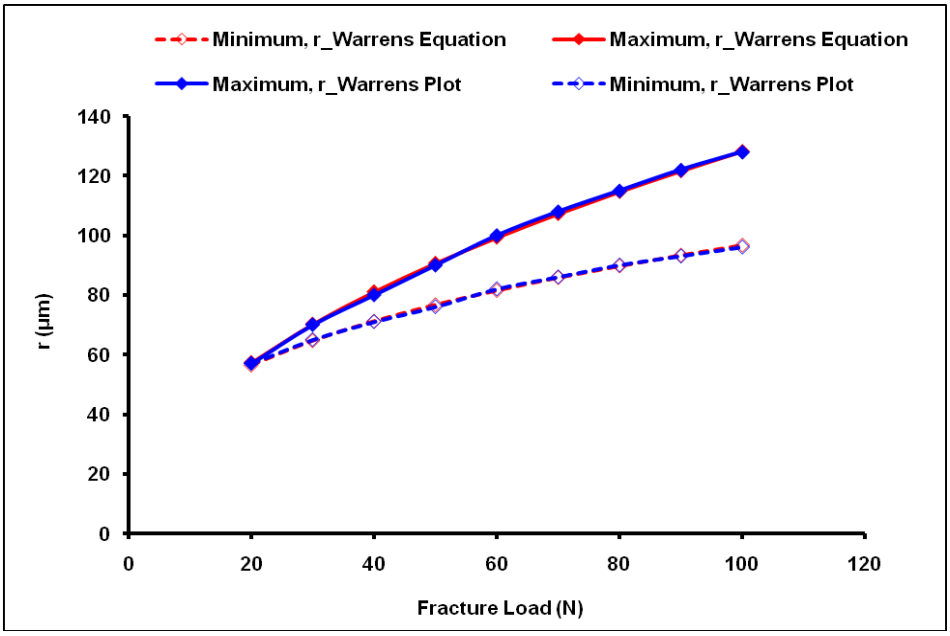

a)

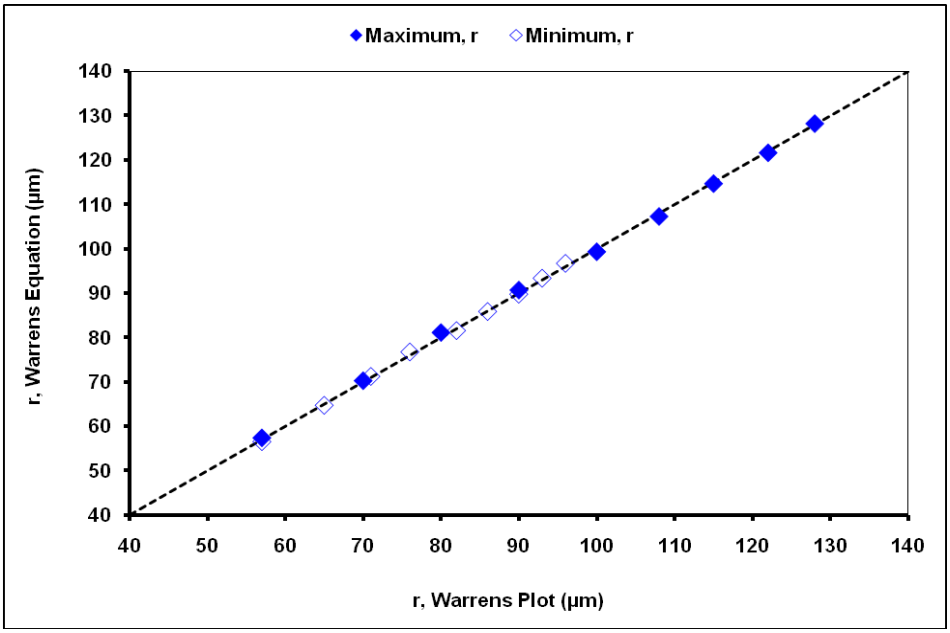

b)

Figure C-1: a) Shows the minimum (r_{min}) and maximum (r_{max}) ring crack radius at stress intensity factor is equal to the fracture toughness versus of applied load. The sphere radius is 2.5 mm sphere radius is 2.5 mm and crack depth is 4 µm. The mechanical properties for this test are ν = 0.24, E = 390 GPa and K_{IC} = 2MPa.m$^{1/2}$ [109] b) shows the correlation of the ring crack radius between the Warren's data and Warren's equation [109].

Figure C-2 shows the results for each of the four indenter sizes (r = 2.5, 5, 10, and 20 mm). The plot used to find the fracture load for each indenter at different sphere radius.

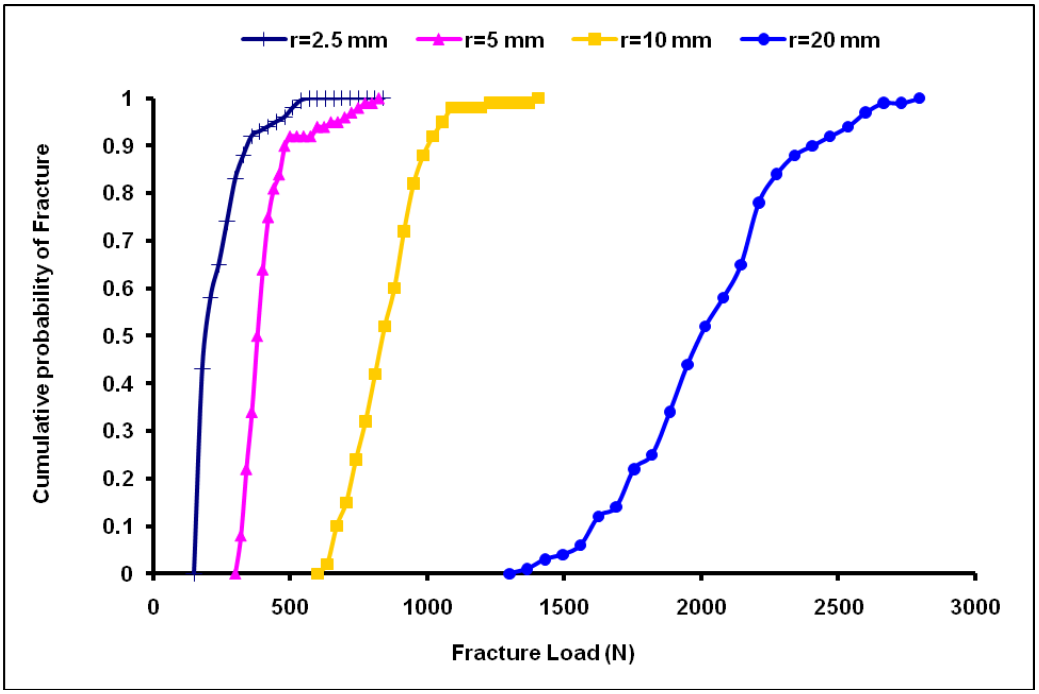

Figure C-2: Shows cumulative probability of failure at different sphere radius against failure load in the Hertzian indentation experiment [109].

Figure C-3 shows the equations were applied correctly by comparing the calculated values with values read from the plots in paper [109] for the small defect size but there is no match between the calculated values with the values read from paper [109] for the large defect size due to Warren used the equations to measure flaw density for small defect size and Warren replaced the equations by a summation. Warren used computer simulation of Hertzian indentation for measuring flaw densities for large defect size [109].

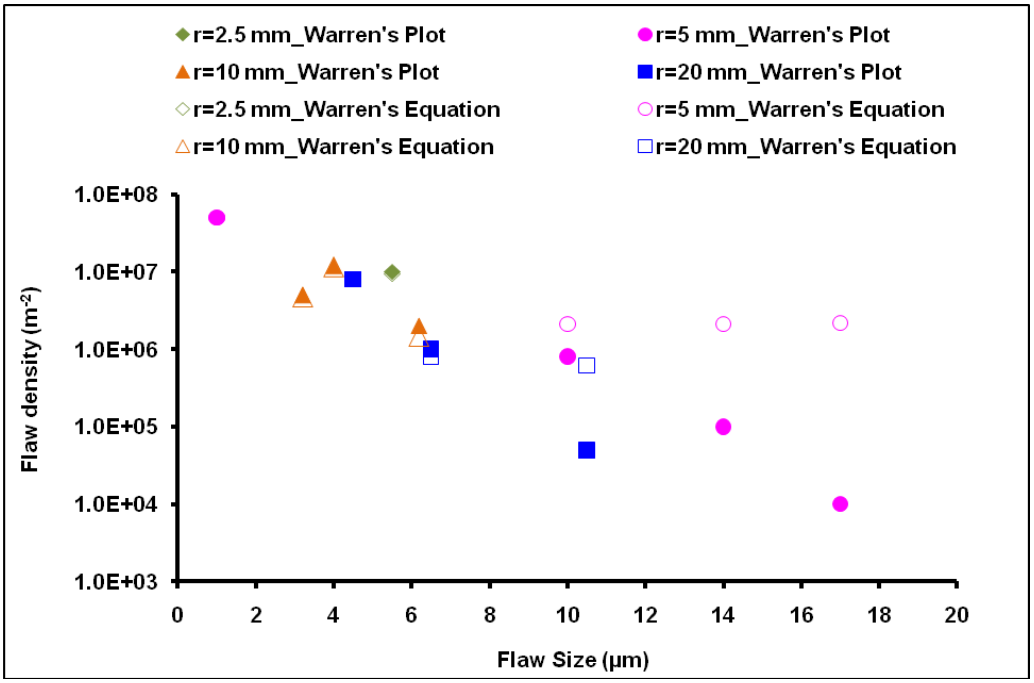

a)

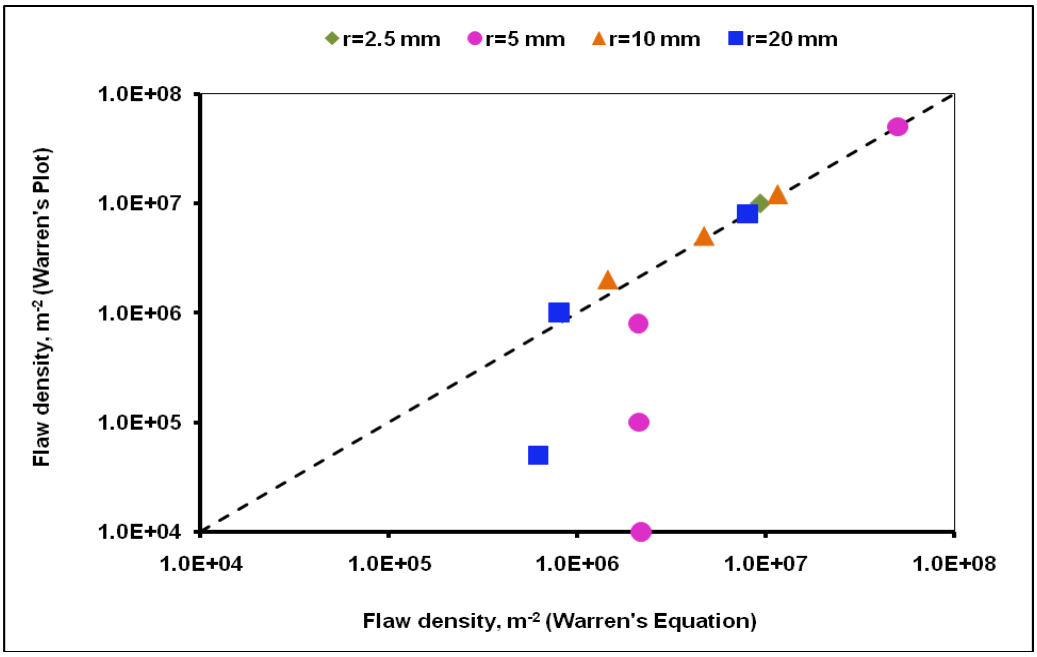

b)

Figure C-3: a) Shows the flaw density calculated from the searched area at different radii against the flaw size for the Warren's data and Warren's plot. B) shows the correlation of the flaw density between the Warren's data and Warren's plot [109].

Appendix D: Atomic Force Microscope

The depth of the thermal groove was measured using an atomic force microscope (AFM) and it was very small then the stress intensity factor (stress concentrator) is negligible. The depth of the thermal groove is 32.22 nm and 21.82 nm for the strain feature A and strain feature B respectively in the P-II sample (see Figure D-1). The depth of the thermal groove was measured using AFM much less than the crack depth was measured using digital image correlation experiments and Hertzian testing.

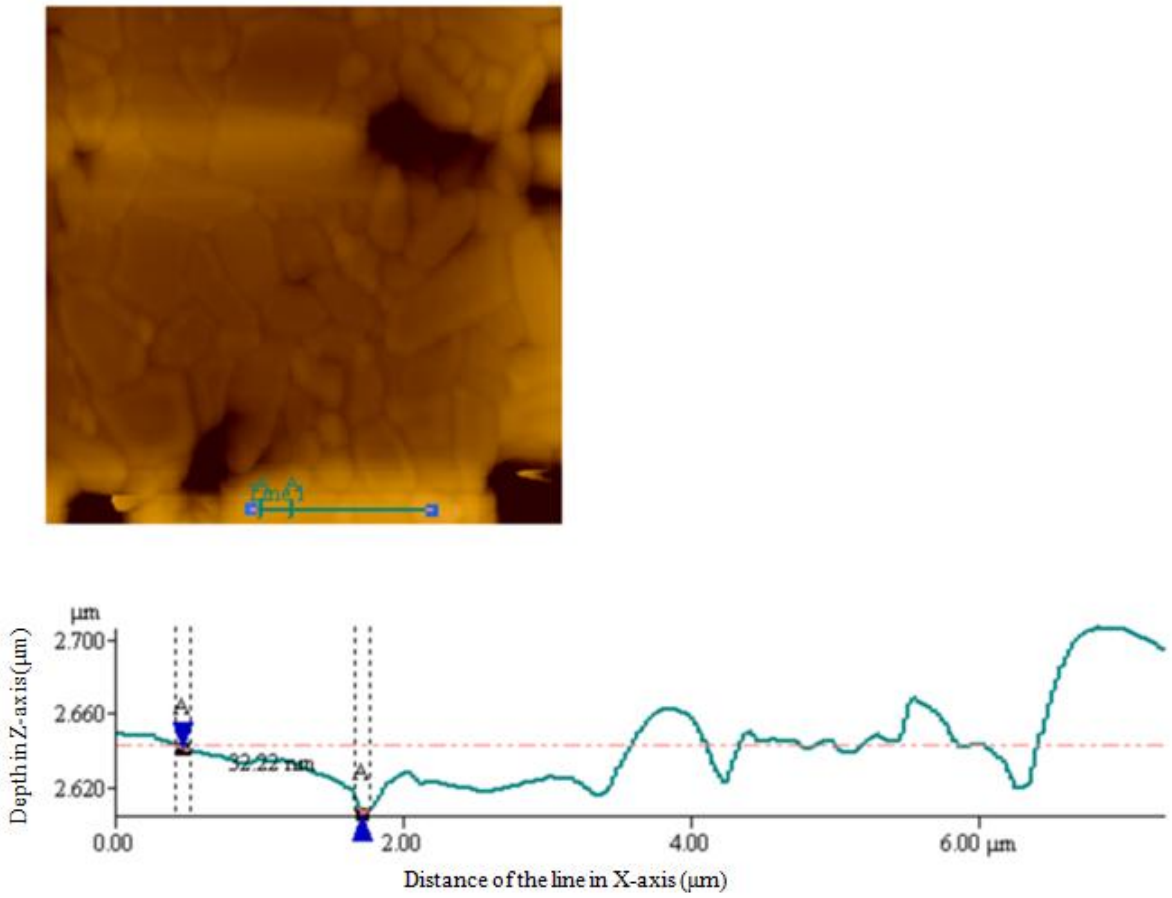

a) Strain Feature A

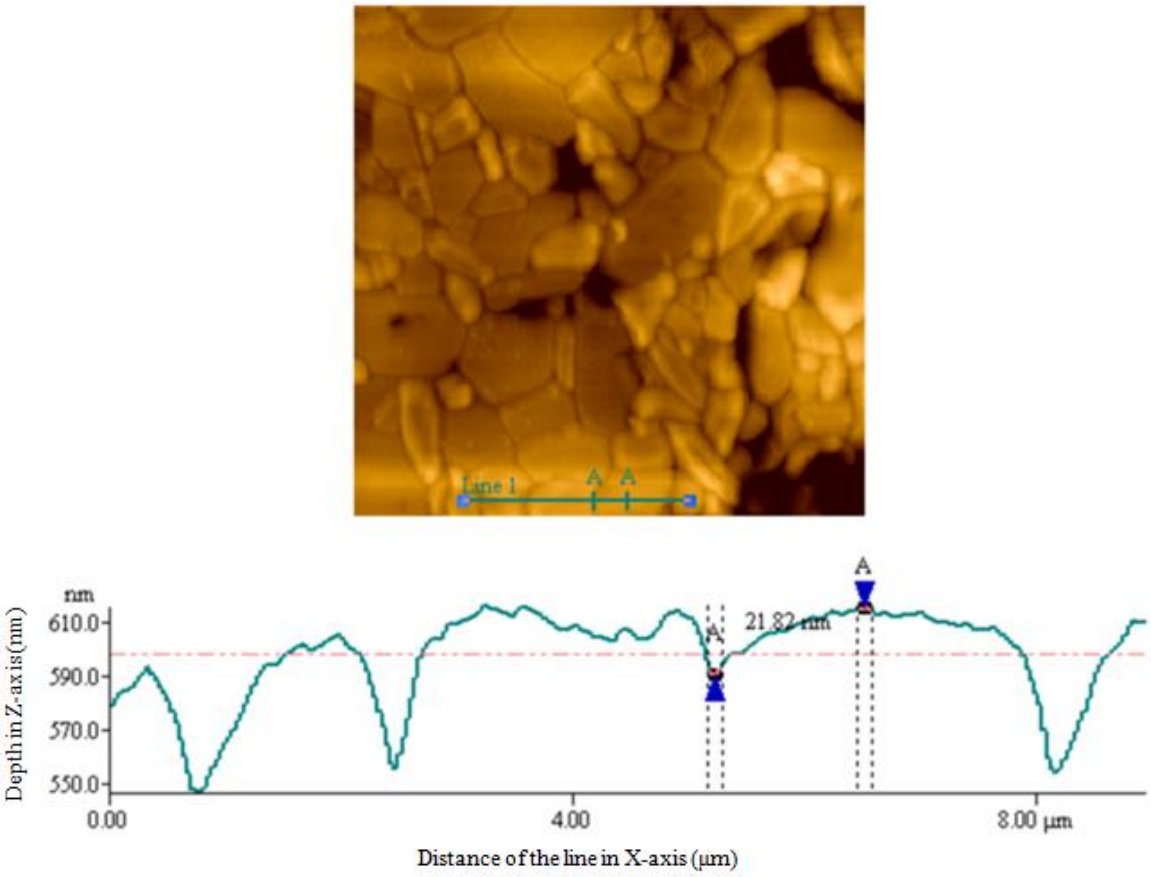

b) Strain Feature B

Figure D-1: Shows the atomic force microscope data for measuring the depth of the thermal groove for the a) strain feature A in P-II sample and b) strain feature B in P-II sample.

Appendix E: List of Publications

1) **M. A. Aswad** and T.J. Marrow: Intergranular Crack Nucleation in Polycrystalline Alumina. Submitted to the Journal of Engineering Fracture Mechanics.
2) T. James Marrow, David Gonzalez, **Mohsin Aswad**, Joao Quinta da Fonseca, Philip J. Withers: In-situ observation and modelling of intergranular cracking in polycrystalline alumina. Journal of Key Engineering Materials Vol. 465 (2011) pp 560-563.
3) **M. A. Aswad** and T. J. Marrow: Intergranular Crack Nucleation in Polycrystalline Alumina. 18th European Conference on Fracture, ECF 18, in Dresden, Germany August 30- September 03, 2010.
4) T. J. Marrow, **M. A. Aswad**, J. Q. Fonseca, and P. J. Withers, In-situ observation and modelling of intergranular cracking in polycrystalline alumina. Sixth international conference on Materials Structure & Micromechanics of Fracture (MSMF6), Brno, Czech Republic, June 28 - 30, 2010.
5) **M. A. Aswad** and T. J. Marrow: Indirect Observation of Defect Size and Density using Hertzian Test.